

Acquisitions and Bibliographic Services Branch

395 Wellington Street Ottawa, Ontario K1A 0N4 Bibliothèque nationale du Canada

Direction des acquisitions et des services bibliographiques

395, rue Wellington Ottawa (Ontario) K1A 0N4

Your life. Votre référence

Our life Notre référence

NOTICE

The quality of this microform is heavily dependent upon the quality of the original thesis submitted for microfilming. Every effort has been made to ensure the highest quality of reproduction possible.

La qualité de cette microforme dépend grandement de la qualité de la thèse soumise au microfilmage. Nous avons tout fait pour assurer une qualité supérieure de reproduction.

AVIS

If pages are missing, contact the university which granted the degree.

S'il manque des pages, veuillez communiquer avec l'université qui a conféré le grade.

Some pages may have indistinct print especially if the original pages were typed with a poor typewriter ribbon or if the university sent us an inferior photocopy.

La qualité d'impression de certaines pages peut laisser à désirer, surtout si les pages originales ont été dactylographiées à l'aide d'un ruban usé ou si l'université nous a fait parvenir une photocopie de qualité inférieure.

Reproduction in full or in part of this microform is governed by the Canadian Copyright Act, R.S.C. 1970, c. C-30, and subsequent amendments.

 $\mathcal{G}_{\mathcal{F}}$

La reproduction, même partielle, de cette microforme est soumise à la Loi canadienne sur le droit d'auteur, SRC 1970, c. C-30, et ses amendements subséquents.

Canadä

Uniqueness and Variability of the Ocean's Thermohaline Circulation

by

Tertia M.C. Hughes

Department of Atmospheric and Oceanic Sciences and Centre for Climate and Global Change Research McGill University, Montréal March, 1995

A thesis submitted to the Faculty of Graduate Studies and Research in partial fulfillment of the requirements for the degree of Doctor of Philosophy.

© Copyright Tertia M.C. Hughes, 1995.



National Library of Canada

Acquisitions and Bibliographic Services Branch

395 Wellington Street Ottawa, Ontario K1A 0N4 Bibliothèque nationale du Canada

Direction des acquisitions et des services bibliographiques

395, rue Wellington Ottawa (Ontario) K1A 0N4

Your file Votre rélérence

Our file Notre référence

THE AUTHOR HAS GRANTED AN IRREVOCABLE NON-EXCLUSIVE LICENCE ALLOWING THE NATIONAL LIBRARY OF CANADA TO REPRODUCE, LOAN, DISTRIBUTE OR SELL COPIES OF HIS/HER THESIS BY ANY MEANS AND IN ANY FORM OR FORMAT, MAKING THIS THESIS AVAILABLE TO INTERESTED PERSONS.

L'AUTEUR A ACCORDE UNE LICENCE IRREVOCABLE ET NON EXCLUSIVE PERMETTANT A LA BIBLIC THEQUE NATIONALE DU CANADA DE REPRODUIRE, PRETER, DISTRIBUER OU VENDRE DES COPIES DE SA THESE DE QUELQUE MANIERE ET SOUS QUELQUE FORME QUE CE SOIT POUR METTRE DES EXEMPLAIRES DE CETTE THESE A LA DISPOSITION DES PERSONNE INTERESSEES.

THE AUTHOR RETAINS OWNERSHIP OF THE COPYRIGHT IN HIS/HER THESIS. NEITHER THE THESIS NOR SUBSTANTIAL EXTRACTS FROM IT MAY BE PRINTED OR OTHERWISE REPRODUCED WITHOUT HIS/HER PERMISSION.

L'AUTEUR CONSERVE LA PROPRIETE DU DROIT D'AUTEUR QUI PROTEGE SA THESE. NI LA THESE NI DES EXTRAITS SUBSTANTIELS DE CELLE-CI NE DOIVENT ETRE IMPRIMES OU AUTREMENT REPRODUITS SANS SON AUTORISATION.

ISBN 0-612-05723-2



Abstract

A numerical modelling approach is chosen to study equilibrium and timedependent aspects of the ocean's thermohaline circulation. In the first part, the roles of basin geometry and surface buoyancy forcing in determining the asymmetry of the present-day thermohaline circulation are considered. An idealized flat-bottomed two-basin model of the Atlantic and Pacific is found to favour equilibria with sinking in the southern hemisphere only (Southern Sinking) or also in the North Atlantic (Conveyor), even under a freshwater flux forcing field with more precipitation over the North Atlantic than over the North Pacific.

Another new result is the range of *Conveyor* equilibria found under mixed boundary conditions. Rare cases with North Pacific sinking are characterized by a very fresh halocline in the Southern Ocean and a reversed pole-to-pole surface density contrast. A more quantitative investigation leads to an approximately linear relationship between the Atlantic overturning and the meridional gradient of zonally-averaged depth-integrated steric height from the northern boundary of the ocean to the southern tip of Africa; on the other hand, the local linear relationships postulated in most two-dimensional plane models of the overturning circulation could not be validated.

In the second part, the climatology of a global ocean model is presented, and the importance in the model of the warm water route of the *Conveyor* through the Indian Ocean relative to the cold water route through Drake Passage is noted. The implied ocean heat and freshwater transports from the Canadian Climate Centre second generation atmospheric general circulation model are then presented, and are shown to be incompatible with the present-day thermohaline circulation.

Finally, in the third part, a simple new parameterization of the sea surface temperature-evaporation feedback is developed as an extension of the traditional mixed boundary conditions. The positive sign of the feedback for the thermohaline circulation is demonstrated, and three examples featuring decadal, century and millennial timescale variability in one-hemisphere idealized basins are discussed. No fundamental alterations of the mechanisms under mixed boundary conditions are found, although the timescale is altered or the variability interrupted sooner in some cases.

Résumé

Une approche numérique est choisie pour modéliser la circulation thermohaline dans l'océan, à l'équilibre et variable dans le temps. Dans la première partie, les rôles de la géometrie du bassin et des flux de densité à la surface sont considérés par rapport à l'asymétrie de la circulation thermohaline actuelle. Il est démontré qu'un modèle idéalisé de deux bassins (Atlantique et Pacifique) à fond plat favorise une circulation à l'équilibre où l'eau profonde se renouvelle uniquement dans l'hémisphere sud ou aussi dans l'Atlantique nord, et ce même en présence d'un excès de précipitation dans l'Atlantique nord qui dépasse celui dans le Pacifique nord.

Un autre résultat nouveau est la gamme de circulations différentes avec renouvellement de l'eau profonde dans l'Atlantique nord possibles sous un même champ de précipitation moins évaporation. De rares cas avec formation d'eau profonde dans le Pacifique nord sont caractérisés par une très basse salinité de la halocline dans l'océan Antarctique et un gradient inverse de la densité à la surface entre les extremités nord et sud du bassin. Une enquête plus quantitative révèle une relation approximativement linéaire entre la circulation thermohaline dans l'Atlantique et le gradient méridional de la profondeur dynamique de la limite nord de l'océan jusqu'à l'extremité sud de l'Afrique; cependant, les relations linéaires et locales postulées dans la plupart des modèles à deux dimensions de la circulation méridionale n'ont pas pu être validées.

Dans la deuxième partie, la climatologie d'un modèle de l'océan global est présentée, et l'importance du trajet de la circulation thermohaline à travers l'océan Indien comparé au trajet empruntant le détroit de Drake est notée. Les transports méridionaux de chaleur et d'eau fraîche dans l'océan déduits du modèle atmosphérique de circulation générale (2^e génération) du Centre canadien pour le climat sont ensuite présentés, et il est démontré qu'ils sont incompatibles avec la circulation thermohaline actuelle.

Enfin, dans la troisième partie, une nouveile paramétrisation de l'interaction entre la température à la surface de l'océan et l'évaporation est développée comme une extension des conditions à la surface mixtes traditionnelles. L'amplification en boucle de la circulation thermohaline est démontrée, et trois exemples de variabilité interne avec des périodes de décennies, de siècles ou de millénaires dans des bassins idéalisés à un seul hémisphere sont discutés. Aucune différence fondamentale par rapport aux mécanismes sous conditions mixtes n'est trouvée, sauf que la période est changée ou la variabilité est interrompue plus rapidement dans certains cas.

Table of Contents

Al	ostrac	t i
Ré	sumé	iii
Ta	ble o	f Contents
St	ateme	nt of Originality
Ac	know	ledgements
Li	st of '	Tables
1.	Intro	oduction
	1.2. 1.3. 1.4.	Equilibrium Theories of the Thermohaline Circulation
2.	Mult	iple Equilibria of an Asymmetric Two-Basin Model
	2.2. 2.3. 2.4.	Spin-ups under Restoring Boundary Conditions
3.	Clim	atology of a Global Ocean Model
	3.2. 3.3.	Spin-up under Restoring Boundary Conditions
4.	Sea S	Surface Temperature - Evaporation Feedback
		Diagnosing Evaporation from the Surface Heat Flux



		4.2.1.	Prelin	ninary	expe	erime	ents		 									.138
	4.3.	Decada	al Vari	ability	/ ·				 									.149
			Under															
		4.3.2.	With	evapo	rativ	e fee	dbac	ck .	 									161
	4.4.	Centur	y Time	escale	Vari	abili	ty .		 									. 168
		Millen																
			Under															
		4.5.2.	With	evapo	rativ	e fee	d'Jac	ck 179
5.	Conc	lusions			• • • •				 . 									193
Ap	pend	ix A	• • • •	• • • •		• • •	• • •	• • •	 • •	• •	• • •	••	• •	• •	• •	• •	• •	.197
Ap	pend	ix B	• • • • •	• • • •				• • •	 	••	• • •	• •	• •	• •	••	••	• •	.199
Ref	feren	CES																202

Statement of Originality

The contributions to original knowledge in this thesis are the following:

Chapter 2

- In an idealized asymmetric two-basin model of the Atlantic and Pacific, a preference of the equilibrium thermohaline circulation for states with sinking in the southern hemisphere only (Southern Sinking) or also in the North Atlantic (Conveyor) is found.
- A range of *Conveyor* equilibria with differing strengths of North Atlantic sinking is found under fixed freshwater flux forcing.
- The hypotheses both of Broecker et al. (1990) that the modern thermohaline circulation is driven by the atmospheric freshwater export from the Atlantic and of Toggweiler and Samuels (1993a, 1995) that the divergence of Southern Ocean winds governs the outflow of North Atlantic Deep Water are shown to be inadequate to describe the two-basin model results.
- Rare cases with North Pacific sinking are associated with the presence of a very fresh halocline in the Southern Ocean.
- An approximately linear relationship is found between the Atlantic overturning and the meridional gradient of zonally-averaged depth-integrated steric height from the northern boundary of the ocean to the southern tip of Africa.
- The linear relationships between meridional velocity and local meridional density gradient postulated in most two-dimensional plane models of the overturning circulation are, on the other hand, not supported.

Chapter 3

- The climatology of a coarse resolution global ocean model for climate studies is presented, and global teleconnections of the Atlantic thermohaline circulation in the model are sought.
- The implied ocean heat and freshwater transports from the Canadian Climate Centre atmospheric general circulation model are shown to be incompatible with the present-day thermohaline circulation.

Chapter 4

- A simple new parameterization for the sea surface temperature-evaporation feedback is developed as an extension of the traditional mixed boundary conditions.
- A positive feedback between the ocean's thermohaline circulation and evaporation at the surface is described, but the magnitude is predicted to be small.
- The effect of the feedback upon a decadal oscillation in a one-hemisphere idealized basin model is a slightly shorter period in general, and a shorter lifetime for the oscillation in some cases. Century timescale variability is also potentially vulnerable under the new feedback, while a regular millennial oscillation is either replaced by decadal variability for at least part of the time, or persists but with a much shorter period. Other than this, all three mechanisms for internal variability of the ocean's thermohaline circulation are essentially unaltered.

往

Acknowledgements

It is with deep appreciation that I acknowledge the guidance and support of my supervisor, Dr. Andrew Weaver, over the past four years. His kindness and generosity throughout this time have lightened the hardest times, while his faith in me has been a gift for a lifetime. I would also like to thank Dan Wright and Jochem Marotzke for their constructive suggestions about the two-basin model, Bill Gough and Norm McFarlane for obtaining the CCC fluxes for me, Mike Berkley for assistance with the CCC computers, and especially Warren Lee for all his help with the global ocean model. I am grateful also to Stefan Rahmstorf, Inez Fung and others for many interesting discussions, to Gus Fanning and Daniel Robitaille for assistance with my thesis, and to all my officemates (particularly Paul Myers) for their loyal friendship and help at various times.

The financial support for this research was provided by doctoral fellowships from the Natural Sciences and Engineering Research Council of Canada (NSERC) and the Eco-Research Tri-Council, and from WOCE (World Ocean Circulation Experiment) / NSERC Collaborative Research Initiative funding awarded to A. Weaver. Finally, I thank the School of Earth and Ocean Sciences of the University of Victoria for their hospitality during the last two years of my Ph.D, and the Canadian Climate Centre for the access to their high-speed IBM workstations.

List of Tables

Table 2.1.	Numerical parameters for two-basin model
Table 2.2.	(P-E) budgets for two-basin spin-ups
Table 2.3.	Multiple equilibria under the Asymmetric Oceans (P-E) field 45
Table 2.4.	Multiple equilibria under the Symmetric Oceans (P-E) field 49
Table 2.5.	Multiple equilibria under reduced winds
Table 2.6.	Equilibria under restoring and mixed boundary conditions in
	the alternate two-basin geometries 68
Table 2.7.	(P-E) budgets for alternate two-basin geometries 68
Table 3.1.	Numerical parameters for global model
Table 4.1.	Numerical parameters for spin-ups in Chapter 4
	Preliminary spin-up under fixed (P-E)
	Decadal variability spin-up
	Century timescale variability spin-up
	Millennial variability spin-up

Chapter 1

Introduction

The ocean's thermohaline circulation plays an important role in climate, both directly by storing and transporting heat, and indirectly as part of the global carbon cycle. The stability and variability of the present-day thermohaline circulation are thus of great interest; among the most exciting discoveries in recent decades have been first that the global conveyor associated with North Atlantic deep water formation (Gordon, 1986) may have operated very differently in the last ice age (Broecker et al., 1985), and secondly that fluctuations may occur even on much shorter timescales (see Weaver and Hughes, 1992 for a review). The purpose of the present thesis is to pursue the search for factors determining the equilibria and internal variability of the global thermohaline circulation.

1.1. Equilibrium Theories of the Thermohaline Circulation

The two most influential steady-state models of the ocean's thermohaline circulation in the short history of its study have been the thermodynamic box model of Stommel (1961) and the dynamic deep ocean circulation theories of Stommel and Arons (1960). The key contribution of Stommel (1961) was the recognition of multiple equilibrium solutions ensuing from different timescales for the atmospheric forcing of temperature and salinity. Fig. 1.1 shows the simplest of horizontal two-box models of a one-hemisphere ocean, re-analysed by Welander (1986), Marotzke (1990), Zhang (1991) and Weaver and Hughes (1992). The warm salty equatorial ocean and the cold fresh polar ocean are modelled as distinct water masses with fixed volumes and homogeneous properties, with a frictional flow law proportional to the pressure gradient at the lower boundary. Two parameters describe the steady state: the ratio of thermal to haline restoring

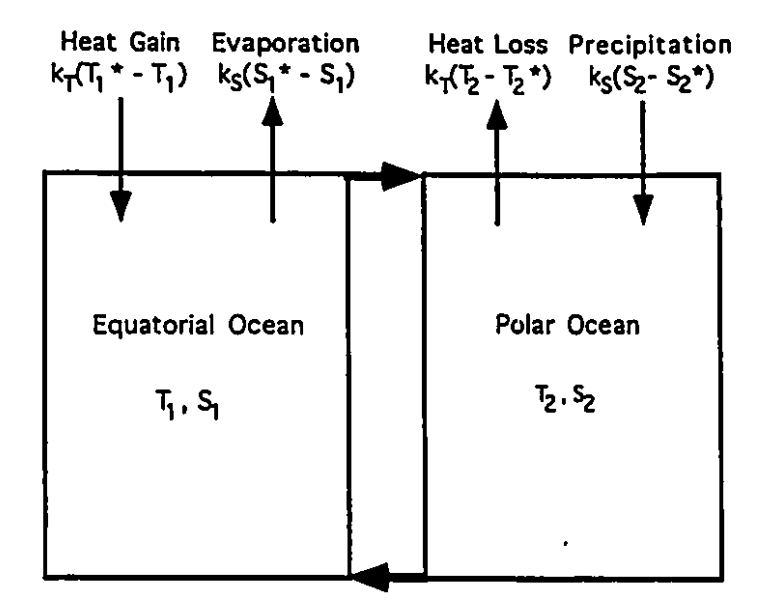


Figure 1.1: Two-box model of the ocean's thermohaline circulation. The temperature T and salinity S are homogeneous within each box, and are restored through the surface exchange to fixed atmospheric values T^* , S^* . The limit $k_s \rightarrow 0$ (mixed boundary conditions) corresponds to fixed salinity fluxes, which are then set equal and opposite in the equatorial and polar boxes to ensure global salt conservation. The positive direction of flow corresponds to a thermally-driven circulation.

timescales and the ratio of thermal to haline forcing gradients (Zhang, 1991, Weaver and Hughes, 1992). Up to three distinct equilibria may exist under identical boundary conditions: the stable solutions are classified as either thermally-driven, with poleward surface flow driven by poleward cooling, or haline-driven, with reverse overturning dominated by the salinity gradient. An important limit known as "mixed boundary conditions" is approached when the restoring timescale on salinity is allowed to grow very large, such that the freshwater fluxes become independent of the surface salinity. Two other fundamental timescales of the thermohaline circulation are revealed in the vertical two-box model by Welander (1982): slow diffusion and fast convection, both acting on the vertical stratification. Increasing the number of boxes allows interhemispheric and even interbasin modes of circulation to be represented (Rooth, 1982, Marotzke, 1990), although without the lag associated with horizontal

advection (Zhang, 1991). But the most difficult feat of all, that still eludes even most two-dimensional meridional plane models of the thermohaline circulation, is to parameterize the coupling between the large-scale zonal and meridional pressure gradients due to the Earth's rotation. One exception is the recent ambitious experiment by Maas (1995) who reduced the three-dimensional circulation in a rectangular ocean to a single point. The interaction between basin-averaged angular momenta and density gradients in the x, y and z planes was illustrated by the discovery of a limit cycle in a purely thermally-forced ocean with a restoring surface boundary condition.

In Stommel and Arons (1960), the attention shifted from the surface boundary conditions to the deep ocean, to predict the abyssal circulation associated with a concentrated deep mass source. For a single deep layer completely filling a flat-bottomed ocean, the linear inviscid vorticity equation:

$$\beta v = f w_z \tag{1.1}$$

(where v and w are the meridional and vertical velocities and f and B are the Coriolis parameter and its derivative) determines a local balance between upwelling and poleward flow. The free (unforced) zonal velocity meanwhile is determined non-locally by integration from an eastern boundary condition (e.g. Hautala and Riser, 1989, Straub and Rhines, 1990). A great success of the Stommel-Arons theory was in anticipating the existence of ageostrophic deep western boundary currents needed to carry the dense water away from its source, and to permit cross-equatorial flow. The boundary currents, unlike the interior flow, respond to the high-latitude source (Straub and Rhines, 1990), while the interior solution is predetermined by the distribution of vertical velocity, a quantity which is not predicted in this model. The relevance of the Stommel-Arons theory has more recently been investigated numerically by Colin de Verdière (1988) in a purely buoyancy-forced planetary geostrophic model with Laplacian friction. Good agreement was found in the equatorward half of a single-hemisphere basin, with both the inviscid vorticity equation and the vertical diffusive-advective heat balance of Munk (1966) holding to first order. However, in addition to the

anticipated western boundary layer, an eastern boundary layer was created to accomodate the downwelling branch of a zonal overturning circulation. Other departures from Stommel-Arons theory were found in the poleward third of the basin, where surface heat losses triggered convective instability, and the western boundary current was diverted into a horizontally-divergent zonal northern boundary layer with a diffusive vorticity balance. The existence of such boundary layers poses a serious challenge in formulating analytical theories of the ocean's thermohaline circulation, as concluded by Colin de Verdière (1988).

Valuable advances in other directions have however been made in recent years. A potentially major influence upon the abyssal flow is the bottom topography. Integrating the linear inviscid vorticity equation (1.1) over the depth (H+η) of the homogeneous deep layer with boundary conditions (Schulman, 1975):

$$w=u\eta_x + v\eta_y + \eta_t$$
 at the upper interface $z=\eta$ $w=-(uH_x + vH_y)$ at the bottom $z=-H$

conservation of potential vorticity along streamlines is obtained:

ï

$$\frac{D(f/H+\eta)}{Dt} = 0 \tag{1.2}$$

where D/Dt = d/dt + ud/dx + vd/dy. Neglecting the interface deflection η compared to the resting thickness H, and prescribing the vertical velocity w_0 at the upper interface, this can be expanded as:

$$[\beta - fH_{x}]v - [fH_{x}]u = fW_{0}$$
(1.3)

A meridional slope of the seafloor reduces the β effect, diminishing western intensification, while an eastward deepening promotes southern intensification (Schulman, 1975). Welander (1969) rewrote the equation as

$$\frac{DF}{Dt} = v_{n} \frac{dF}{dn} = \frac{w_{0}}{H}$$
 (1.4)

 $\tilde{\mathcal{X}}$

(where F=ln(f/H) and n is the direction normal to f/H contours) to emphasize the resemblance between the flat-bottomed (equation 1.1) and topographic (equation

1.4) models, save that flow is now driven across f/H (potential vorticity) contours instead of latitude circles by the upwelling. The example of a meridional ridge was considered by Hautala and Riser (1989) in a nonlinear three-layer Stommel-Arons type (i.e. with prescribed interfacial mass fluxes) model. Vortex shrinking and stretching caused by eastward flow across the ridge respectively diminished and enhanced the meridional velocity over the flat-bottomed prediction. Straub and Rhines (1990) showed how the pseudo-zonal (tangent to f/H contours) component of the flow was doubly affected to the west of a topographic hump, both by the increased length of characteristics curving around the hump, and by gradients in the characteristic speed (proportional to the spacing of f/H contours), and noted that the primary forcing for the pseudo-zonal flow might occur at topography far from the region under study.

Straub and Rhines (1990) further investigated what happened when high topography caused closed contours of potential vorticity ("planetary islands") inside which the solution cannot be determined by integration from an eastern boundary condition. A saddle point in the potential vorticity excited a pair of intense antiparallel zonal jets linking the planetary island to the western boundary layer of the basin. Kawase and Straub (1991) explained this feature by the infinite propagation time for Rossby waves to reach the saddle point along the f/H contour, which prevented the spin-up of the interface along this isoline west of the saddle point, causing a local minimum in interface height. The circulation inside the region of closed contours was studied by Kawase and Straub (1991), who showed that upwelling across the layer interface would cause a strong cyclonic recirculation above the topography regardless of whether it was a bump or a depression. They estimated that the strength of the trapped recirculation might be two orders of magnitude larger than the Stommel-Arons flow, depending on the magnitude of the friction. Isolated topographic features are thus capable of major perturbations to the background poleward and eastward interior flow.

An even more fundamental consideration may be the shape of the basin itself. Kawase (1993) considered a bowl-shaped basin - equivalent to a region of

closed concentric f/H contours, with peak value somewhere equatorward of centre. The deep flow in the poleward half of the basin aligned itself westward along the geostrophic contours, while the eastward flow closest to the equator was compressed into almost a boundary layer. The resulting basinwide cyclonic circulation was significantly intensified over the flat-bottomed estimate. Rhines (1993) further argued that, if layers other than the deepest are considered, an anticyclonic circulation might arise from the increasing area of the basin at shallower depths (the "hypsometric effect"), which allows diminishing vertical velocities $w_z < 0$. Few of these ideas have been applied to numerical models of the large-scale thermohaline circulation, as Colin de Verdière did for the flat-bottomed theory: two reasons (which also apply to the present study) are no doubt the crude representation of topography in ocean models for climate studies, and the unfortunate vulnerability of the vertical velocity to resolution-related numerical problems.

Baroclinicity is another effect which may considerably alter the equilibrium thermohaline circulation in a stratified ocean from the Stommel-Arons description. Pedlosky (1992) demonstrated that an upwelling distribution strengthening eastward (chosen to correspond to the observed shallowing of the thermocline in the real ocean) could give rise to stacked layers of reversing meridional velocity in the deep layer of an idealized flat-bottomed basin. The baroclinic velocities at any given depth were potentially much larger than the vertically-averaged value fixed by the linear vorticity relation. Pedlosky and Chapman (1993) combined this result with a northward-deepening bottom slope to demonstrate that an easterntrapped boundary current might appear, and suggested this as an explanation for the migration of Antarctic Bottom Water crossing the equator into the North Atlantic. Alternate explanations were tendered by Speer and McCartney (1992), who suggested that strong enough upwelling might cause an abyssal layer to intersect with the ground in the western basin, and by Kawase (1987), in a seminal paper describing the spin-up of the deep circulation by travelling Kelvin and Rossby waves. In this study, dissipation was found to be capable of freezing the

developing circulation into a primitive stage where the eastern boundary layer due to coastal Kelvin waves had not yet been radiated away into the interior by long Rossby waves. An original, if somewhat controversial, feature of the analytical model of Kawase (1987) was the parameterization of cross-interfacial fluxes, which were determined internally via a damping-like term in the continuity equation rather than prescribed as in many of the other models described above.

The crucial question addressed by none of these models is in fact the determination of the long-term stratification of the ocean, which is intimately linked to the issue of cross-interfacial fluxes. In the upper ocean, and away from boundaries, the depth of the thermocline may be estimated from an advective-diffusive Munk (1966) balance, unless the vertical diffusivity k_v is low enough for the wind-driven convergence to dominate (Bryan, 1987). The thermocline depth is presumed to then determine the large-scale pressure gradients that drive the meridional overturning. In turn, the deep branch of the overturning circulation affects the deep stratification and the upwelling of cool water into the base of the thermocline that counterbalances the downward diffusion of heat. Thermocline scalings based on such principles have proven remarkably successful at predicting the meridional overturning in numerical models (e.g., Bryan, 1987; Weaver and Garrett, unpublished manuscript, 1993), despite the major assumptions required (the neglect of boundary layers, the assumption of isotropy for zonal and meridional density gradients, etc.).

The role of deep ocean cross-isopycnal fluxes has been explored in a layer model by Yin et al. (1992), who described the interaction between upwelling due to deep and bottom water sources. As in other models, the circulation exhibited strong sensitivity to k_v , with smaller values corresponding to a longer detrainment timescale, allowing the deep circulation to intensify and penetrate further into the other hemisphere, concurrently with the shallowing of the thermocline and the strengthening of the wind-driven circulation in the upper layer. In summary, the vertical diffusivity ultimately must be considered a part of the diabatic forcing in models in the same right as the surface heat and freshwater fluxes (Tziperman,

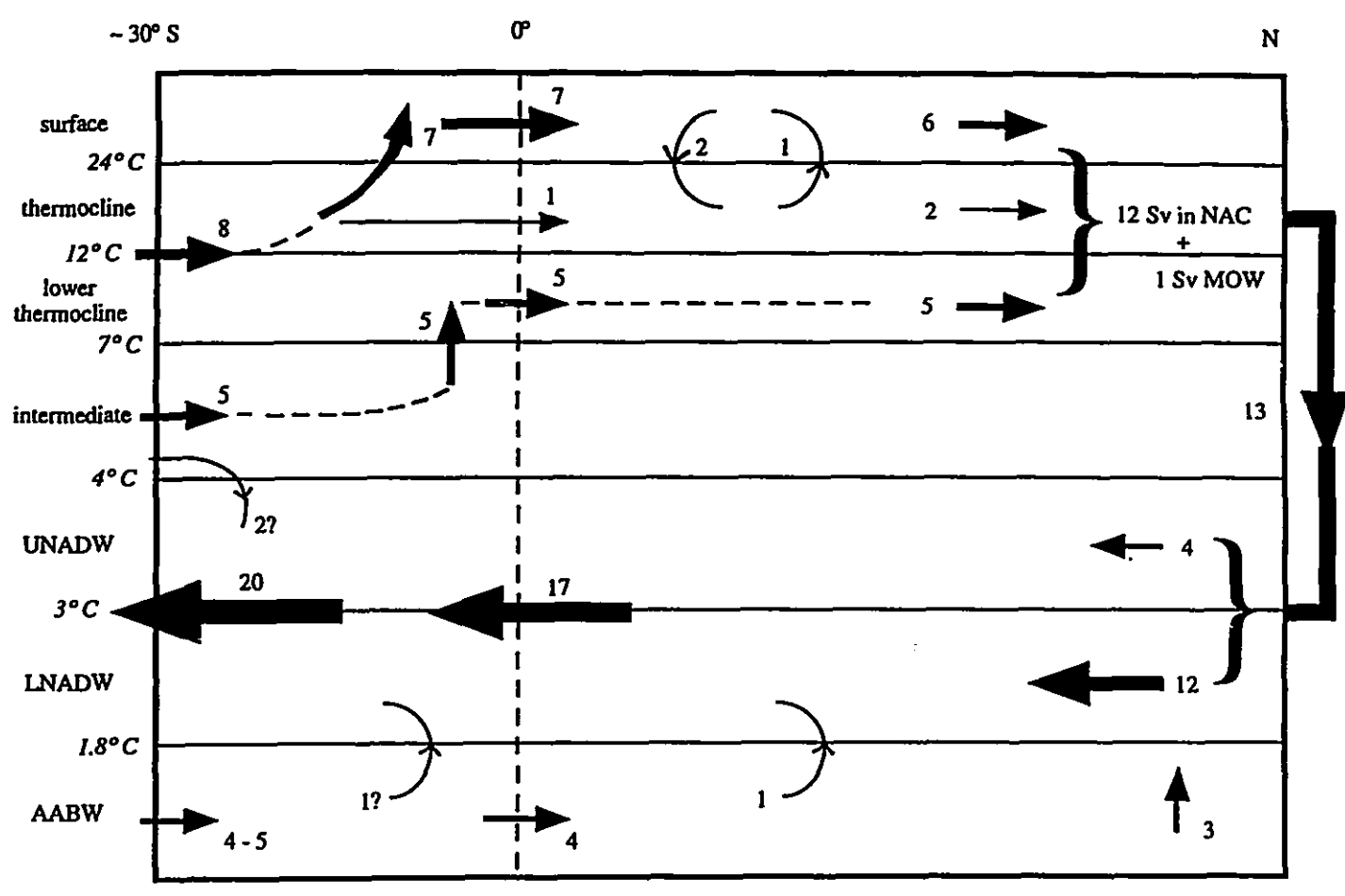
1.2. The Observed Present-Day Thermohaline Circulation

The most complete picture to date of the Atlantic thermohaline circulation was presented in the recent review by Schmitz and McCartney (1993); a more modest summary is sketched in Fig.1.2, revealing a giant asymmetric meridional overturning cell spanning both hemispheres. (It is cautioned that Fig.1.2 is not a true zonal average, but a looser interpretation biased toward western boundary current transports.) Approximately 13 Sv¹ of warm water, unequally distributed between the thermocline and intermediate layers, is imported across 32°S into the South Atlantic to feed the northern overturning. 4-5 Sv of Antarctic Bottom Water (AABW) also flows northward across this latitude in the coldest temperature range. Much of the thermocline and intermediate water upwells to even shallower depths somewhere between 32°S and 0°N, most likely in the vicinity of the equator. The whole 13 Sv of upper-ocean water then crosses into the North Atlantic where it loops through the Caribbean and out through the Straits of Florida. The transport is more than doubled by now due to the winddriven contribution (not included in Fig.1.2); however a bifurcation occurs at about 40°N following the separation of the Gulf Stream, with one branch continuing eastward across the interior as the northern boundary of the subtropical gyre while a second branch forks off towards the Norwegian Sea as the North Atlantic Current. 2 Sv of Gulf Stream water cools and leaves the surface range as 18°C water even before Cape Hatteras; however, 1 Sv also upwells into the warmest layer off the coast of Africa, so that a total of 12 Sv reaches the high latitudes. This is joined by another Sv of warm salty water whose source is the Mediterranean outflow in the 12-24°C layer, so that the total rate of North Atlantic Deep Water (NADW) production is again 13 Sv. Less than half of this comes

 $^{^{1}}$ 1 Sverdrup = 10^{6} m 3 /s.

Figure 1.2: Thermo McCartney (1993). 'transports are in Sv.

Thermohaline circulation of the North Atlantic, after Schmitz and 1993). The layers are defined by their temperatures in °C and



NADW=North Atlantic Deep Water
(UNADW=Upper NADW / LNADW=Lower NADW)
AABW=Antarctic Bottom Water

MOW=Mediterranean Outflow Water NAC=North Atlantic Current AAIW=Antarctic Intermediate Water

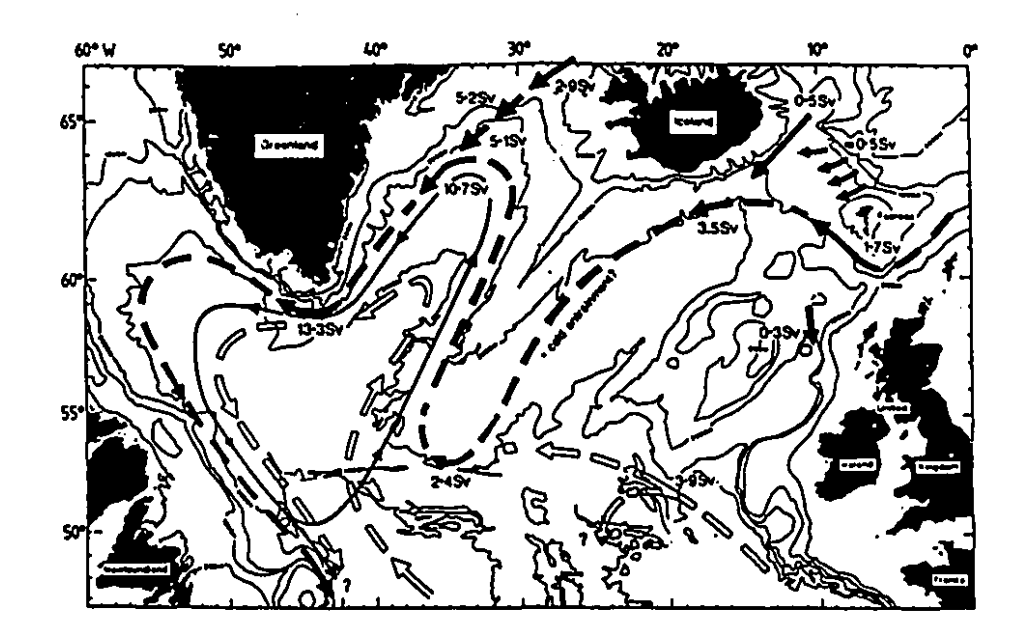


Figure 1.3: Deep overflows and western boundary currents in the northern North Atlantic, taken from Dickson and Brown, 1994. Transports for water masses denser than $\sigma_0=27.8$ are in Sv.

from recent water mass transformation in the Greenland-Iceland-Norwegian (GIN) Seas however: the remainder is old deep water entrained into the dense overflows (Fig.1.3). In the deep western boundary current that travels southward along the coast of North America, an upper prong of about 4 Sv of lighter UNADW (Upper North Atlantic Deep Water) originating in the Labrador Sea overlies a denser saltier core of about 12 Sv of LNADW (Lower North Atlantic Deep Water) tracing back to the GIN Seas. The mass budget at high latitudes is balanced by a poleward flow of 3 Sv of modified AABW in the interior; the remaining 1 Sv of AABW crossing the equator into the North Atlantic warms and passes into the LNADW layer at lower latitudes and hence figures into the total of 17 Sv of southward-bound NADW estimated at 0°N. Additional mixing, with Antarctic Intermediate Water (AAIW) and AABW (1 Sv that was diverted into the eastern basin through the Romanche Fracture Zone near the equator), may swell the deep outflow to as much as 20 Sv further south. A number of interior recirculations complicate this two-dimensional picture. For example, the recirculation of

Labrador Sea Water within the subpolar gyre increases the westward transport of deep water off the southern tip of Greenland by perhaps about a third (Dickson and Brown, 1994), while McCartney (1993) measured southward deep western boundary current strengths of 35 Sv and 40 Sv near the equator and 11°S respectively, with nearly 20 Sv returning northward offshore at both latitudes.

A key aspect of the NADW conveyor depicted by Schmitz and McCartney (1993) is that the upwelling path for the return flow is concentrated in the circumpolar and Atlantic equatorial regions, rather than involving the global ocean. This is in agreement with the Southern Ocean hydrographic survey by Rintoul (1991), who found that the outflow across 32°S might be almost entirely compensated by AAIW entering through Drake Passage (plus the smaller volume of AABW at the ocean floor). A seminal paper five years earlier by Gordon (1986) had suggested a minor role (less than 25% of the total) for this cold water route compared to a warm water route in which Atlantic deep water upwelled into the Pacific and Indian thermoclines and returned past the Agulhas Retroflection off the tip of Africa. Some ambiguity does still remain. Deep water with NADW-derived properties undeniably does spread into the Pacific and Indian Oceans (Reid and Lynn, 1971, Tomczak and Godfrey, 1994). The magnitude of the Indonesian throughflow is poorly known, and the proportion of throughflow water entering the Agulhas Current is also poorly constrained (Tomczak and Godfrey, 1994). However, Macdonald (1993) used an inverse model of the same family as Rintoul (1991) to show that even with throughflow estimates ranging from 0 to 20 Sv, the Atlantic circulation was unaffected, and concluded again that the cold water route was dominant. A strong throughflow is not an absolute requirement for a significant warm water route, but recently Gordon et al. (1992) showed that the net transfer of thermocline waters from the South Indian into the South Atlantic is also small, due to an offshore return flow of South Atlantic Central Water (SACW) poleward of the Agulian Retroflection. Gordon et al. (1992) emphasized that the interbasin exchange might nonetheless be crucial for the conveyor, since more than half of the Benguela Current transport in the

: ::

thermocline and intermediate layers was found to be produced from South Indian water, representing a significant mechanism for enriching the salinity of South Atlantic water and preconditioning it for eventual deep water formation. Gordon et al. (1992) further suggested that the cold water route might be more indirect than originally proposed, with AAIW crossing eastward in the South Atlantic Current and looping into the southwestern Indian Ocean before spreading northward in the subtropical South Atlantic.

A truly global thermohaline circulation may still exist, but perhaps it should be associated instead with Antarctic deep water formation. Deep northward-flowing western boundary currents have been detected in both the Pacific and Indian basins (some references are given in Weaver and Hughes, 1992). The southwestern Atlantic has the deepest connection to the Antarctic and receives the purest and densest AABW while the deep South Pacific is almost isolated by topographic ridges and consequently has the warmest, lightest and most saline bottom water, but almost every basin of the deep world ocean receives some mixture of Antarctic deep water (Fig.1.4). The upwelling path for this abyssal water is poorly known: Toggweiler and Samuels (1993b) have suggested that in the Pacific, most flows southward at mid-depths instead of penetrating up into the thermocline. (A separate upper-ocean thermohaline circulation also exists in the North Pacific with 3-4 Sv of relatively light water sinking to shallow depths in the subpolar gyre and flowing southward at intermediate depths, but this is decoupled from the deep circulation (Hautala et al., 1994).)

There are however fundamental dynamical differences between the Circumpolar and northern oceans. The absence of meridional barriers in the ACC (Antarctic Circumpolar Current) prohibits geostrophically-balanced zonal-mean meridional flow across those latitudes except at depths below the topographic ridges (Gill and Bryan, 1971). The deep water formation regions adjacent to the Antarctic continent are thus isolated from the warm thermoclines at lower latitudes, so that no hemisphere-wide overturning circulation and large poleward heat transport by it as in the North Atlantic can exist. Instead the surface flow is

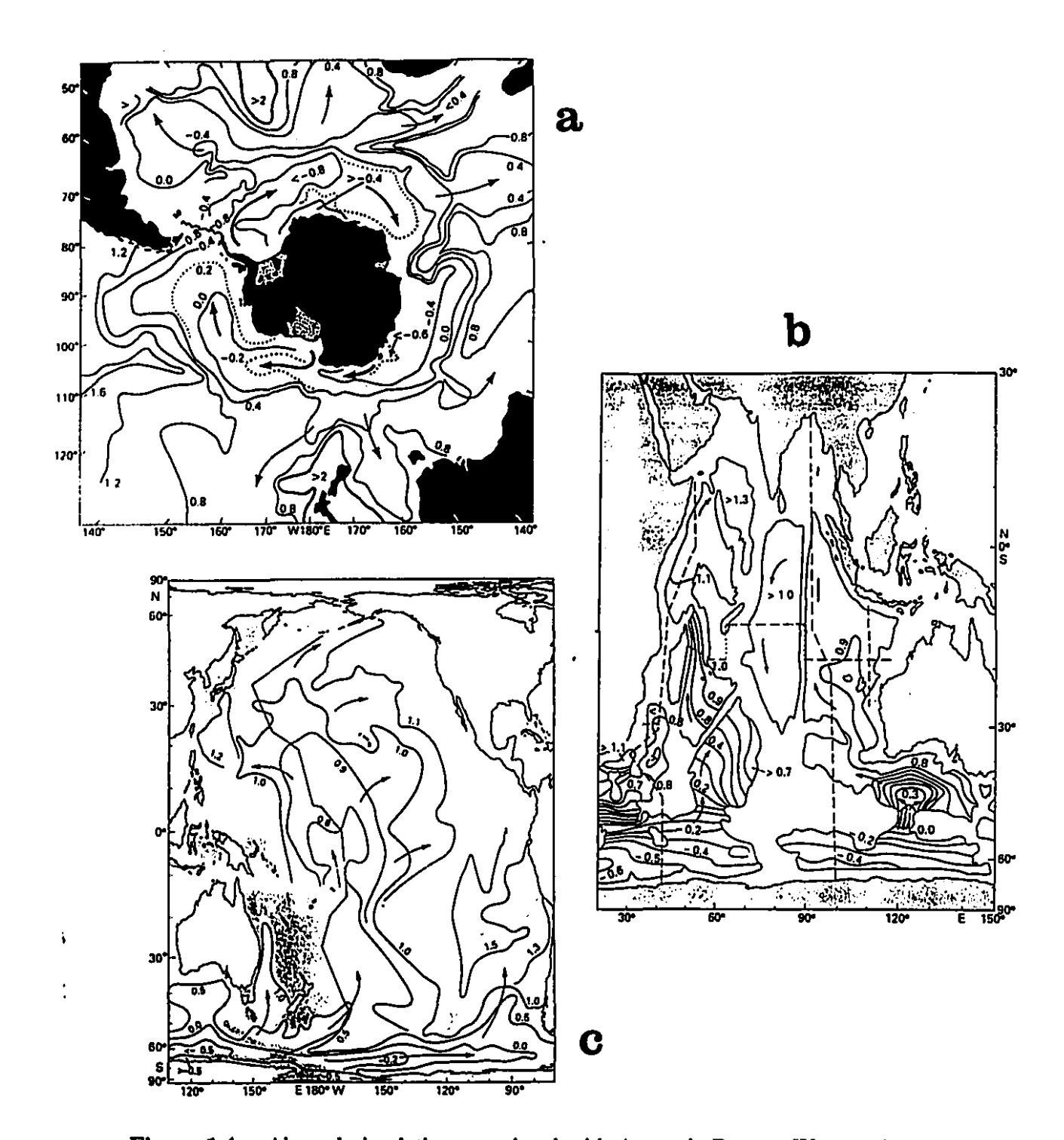


Figure 1.4: Abyssal circulation associated with Antarctic Bottom Water, taken from Tomczak and Godfrey, 1994 a) bottom potential temperature in the Southern Ocean b) potential temperature at 4000 m in the Indian Ocean c) near bottom potential temperature in the Pacific Ocean.

1

northward in the westerly wind belt due to Ekman forcing, allowing heat uptake from the atmosphere (and equatorward heat transport in the South Atlantic potentially even without input from the Indian Ocean, Matano and Philander, 1993). The meridional divergence of the westerly wind draws warm salty NADW up from depths of more than 2000 m to within 200 m of the surface, where it melts floating sea ice and is diluted by rain and snow until it is subducted again as the low salinity AAIW (Tomczak and Godfrey, 1994). Meanwhile, the remainder of the NADW outflew mixes with AABW and spreads into the deep Indian and Pacific Oceans as Circumpolar Water (CPW), as mentioned above.

In summary, the Southern Ocean has more than one role in the global thermohaline circulation: it allows communication between the northern oceans. and simultaneously isolates them from the southern polar regions; it serves as the crucible for water mass transformation (NADW into AAIW), and as "the great mix-master" of the world ocean (Broecker, 1991), efficiently blending NADW and AABW into CPW in less than one revolution of the Antarctic continent. Toggweiler and Samuels (1993a, 1995) go further still to suggest that the divergent winds encircling Antarctica even control the Atlantic thermohaline circulation usually associated with NADW formation. They point out that the equatorward Ekman drift at the surface must be balanced by a poleward flow at greater depths. The return flow can be geostrophically balanced if it occurs below the topographic sill, coinciding with the depth range of the dense NADW outflow. Toggweiler and Samuels (1993a) hypothesize that the magnitude of the outflow might therefore be directly proportional to the strength of the upward suction in the Southern Ocean. In their view, the basin-scale pressure gradients and meridional overturning the whole length of the Atlantic exist not to satisfy the deep water formation in the north, but to subduct buoyant surface water displaced by the wind in the south.

This contrasts with the hypothesis of Broecker et al. (1990a), who proposed as driving force for the conveyor the net divergence of atmospheric water vapour flux over the Atlantic basin, which at equilibrium requires a compensating export

of salt within the ocean. About 0.54 Sv of net evaporation is distilled off the relatively warm Atlantic Ocean, while the Pacific gains around 0.89 Sv from precipitation and continental runoff (Wijffels et al., 1992). The purity of the freshwater transport compared to the salty ocean allows this small exchange to potentially drive a large baroclinic circulation (e.g. Huang, 1994). In Chapter 2 of this thesis, both of these theories will be considered in the context of an idealised two-basin model of the Atlantic and Pacific.

1.3. Multiple Equilibria of the Thermohaline Circulation

The present-day thermohaline circulation is however not unique: it is by now well established that during the last of the Pleistocene glaciations, which ended some ten thousand years ago, the North Atlantic thermohaline circulation was operating in a partially shut-down state (Boyle and Keigwin, 1985, Duplessy and Shackleton, 1985). Deep convection in the GIN Seas may still have been active (Veum et al., 1992), but the outflow of dense LNADW into the North Atlantic was suppressed (Veum et al., 1992, Imbrie et al., 1993). Despite generally lower sea surface salinities (Duplessy et al., 1991), convection continued in the northern North Atlantic through brine rejection under sea ice or in the open ocean swept by enhanced glacial winds (Oppo and Lehman, 1993). A glacial intermediate water mass (similar to modern UNADW) was formed which sank to depths of about 2000 m and was exported to the southern hemisphere by a vigorous intermediate-depth overturning circulation (Oppo and Lehman, 1993). Below this, southern ocean waters penetrated far into the deep North Atlantic (Oppo and Fairbanks, 1987). The thermocline in the subtropical North Atlantic was shallower and 2-4°C cooler (Slowey and Curry, 1992), while sea surface temperatures in the northern North Atlantic dropped by as much as 7°C (Broecker and Denton, 1990). Lehman and Keigwin (1992) have noted that nearly twice as much heat is released in the production of LNADW compared to UNADW.

Ġ

despite similar sea surface temperatures preceding convection, hence its much greater climatic importance. Remote areas of the deep world ocean also cooled by up to 2°C (e.g. Kallel et al., 1988 for the Indian Ocean) for reasons that are still unknown (Boyle, 1990). The Antarctic glacial circulation is also poorly constrained, and may have been either significantly less well ventilated than today or about the same (Boyle, 1990). Glacial AAIW may have been cooler and fresher due to a reduced input of saline North Indian surface water (Lynch-Stieglitz et al, 1994); intermediate depth ventilation of the North Pacific was almost certainly strengthened (Duplessy et al., 1988) for much the same reasons as in the North Atlantic.

The termination of the last ice age is linked beyond doubt to the return to full vigour of the deep conveyor, although the precise timing of individual meltwater events and the resumption of convection has attracted some controversy (Fairbanks, 1989, Keigwin et al., 1991, Veum et al., 1992). The relatively uniform climate of the Holocene too is associated with the remarkable steadiness of the Atlantic thermohaline circulation during this time (White, 1993, Sarnthein et al., 1994). Consistent with this pattern, deep water formation is believed to have occurred in the Norwegian Sea during the previous (Eemian) interglacial, with deep water temperatures quite similar to the modern ones (Labeyrie et al., 1987), although new findings suggest that there may have been large variability too (see next Section). Even further back in time, deep circulation in the Pliocene, when the closing of the Isthmus of Panama allowed the North Atlantic conveyor to first be initiated, may have resembled the present-day configuration (Sikes et al., 1991). A similar body of evidence inspired Broecker et al. (1985) to suggest that there might be two modes of operation of the North Atlantic conveyor, with the on/off switch controlled by the hydrological cycle (salt build-up due to evaporation and freshwater input from melting ice sheets). Very soon after, Bryan (1986) confirmed the existence of such multiple equilibria in a numerical model, and demonstrated that transitions from a conveyor "on" to a conveyor "off" (a collapsed thermohaline circulation) could occur through a "polar halocline catastrophe", a rapid irreversible freshening of the subpolar ocean caused by the nonlinear feedback between surface salinity anomalies and the meridional overturning. The proof was completed by Manabe and Stouffer (1988), who found two stable equilibria of the Atlantic thermohaline circulation in a coupled atmosphere-ocean model.

In more recent years however, a more complex picture has evolved of a continuum of circulations between the glacial and interglacial extremes (Oppo and Fairbanks, 1990). Sarnthein et al. (1994) classified eight reconstructions of the Atlantic circulation over the last 30,000 years into three fundamental types: an interglacial mode like the present-day conveyor, a glacial mode with a reduced conveyor driven by sinking south of Iceland (to as deep as 3600 m), and a meltwater mode, with minimal ventilation below 2000 m. (To this should perhaps be added evidence from Duplessy et al. (1991) that in the early centuries of the deglaciation, the thermohaline overturning may have been very vigorous - perhaps more than double its present strength.) Teleconnections of these modes to the rest of the world ocean are largely unexplored, although the description in the previous section would suggest strong repercussions in the Southern Ocean where the shallowest NADW is upwelled to become new AAIW and older AAIW from the Pacific or Indian Ocean in turn flows northward as compensation for new NADW production. (Independent Southern Ocean modes of variability are also of course possible, with their own distinct teleconnections, and the atmosphere forms another link between the hemispheres.) In Chapter 3, a couple of very simple experiments designed to reveal the global response to changes in the North Atlantic thermohaline circulation in a numerical model will be described.

One of the most distinctive characteristics of the present-day global thermohaline circulation is the conspicuous asymmetry between the Atlantic and Pacific Oceans. The debate over whether North Pacific Deep Water has been produced at any time in the past continues to rage. Berger (1987) suggested it as a natural counterpoint to the diminished NADW production during the last glaciation, and Dean et al. (1989) and Zahn et al. (1991) both found some

 \odot

evidence for this, with these three authors supporting sites in the Bering Sea, the eastern Gulf of Alaska and the Sea of Okhotsk respectively. On the other hand, Shackleton et al. (1988) established that the ventilation age of the deep Pacific was about 500 years greater during the last glaciation than it is today. Zahn and Mix (1991) concurred with Duplessy et al.'s (1988) claim of a Southern Ocean origin for deep water in the glacial North Pacific, while Keigwin (1987) and Southon et al. (1990) found no evidence of deep water formation in the North Pacific during this period. Finally, Zahn et al. (1991) concluded from a longer paleoclimatic record that no deep water formation had existed in the North Pacific as long ago as the late Pleistocene. The most recent contribution to the debate comes from Lynch-Stieglitz and Fairbanks (1994), who combined conflicting information from two different paleoclimatic tracers to infer that deepwater production may have existed after all in the glacial North Pacific. They cautioned however that uncertainty remained about the reliability of benthic foraminifera as the recorders of paleo-circulation, so it is probably fair to say that the case is not closed yet.

What is clear is that the North Atlantic conveyor has been revived more than once since the continents assumed their present shape and distribution, while a similar mode of circulation in the Pacific is perhaps less favoured. Whether the absence of deep water formation in the North Pacific today is coincidental (as suggested by Stommel and Arons, 1960) or more fundamental is still an open question. Warren (1983) explained it by the more stable salinity stratification of the North Pacific compared to the North Atlantic, and identified a number of causes for this. For example, there is nearly twice as much evaporation over the latter; the water introduced into the northern North Atlantic from lower latitudes is more saline than its counterpart in the Pacific, and the residence time of this water in the region of net precipitation at high latitudes is shorter. However, as Warren (1983) conceded, none of these factors is truly independent of the already existing thermohaline circulation in the North Atlantic. The salinities of the surface and bottom water masses are similar because the one is actively being converted into the other; the higher evaporation is related to higher sea surface

temperatures, which are due in part to the greater northward advection of warm subtropical water by the Gulf Stream, but the Gulf Stream itself is partly thermohaline driven. Finally, the thermohaline contribution to the western boundary current accounts for the faster throughflow rate.

Geographical (i.e. built-in) clues do also exist: the first and most obvious one is that the North Atlantic extends farther north than the Pacific does, and has a deeper connection with the Arctic. In connection with the Broecker et al. (1990a) argument that the interbasin atmospheric water vapour transport drives the conveyor, the narrow Isthmus of Panama at low latitudes allows westward export via the trade winds (Weyl, 1968), while the Rocky Mountains block an opposite flow at higher latitudes. Schmitt et al. (1989) have proposed that the narrower width of the Atlantic compared to the Pacific would cause a greater fraction of its area to be susceptible to the incursions of cold dry continental air that favour Within the ocean, the salty Mediterranean outflow assists in evaporation. preconditioning intermediate water flowing into the Norwegian Sea to undergo deep convection, and as seen above, so does the exchange with South Indian waters off the Cape of Good Hope. Finally, Reid (1961) has hypothesized that the poleward extension of South America compared to South Africa might impede the transport of fresh water out of the Pacific by the ACC. Most studies of the thermohaline circulation to date have taken place in idealized box oceans; in the present thesis (Chapters 2 and 3), the role of geography will be emphasized a little more although many aspects of the models herein are still quite idealized.

1.4. Variability of the Thermohaline Circulation

Transitions between equilibria can occur amazingly fast. Greenland ice cores record an abrupt warming of 5-7°C in less than 50 years during the last deglaciation (Lehman and Keigwin, 1992). Even more dramatically, this shift appears to be only the last and warmest of a succession of warm interludes (the

Dansgaard-Oeschger events) that punctuated the last ice age. The duration of the irregularly-occurring interstadials (excluding the present one) ranged between about 500 and 2000 years, each typically beginning with an abrupt warming of around 7°C and ending with more gradual or stepwise cooling (Johnsen et al., 1992). The century/millennial variability is seen also in deep sea sediments from the North Atlantic (Broecker et al., 1990a, Bond et al., 1993) but more weakly in Antarctic ice cores, suggesting a link to the Atlantic thermohaline circulation. Keigwin and Jones (1994) have further suggested that the oscillations are cyclical, with a dominant frequency of about 4000 years. Most recently, the discovery (GRIP, 1993, Dansgaard et al., 1993, Tzedakis et al., 1994, Thouveny et al., 1994, Field et al., 1994) that the last interglacial (125-115,000 years ago) also was interrupted by rapid climate shifts, with cool intermissions lasting decades to millennia, has focussed the search still further since large ice volumes were not vet present at that time. On an even longer timescale, the present and Eemian interglacials and the intervening glaciation are the tail end of a 100,000 year oscillation of the northern hemisphere continental ice sheets (Broecker et al., 1985). Although this cycle is most likely a nonlinear response to orbital variations, the close correspondence of the atmospheric CO₂ record indicates the involvment of the deep ocean (Imbrie et al., 1993), and Keigwin and Jones (1994) have suggested based on ocean sediment data that cooling of the northern North Atlantic takes place through similar mechanisms on orbital timescales as on millennial timescales.

Ocean-related climatic changes also occur on shorter timescales. Stocker and Mysak (1992) have reviewed the evidence for Holocene variability on the fifty to five hundred year timescales, while Greatbatch and Zhang (1995) and Döscher et al. (1994) have summarized some of the evidence for interdecadal fluctuations of the North Atlantic thermohaline circulation in the present century. One very well-known example is the Great Salinity Anomaly (GSA) of Dickson et al. (1988). A cold fresh surface anomaly was first detected north of Iceland and circulated around the subpolar gyre to return to the Greenland Sea after a period

i

of about 14 years. The interruption of deep convection in the Labrador Sea in the 1960's caused the upper branch of the North Atlantic conveyor to become warmer and saltier in the early 1970's (Levitus, 1989) and weakened the transport of the Gulf Stream (Greatbatch et al., 1991) through JEBAR (the Joint Effect of Baroclinicity and Relief, Holland, 1973). Decadal timescale changes have also occurred in the Pacific in this century (Trenberth, 1994), but for different reasons since there is no strong thermohaline circulation there.

All three timescales (decadal, century and millennial) of variability have been found in uncoupled ocean models, and Weaver (1994) relates these to three fundamental internal timescales of the ocean's thermohaline circulation due to horizontal advection, meridional overturning and diffusion respectively. Weaver and Sarachik (1991a) found a regular decadal oscillation in a one-hemisphere idealised sector model under mixed boundary conditions, with an advective mechanism rather reminiscent of the GSA. A warm salty anomaly was generated at the surface in between the subtropical and subpolar gyres by upwelling from the subsurface separated western boundary current. Eastward and poleward advection of the anomaly induced convective overturning and a reverse thermohaline cell at high latitudes. The boundary condition allowing the existence of this oscillation was the fixed salt flux, which minimized damping of the salty anomaly as it propagated around the subpolar region. A very different thermally-dominated oscillation was found in a low resolution North Atlantic model by Weaver et al. (1994), the timescale of which was set by the advective establishment of zonal pressure gradients in the Labrador Sea and their removal by convection. The Labrador Sea was also the source of decadal variability in a global ocean model under white noise freshwater fluxes for Weisse et al. (1994): the oscillation depended upon the faster accumulation of a salinity anomaly in the marginal sea than could be removed by the outflow into the North Atlantic. The importance of model geometry was further emphasized by Moore and Reason (1993), in whose global model a decadal oscillation appeared in the northern North Atlantic and Arctic only in the absence of bottom topography in those regions. The

pertinence of the advective mechanism discovered in uncoupled models has been confirmed in a fully coupled atmosphere-ocean model by Delworth et al. (1993), who reported an irregular thermohaline oscillation with an approximately 50-year period. The mechanism was quite complex: a weak thermohaline overturning caused low heat transport into the northern North Atlantic and a cold anomaly. The density anomaly gave rise to a cyclonic circulation around it, which allowed an accumulation of salt to the west, and this in turn accelerated the meridional overturning. Changes in freshwater flux appeared to be of secondary importance to the oscillation and changes in surface heat flux actually opposed changes in poleward heat transport (as would a restoring condition on temperature), hence the variability was best described as an internal oceanic mode rather than a coupled mode (Delworth et al., 1993).

The decadal oscillations described above are intrinsically three-dimensional. Century-scale variability in contrast is frequently identified with two-dimensional "loop oscillations" where positive and negative salinity anomalies are advected around the overturning circulation, accelerating or decelerating it through their influence on the density gradient (Welander, 1986). The interaction with evaporation and precipitation at the surface may assist the oscillations to be selfsustaining (e.g. Winton, 1993). The best known case in a three-dimensional model is the 320-year oscillation excited in a global ocean model by Mikolajewicz and Maier-Reimer (1990) by a white noise modulated freshwater forcing field; however, a small range of loop oscillations superimposed upon millennial scale variability was found by Winton (1993) in a hemispheric box model under steady The millennial timescale of the "deep-decoupling" oscillations in Winton's study came from the diffusive warming of the deep ocean following a collapse of the thermohaline circulation. As in Weaver and Sarachik (1991b), this eventually destabilized the high latitude region, triggering a violent overturning event or "flush" during which widespread deep convection released very rapidly the heat stored during the previous centuries of slow warming. The strong overturning soon exhausted itself by cooling the deep ocean and was further stabilized by surface freshening until a polar halocline catastrophe occurred. In Marotzke (1990), meridional salt transport by the wind-driven gyre circulation was instrumental in re-establishing the thermohaline circulation following a polar halocline catastrophe, however in Weaver and Sarachik (1991b) and Winton (1993), the flush/collapse sequence was repeated thereafter.

Weaver et al. (1993) sought to describe the stability and variability properties of the thermohaline circulation in idealised models under mixed boundary conditions in terms of the relative importances of freshwater fluxes, restoring condition on temperature and wind-driven circulation. classification, "thermally-dominant" cases are those in which no internal variability is expected to exist. Stronger freshwater flux gradients in "haline-important cases" permit multiple equilibria and variability, while in "haline-dominated" oceans, high latitude freshening can overpower the meridional overturning and trigger flush/collapse oscillations. More precise predictions are difficult because of the nonlinear feedbacks within the ocean. One familiar example is the positive feedback between meridional overturning and the meridional salinity gradient advected by it: Bryan (1986) showed that a high latitude salinity anomaly might cause a transition from a symmetric to an asymmetric pole-to-pole circulation in a two hemisphere basin on a roughly centuries timescale. A faster mechanism kicked in when a fresh salinity anomaly interfered directly with convection, inhibiting the overturning circulation (and poleward salt transport) and inducing the pole-to-pole mode in only decades (Bryan, 1986). Stabilizing negative feedbacks on the other hand include mean advection of an anomalous salinity gradient and anomalous poleward heat transport by the perturbation overturning (Marotzke, 1994). Under a traditional restoring boundary condition, the influence of ocean heat transport on near-surface temperature gradients is significantly weakened. This has motivated Zhang et al. (1993) and Rahmstorf and Willebrand (1995) in recent years to develop more sophisticated boundary conditions with finite implied atmospheric heat capacities. Another potentially important feedback that has been neglected up to now is the dependence of evaporation on sea surface

temperatures, and in Chapter 4, the role of this feedback in the decadal, century and millennial variability described in the previous two paragraphs will be explored.

1.5. Modelling the Ocean's Thermohaline Circulation

The numerical modelling approach chosen in the present thesis has the advantage of combining both dynamical and thermodynamical processes. The three-dimensional representation allows the fundamental asymmetry of the ocean's thermohaline circulation to be resolved: small sinking regions versus broad upwelling regions, narrow western boundary currents versus the wide interior, and shallow thermocline versus whole ocean depth. To ensure the best description of cross-equatorial flow and deep ocean stratification, a primitive equation model with Laplacian mixing and a fully nonlinear pressure-dependent equation of state is used: the well-known Bryan-Cox-Semtner model (Cox, 1984). Since there already exist a number of excellent descriptions of the numerics and equations of this model (e.g. Bryan, 1986, Semtner, 1986), only a shorter overview is given in Appendix A, and this section is dedicated more specifically to the practical use of the model in this thesis. (A fuller review of various aspects of modelling the thermohaline circulation is given in Weaver and Hughes, 1992.)

All of the applications in this thesis use low resolution, which is mandated by the long timescales involved in modelling the ocean's thermohaline circulation. This rules out detailed representation of convective plumes, boundary layers or mesoscale eddies. For computational economy, a more physical isopycnal/diapycnal mixing scheme is also eschewed in favour of the simpler horizontal/vertical parameterization, and the surface mixed layer is approximated by the fixed-depth topmost layer of the model (the seasonal cycle is ignored). The profile of vertical diffusivity k_v , which is crucial in determining both the thermocline depth and the overturning circulation as discussed in Section 1.1., is

-<'.

kept fixed rather than being related to the stratification, and for numerical reasons is generally chosen larger than indicated by observations. One of the major advantages of using the Bryan-Cox OGCM (Ocean General Circulation Model) is the great number of sensitivity studies that have been carried out over the years: the effects of k, for example have been throughly explored by Bryan (1986), Cummins (1991) and Hirst and Cai (1994) in both idealized basin and global ocean models. The horizontal and vertical coefficients for mixing momentum are also large, to overcome numerical instabilities associated with grid resolution at the western boundary and the equator respectively (Bryan et al., 1975; Weaver and Sarachik, 1990). Convection is parameterized by the implicit vertical diffusion scheme of Cox (1984), which causes k, to be increased by approximately four orders of magnitudes whenever static instability is detected, effectively mixing the unstable regions completely in the vertical direction over one timestep. Finally, the nonlinear advection terms are removed from the momentum equations (the low Rossby number approximation), since the viscous western boundary currents at coarse resolution are not inertial (Marotzke, 1990, Weaver et al., 1993), and different timesteps are used for the barotropic vorticity and tracer equations (splittimestepping).

The boundary conditions in all experiments are conventional: a rigid-lid approximation at the surface to filter out fast external gravity waves, insulating side and bottom walls, no slip at lateral boundaries and quadratic bottom friction (with a coefficient of 1.3×10^{-3} and a turning angle of 10°). Even these well-worn choices do of course have their consequences. The rigid lid eliminates the small barotropic component of the thermohaline circulation due to surface freshwater fluxes (the Goldsbrough gyres - Huang, 1993), and more importantly, forces the substitution of a virtual salt flux for the (P-E) (precipitation minus evaporation) field. To ensure a vanishing global mean salt flux, a constant reference salinity is used which may differ from the actual in situ salinity, biasing the implied freshwater flux in some locations (Huang, 1993). The no slip lateral boundary condition affects the vorticity balance in the boundary layers. The thermohaline

circulation in idealised sector models with standard Laplacian friction and a no slip boundary condition typically has deep sinking concentrated in the northeastern corner (assuming a northern hemisphere model). Winton (1993) showed that with Rayleigh friction and a "no normal flow" boundary condition, this was transformed into shallow sinking and the subsurface northern boundary current then sank more vigorously in the northwestern corner of the basin.

The first model used in this thesis (Chapter 2) is a simple idealised twobasin model of the Atlantic and Pacific Oceans. Diagnosed (P-E) fields in the manner of Bryan (1986) are used: that is, the model is spun up from rest under restoring boundary conditions and the implied surface salt fluxes at equilibrium are retained as the (P-E) field consistent with the desired climatology. This approach is still quite commonly used even in studies employing global models with realistic geography; a principal reason is the scarcity and poor quality of data in many regions of the world ocean. Anderson and Willebrand (1993) have estimated that the uncertainty associated with wind stress fields approaches 20-30%, while annual mean surface heat fluxes are not known to better than 30-40 W/m², and annual freshwater fluxes to only 0.20-0.50 m/y. A different approach is to use the information from an atmospheric general circulation model (AGCM), which will have the added advantage of being internally consistent. In Chapter 3 of this thesis, a global model is forced with the annual mean fluxes from the Canadian Climate Centre AGCM. While the main focus of both Chapters 2 and 3 is upon equilibrium aspects of the ocean's thermohaline circulation, a couple of simple time-dependent experiments illustrating properties of the global geometry are also included in the latter. Finally, a one-hemisphere flat-bottomed sector model will be used for the process study in Chapter 4 of the role of sea surface temperature-evaporation feedback in variability of the ocean's thermohaline circulation.

Chapter 2

Multiple Equilibria of an Asymmetric Two-Basin Model

One of the first systematic investigations of multiple equilibria of the thermohaline circulation in a multiple-basin ocean was the study of Marotzke and Willebrand (1991 - hereafter MW) in an idealised flat-bottomed model of the Atlantic and Pacific (Fig.2.1). The two symmetric basins were connected in the south by a wide circumpolar channel carrying a fixed zonal transport of 200 Sv. Identical sinusoidal profiles of restoring temperature and salinity were used in each basin and, following Bryan (1986), the equilibrium salt flux field was diagnosed as a fixed boundary condition for subsequent analysis of the possible steady states and their stability. However, the (P-E) field diagnosed from the spin-up had a net excess of precipitation of about 0.1 Sv in the northern hemisphere of either basin, requiring a cross-equatorial freshwater transport of equal magnitude at equilibrium. A second unbiased (P-E) field was therefore constructed from the spin-up of a single-hemisphere model under the same temperature and salinity profiles, then both zonally averaged and reflected about the equator. Under the unbiased field, four qualitatively different steady states were found:

- 1) Northern Sinking, with deep sinking at high latitudes in the northern hemisphere of both basins,
- 2) Southern Sinking, with deep sinking in the southern hemisphere of both basins,
- 3) a Conveyor, with deep sinking in the northern North Atlantic and upwelling in the North Pacific, and necessarily,
- 4) an *Inverse Conveyor*, the mirror image of (3), since the Atlantic and Pacific basins were interchangeable. No further equilibria were discovered in approximately 25 additional experiments, but a preference of the model geometry for the *Northern Sinking* state was revealed. Under the biased

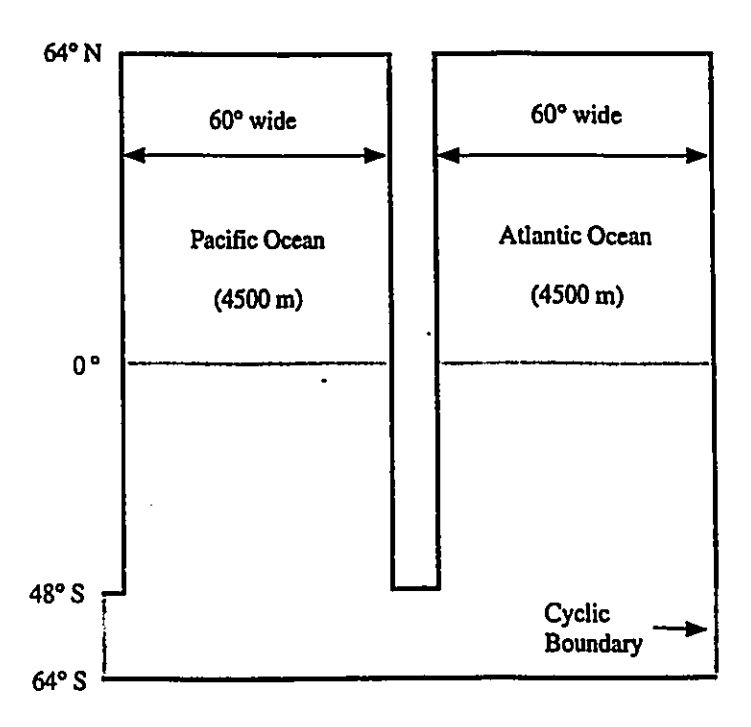


Figure 2.1: The two-basin OGCM of Marotzke and Willebrand (1991). The bottom is flat and the strength of the zonal transport in the circumpolar ocean is prescribed. The Atlantic and Pacific are identical.

spin-up fluxes, in contrast, the *Southern Sinking* emerged favourite; a second major conclusion was therefore the sensitivity of the model preference to the (P-E) field.

An asymmetric two-basin ocean was considered by Stocker and Wright (1991a) with their zonally-averaged latitude-depth model; the angular widths of the Atlantic and Pacific were set to 60° and 120°, and the northern boundaries of the oceans fixed at 80° and 50°N respectively. Under mixed boundary conditions diagnosed from symmetric restoring salinity profiles, a Northern Sinking equilibrium again appeared, indicating that the geometrical asymmetry was not a sufficient condition to induce a modern thermohaline circulation. Stocker and Wright (1991b) further showed that a transition from a Southern Sinking to a Conveyor circulation could be produced in this model by increasing evaporation over the Atlantic, with the location of the transition point suggesting that an atmospheric freshwater export from the Atlantic might be essential to maintaining the salinity contrast between the two oceans and the direction of thermohaline

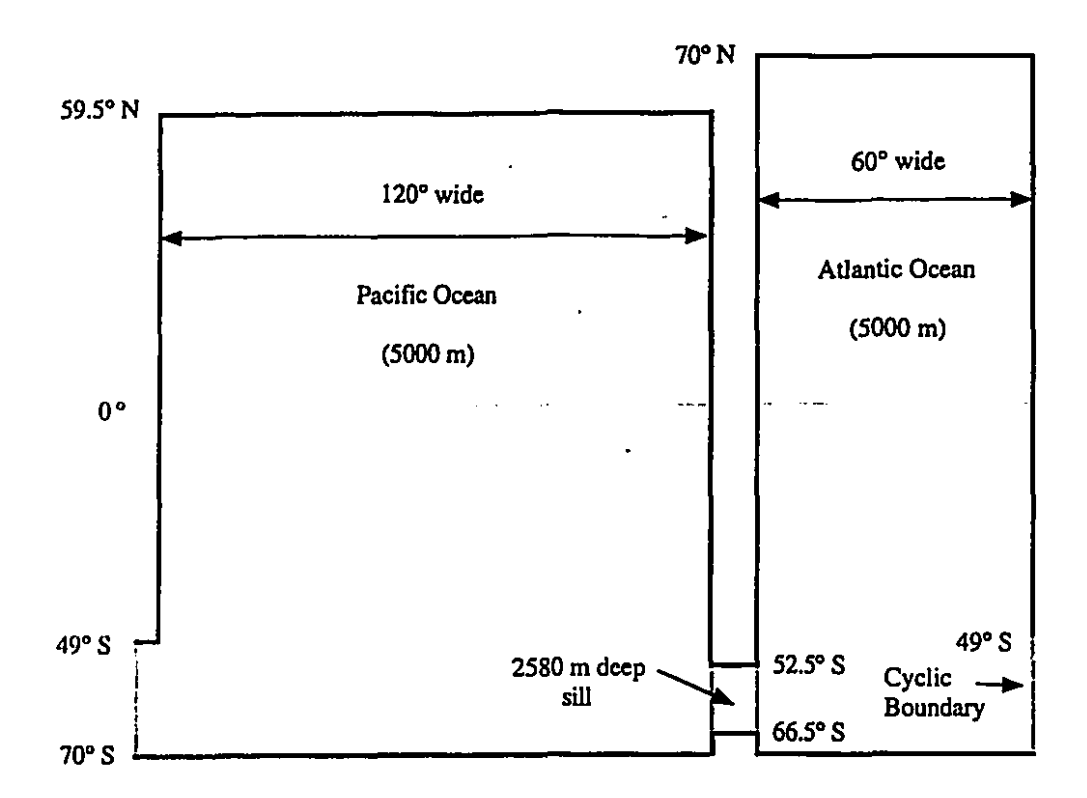


Figure 2.2: The geometry of the present two-basin model with distinct Atlantic and Pacific.

flow. In Stocker et al. (1992), a three-basin model was coupled to an energy-balance atmosphere, and all four qualitatively different states of MW were found, including a single *Conveyor* starting from several initial different conditions.

In this chapter, this investigation into the role of basin geometry and surface boundary conditions in causing the asymmetry of the present-day global thermohaline circulation is pursued in an asymmetric three-dimensional OGCM under more realistic buoyancy forcing profiles than hitherto attempted.

2.1. Spin-ups under Restoring Boundary Conditions

÷,

The geometry of the model is illustrated in Fig.2.2, and is fairly similar to that of MW. Important new features are the greater width of the Pacific compared to the Atlantic, the northward extension of the Atlantic compared to the Pacific,

Table 2.1. Numerical Parameters for Two-Basin Model

numerical model: Cox (1984)

resolution: zonal: 3.75°

meridional: 3.5°

vertical: 19 levels (depths in m: 50, 100, 160, 240, 350, 490, 670, 890, 1150, 1450, 1800, 2180, 2580, 2980, 3380,

3780, 4180, 4580, 5000)

timesteps: barotropic vorticity: 0.5 hours

tracer: 5 days

eddy mixing coefficients:

horizontal viscosity $A_{MH}=2.5 \times 10^5 \text{ m}^2/\text{s}$ vertical viscosity $A_{MV}=1\times 10^{-3} \text{ m}^2/\text{s}$ horizontal diffusivity $A_{TH}=2\times 10^3 \text{ m}^2/\text{s}$

vertical diffusivity A_{TV} (k_v)=

 $[1.39 + (2.51/\pi)\arctan(5.0x10^{-3}(z-1.0x10^{-3}))] x10^{-4} m^{2}/s$

where z=depth in m

boundary conditions:

wind stresses: analytical profile of Bryan (1986), see Fig.4.5

restoring T*, S*: see Fig.2.3 restoring timescale: 50 days

and the sill in Drake Passage between the Pacific and Atlantic. The souther: gap extends only to 66.5°S instead of all the way to Antarctica, allowing zonal pressure gradients to be set up around 70°S. Meridional overturning can thus exist in geostrophic balance at this latitude, with outflow beneath the sill, unlike in the models of MW and Stocker and Wright (1991a) where the circumpolar channel acted as an effective barrier to meridional flow at high southern latitudes. The zonal transport in the ACC is free to evolve, and was enhanced by JEBAR from 108 Sv in one spin-up without a sill to 180 Sv under the same boundary conditions with a sill. Finally, the numerical parameters and model level depths are listed in Table 2.1.

Five spin-ups are performed under three different profiles of restoring temperature T* and salinity S*, illustrated in Fig.2.3. All start from isothermal, isohaline oceans at rest, and winds when present follow the analytical formula of Bryan (1986, see Fig.4.5) approximating the observed meridional variation of the zonally-averaged zonal wind stress (the meridional component is neglected). In the first experiment, hereafter "Symmetric Hemispheres", equatorially-symmetric profiles of T* and S* (Fig.2.3a) are constructed by combining both hemispheres of the zonally-averaged Levitus (1982) data for the global ocean, and reflecting the result about 0°N. The unexpected minima of S* at ~58°N and S come from including the very fresh Hudson Bay in the global mean. Despite these symmetric restoring conditions, the resulting meridional overturning at equilibrium is decidedly asymmetric, between both north and south and Atlantic and Pacific (Fig.2.4). More than twice as much deep water is sinking in the north than in the south, and nearly all of the northern sinking takes place in the Atlantic. Both the North Atlantic and the southern sinking occur right at the polar boundaries, but the deep water formed in the Southern Ocean is about 1°C colder. Some sinking does also occur to intermediate depths in the northern North Pacific, which ends up with the warmest and saltiest deep ocean. Since the same restoring timescale is used for both temperature and salinity, an implied surface density profile can be calculated, and is sketched in Fig.2.5a. The importance of model geometry is immediately seen: the densest water in the south is isolated by the circumpolar current, allowing the northern North Atlantic (where the densest surface water north of the ACC is formed) to dominate the sinking. It has not been investigated whether the deep water flowing into the South Pacific comes from the Atlantic or Southern Ocean; in either case, it upwells to shallow depths in the northern hemisphere and either flows out again just below the Ekman-driven surface cells or reaches the surface in the equatorial divergence.

The equilibrium salt flux field in the Symmetric Hemispheres spin-up is shown in Fig.2.6. Through the use of observed data rather than idealized cosine profiles for the restoring temperature and salinity conditions, a slightly more

11

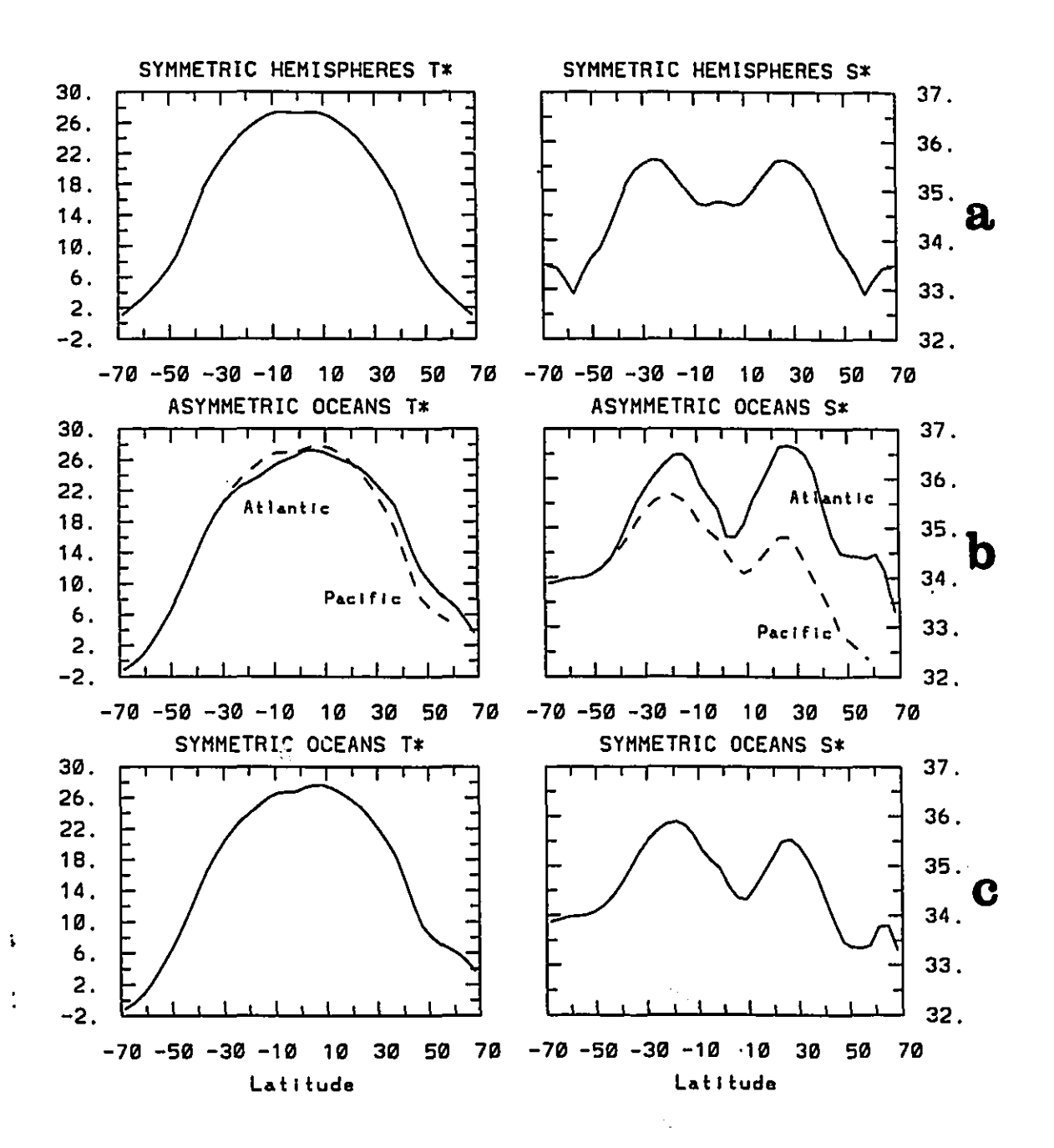


Figure 2.3: Meridional profiles of restoring temperature (°C) and salinity (ppt) for the spin-ups a) Symmetric Hemispheres b) Asymmetric Oceans (solid line: Atlantic; dashed line: Pacific) c) Symmetric Oceans.

1

.≥_`.

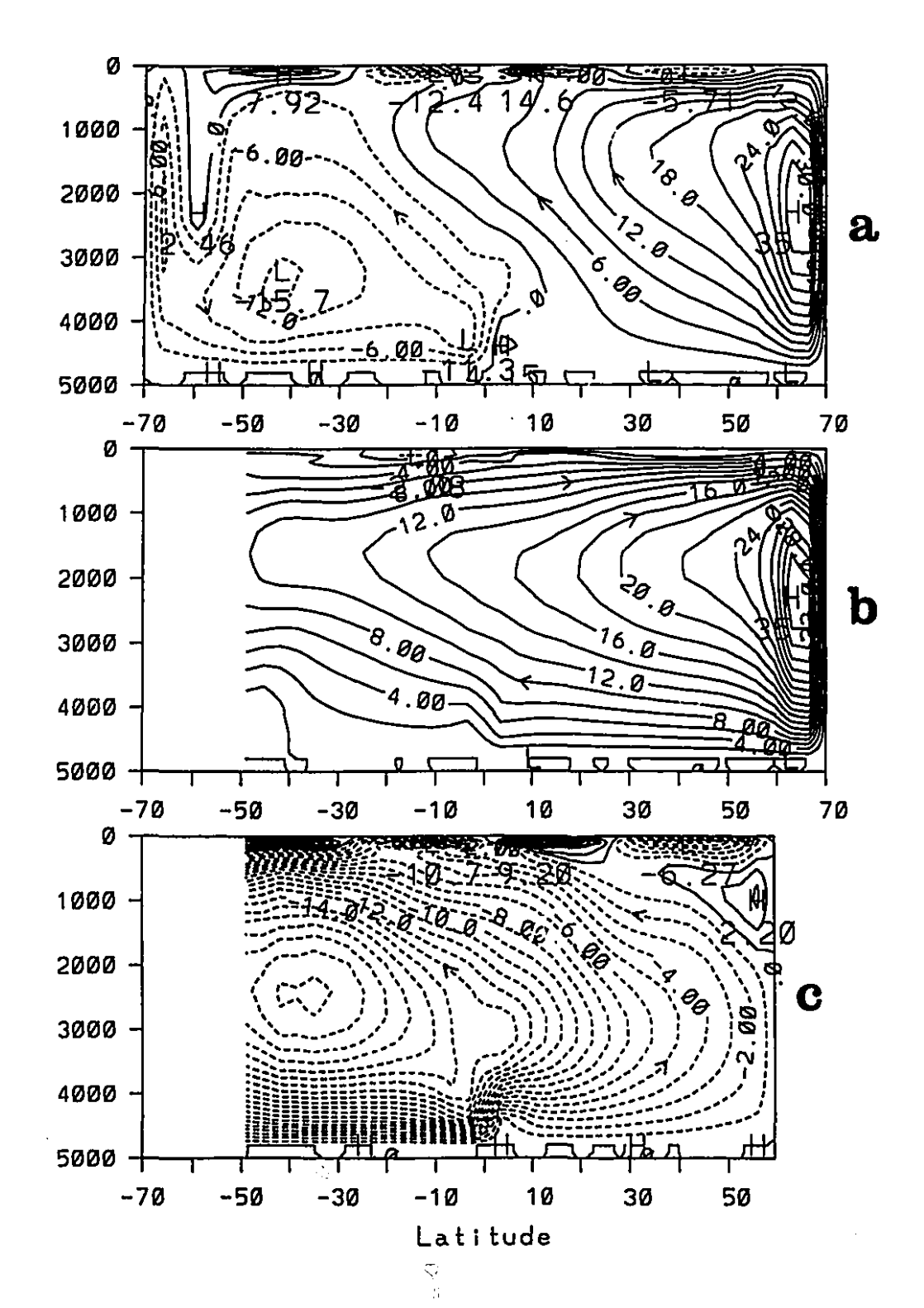


Figure 2.4: Meridional overturning streamfunction (Sv) for a) both oceans together b) the Atlantic c) the Pacific in the Symmetric Hemispheres spin-up under restoring boundary conditions.

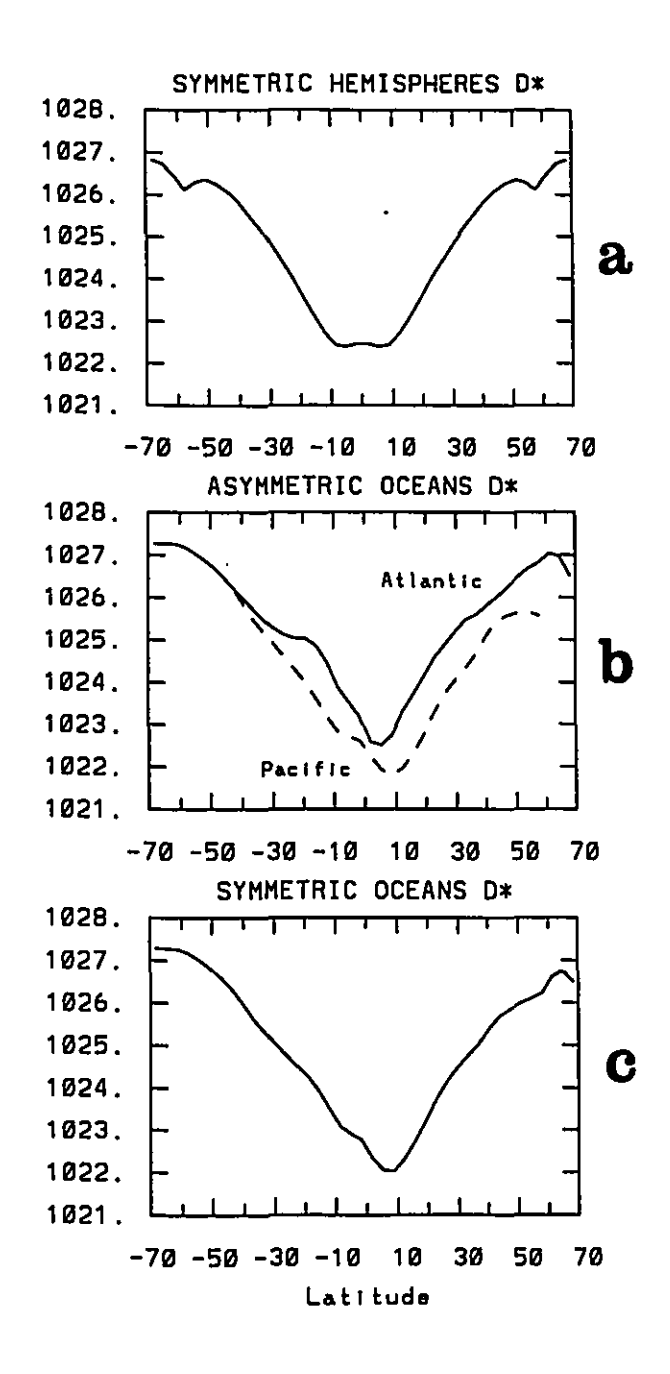


Figure 2.5: Meridional profiles of implied restoring density (kg/m³) for the spinups a) Symmetric Hemispheres b) Asymmetric Oceans c) Symmetric Oceans.

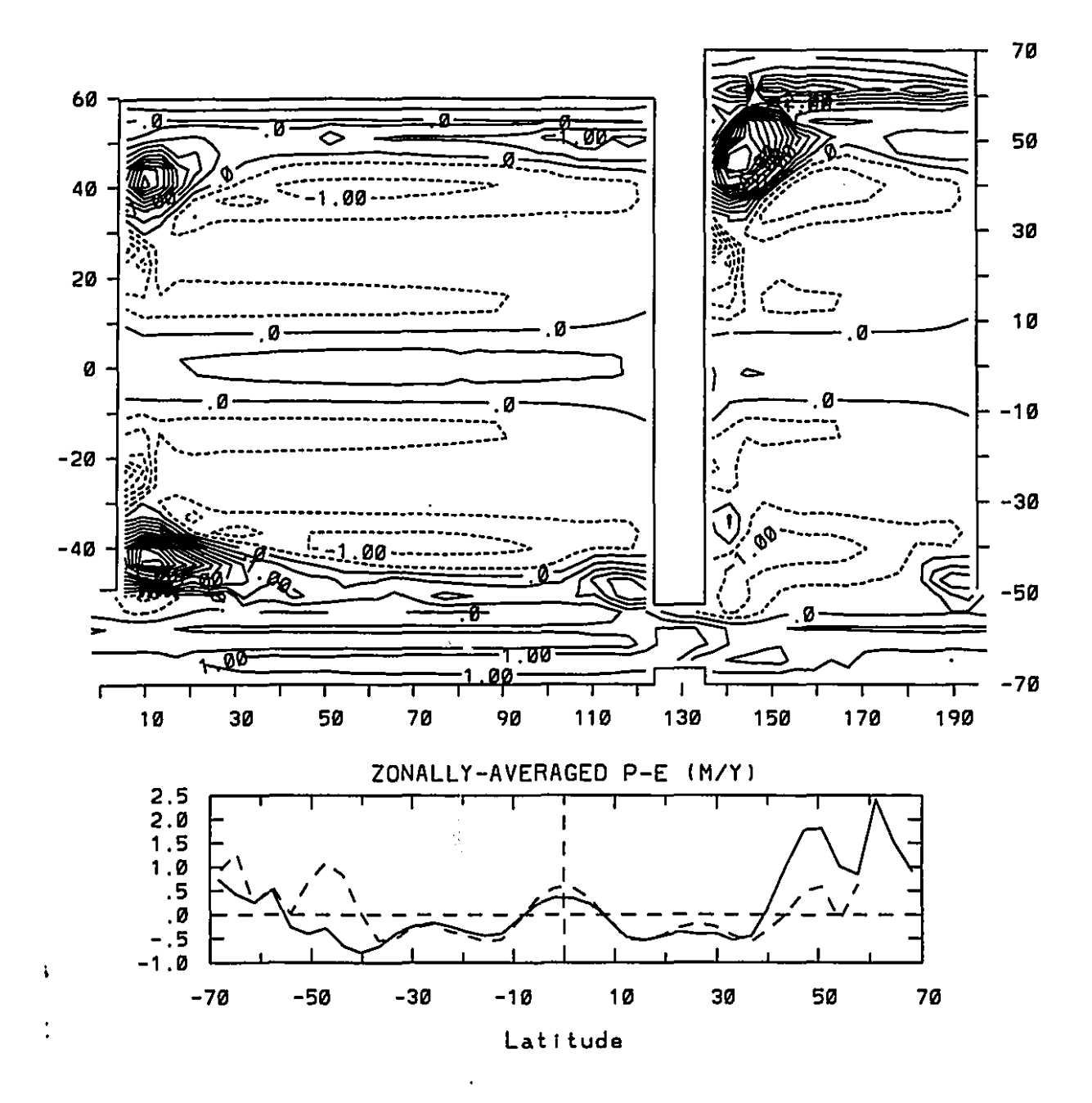


Figure 2.6: Horizontal distribution and zonally-averaged profiles (solid line: Atlantic; dashed line: Pacific) of diagnosed P-E (m/y) for the Symmetric Hemispheres spin-up.

Table 2.2. Equilibrium freshwater budgets of the spin-ups under various surface boundary conditions. The numbers represent the integral of the diagnosed (P-E) over the surface of each ocean in Sv.

		North Atlantic	North Pacific	South Atlantic	South Pacific	Southern Ocean
	Symmetric Hemispheres	+0.298	-0.219	-0.278	-0.150	+0.349
	Asymmetric Oceans	-0.014	+0.119	-0.235	-0.425	+0.555
43	Symmetric Oceans	+0.022	+0.009	-0.191	-0.386	+0.547
	No Wind	-0.011	+0.051	-0.134	-0.242	+0.336
	Half Wind	-0.006	+0.089	-0.180	-0.349	+0.445

realistic representation of the water masses and surface exchanges is achieved. In the zonally-averaged (P-E) profile for example, the correct triple-humped structure is produced, with high-latitude freshening, subtropical evaporation and equatorial precipitation; this may be compared to the (P-E) profile used by MW with net evaporation over the equator. However, the overly strong *Conveyor* circulation in the spin-up results in very large freshwater fluxes (> 6 m/y) being diagnosed over the model Gulf Stream, to compensate for excessive northward salt transport within the ocean. As summarized in Table 2.2¹, net precipitation is predicted for the North Atlantic, while the North Pacific loses an almost equal amount of freshwater by evaporation. The Atlantic as a whole also has net precipitation while the Pacific is an evaporative basin, in direct contradiction to the observed hydrological cycle. Upon switching to mixed boundary conditions, a freshwater cap develops over the entire North Atlantic and the circulation undergoes a

¹ All of the diagnosed heat and salt flux fields used in this thesis are corrected to have vanishing global mean.

transition into an *Inverse Conveyor* mode with strong overturning (44 Sv) in the North Pacific and none in the North Atlantic. This confirms the conclusion of Stocker and Wright (1991a) that geography alone may not be enough to produce a modern thermohaline circulation.

In the second spin-up (hereafter "Asymmetric Oceans"), the individual Levitus (1982) profiles for the Atlantic and Pacific are used in the corresponding basins, with averaging only in the Antarctic (Fig.2.3b). The implied surface density profile (Fig.2.5b) has higher values at nearly every latitude in the Atlantic compared to the Pacific, but the density just north of the ACC is nearly as large as the maximum in the northern North Atlantic. Thus, despite initializing the Atlantic with the distinctive high temperatures and salinities that are usually associated with the presence of an active thermohaline circulation there, the equilibrium under restoring boundary conditions is only a very weak Conveyor, with about 4 Sv overturning in the North Atlantic penetrating to depths of less than 1500 m. In the Southern Ocean, deep sinking occurs almost exclusively north of the circumpolar current (although there is convection right down to the ocean floor around Antarctica, compared to only the upper kilometer or so in the northern North Atlantic). Plots of the vertical velocity (not shown) reveal that the sinking at ~51°S is concentrated in a few localized regions, especially just west of the tips of the continental barriers where the ACC must narrow to fit through the straits. These few patches of strong downwelling dominate the weaker upwelling at most points around that latitude. In the global water mass model of England (1993), a coastal region west of Cape Horn was the location for the formation of AAIW. Such deep sinking (easily 4500 m) in the present model may therefore imply too weak stratification of the bottom water compared to climatology, a defect which England (1993) associated with the summer bias of salinity observations in the Antarctic.

 \mathbb{S}_{2n+1}

The (P-E) field diagnosed from this second spin-up (Fig.2.7, Table 2.2) is more like the observed modern hydrological cycle, with net evaporation (~0.01 Sv) over the North Atlantic and net precipitation (~0.12 Sv) over the North Pacific,

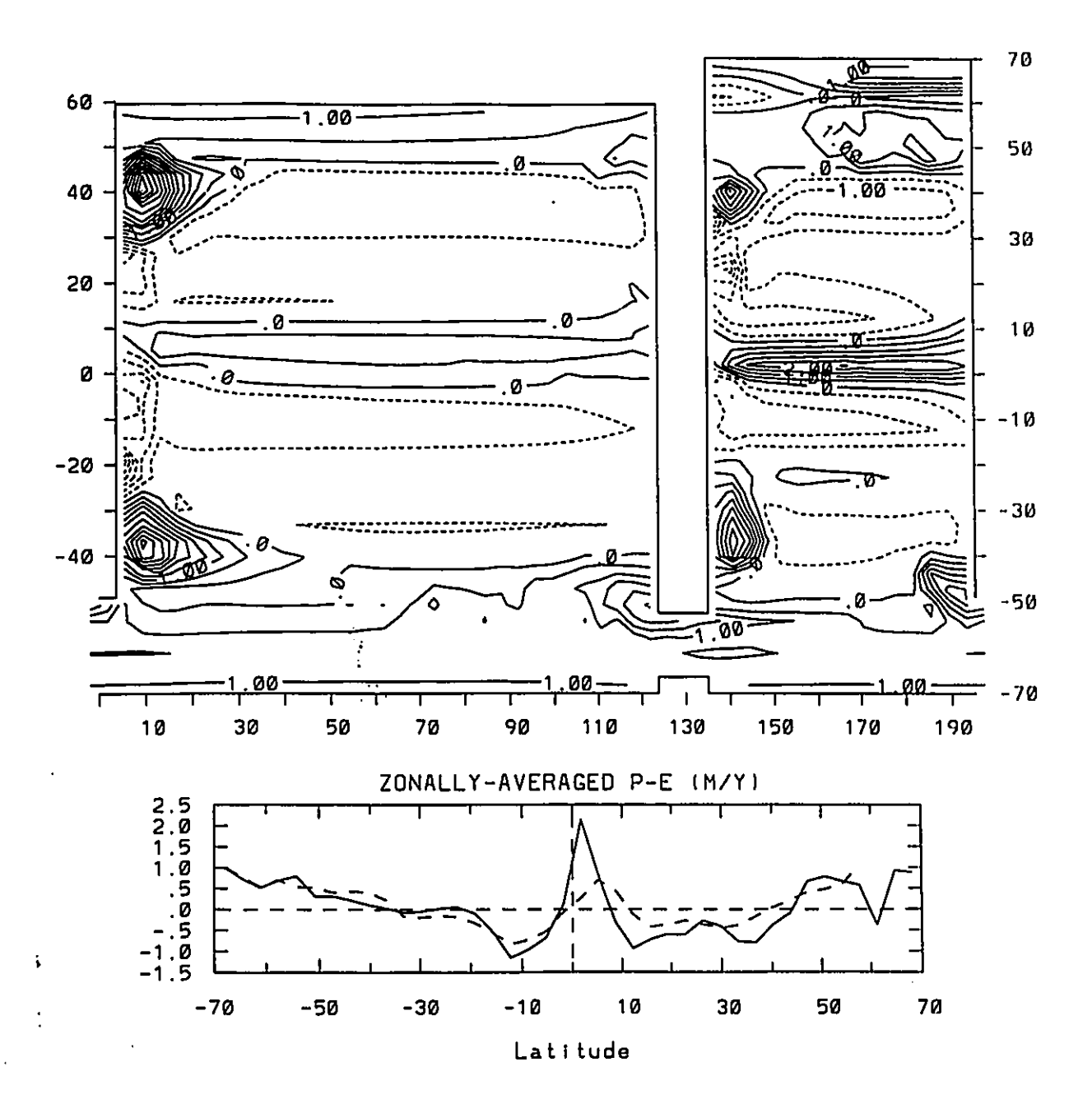


Figure 2.7: Horizontal distribution and zonally-averaged profiles (solid line: Atlantic; dashed line: Pacific) of diagnosed P-E (m/y) for the Asymmetric Oceans spin-up.

although the magnitudes are too small. Both basins as a whole have net evaporation, with the larger amount in the Pacific - this is balanced by net precipitation over the Southern Ocean. The second spin-up also is unstable upon switching to mixed boundary conditions: the North Atlantic overturning intensifies to about 10 Sv, and the southern sinking splits into two branches north and south of the sill (Fig.2.8). A fresh halocline appears in the Southern Ocean, shutting off convection in the centre of the channel although not to the immediate north or south of it, and a slight barotropic acceleration of the ACC occurs (Fig.2.9). The other large-scale circulation change visible in Fig.2.9 is the northward acceleration of the surface velocities all the way along the western boundary from the far South Atlantic till nearly 60°N where the flow turns eastward across the ocean and sinks at the eastern boundary. The opposite pattern appears at deeper levels, consistent with the intensification of the zonally-averaged overturning in the North Atlantic noted above. The latitude of strongest sinking in the overturning streamfunction is ~61°N, rather than right at the northern boundary, and coincides with the maximum negative surface buoyancy flux in zonal average.

A third spin-up (hereafter "Symmetric Oceans") is carried out in which identical T* and S* profiles are used in each basin, constructed as area-weighted averages of the Atlantic and Pacific profiles in the previous experiment (Fig.2.3c). The bias due to using warmer temperatures and higher salinities in one ocean is thus removed, while the fundamental asymmetry between northern and southern hemispheres is maintained. The restoring density north of the ACC is indeed again almost equal to the maximum in the northern hemisphere, however, since the northern maximum lies north of 60°N, the Atlantic may be expected to dominate the Pacific (Fig.2.5c). In agreement with this, the meridional overturning consists once again of a very weak conveyor belt, with ~3 Sv sinking in the North Atlantic, and 28 Sv sinking in the Southern Ocean, mostly north of the gap. However the hydrological cycle diagnosed (Fig.2.10, Table 2.2) is distinctly different, with 1 ½ times as much rain over the North Atlantic (~0.02

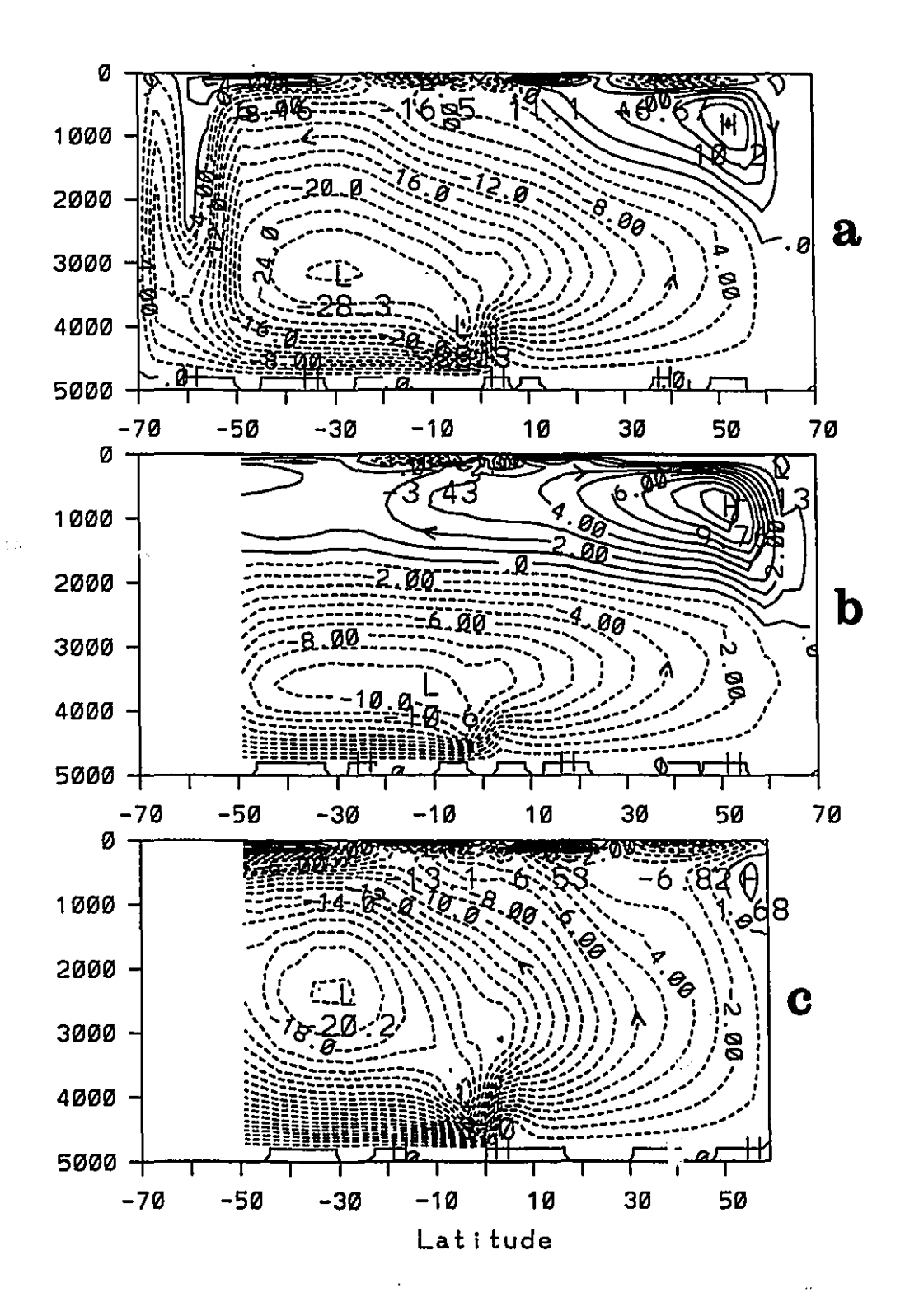


Figure 2.8: Meridional overturning streamfunction (Sv) for a) both oceans together b) the Atlantic c) the Pacific in the Asymmetric Oceans spin-up under restoring boundary conditions.

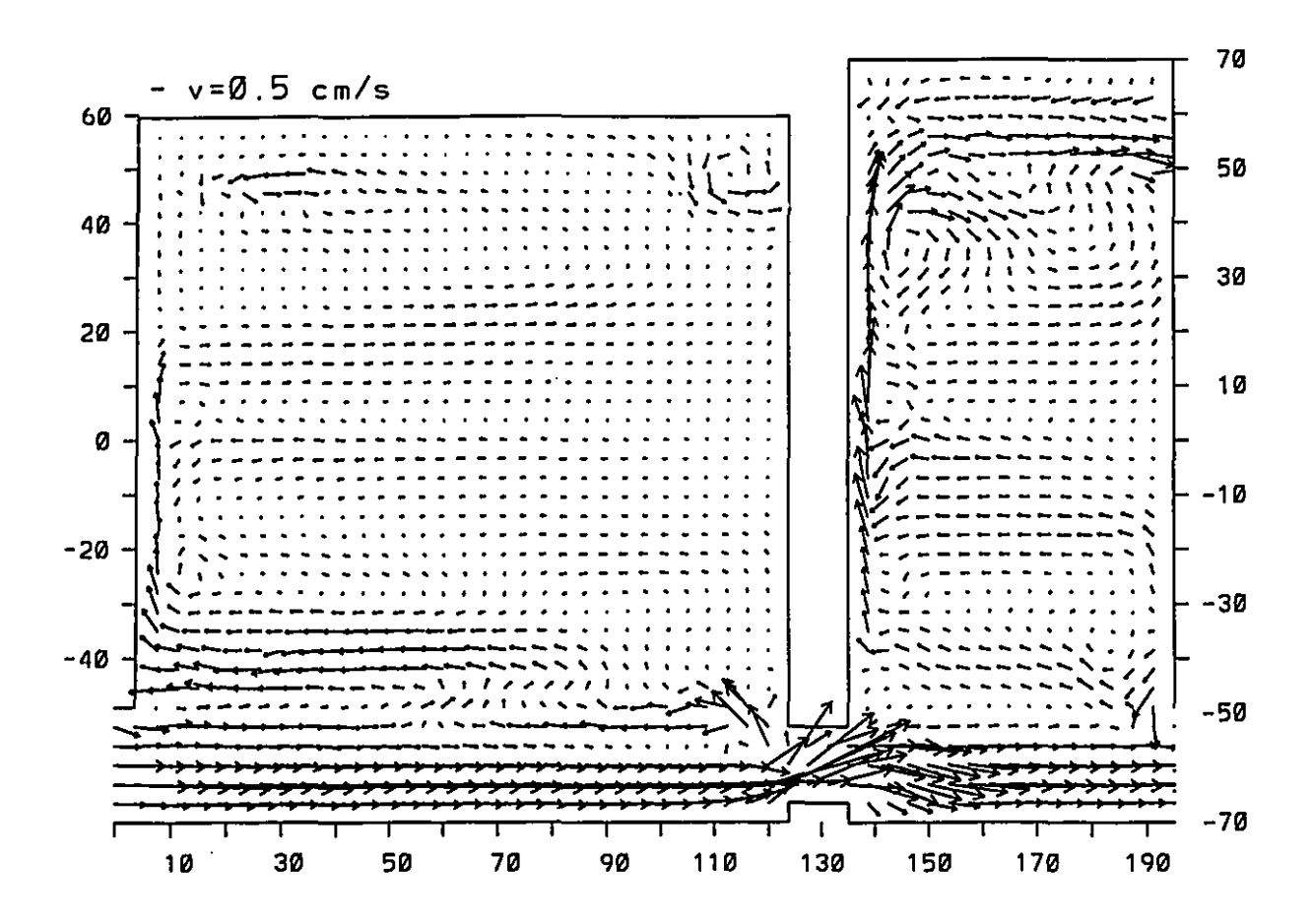


Figure 2.9: Difference in velocity between the equilibria under mixed and restoring boundary conditions for the Asymmetric Oceans experiment.

Sv) as there was evaporation in the previous experiment, and more than twice as much rain over the North Atlantic as over the North Pacific (only ~0.009 Sv in an ocean which is twice as wide). (The sum over both hemispheres shows that there is still net evaporation in both basins, with the larger sum in the Pacific.) Upon switching to mixed boundary conditions, the North Atlantic overturning again intensifies slightly (from 2.6 to 3.3 Sv), but the approach to equilibrium instead of being smooth is characterized by regular oscillations with a period just under 20 years. Spontaneous internal variability was also excited in two of the later mixed boundary conditions experiments under this (P-E) field, suggesting that the total buoyancy forcing is less thermally-dominated than in the Asymmetric Oceans case. As before, the transition to mixed boundary conditions is accompanied by the interruption of convection in the northern half of the ACC, although in this case the overturning in the Antarctic does not appear to be much affected.

The fourth and fifth spin-ups will be described later, and employ the same profiles of restoring temperature and salinity as in the second experiment, but with the magnitude of the wind stress forcing set to zero, or halved, respectively. The results thus far can therefore be summarized by noting that under restoring boundary conditions, the equilibrium overturning in the two-basin model can conveniently be anticipated from the implied zonally-averaged surface density profile. The role of the ACC in isolating the high southern latitudes was demostrated, and climate drift was observed in each of the spin-ups upon switching to mixed boundary conditions. It cannot immediately be concluded that multiple equilibria in the sense of Bryan (1986) have been found, as small inaccuracies in the salt flux field related to intermittent convection in the spin-up at the time of diagnosing (or even the small correction to ensure a vanishing global mean) could in theory be responsible for the transitions, but the next section will verify that they do exist.

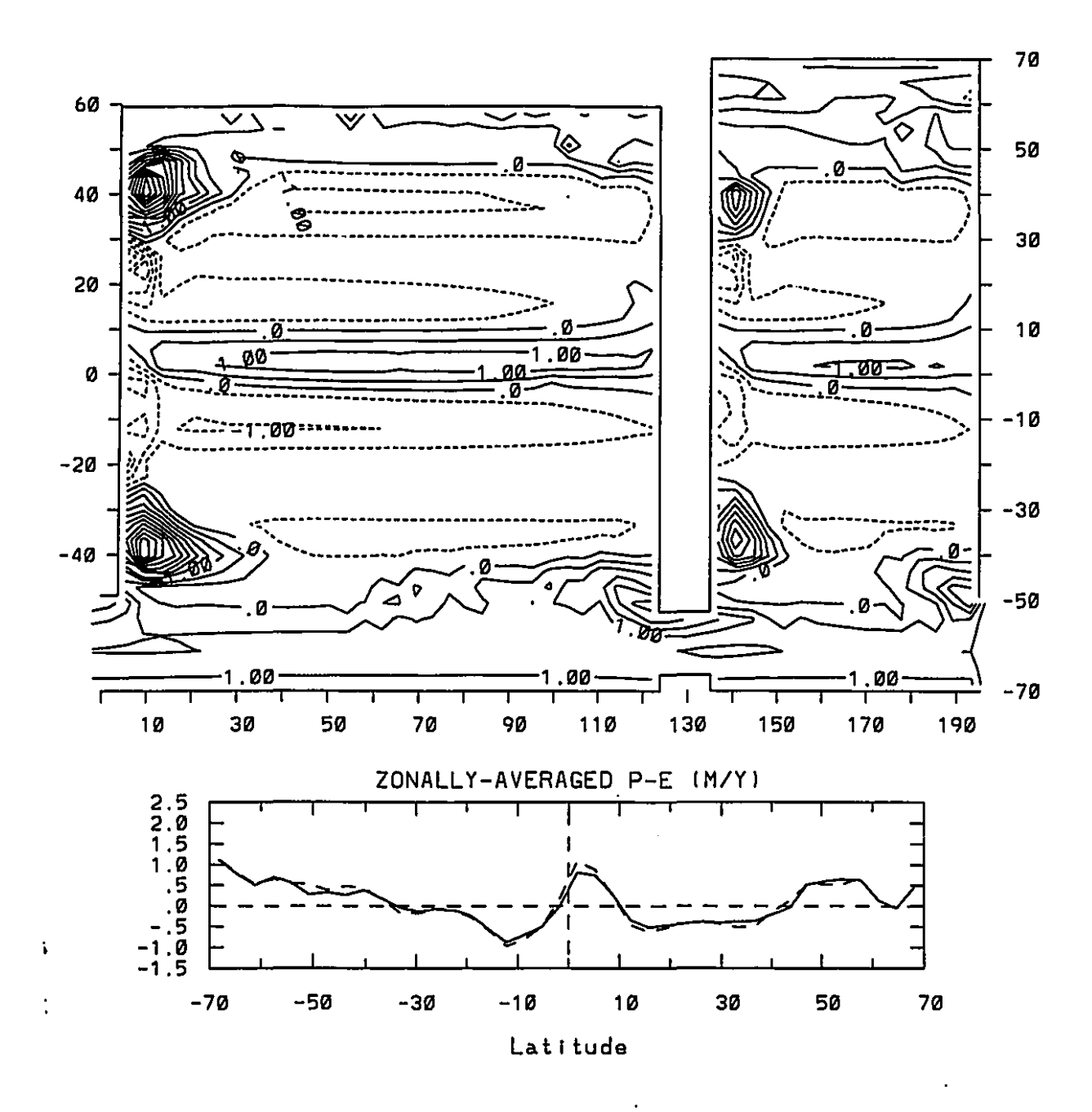


Figure 2.10: Horizontal distribution and zonally-averaged profiles (solid line: Atlantic; dashed line: Pacific) of diagnosed P-E (m/y) for the *Symmetric Oceans* spin-up.

2.2. Multiple Equilibria under Fixed P-E

In this section, the properties of the two-basin model are investigated more exhaustively by searching for multiple equilibria under the (P-E) fields diagnosed above. (Only the Symmetric Hemispheres experiment is not pursued, given the very strong bias of its hydrological cycle in the direction opposite to the observed). The methodology is to obtain a range of initial conditions which are as different as possible from each other, and to integrate these out to equilibrium under the chosen (P-E) field. The initial states are obtained by switching the salinity boundary condition to an artificial salt flux field designed to encourage a specific configuration (*Inverse Conveyor*, *Northern Sinking*, etc.), and maintaining this forcing for a few centuries until the desired features are produced in the overturning. Practical considerations limit the number of experiments that can be carried out, and due to the unpredictability of the thermohaline circulation under fixed freshwater fluxes, it is not possible to space the initial conditions regularly in any sense. Nonetheless, some interesting traits of the asymmetric geometry appear quite rapidly.

The "normal" hydrological cycle (i.e. with net evaporation over the North Atlantic and net precipitation over the North Pacific) from the Asymmetric Oceans experiment is considered first. A total of eleven different initial conditions (including the spin-up) are tested: both initial and final states are summarized in Table 2.3, using only the maximum overturning² in the North Atlantic, North Pacific and southern hemisphere (both basins combined) for conciseness. The sense of the overturning is always positive/thermally dominated (i.e. surface flow

15

²"Maximum overturning" here means the maximum of the zonally-integrated meridional overturning streamfunction cell associated with sinking in the hemisphere in question. In some of the cases with strong sinking in the northern hemisphere, the southern hemisphere cell is not ventilating surface waters but appears as a deep recirculation in the vicinity of the equator. In these cases, the southern overturning is reported as zero.

Table 2.3. Multiple equilibria under the Asymmetric Oceans (P-E) field. The numbers in the table are the maxima of the meridional overturning (in Sv) in the North Atlantic, the North Pacific and the Southern Ocean (both oceans combined), with the initial conditions in the three columns on the lefthand side and the final equilibria on the righthand side. The initial condition for ASYMM 0 is the spin-up, under restoring boundary conditions, and all other equilibria (classed in order of the strength of the NA sinking in the final equilibrium) are under mixed boundary conditions.

	Initial Condition			Final Equilibrium			
	NA	NP	SO	NA	NP	SO	
ASYMM0	4	1	28	10	2	28	
ASYMM1	0	1	39	1	2	30	
ASYMM2	1	17	28	2	2	27	
ASYMM3	1	45	0	2	2	29	
ASYMM4	9	5	36	6	2	26	
ASYMM5	6	13	29	10	2	28	
ASYMM6	7	5	29	22	2	28	
ASYMM7	2	64	0	22	2	28	
SYMM8	26	2	26	26	2	26	
ASYMM9	40	1	4	28	2	26	
ASYMM10	32	23	0	35	2	25	
MARKOV1	same as ASYMM3		2	2	29		
MARKOV2	same as ASYMM10		45	1	20		
MARKOV3	same as ASYMM10			2	2	29	
MARKOV4	same as ASYMM2			2	2	31	
MARKOV5	same as ASYMM4			32	2	31	
MARKOV6	same as ASYMM3			36	1	31	

down the meridional temperature gradient) in each hemisphere, as the symmetric haline-dominated solution with sinking at the equator could not be obtained even as an initial condition despite repeated attempts. For the southern hemisphere cell, no distinction is made between Antarctic deep water travelling northward and

Atlantic deep water that has crossed into the Pacific. Each experiment is integrated for a fixed length of time (2740 years) rather than applying some formal definition of equilibrium, but to verify that this is long enough to trust the final steady state, a number of the runs were prolonged another 1370 years. No qualitative changes and only small quantitative adjustments to the overturning circulations were observed, hence all subsequent experiments were allowed to finish at 2740 years.

The principal result that is illustrated in Table 2.3 is the strong bias of the present model against North Pacific sinking under the *Asymmetric Oceans* boundary conditions. The 2 Sv of North Pacific overturning reported in ASYMM 0 through 10 (the small cell trapped up against the northern boundary in Fig.2.8) is most probably a wind-driven effect, since it is reduced to 1 Sv in later experiments with the wind stress halved, and to 0 under no wind. In the North Atlantic, the thermohaline circulation can tentatively be classified in three ways (examples are shown in Fig.2.11):

- 1) almost no North Atlantic sinking (ASYMM 1, 2, 3),
- intermediate sinking (< 10 Sv, to intermediate depths only, with sinking centered on ~61°N and a fresh halocline in the northern North Atlantic) (ASYMM 0, 4, 5)
- 3) strong (>20 Sv) sinking, occurring right at the northern boundary and with no polar halocline (ASYMM 6, 7, 8, 9, 10).

The first category can be identified with MW's Southern Sinking, and the other two are variations on the Conveyor. This classification is not of course rigorous: it cannot be ruled out that if other initial conditions were tested, new steady states with overturning between 10 and 20 Sv would not be discovered. It is merely noted that while a continuous range of overturning strengths seems theoretically plausible, in practice distinct recognizable patterns did emerge. (This is even more apparent in the SYMM experiments in the paragraph after next). Three different configurations also appear in the Antarctic (again illustrated in Fig.2.11):

1) sinking to the north of the ACC only, with convection everywhere in the

-1-1-2

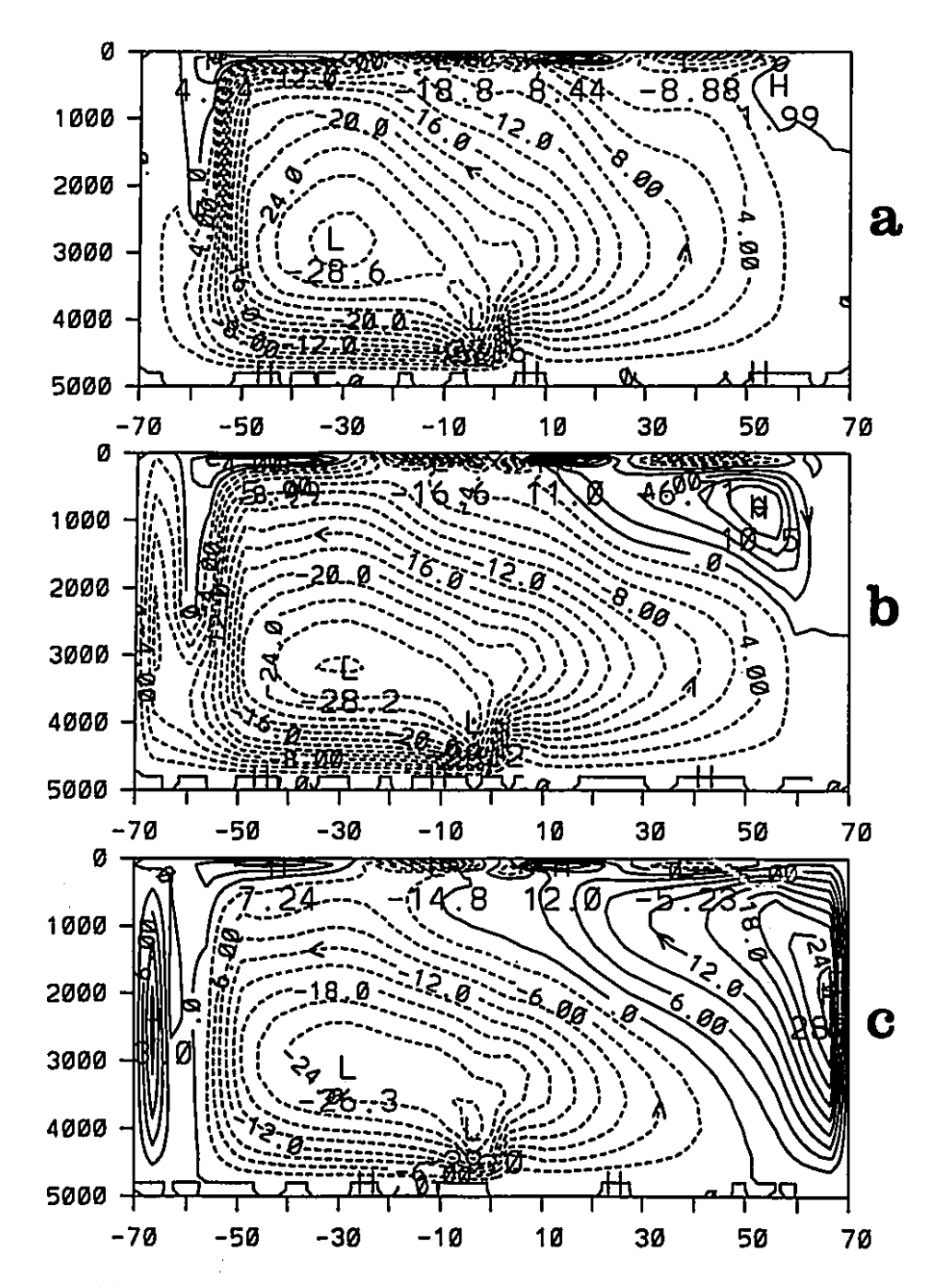


Figure 2.11: Global ocean meridional overturning (Sv) for three equilibria under the Asymmetric Oceans boundary conditions. In the first (ASYMM 3), the southern sinking all occurs north of the ACC and there is almost no northern sinking. In the second (ASYMM 5), the southern sinking has split into two branches north and south of the ACC and there is intermediate North Atlantic sinking at ~61°N, while in the third (ASYMM 9), there is strong overturning in the North Atlantic right at the northern boundary (70°N) and a trapped recirculation next to Antarctica.

ACC (ASYMM 2,5,8)

- 2) sinking both north and south of the gap with no convection in the ACC (ASYMM 0, 3, 10 and perhaps 6 and 7),
- 3) an intense (~12 Sv) recirculation trapped against Antarctica (ASYMM 4.9).

Despite this, the magnitude of the southern cell is remarkably stable, varying over a narrow range of only 5 Sv. No strong link between the northern and southern hemispheres appears otherwise to exist, since any configuration in the Antarctic may seemingly coexist with any overturning strength in the North Atlantic. The barotropic transport in the ACC ranges from about 140 to 220 Sv between the different runs, but is apparently uncorrelated with the North Atlantic overturning.

To test the robustness of the equilibria in Table 2.3, a subset of these experiments are repeated with the same initial conditions and a white noise perturbation superimposed upon the freshwater forcing field. The stochastic component is obtained by integrating a first-order Markovian process with an autocorrelation timescale of 1 month and an isotropic spectrum constant for wavenumbers 6 through 27 in a basin 195° wide (see Weaver et al., 1993 for more details). The standard deviation of the random forcing is initially set to 0.192 m/year or about 20% of the globally-averaged annual mean precipitation (Baumgartner and Reichel, 1975), and two of the initial conditions used earlier are subjected to the perturbation (experiments MARKOV 1 and 2). Both reached steady states qualitatively quite similar to the corresponding unperturbed experiments, hence four more runs (MARKOV 3-6) are carried out under a stronger stochastic field (standard deviation five times larger). This time, there is little relation between the steady states obtained with and without perturbation, however the new equilibria are still not outside the range of Conveyor and Southern Sinking solutions previously obtained. (Two of the circulations under stochastic forcing are also unstable, and undergo repeated collapse/flush events in the southern hemisphere - deep-decoupling oscillations have not been reported previously in multiple basin models.) Thus, although the model's thermohaline

Table 2.4. As in Table 2.3, but for the Symmetric Oceans experiment with net precipitation over the North Atlantic.

	Initial Condition			Final Equilibrium		
	NA	NP	so	NA	NP	so
SYMM0	3	2	. 28	3	3	28
SYMM1	1	17	25	3	3	29
SYMM2	2	6	30	3	3	29
SYMM3	8	4	29	15	3	28
SYMM4	8	4	32	16	2	28
SYMM5	38	29	0	16	2	28
SYMM6	1	34	0	16	3	28
SYMM7	17	2	28	17	2	28
SYMM8	1	1	36	19	2	27
SYMM9	32	19	0	42	_ 5	14

circulation is sensitive to disturbances in the (P-E) field, the attempt to dislodge it into an equilibrium with North Pacific deep water formation was not successful.

Nine new initial conditions (in addition to the spin-up) are then tested with the *Symmetric Oceans* boundary conditions. The distribution of the final equilibria is shown in Table 2.4: once again, North Atlantic sinking is favoured while North Pacific deep sinking is not produced, eliminating the *Inverse Conveyor* and *Northern Sinking* solutions from among the four choices of MW. The equilibria are also even more tightly clustered, with two states with approximate magnitudes of overturning of ~3 Sv and ~16 Sv predominating.

The main conclusion from this section is that multiple equilibria do exist in the asymmetric two-basin model. The preference for *Conveyor* circulations is interesting as it may be a property of the real ocean also (see Chapter 1), and will be revisited in Section 2.5. Its credibility in the present model is supported by the fact that two of the steps that one might wish to take to improve the resemblance with reality would be to tune the magnitude of the hydrological cycle (to increase

the transport of fresh water from the North Pacific to the North Atlantic) and to enhance the restoring salinity at high southern latitudes so as to increase the density of Antarctic bottom water. Both of these adjustments would seem to favour North Atlantic or Southern Ocean sinking at the expense of North Pacific sinking, hence the bias is ostensibly fairly robust. North Pacific sinking is however possible in the present model, under certain special circumstances, which will be described in the next section.

Another new result is the multiplicity of different *Conveyor* states, which develop the original classification into four types by MW. This is interesting in view of paleoclimatic descriptions of a shallower weaker North Atlantic thermohaline circulation during the last glacial maximum. As noted, the overturning in the various equilibria could be loosely bunched into weak, strong and intermediate North Atlantic circulations; this observation is reinforced by the time-dependent experiments of Weaver and Hughes (1994), who found millennial timescale variability with transitions between the same three modes under strong stochastic forcing. Finally, although some degree of similarity between the initial and final states in Tables 2.3 and 2.4 often exists, clear exceptions also occur (ASYMM 7 is one) and initial conditions that are quite similar could diverge strongly (e.g. ASYMM 4 and 6), as is characteristic of chaotic systems.

2.3. Role of the Southern Ocean

Equilibria with North Pacific sinking appeared in a somewhat diverse set of experiments in the standard geometry. The first group are runs under reduced winds. A fourth and fifth spin-up are done under the Asymmetric Oceans T* profile with the magnitude of the winds set to zero or ½ respectively. The Nowind spin-up is depicted in Fig. 2.12, and is superficially quite similar to the Asymmetric Oceans spin-up (except for the absence of Ekman cells), with weak (2.6 Sv) sinking at ~61°N in the North Atlantic, and about 25 Sv southern sinking

ij.

į,

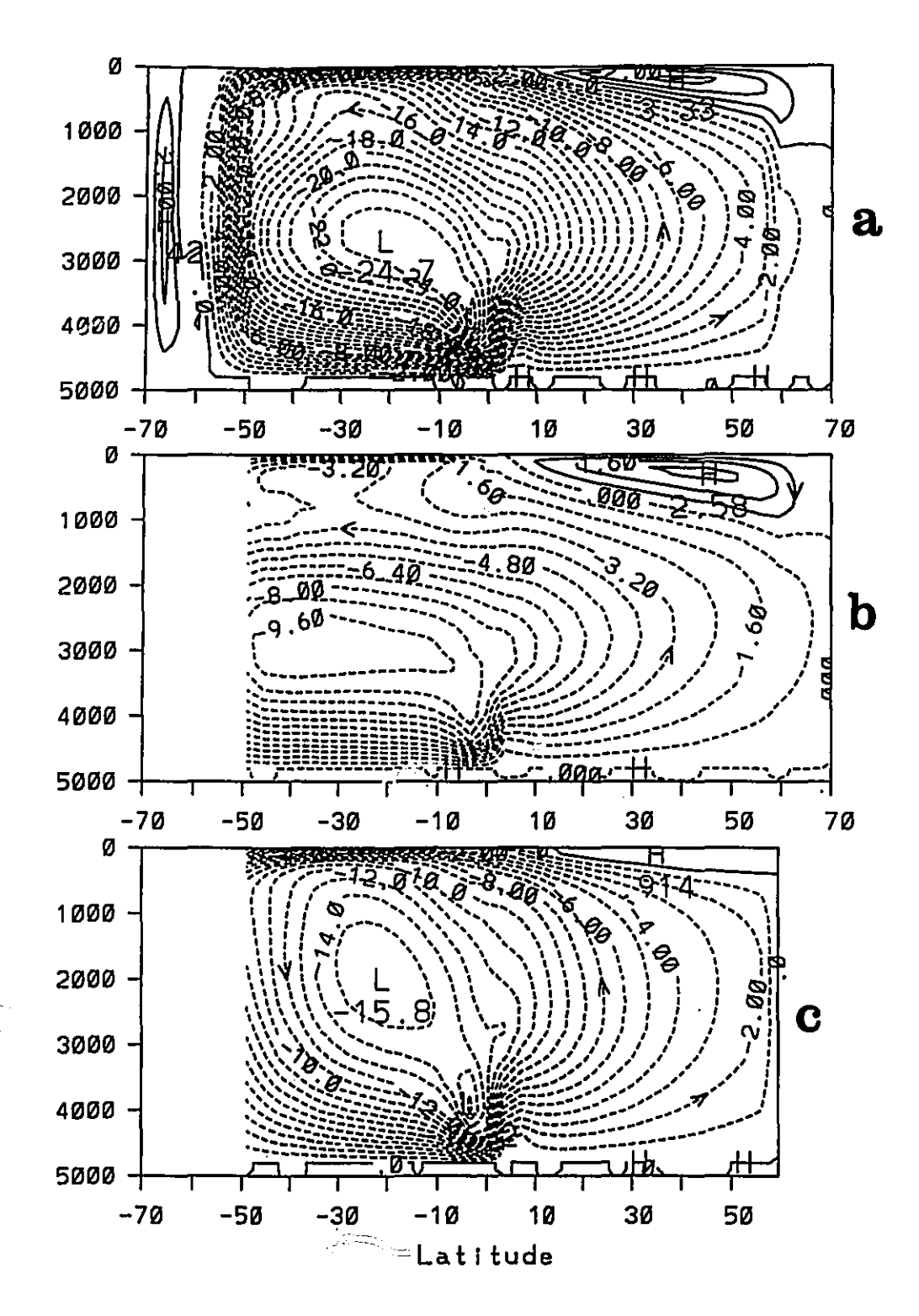


Figure 2.12: Meridional overturning streamfunction (Sv) for a) both oceans together b) the Atlantic c) the Pacific in the *Nowind* spin-up under restoring boundary conditions.

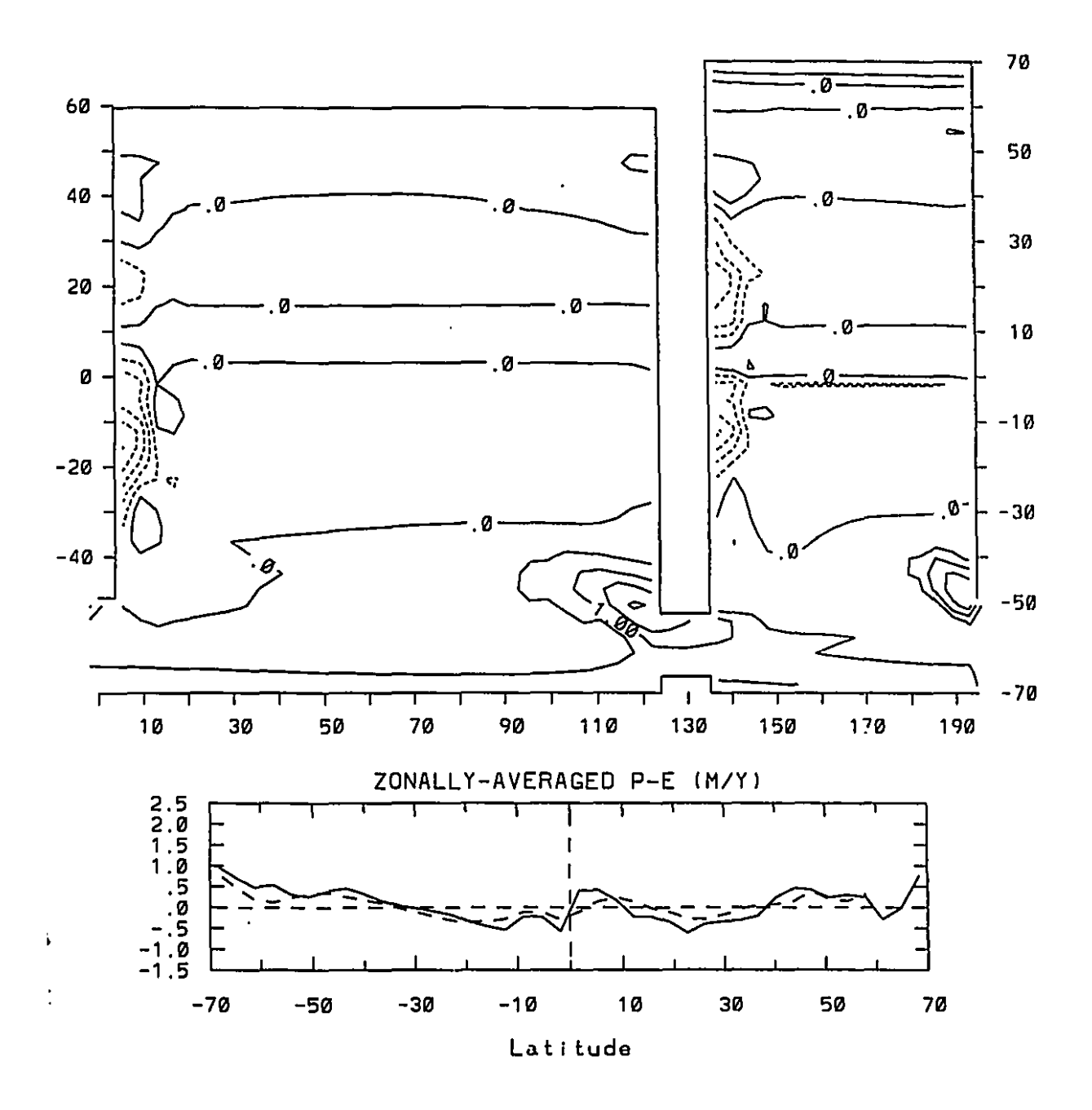


Figure 2.13: Horizontal distribution and zonally-averaged profiles (solid line: Atlantic; dashed line: Pacific) of diagnosed P-E (m/y) for the *Nowind* spin-up.

mostly north of the ACC plus a weak positive recirculation adjacent to Antarctica. The diagnosed freshwater fluxes are shown in Fig.2.13 and Table 2.2, and have the same sign in each hemisphere as in the Asymmetric Oceans experiment, but magnitudes reduced by one-third to one-half. Under mixed boundary conditions, the North Atlantic sinking intensifies to 5.0 Sv, but remains weaker than the Conveyor with wind stress forcing. The new freshwater fluxes are then applied to seven of the initial conditions tested earlier, and integrated out to equilibrium under no winds: the results are shown in Table 2.5. A Northern Sinking equilibrium, with strong overturning in both oceans, is produced in three out of the seven cases. Similarly, under the Halfwind (P-E) field and winds weakened accordingly, two out of eight initial conditions (counting the spin-up) select a Northern Sinking state (Table 2.5). In two further experiments, the wind stress forcing is either eliminated or halved in the Southern Ocean only, everywhere south of 49°S. Starting from the ASYMM 10 initial condition (which resulted in Northern Sinking under no winds), both runs select an equilibrium with strong North Atlantic overturning and 11-12 Sv North Pacific sinking (last 2 lines in Table 2.5). Three more experiments are done that confirm the importance of the Southern Ocean region for the model's global thermohaline circulation. In the first two, enhanced zonal mixing completely homogenizes the temperature and salinity around latitude circles at each timestep for the three gridpoints between 61.25°S and 54.25°S. Both runs, under no winds and under full winds, produced Northern Sinking equilibria. The final experiment is to disable convection in the Southern Ocean, which also produced North Pacific sinking under full winds.

The common characteristic of all these runs is the appearance of a very fresh halocline over the whole Antarctic (e.g. Fig. 2.14). The circulation in the southern hemisphere is of course much altered by this: in particular, the zonal circumpolar current which couples the two basins is drastically weakened even in the runs with wind. The transient development of the polar halocline catastrophe in these experiments has been left unexplored, since the focus of this chapter is

Table 2.5. As in Table 2.3, but under no winds or half winds or reduced winds in the Southern Ocean only.

	Initial Condition			Final Equilibrium		
	NA	NP	· so	NA	NP	so
NOWIND0	3	0	25	5	0	24
NOWIND1	same as ASYMM2			4	0	24
NOWIND2	same as ASYMM5			5	0	24
NOWIND3	same as ASYMM9			11	0	24
NOWIND4	same as ASYMM4			12	0	24
NOWIND5	same as ASYMM3			29	33	0
NOWIND6	same as ASYMM1			30	24	0
NOWIND7	same as ASYMM10			34	30	0
HALFWIND0	3	1	27	0	1	27
HALFWIND1	sam	e as ASY	MM1	0	i	27
HALFWIND2	same as ASYMM5		11	1	27	
HALFWIND3	same as ASYMM10			19	1	29
HALFWIND4	same as ASYMM9		20	1	29	
HALFWIND5	same as ASYMM3			32	38	0
HALFWIND6	end of NOWIND6			0	1	28
HALFWIND7	end of NOWIND7			44	17	0
no wind in SO	same	as ASYI	MM10	47	12	8
half wind in SO	same	as ASYI	MM10	47	11	9

on equilibrium aspects of the thermohaline circulation, but the consequences are certainly relevant. The zonally-averaged surface density under mixed boundary conditions is plotted in Fig.2.15 for two runs. In both the weak *Conveyor* of NOWIND 1, and the strong *Northern Sinking* of NOWIND 7, the peak density in the North Atlantic is greater or equal to the surface density at the boundary between the South Atlantic and the Southern Ocean. But the pole-to-pole gradient

Figure 2.14: Zonally-averaged salinity (ppt) in the upper km of the NOWIND 7 run.

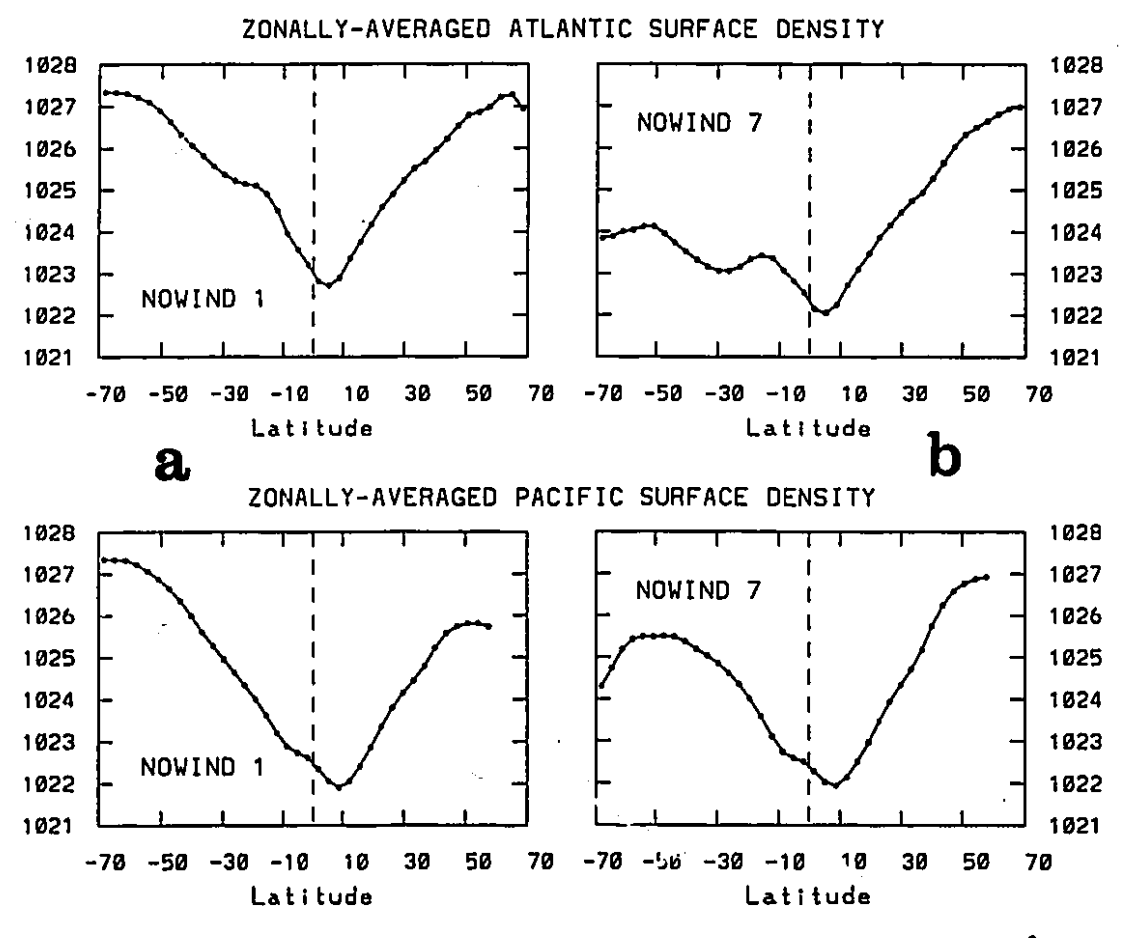


Figure 2.15: Meridional profile of zonally-averaged surface density (kg/m³) in the Atlantic and Pacific basins for the NOWIND 1 (with weak sinking in the North Atlantic) and NOWIND 7 (with strong sinking in both North Atlantic and North Pacific) runs.

in the Pacific slopes down to the north (Fig.2.15a) in every case except in the North Pacific sinking runs when the freshening of the Antarctic reverses the sign (Fig.2.15b). This relationship, anticipated in Section 1.1, also suggests a clue to an earlier observation: the apparent insensitivity of the Southern Ocean overturning to the strength of the North Atlantic circulation. The seeming independence breaks down in the extreme cases of North Atlantic sinking greater than about 40 Sv (e.g. MARKOV 2, SYMM 9) or strong overturning in both northern oceans, when the southern overturning is drastically reduced. It appears that in some sense, the intra-hemispheric gradient south of the equator in these circulations is overcome by the inter-hemispheric contrast to produce a single pole-to-pole overturning cell with sinking only in the north.

The reasoning in both the present section and Section 2.1 has relied upon the analogy with the box models (Stommel, 1961 and successors) where the meridional flow is parameterized as directly proportional to the meridional surface density gradient. In a stratified model, surface density is not a dynamic quantity, but more importantly, the driving force for the meridional flow should come from an <u>east-west</u> pressure gradient rather than a north-south one, because of the Coriolis effect. Theoretical understanding of how the large-scale zonal and meridional pressure gradients change together to set up the overturning circulation is at present very scanty. A rather empirical investigation of the relationship between the equilibrium overturning and the density field in the numerical model is therefore attempted in the next section. While this approach is not the ideal one, it will confirm the principal conclusion from this section: the importance of the Southern Ocean in the global thermohaline circulation.

2.4. Relationship Between Large-Scale Pressure Gradients and the Meridional Overturning

The simplest possible initial hypothesis is a linear frictional balance for the

zonally-averaged meridional flow, as traditionally assumed in box models:

$$r\overline{v} = -\frac{1}{\rho} \frac{\partial \overline{p}}{\partial y} \tag{2.1}$$

where ρ and p are reference density and hydrostatic pressure, r is an unspecified friction coefficient, v is meridional velocity and an overbar signifies a zonally-averaged quantity. Even in runs without wind stress forcing, there appeared to be little evidence for such a simple balance holding. However, if a further assumption is made of a level of no motion v=0 at a depth z_0 , a weaker condition on the depth-integrated steric height can be derived:

$$\int_{z_0}^{0} \overline{v} dz' = - \frac{1}{\rho gr} \frac{\partial}{\partial y} \int_{p(z_0)p(z_0)}^{p(0)} \overline{\delta} dp'' dp'$$
(2.2)

where δ is the steric volume anomaly. In the Atlantic, such a level of no motion might most plausibly be assigned to the mid-depth of the northern overturning cell, at the transition between northward surface flow and southward deep flow. The depth-integrated zonally-averaged meridional velocity and steric height relative to z₀=1500 m are plotted in Figs.2.16a,b as a function of latitude for the run NOWIND 4 with 12 Sv overturning in the North Atlantic (Table 2.5). Some correspondence is evident but the scatter plot in Fig. 2.16c indicates that any relationship is quite nonlinear, and may differ between the two hemispheres. Surprisingly, however, a linear proportionality does emerge for the basin-averaged relationship in a large ensemble of runs. In Fig. 2.17a, the meridional overturning for each of the experiments in Tables 2.3, 2.4 and 2.5 is plotted as a function of the difference in depth-integrated steric height between the northern boundary of the Atlantic and the first gridpoint north of the ACC. (An equally good linear slope can be obtained if the southern limit is chosen as 1.75°N instead, but the basin length seems the more appropriate distance from the previous discussion. In agreement with this, the North Atlantic overturning under restoring boundary conditions increases from 4 Sv to 7 Sv to 8 Sv as the tip of South America in the model is moved back from 52.5°S to 45.5°S to 42°S.) In Fig.2.17a, runs with full

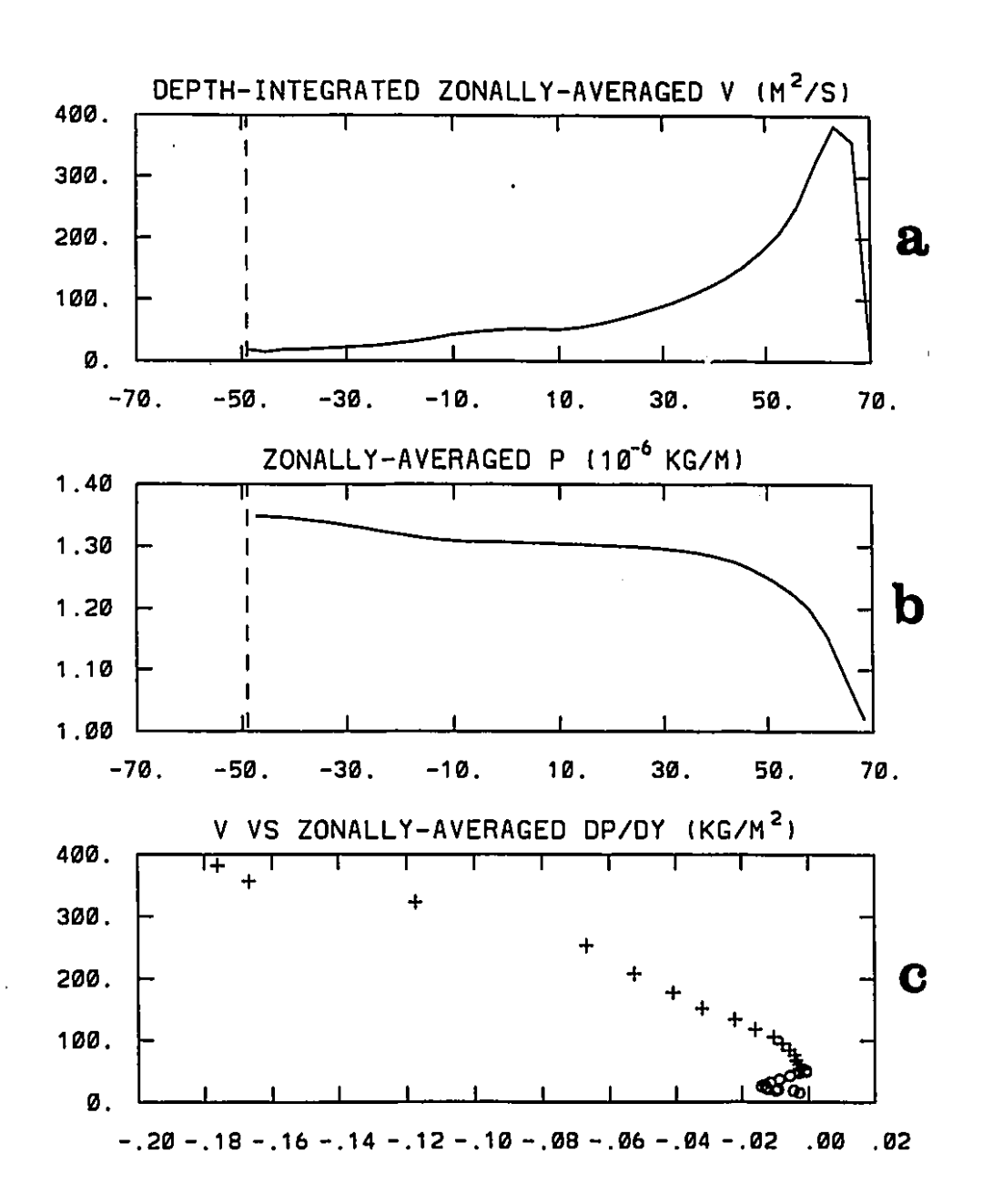


Figure 2.16: Meridional profile of a) the depth-integrated zonally-averaged meridional velocity (m^2/s) and b) the depth-integrated zonally-averaged steric height (10^{-6} kg/m) above a reference level z_0 =1500 m for the NOWIND 5 run. c) Scatter plot of these two quantities (crosses: northern hemisphere; circles: southern hemisphere).

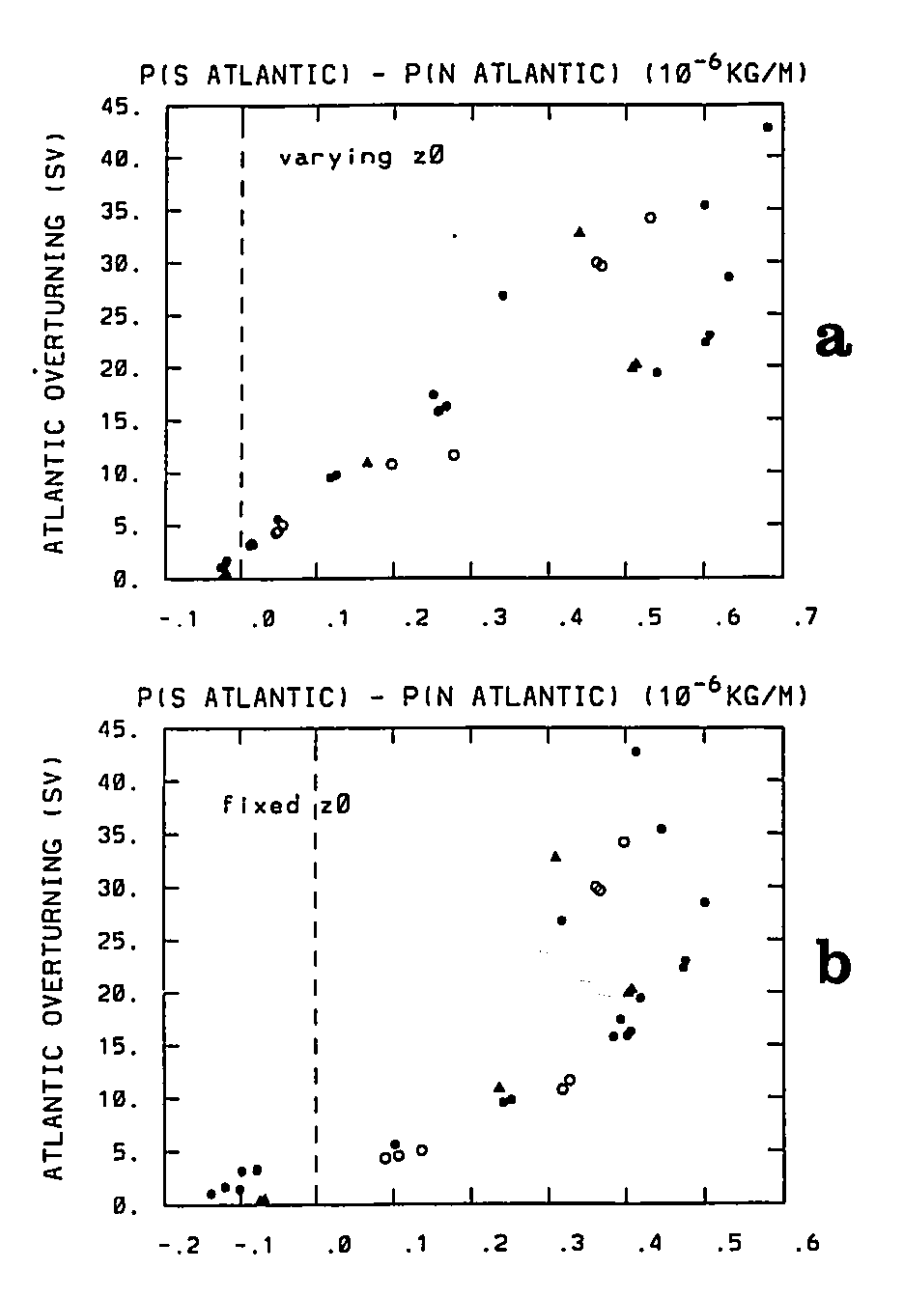


Figure 2.17: North Atlantic overturning (Sv) versus the north-south contrast in depth-integrated zonally-averaged steric height $P(10^{-6} \text{ kg/m})$ between 68.75°N and 47.25°S. In a), a different reference level is chosen for each equilibrium at the approximate mid-depth of the overturning cell in the North Atlantic, while in b) a single reference level ($z_0=1500 \text{ m}$) is used for all runs. In c), the Atlantic overturning is plotted versus the steric height gradient from the Pacific in the same equilibrium. Full-wind runs are identified by black circles, half-wind runs by black triangles, and no-wind runs by white circles.

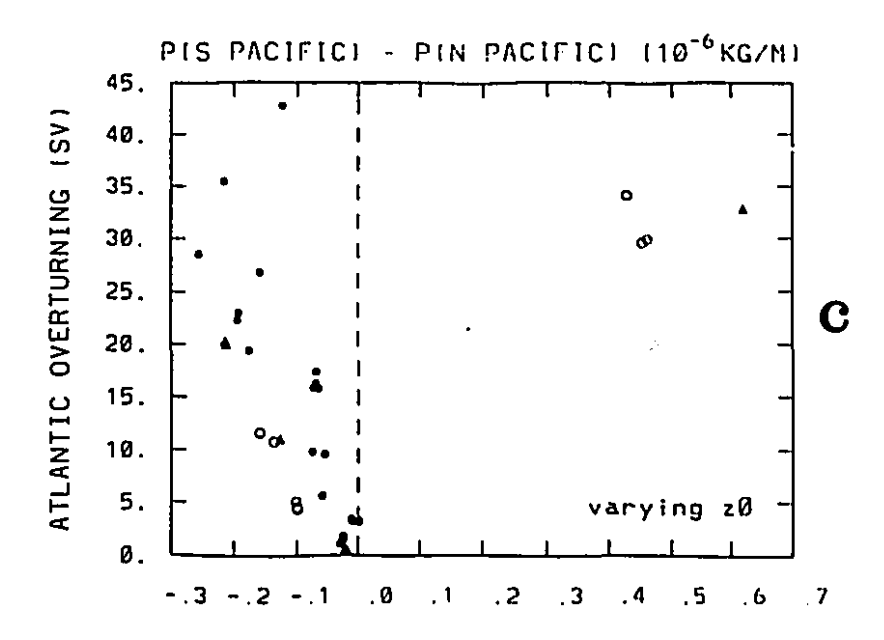


Figure 2.17. Suite.

wind forcing are identified by black circles, half-wind runs by black triangles, and no-wind runs by white circles. A different z_0 has also been assigned to each equilibrium, corresponding to the depth of the overturning maximum in the northern hemisphere³. If a fixed z_0 is used instead, the correlation is still tight but the curve becomes almost quadratic (Fig.2.17b).

It is not clear how much information is contained in Fig.2.17a, given that z_0 itself increases approximately linearly with the overturning. To verify that the linear slope is not an artifact of the varying z_0 , the calculations can be repeated using the density field from the Pacific: the linear dependence is indeed destroyed as hoped (Fig.2.17c) so does seem to be real in the Atlantic. It is frankly quite surprising to find such a result at all, given that pressure variations due to the wind-driven circulation have been ignored, as have the different dynamical

³ This is one of a number of small differences between Fig.2.17a and the very similar plot in Hughes and Weaver (1994, their Fig.13) where the reference levels were more arbitrarily chosen by visual inspection of the overturning plots. Other differences are that the Knudsen equation of state has been used instead of the UNESCO version, to conform with the Cox model, and a fixed latitude has been used for the northern boundary instead of choosing the latitude of maximum surface density.

regimes in the western boundary and interior of the ocean, and finally, the friction in the model is Laplacian rather than linear. It is possible that the relative success of the hypothesis is related to the intensification of the thermohaline circulation into a frictional western boundary current (e.g.Fig.2.9), but a more complete justification is lacking. The practical applications of this result are also rather limited: it is a description of rather than an explanation for the multiple equilibria, and the relationship is without predictive value. One possible benefit is to provide some physical foundation for the simple linear flow laws used in box models, but the more significant conclusion is to confirm the importance of the Southern Ocean not only as an on/off switch for Pacific deep sinking but also in anchoring the meridional pressure gradients that control the Atlantic thermohaline circulation.

A definite relationship between meridional and zonal pressure gradients must be postulated in order to develop two-dimensional models of the thermohaline circulation, whose greater simplicity and more economical application are highly appealing to climate modellers. The original prototype by Marotzke et al. (1988) assumed the local and linear relationship (2.1), valid in the limit of a narrow basin. But the most successful model of this class has been the zonally-averaged model of Wright and Stocker (1991) which includes the effect of rotation. Starting from a pure geostrophic balance for the meridional flow and linear damping in the zonal direction, a closure relationship between the crossbasin and zonally-averaged meridional pressure gradients was derived. This was written in spherical coordinates as (Wright and Stocker, 1992):

$$(p_E - p_W) = -\varepsilon \sin(2\phi) \frac{\partial(\bar{p})}{\partial \bar{\phi}}$$

$$(2.3)$$

where p_E and p_W are pressure at the eastern and western boundaries respectively, and ϕ and λ are latitude and longitude. The parameter ϵ was given physical significance by relating it to the departure from geostrophy of the zonally-averaged zonal velocity:

$$\varepsilon = \frac{\Omega}{r} \left(1 - \frac{\bar{\mathbf{u}}}{\bar{\mathbf{u}}_{g}} \right) \tag{2.4}$$

where Ω is the Earth's rotation, r the coefficient of linear damping, and $\bar{\mathbf{u}}_{\mathbf{z}}$ the geostrophic component of the mean zonal velocity $\bar{\mathbf{u}}$. The derivation of equation (2.3) was later modified by Vreugdenhil and Wright (1993, unpublished manuscript) who suggested that the relationship should more correctly be formulated in terms of density gradients, or equivalently in pressure minus surface pressure:

$$\frac{(p_E - p_{ES}) - (p_W - p_{WS})}{(\lambda_E - \lambda_W)} = -\epsilon \sin(2\phi) \frac{\partial (\bar{p} - \bar{p}_S)}{\partial \phi}$$
(2.5)

where ps stands for surface pressure. Wright and Stocker (1991) obtained an approximate order of magnitude for ε by evaluating both sides of (2.5) at 27 different latitudes (2° intervals omitting equatorial and deep convective regions) in a single run of a one-hemisphere 60°-wide model using the Bryan-Cox OGCM. For depths below about 500 m, a linear fit produced quite high correlations and a mean slope of about 0.3. The fit did deteriorate towards z=0 (Fig.2 of Wright and Stocker, 1991) which was attributed to the zonally-uniform restoring boundary conditions damping zonal density variations at the surface. For their multiplebasin model, Stocker and Wright (1991a) reasoned that ε should also be inversely proportional to the angular width of the basin so that the pressure drop across the basin for a given north-south gradient would be independent of the width. A much smaller value of ε =0.0001 was used in the Southern Ocean to acknowledge the absence of east-west pressure gradients there. Apart from this however, a constant value was used in each basin, which as D. Wright (personal communication) has pointed out, reduces (2.5) to a frictional parameterization similar to (2.1).

A final service to which the data from the present OGCM runs can be put is to test the universality of this parameterization more strenuously. Fig.2.18 shows two meridional sections of ε from equation (2.5) at each latitude and depth of the Atlantic basin in the NOWIND 1 and NOWIND 7 final equilibria with very weak and very strong overturning respectively. The relationship deteriorates near the equator, as expected from the failure of geostrophy at low latitudes.

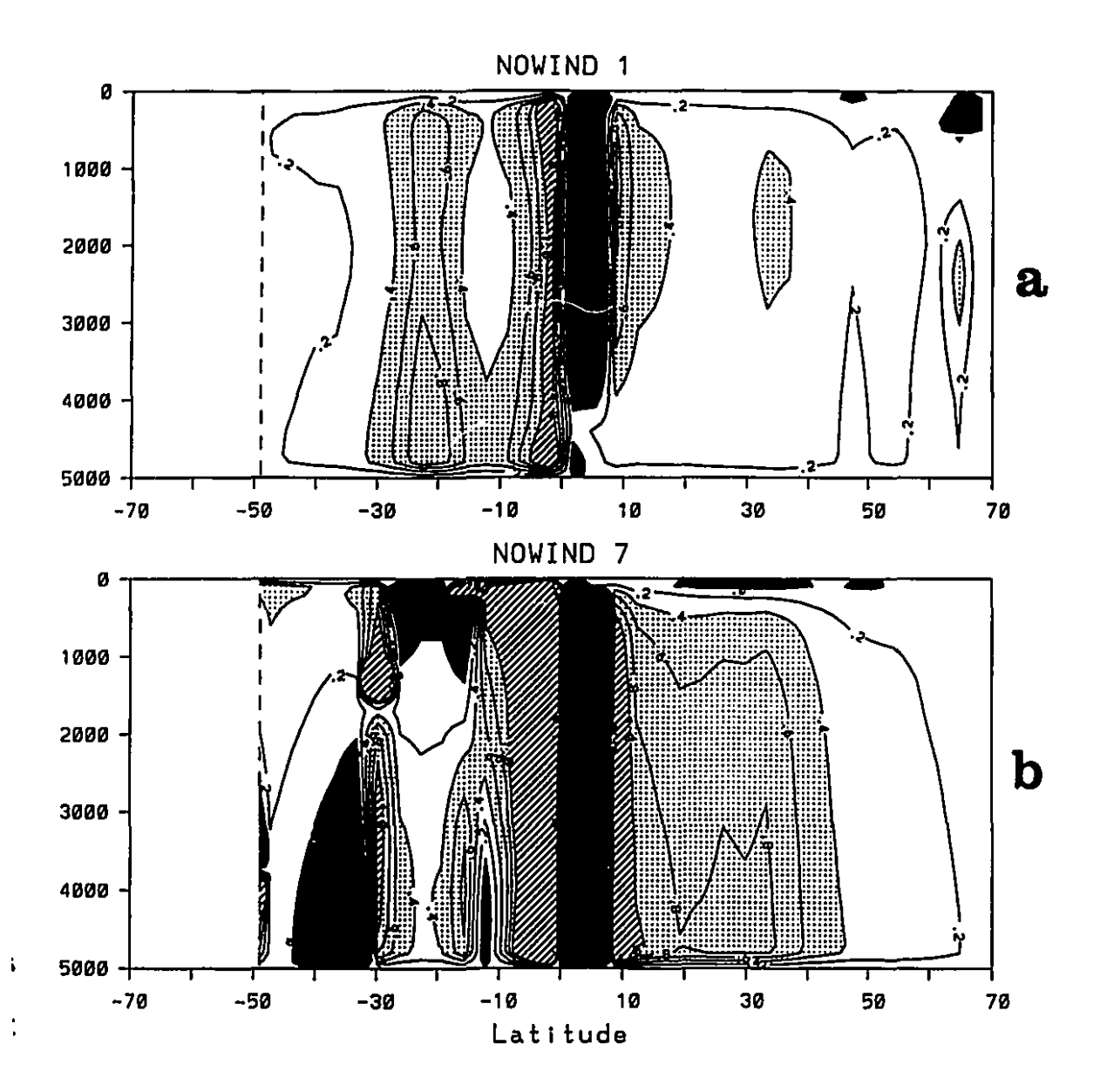


Figure 2.18: Latitude-depth section of the Wright and Stocker (1991) parameter ε evaluated without surface pressure (equation 2.5) for the Atlantic basin of a) the NOWIND 1 equilibrium b) the NOWIND 7 equilibrium. The field is contoured by intervals of 0.2 between -1.0 and +1.0; additionally, values greater than 0.4 are dotted, values greater than 1.0 are striped, and values less than 0.0 are in solid black.

More worrying are the streaks of high negative ε in the southern hemisphere in Fig. 2.18b. In the northern hemisphere, the field is smoother but has a distinct meridional gradient, which is apparently related to the strength of the meridional overturning since it disappears progressively from NOWIND 7 to NOWIND 1 (ordered in Table 2.5 by increasing levels of overturning). The basin averages shown in Fig.2.19 are much more reassuring, with generally relatively high (> 0.6) correlations to the linear fit and fairly constant magnitudes both with depth and between different runs (compare Figs. 2.19c,d for NOWIND 7 with Figs. 2.19e,f for NOWIND 1). The inverse proportionality to the width of the basin is a good fit (compare Figs 2.19a and b for the Atlantic and Pacific respectively), and ε is also several orders of magnitude smaller in the Southern Ocean as suggested (not shown). However, there are negative values of ϵ near the surface in the North Atlantic, and ε becomes more highly correlated and more uniform with depth as the overturning increases, which is opposite to what the meridional sections (Fig.2.18) seem to show. In summary, the relationship appears to work much better in a basin-averaged sense than in a local sense, which seems consistent with the basin-averaged linear steric height relationship described above. However, the most significant improvements in parameterizations for two-dimensional models are more likely to come from better dynamics, and recently Wright et al. (1995) have suggested a fundamentally different scheme which includes nonlocal effects and Laplacian viscosity in western boundary layers.

2.5. What Determines the Preference for the Conveyor in the Two-Basin Model?

ï

More than one cause of the preference for the conveyor in the two-basin model probably exists. The northern extension of the Atlantic must certainly contribute; to isolate which other geographical factors play a role, three slightly different two-basin geometries (illustrated in Fig.2.20) are designed.

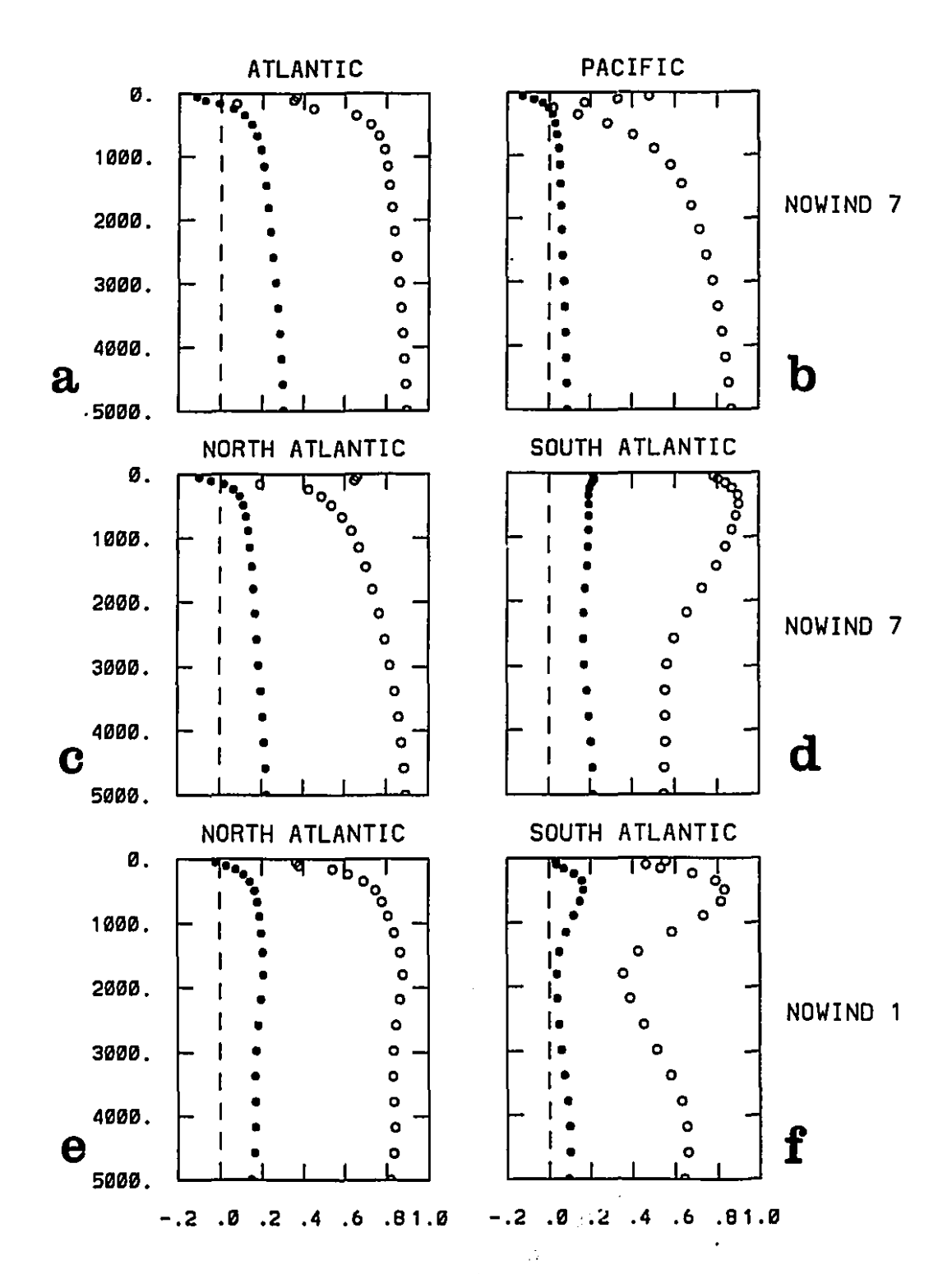
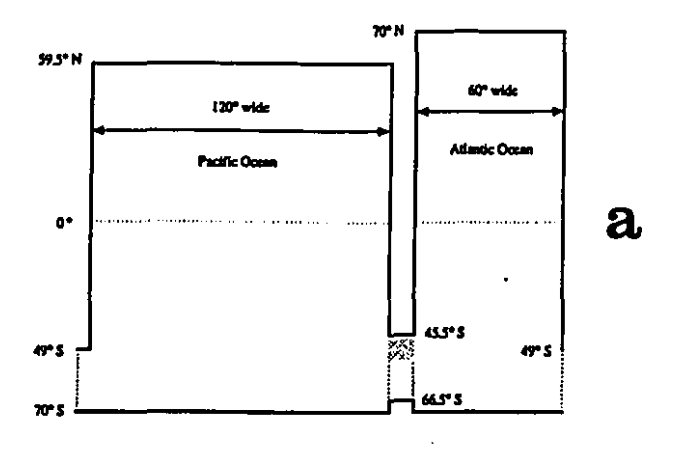
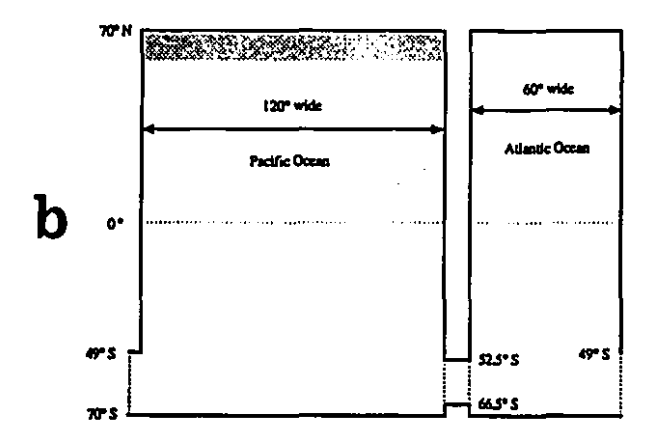


Figure 2.19: Linear fit (black circles) to ε and correlation (open circles) as a function of depth for a) the whole Atlantic (north of 50.75°S) b) the whole Pacific c) the North Atlantic only d) the South Atlantic only for the NOWIND 7 run, and e) North and f) South Atlantic for the NOWIND 1 run.

BASIN 1 is identical to the standard model except that the southern tip of South America has been shortened by two grid points (7°), so that this barrier now extends less far south than the continent to the east of the Atlantic. BASIN 2 also differs from the standard geometry in one way only: the Pacific Ocean has been expanded northward to the same latitude as the Atlantic. Finally, in BASIN 3, the Pacific has its original meridional length but its width is halved to match the Atlantic. Each of these configurations produced Conveyor or Southern Sinking circulations under both restoring and diagnosed mixed boundary conditions, and for both Asymmetric Oceans and Symmetric Oceans T* and S* profiles (Table 2.6: the first two columns). The (P-E) budgets are summarized in Table 2.7: two have net evaporation over the North Atlantic and the other four have net precipitation over both northern oceans. (In hindsight, the comparison of these experiments would have been simpler if a fixed (P-E) field had been used as in Winton and Sarachik (1993), although there are some disadvantages to this method also, as discussed in Chapter 4.) A single experiment was then performed for each spinup, starting from an Inverse Conveyor initial condition. In each of the six cases, an equilibrium with North Facific sinking (either an Inverse Conveyor or a Northern Sinking state) was obtained on the very first try. It appears that the northern extension of the Atlantic basin, although the most obvious culprit, is not by itself capable of producing the bias towards North Atlantic sinking. The modifications producing BASIN 2 and BASIN 3 both increase the symmetry of the model, so it seems reasonable that their solutions should start to approach the results of MW, but it is more disconcerting that the relatively small difference between BASIN 1 and the standard model alters the preference so easily. The very large evaporation over the South Pacific in both BASIN 1 spin-ups may be important: on the other hand, there is net precipitation over the North Pacific in both cases.

The origin of the preference in the original two-basin model is thus difficult to pin down. Certainly, the *Conveyor* in the model cannot be said to be





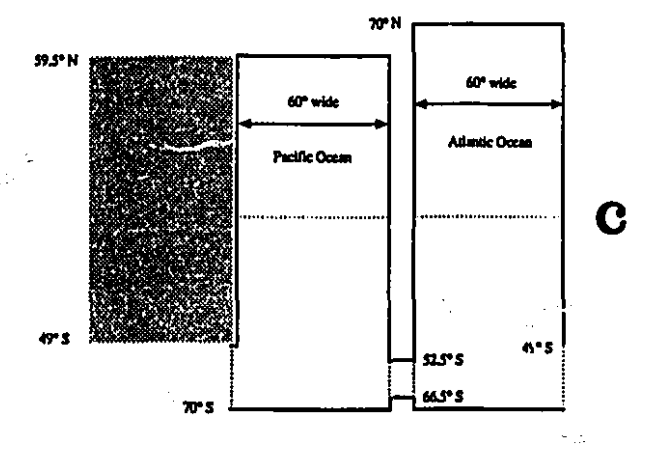


Figure 2.20: Alternate two-basin geometries: a) BASIN 1 has the tip of South America shortened by 7° b) BASIN 2 has the Pacific Ocean elongated to the same latitude as the North Atlantic c) BASIN 3) has the width of the Pacific halved to 60° (the same as the Atlantic).

Table 2.6. As in Table 2.3 with steady states under both restoring and mixed boundary conditions plus one perturbation experiment for each of the alternate two-basin geometries.

	Initial Condition (Spinup)			Final Equilibrium			Initial Condition (Perturbation)			Final Equilibrium		
	NA	NP	so	NA	NP	so	NA	NP	so	NA	NP	SO
Asymmetric Oceans T and S profiles												
BASIN1	7	1	28	1	2	28	0	44	0	2	51	0
BASIN2	4	2	29	20	2	29	0	52	0	2	55	0
BASIN3	3	1	20	1	1	21	0	28	0	40	23	0
Symmetric Oceans T and S profiles												
BASIN1	4	2	27	5	3	28	1	38	0	45	37	0
BASIN2	3	4	29	5	4	29	1	42	0	31	45	0
BASIN3	2	1	20	2	1	21	1	26	0	40	17	0

Table 2.7. Equilibrium (P-E) budgets (in Sv) for the alternate two-basin geometries in Table 2.6.

		North Atlantic	North Pacific	South Atlantic	South Pacific	Southern Ocean
Asymmetric	BASIN1	+0.073	+0.143	-0.261	-0.593	+0.638
Oceans To a selection	BASIN2	-0.011	+0.125	-0.234	-0.432	+0.554
T and S profiles	BASIN3	-0.038	+0.035	-0.217	-0.169	+0.388
Symmetric	BASIN1	+0.080	+0.023	-0.199	-0.502	+0.598
Oceans T and S profiles	BASIN2	+0.018	+0.036	-0.193	-0.395	+0.534
	BASIN3	+0.006	+0.003	-0.189	-0.162	+0.341

driven by the hydrological cycle, since Conveyors of any strength can exist under the same (P-E) field, sinking is not produced in the Pacific despite strong evaporation there, and the Symmetric Oceans (P-E) field which is so different to the present-day still favours Conveyors. Similarly, the two equilibria of Manabe and Stouffer (1988) have very similar integrated freshwater fluxes over the Atlantic, and Birchfield et al. (1994) cite evidence by Broecker (1989) and Zaucker (1992) that the interbasin water vapour transport may have changed little from glacial to interglacial times. Recently, Zaucker et al. (1994) used a twodimensional ocean model to quantify the relationship between meridional overturning in the model Atlantic and the atmospheric water vapour export from that basin. They found that the Atlantic thermohaline circulation did increase with increasing net evaporation, but in a nonlinear manner; the explanation was the positive feedback between salinity anomalies and the overturning circulation described in Chapter 1 (Rooth, 1982, Bryan, 1986). Zaucker et al. (1994) concluded that a net freshwater loss from the Atlantic was a necessary condition (although not a sufficient one) for a modern thermohaline circulation in their model. It is not clear that this is true in general: although this needs to be tested, there is no obvious reason why strong local evaporation could not dominate over weak net precipitation in basin average to drive a Conveyor type circulation. As an example, Zaucker et al. (1994) found stronger overturning in a run forced with zonally-averaged (P-E) from the ECMWF (European Centre for Medium-Range Weather Forecast) assimilation than in a run forced with climatological observed (P-E), although the freshwater export from the Atlantic drainage basin was twice as large in the latter case - the reason was less water vapour transport across the Arctic Circle.

The other hypothesis for the *Conveyor* referred to in Chapter 1 was that of Toggweiler and Samuels (1993a - hereafter TS). In Fig.2.21, the outflow from the North Atlantic is plotted first as a function of the wind at the latitude of Drake Passage and then as a function of the maximum overturning in the northern hemisphere. Once again, black circles are full-wind runs, black triangles are half-

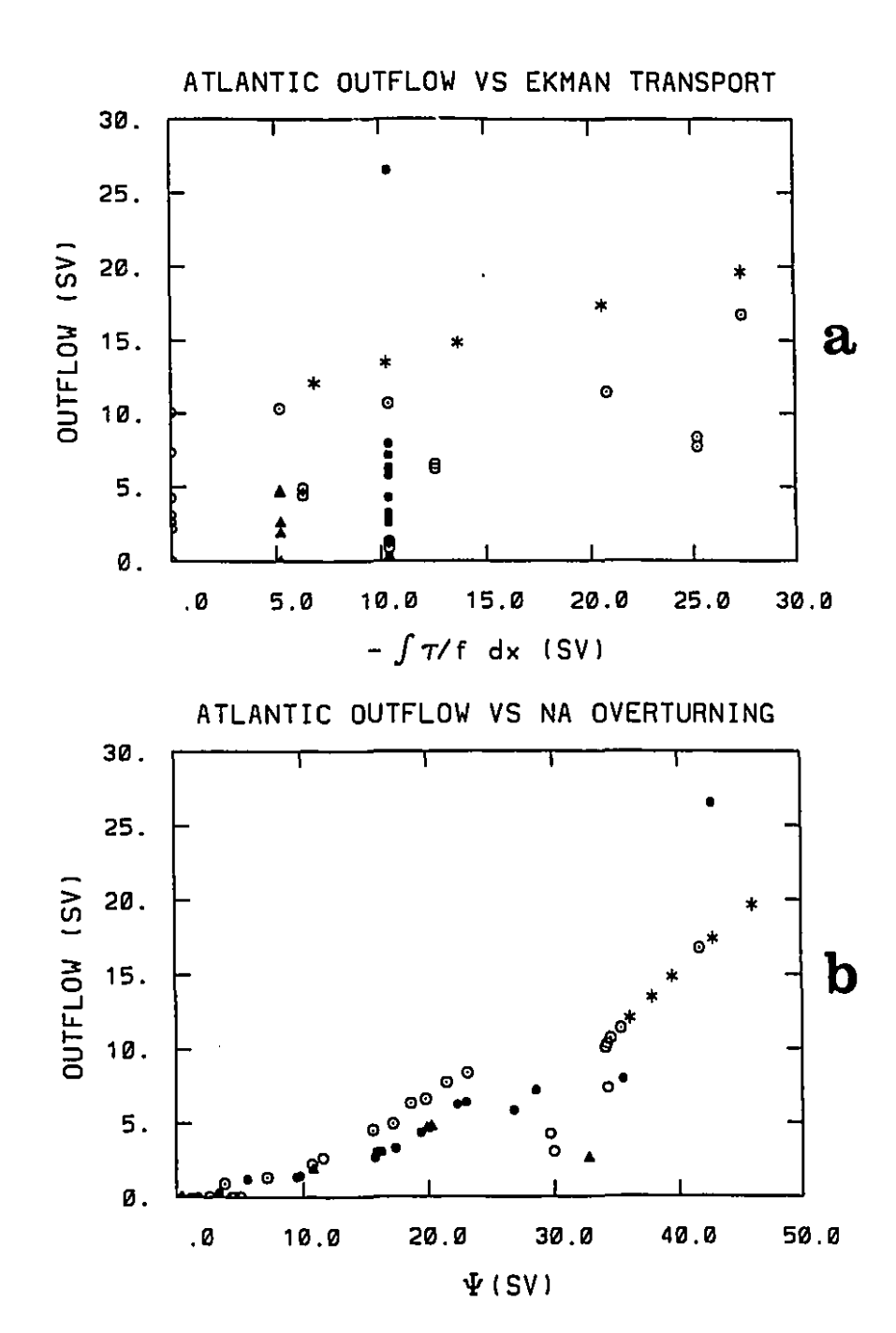


Figure 2.21: Outflow from the North Atlantic (Sv) as a function of a) the calculated Ekman transport (Sv) at the latitude of the tip of South America b) the maximum overturning (Sv) in the Atlantic. As in Fig.2.17, black circles are full-wind runs, black triangles are half-wind runs, and white circles are no-wind runs in the standard geometry. Stars and dotted circles are additional runs in which only the wind in the southern hemisphere is varied and the tip of South America is also shortened.

wind runs and white circles are no-wind runs, while the stars and dotted circles are a separate series of runs under restoring boundary conditions, in which the wind is varied only in the southern hemisphere and the tip of South America may be displaced northward. The TS hypothesis clearly does not describe the data points in Fig.2.21a; in contrast, a quasi-linear relationship seems quite probable in Fig.2.21b.

There are two reasons however why the TS effect might be difficult to see in the present GCM. The first is that the winds at the tip of South America are significantly weaker in this model than in the test runs of TS. The high level of viscosity may therefore allow so much of the northward Ekman transport at the surface to be balanced ageostrophically above the level of the sill that the requirement for NADW outflow is lost. The second reason is that the high horizontal diffusivity allows much of the upwelling associated with deep sinking in the North Atlantic to occur in the western boundary layer (e.g. Toggweiler et al., 1989), long before the outflow reaches the Southern Ocean, so that the wind in the ACC is not necessary to close the Atlantic thermohaline circulation (Toggweiler and Samuels, 1995). Furthermore, the TS effect can be detected in some experiments. For example, in a series of runs under restoring boundary conditions in which only the wind in the Southern Ocean is varied (the stars in Fig.2.21), both the outflow and the overturning do vary linearly with the Ekman drift in the Southern Ocean. The line does not intersect the x-axis anywhere near the origin however, possibly because of the viscous and diffusive effects mentioned above.

There are also other possible explanations for a linear relationship between North Atlantic outflow and Southern Ocean winds. One hypothesis might be that the wind in the South Atlantic changes the pressure/steric height gradient across the basin (e.g. Godfrey, 1989), which would then affect both the outflow and the overturning. It has been even more difficult to confirm a relationship between an east-west gradient and the overturning than it was with the north-south gradient, so this suggestion remains uncorroborated. Another idea might be that the different

Ekman transports change the surface density in the Southern Ocean, affecting the meridional pressure gradient directly, but this too is yet unverified.

In conclusion, the overall asymmetry of the basin, rather than any one feature like the northern extension of the Atlantic, appears to determine the preference of the two-basin model for *Conveyor* or *Southern Sinking* circulations. In the model, the bias is not dictated by either the hydrological cycle or the Southern Ocean winds, although neither possibility can be conclusively ruled out for the real world based on the experiments in this thesis. However, a more general principle is suggested by the results in this chapter: that a number of different factors, including winds, may contribute to setting up the large-scale pressure gradients that drive the meridional overturning. This would signify first that the local buoyancy forcing in the North Atlantic is of at least equal importance to remote or basin-integrated effects, but also that a realistic representation of the Southern Ocean may be a necessary ingredient in modelling the global thermohaline circulation.

Chapter 3 Climatology of a Global Ocean Model

The sensitivity to basin geometry of the simple model in Chapter 2 is likely to be an even more fundamental aspect of a global ocean model, where bottom topography also comes into play as described in Chapter 1. The expense of integrating such a model prohibits doing many equilibrium runs as in Chapter 2, but in Section 3.3, the time-dependent response of the *Conveyor* in the global geometry is illustrated through a couple of perturbation experiments. The greater realism of the global model is also exploited in Section 3.4 where the ocean is forced with the climatological surface fluxes of a global atmospheric model. But the first responsibility incurred by the more realistic setting is that of validating the basic climatology of the model, and this is attended to immediately.

3.1. Spin-up under Restoring Boundary Conditions

The global ocean model described in this chapter was originally developed as a lower resolution version of the new 1.875° (zonally) x 1.8555° (meridionally) x 29 levels (vertically) model which is presently being coupled to the Canadian Climate Center (CCC) atmospheric GCM (Weaver and Lee, 1995). The intent was to use the AGCM wind stresses and heat and freshwater fluxes into the ocean as forcing fields for the low resolution model, with the three purposes of: 1) improving upon the traditional diagnosed mixed boundary conditions, 2) evaluating the readiness of the AGCM for coupling, and 3) comparing the equilibrium circulation in the ocean under the AGCM fluxes from runs with present-day and doubled CO₂ levels. However, as described in Section 3.4, even the control run under annual mean 1xCO₂ fluxes resulted in such unconventional circulation in the ocean model that this line of investigation was discontinued. The legacy of these early intentions lives on nonetheless in the design of the ocean model which still



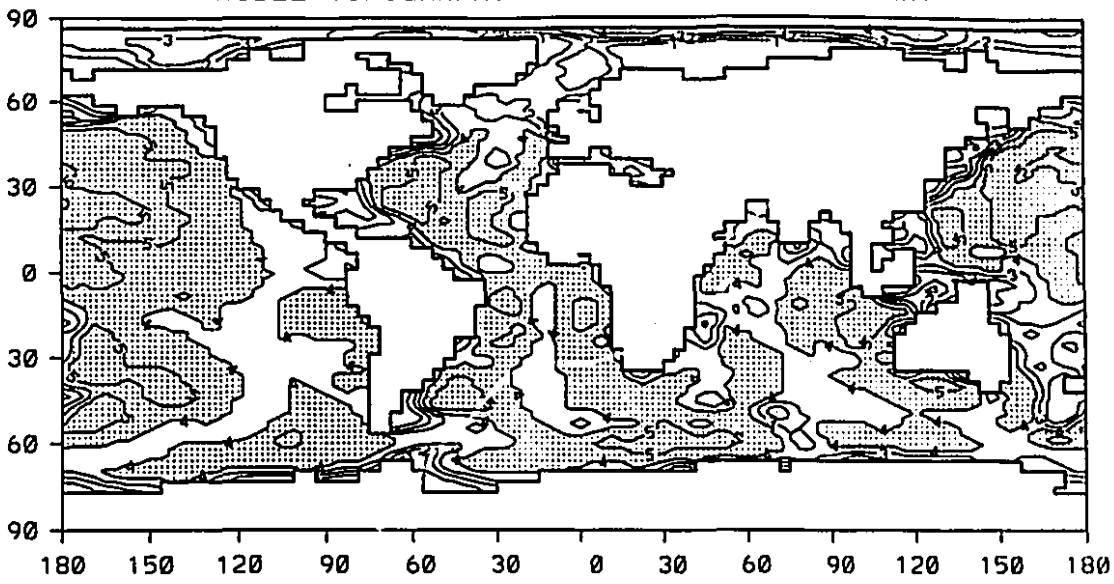


Figure 3.1: Topography for the global ocean model. Contour interval is 1 km, and depths greater than 4 km are shaded.

closely resembles that of Weaver and Lee (1995). The purpose of this section will be to demonstrate that the present model <u>can</u> achieve a climatology which is quite satisfactory compared to other global models currently in use around the world, under more standard buoyancy and momentum forcing fields.

The basic climatology under restoring boundary conditions was obtained as the outcome of a number of sensitivity tests aimed at establishing the optimum levels for the eddy mixing coefficients, topographical smoothing, numerical parameters, etc. Since the majority of these preliminary runs largely parallelled the model development published by other authors (Bryan and Lewis, 1979, England, 1993, Weaver and Lee, 1995, etc.), only the final results will be described here. A summary of the model specifications is presented in Table 3.1: briefly, the resolution is 3.75° zonally by 1.8555° meridionally, with 19 unequally spaced levels in the vertical and a maximum depth of 5400 m. The land mask was adapted from the atmospheric model's mask, and resolves only three islands: Australia, Antarctica and New Zealand. Bering Strait is closed but the Straits of Gibraltar are open to baroclinic throughflow. The topography (Fig.3.1) was

Table 3.1. Numerical Parameters for Global Model

numerical model: MOM (Pacanowski et al., 1991)

resolution: zonal: 3.75°

meridional: 1.8555°

vertical: 19 levels (depths in m: 50, 100, 150, 200, 260, 340, 450, 600, 800, 1050,1350, 1700, 2100, 2550, 3050,

3600, 4200, 4800, 5400)

timesteps:

barotropic vorticity: 0.5 hours

tracer: 2 days

eddy mixing coefficients:

horizontal viscosity A_{MH} =[2 + 2 cos(ϕ)] x 10⁵ m²/s where ϕ =latitude in radians vertical viscosity A_{MV} =2x10⁻³ m²/s horizontal diffusivity A_{TH} =1x10³ m²/s vertical diffusivity A_{TV} = [0.61 + (1/ π)arctan(...5x10⁻³(z - 1.0x10³))] x10⁻⁴ m²/s

 $[0.61 + (1/\pi)\arctan(1.5x10^{3}(z - 1.0x10^{3}))] \times 10^{-4} \text{ m}^{-7}$ where z=depth in m

Fourier filtering applied poleward of 69.58125 for tracers and 70.50900 for velocity

boundary conditions:

wind stresses: Hellerman and Rosenstein (1983) annual mean winds restoring T*,S*: modified annual mean Levitus (1982) SST and SSS

restoring timescale: 50 days

interpolated from the Gates and Nelson (1975) world topography and first smoothed using a 5-point centrally-weighted smoother and then checked for "holes" (isolated points which are deeper than all four surrounding points) which were filled to the deepest adjacent depth. The northernmost row of grid points in the Arctic (centered at 88.13625°N) was set to land, for numerical reasons, and Fourier filtering was also used everywhere poleward of approximately 70° in both

hemispheres. Finally, the Mediterranean passage was deepened to 350 m and the Icelandic hump was removed entirely to create a sill 1200 m deep, following Toggweiler et al. (1989) and Weaver and Lee (1995) who employed a similar tactic to shift the deep water formation branch of the *Conveyor* from south of Iceland (as sometimes occurs in coarse resolution models) into the GIN Seas. The cosine dependence with latitude (Table 3.1) of the horizontal viscosity A_{MH} (varying from 4×10^5 m²/s at the equator to 2×10^5 m²/s at the poles) was chosen for numerical reasons, while the arctangent profile of the vertical diffusivity k_v (increasing from $\sim3\times10^{-5}$ m²/s at the surface to $\sim1\times10^{-4}$ m²/s in the deep ocean) is more physically based (Bryan and Lewis, 1979).

A resting homogeneous ocean was spun up under Hellerman and Rosenstein (1983) annual mean winds and Levitus (1982) annual mean sea surface temperatures and salinities (see the timeline in Fig.3.2). At 1600 years, the restoring timescale was decreased from 60 to 50 days to conform with the value used by Weaver and Lee (1995). Another 400 years was allowed for the circulation and tracer fields to adjust, at the end of which time the barotropic and overturning streamfunctions and the meridional heat transport were verified to be quite acceptable. However, a comparison of the zonally-averaged temperatures and salinities with observed maps in Levitus (1982) revealed that the deep ocean was too warm and too fresh (especially in the southern hemisphere, and in the Pacific). The original restoring temperatures and salinities were therefore replaced with the modified fields described in Weaver and Lee (1995) where the values in the Arctic were averaged over the top 50 m of Levitus data, while in the Antarctic T* and S* were ramped linearly up to fixed values of -1.8°C and 35.1 ppt respectively at the southernmost ocean latitude. The spin-up was pursued for another 2000 years under the new restoring boundary conditions, during which time the salinity of the deep ocean increased significantly (as desired) and the deep temperature cooled somewhat (by about 1°C). Time series of both kinetic energy and basin mean surface heat flux (not shown) seemed to show that the model was close to equilibrium by the end of this time, and plots of the basin-

Added Evaporation 300 y H & R winds **Mixed Boundary Conditions** restoring boundary conditions no acceleration of deep ocean 3950 y Added Fluxes are diagnosed here Precipitation 300 y 400 y Diagnosed Fluxes Restoring to Restoring to Levitus Modified Levitus 2000 y 2000 y 2000 y CCC Fluxes 400 y 2000 y CCC winds restoring boundary conditions no acceleration of deep ocean

Figure 3.2: Timeline of spin-up and subsequent experiments with the global ocean model, with integration times in years. Figure 3.2:

Д. П mean temperature at each level confirmed that both the surface and deep ocean temperatures had more or less equilibrated. The intermediate layers were still adjusting but the residual trends were very small (less than 0.01°C in the last 300 years at 1200 m, for example). Accelerated convergence as in Bryan (1984), with an acceleration factor of either 2 or 4 in the bottom five levels, was used throughout this first 4000 years of the spin-up but not thereafter. The delayed spin-up of the intermediate layers is a general phenomenon however, as confirmed by subsequent long integrations without deep ocean acceleration; this is consistent with the prognostic model of Toggweiler et al. (1989) who found both the oldest water mass ages and the highest temperature and salinity anomalies compared to observations at intermediate depths. For present purposes, it is not very crucial that the ocean be in perfect equilibrium (which may not be attained even after 7000 years, I.Fung, personal communication) hence the spin-up phase is terminated here.

The equilibrium climatology of the ocean model is illustrated on the following pages, starting with the barotropic and meridional overturning streamfunctions in Figs. 3.3 and 3.4 respectively. The main features are very similar to those in other coarse resolution ocean models: the distinguishing characteristics of the present simulation are a strong Indonesian throughflow (24.0 Sv) and a relatively strong ACC (175.5 Sv)¹. The wind-driven gyres are weak, as is often the case (partly because of the high viscosities, and partly because the smoothing of topography causes the JEBAR contribution to be underestimated,

¹ Estimates for the transport of the ACC have spanned the range -15 to 237 Sv (Peterson, 1988) but the most commonly accepted magnitude is on the order of 130-140 Sv (Read and Pollard, 1993). Since however this current is particularly difficult to represent in non-eddy resolving numerical models, many authors settle for higher values, e.g. 180 Sv in the 1°x1° model of Washington et al. (1994), 155 Sv in the 2°x2° diagnostic model of Fujio et al. (1992), etc. The most recent measurements of the Indonesian throughflow, by Fieux et al. (1994), suggest an transport of only 18.6 Sv, but with a large error of ±7 Sv. The Indonesian throughflow also tends to be overestimated in climate models, either because of reduced friction due to neglecting islands in the Indonesian archipelago (Fujio et al., 1991) or because of the deep thermocline associated with high vertical mixing.

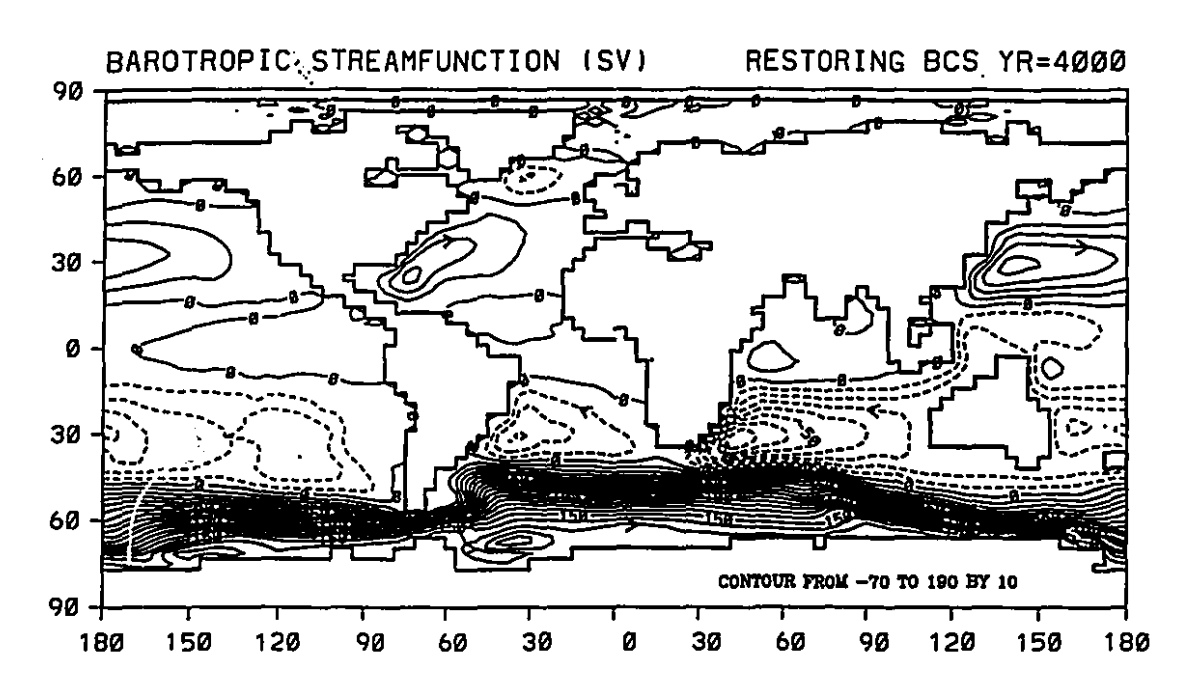


Figure 3.3: Barotropic streamfunction (Sv) for the spin-up under restoring boundary conditions using modified Levitus sea surface temperatures and salinities and Hellerman and Rosenstein winds.

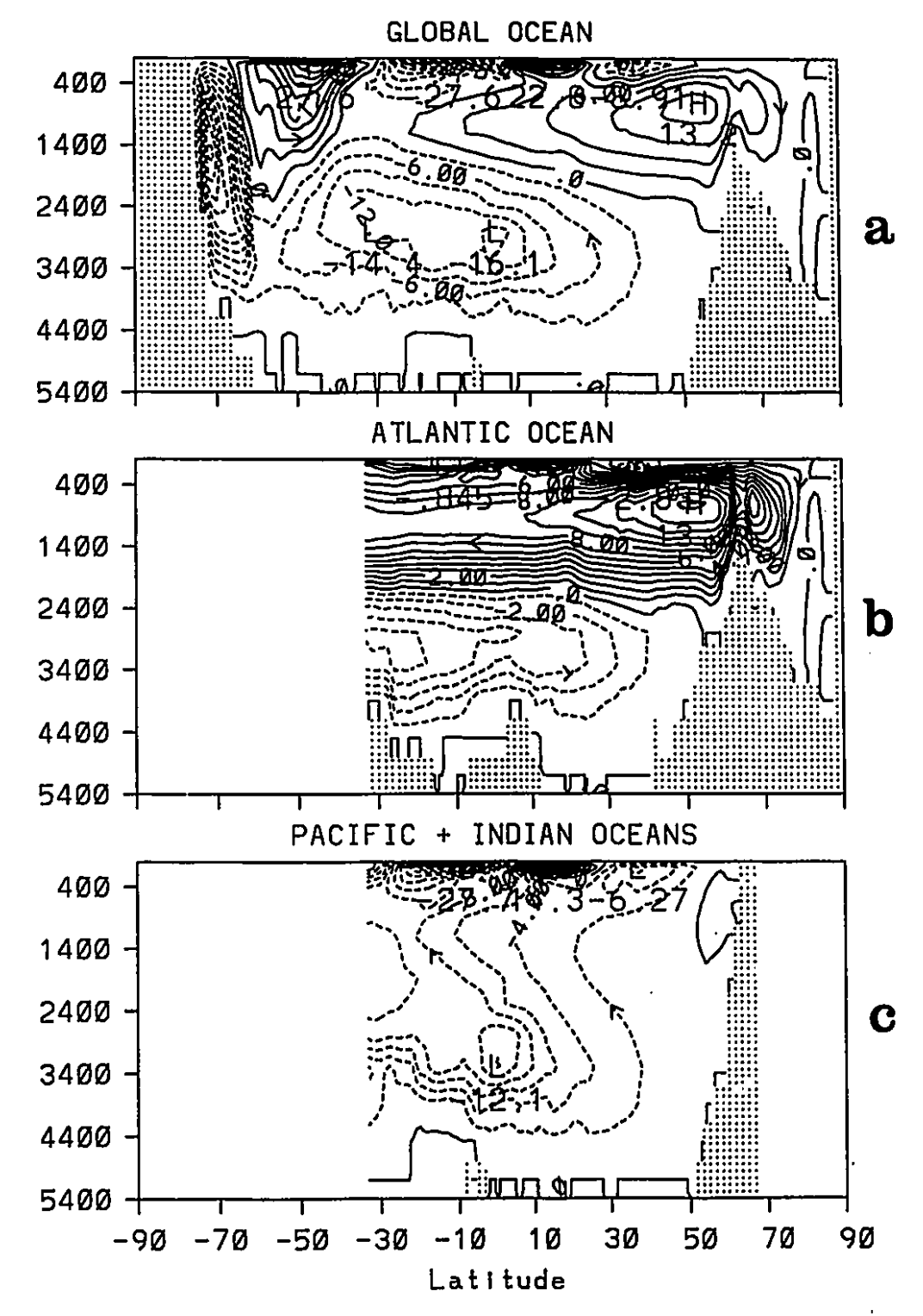


Figure 3.4: Meridional overturning streamfunction (Sv) for the spin-up under restoring boundary conditions a) global ocean b) Atlantic Ocean c) Pacific and Indian Oceans.

Matano and Philander, 1993), but the barotropic circulation in the Indian Ocean is stronger, with the Agulhas Current transport exceeding 70 Sv. The meridional overturning is, as expected, a *Conveyor* circulation, with a maximum overturning of ~13 Sv in the North Atlantic (cf. Fig.1.2). More than half of this is sinking in the GIN Seas, and an outflow of about 8 Sv also exists across 30°S at intermediate depths (~2000 m, so slightly shallower than observed). At deeper levels, a counterclockwise cell of presumably Antarctic source water penetrates as far north as 40°N. The upwelling branch of the conveyor in the Indian and Pacific Oceans is quite diffuse and has a closed cell in the deep ocean above the equator which may be a numerical effect. The deep Deacon Cell (the Ekman cell at the latitude of Drake Passage) and the recirculation next to Antarctica are similar to those in the two-basin model.

The zonally-averaged temperature and salinity are shown in the next figure (Fig.3.5). The overall properties of the Atlantic, Pacific and Indian Oceans are reasonably well reproduced: the northward deepening thermocline in the Atlantic with the especially deep penetration at 35°N identifying the Mediterranean outflow (while the Pacific and especially the Indian thermoclines deepen southward); the thick layer of fresh intermediate water in the North Pacific; the northward increase of deep salinity in the Indian (and northward decrease in the deep Pacific) and the polar haloclines in both Arctic and Antarctic. The main deficiencies are the weak northward penetration of the fresh Antarctic Intermediate Water tongue (which may require isopycnal mixing for best results, England, 1993), the warm deep ocean (2° too warm in the Pacific and Indian) and the salinity front between the Arctic and Atlantic. The deep Arctic is more than 0.3 ppt too fresh, but the abyssal salinity is approximately right (> 34.6 ppt) in the rest of the world ocean. However, the Antarctic bottom water is not penetrating far enough northward, either in the Atlantic (where the 2° isotherm grounds at the equator instead of approximately 40°N as in the observations) or in the Pacific where high salinities are being trapped around Antarctica at the bottom. Many other smaller details (the Alaska and West Greenland Currents, for example) are also not well reproduced.

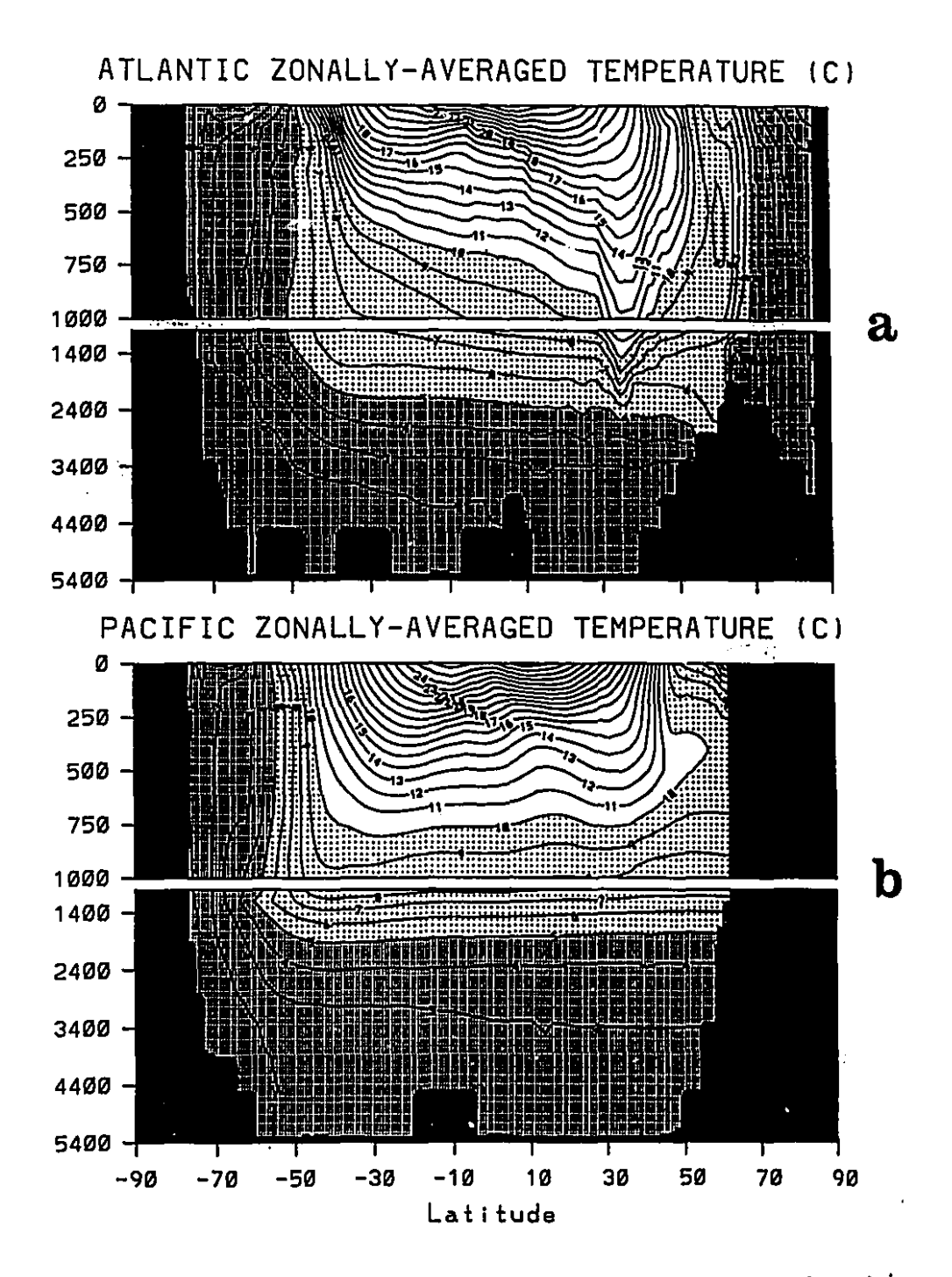


Figure 3.5: Zonally-averaged temperature (°C) and salinity (ppt) for the spin-up under restoring boundary conditions a) Atlantic T b) Pacific T c) Indian T d) Atlantic S e) Pacific S f) Indian S. Temperatures colder than 10°C or salinities greater than 34.6 ppt are lightly shaded, and temperatures colder than 5°C or salinities greater than 35.0 ppt are more heavily shaded.

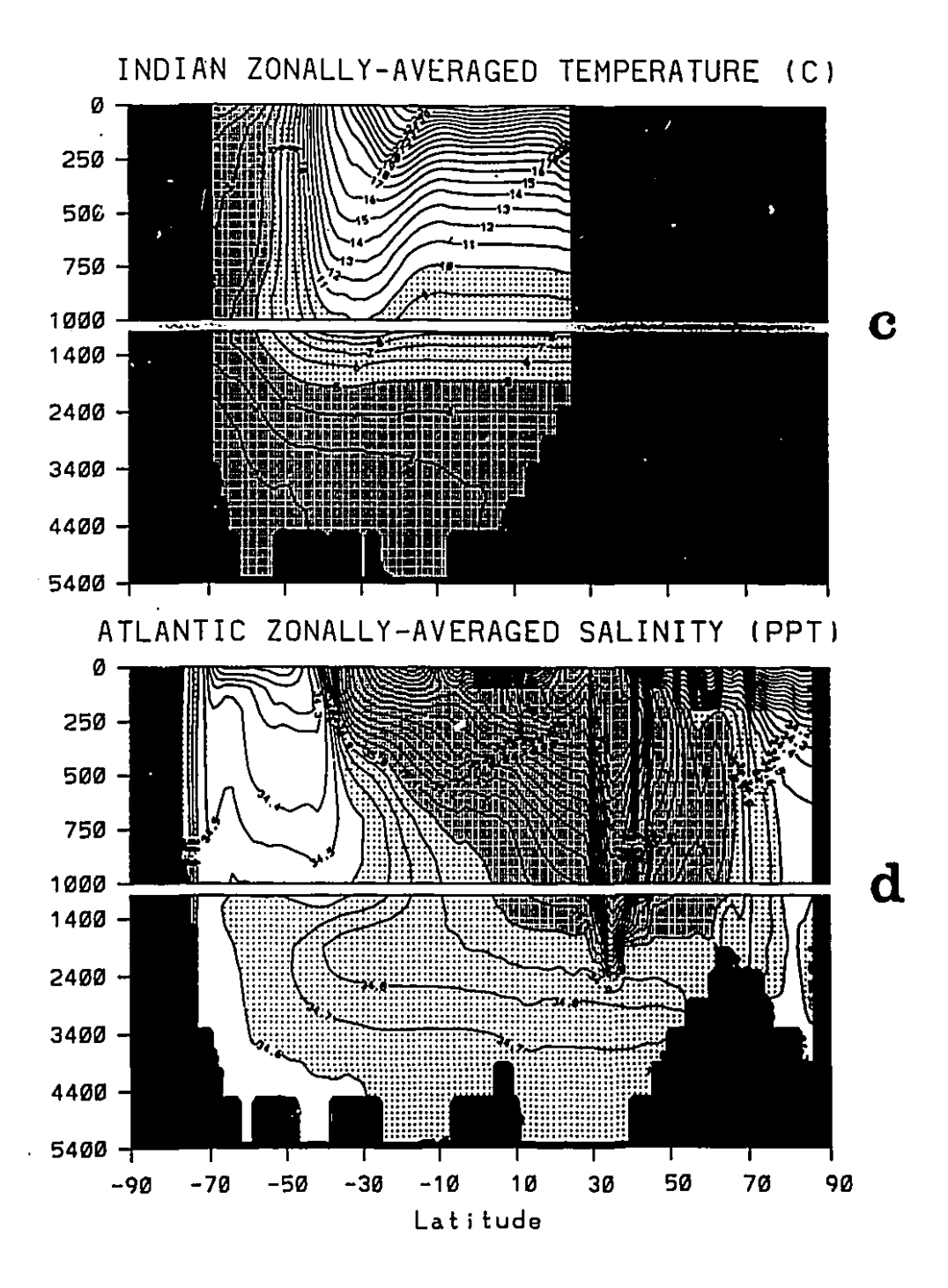


Figure 3.5. Suite.

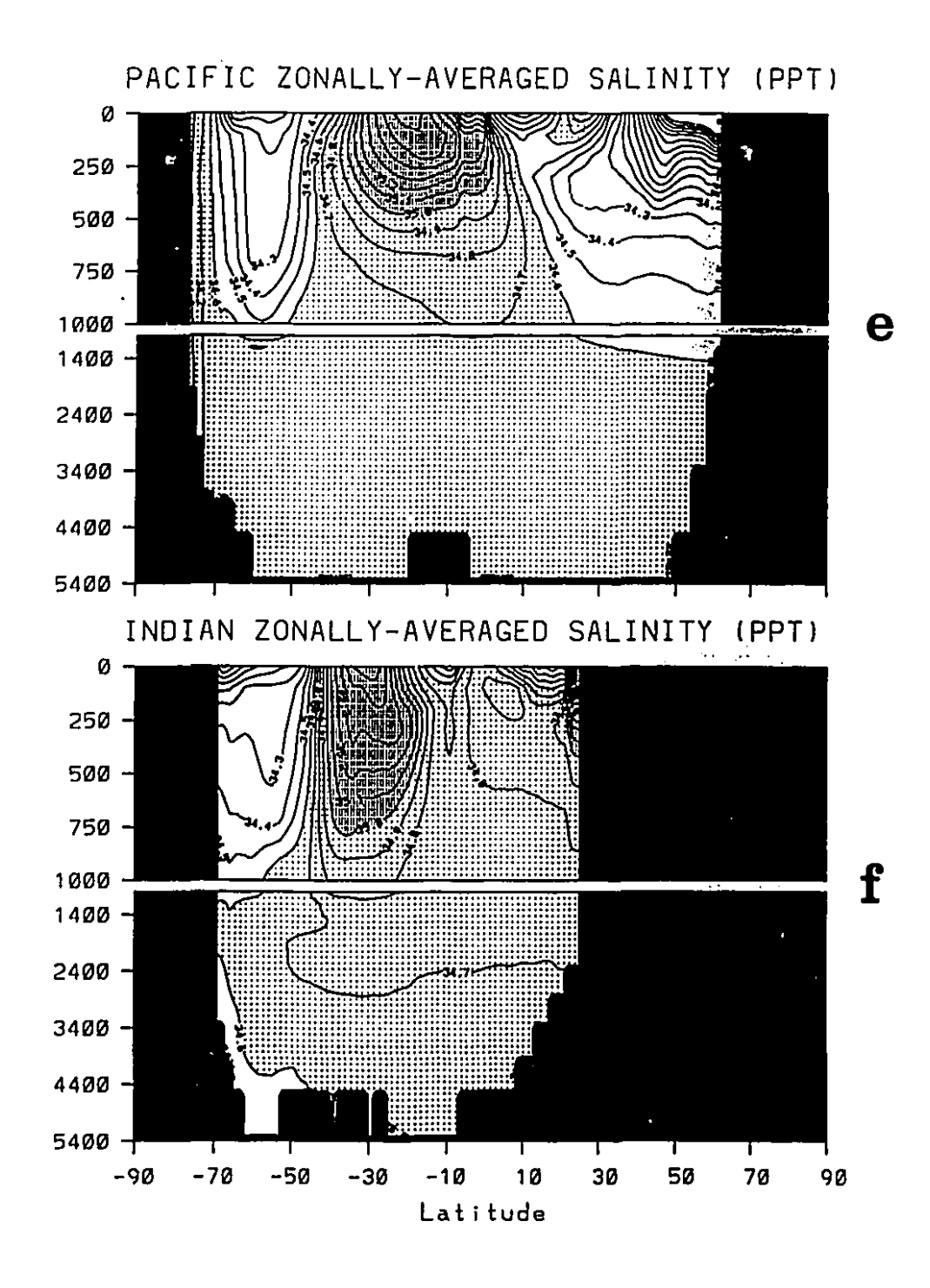


Figure 3.5. Suite.

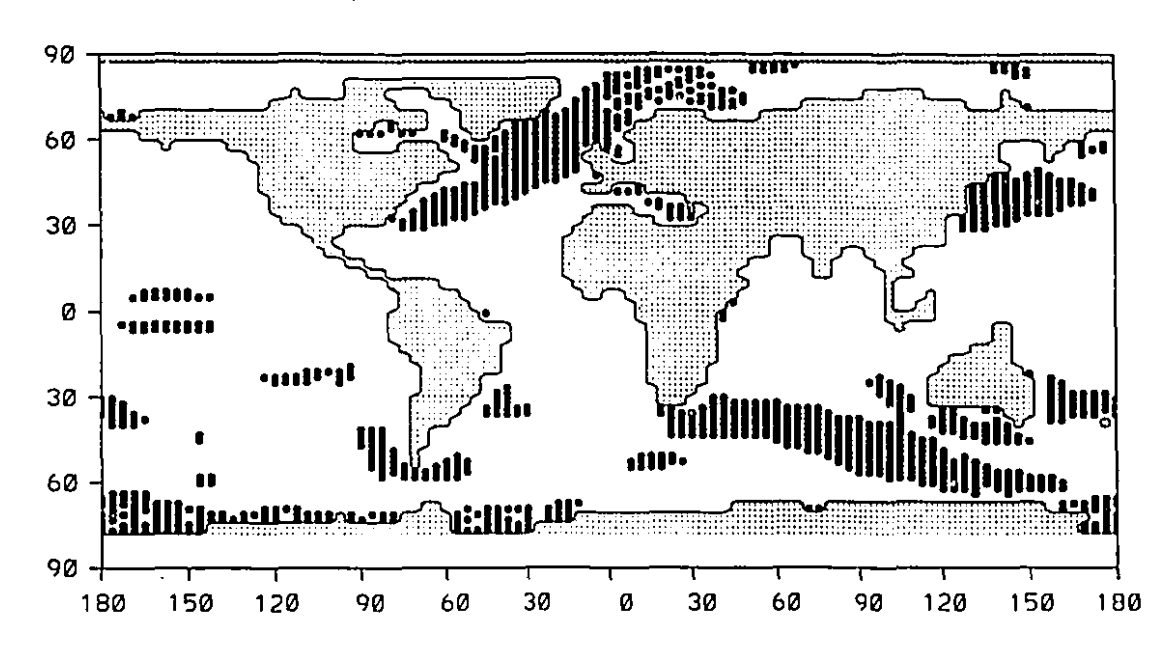


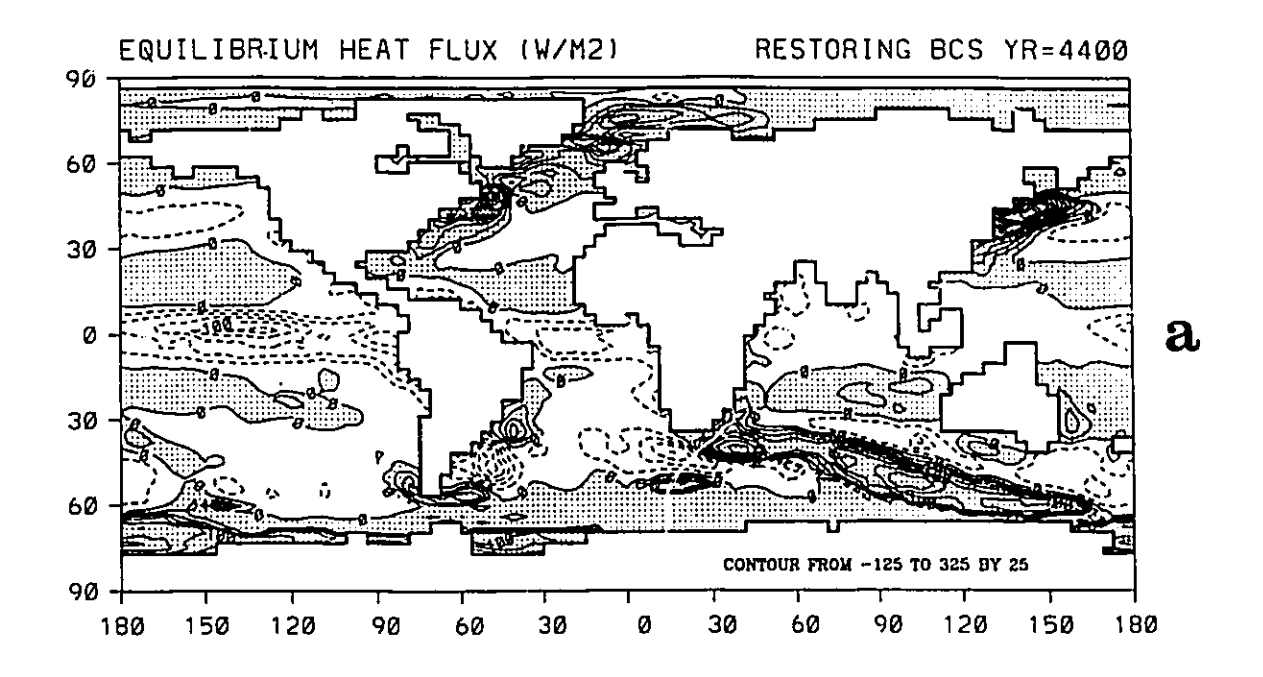
Figure 3.6: Instantaneous convection between the first two levels for the spin-up under restoring boundary conditions.

Warm water flowing southeastward out of the Agulhas Retroflection causes a prominent streak of convection slanted across the Indian Ocean sector of the ACC (Fig.3.6) and an eastward-deepening mixed layer as described by Hirst and Godfrey (1993). Toggweiler et al. (1989) relate a similar feature in their world ocean model also forced by Hellerman and Rosenstein (1983) annual mean winds to meridional shear in the westerlies producing convergent Ekman transport which weakens the upper ocean stratification. In the present model, unlike Hirst and Godfrey (1993), there is little convection east of Australia probably because the stronger Indonesian throughflow causes a weaker East Australian Current. Despite the annual mean conditions, convection is occurring in most of the northern North Atlantic (extending into the Norwegian Sea) and in both the Ross and Weddell Seas, but is rare in the rest of the Arctic and Antarctic, both stabilized by polar haloclines.

Before diagnosing the equilibrium surface heat and salt fluxes, the model is run for another 400 years with the deep ocean acceleration switched off (Fig.3.2). Given the methodology, the appearance of the diagnosed fluxes

(Fig.3.7) is surprisingly acceptable compared to the heat flux atlas of Esbensen and Kushnir (1981) or the North Atlantic (P-E) of Schmitt et al. (1989). The warm western boundaries and cold eastern boundaries of each ocean (except the Leeuwin Current region west of Australia) and the cool equatorial upwelling zone are all reproduced, as are the subtropical dry zones and the rainy patches at higher latitudes and near the equator. Other aspects are less pleasing: the Kuroshio is releasing more heat than the Gulf Stream, the Pacific equatorial cold pool is a little far to the west, and the prominent convective streak across the southern Indian Ocean is associated with excessively large heat losses and freshwater gain that are unlikely to be realistic (although there is little data to compare with in this region). The extrema of the (P-E) field are in fact generally larger than observed, with peaks of more than 5 m/y when Schmitt et al. (1989) estimate only 2 m/y net evaporation even in the Gulf Stream. One reason is that the diagnosed (P-E) field implicitly parameterizes the entire hydrological cycle including river runoff and sea ice processes (brine rejection and ice melting) rather than just precipitation and evaporation, and a second reason is the high diffusion in the ocean model which dissipates the influence of the restoring boundary condition requiring larger fluxes to achieve the desired surface salinity. The salt gain around the Antarctic continent is due to the spiked S* field and may most conveniently be thought of as representing the effect of brine rejection under ice, since the cold temperatures at this latitude would discourage evaporation.

The poleward heat and salt transports by the ocean that are the integrated measure of these fluxes are shown in Fig.3.8. As suggested by observations (e.g. Hastenrath, 1982, Hsiung, 1985), the global heat transport is poleward in either hemisphere, with near zero cross-equatorial transport, while the Atlantic has northward heat transport at all latitudes and the Indo-Pacific is asymmetric with greater southward transport in the southern hemisphere. The meridional salt transport has been converted to a freshwater transport by dividing by -34.7 ppt following Semtner and Chervin (1992), so as to compare with Wijffels et al. (1992, their Fig.3). The main peaks at 40°N and 40°S are relatively well



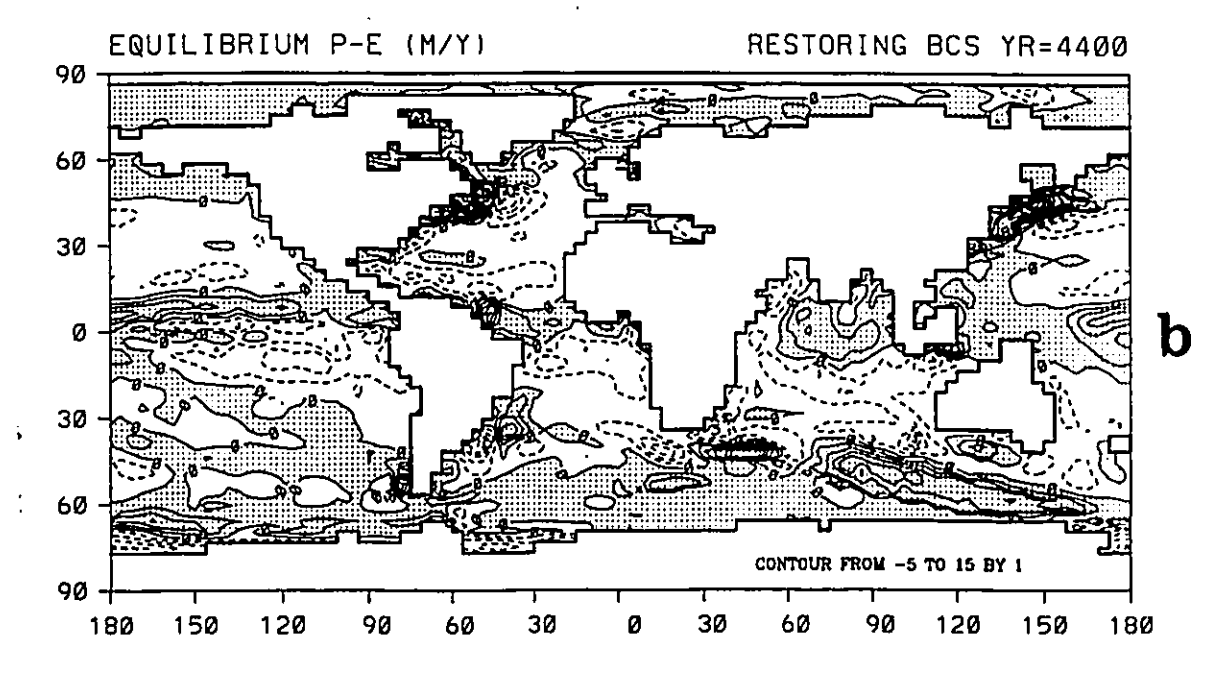


Figure 3.7: Diagnosed surface fluxes at equilibrium for the spin-up under restoring boundary conditions a) heat flux (W/m²) b) freshwater flux (m/y). Heat flux is positive out of the ocean, and positive values for both Q and (P-E) are shaded.

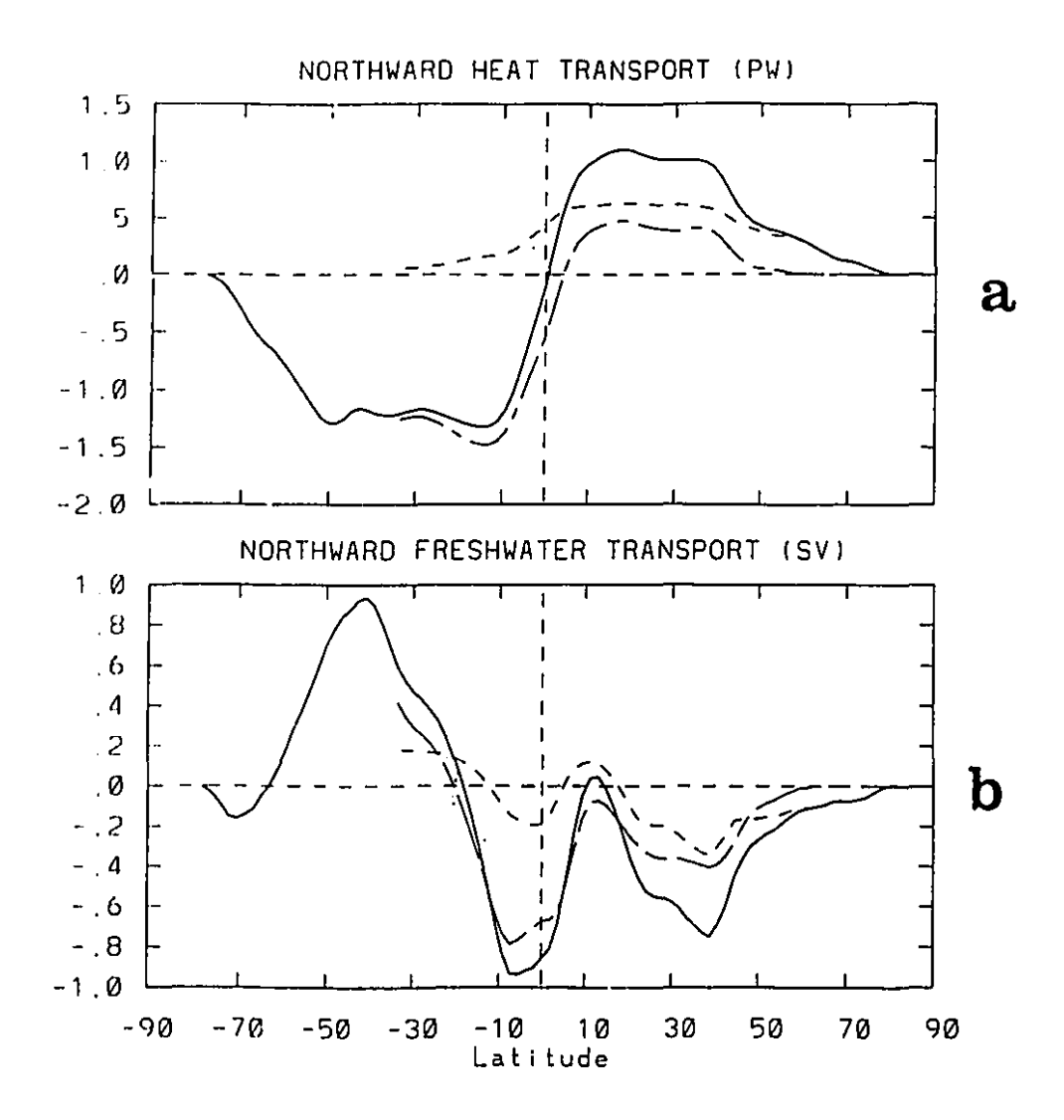


Figure 3.8: Meridional heat (a) (10¹⁵ W) and freshwater (b) (Sv) transports at equilibrium for the spin-up under restoring boundary conditions. Solid line: global ocean; dashed line: Atlantic; long dashes: Pacific + Indian.

reproduced: however, the secondary peaks closer to the equator are biased negatively with respect to observations.

3.2. Response under Mixed and Flux Boundary Conditions

The robustness of the *Conveyor* circulation in the present model may be illustrated by presenting the equilibrium circulation under diagnosed mixed and flux boundary conditions. The equilibrium overturning in the two cases is shown in Figs.3.9 and 3.10: both are almost indistinguishable from the spin-up (Fig.3.4). Significant changes occur only in the Antarctic, with the barotropic transport in the ACC increasing by more than 50 Sv in the mixed boundary conditions run (Fig.3.11a) and decreasing slightly in the flux boundary conditions run (Fig.3.11b). (It should however be cautioned that the ACC equilibrates on a longer timescale than any other region of the global model, and only the mixed boundary conditions experiment has been integrated for long enough - 3950 years compared to only 2000 for the flux run - to be confident of the results.) Velocity vectors indicate that baroclinic changes are also confined to the Southern Ocean, but the deep Arctic cools in both runs (not shown).

An even more primitive test of the global geometry is to spin the ocean model up again from rest without winds under smooth symmetric profiles of restoring temperatures and salinities that follow a cosine distribution in either hemisphere (ranging from 27° to 0°C for T* and 35.0 to 33.0 ppt for S* over latitudes 0-90°). At equilibrium (4000 years of unaccelerated integration), the meridional overturning (Fig.3.12) shows a positive thermally-dominant cell in either hemisphere, but with visible asymmetries between north and south and between Atlantic and Pacific. The southern overturning sinks to much greater depths than does the northern branch (despite approximately equal magnitudes near the surface) and is accompanied by a strong recirculation next to Antarctica. The North Atlantic thermohaline circulation is deeper and stronger than its North

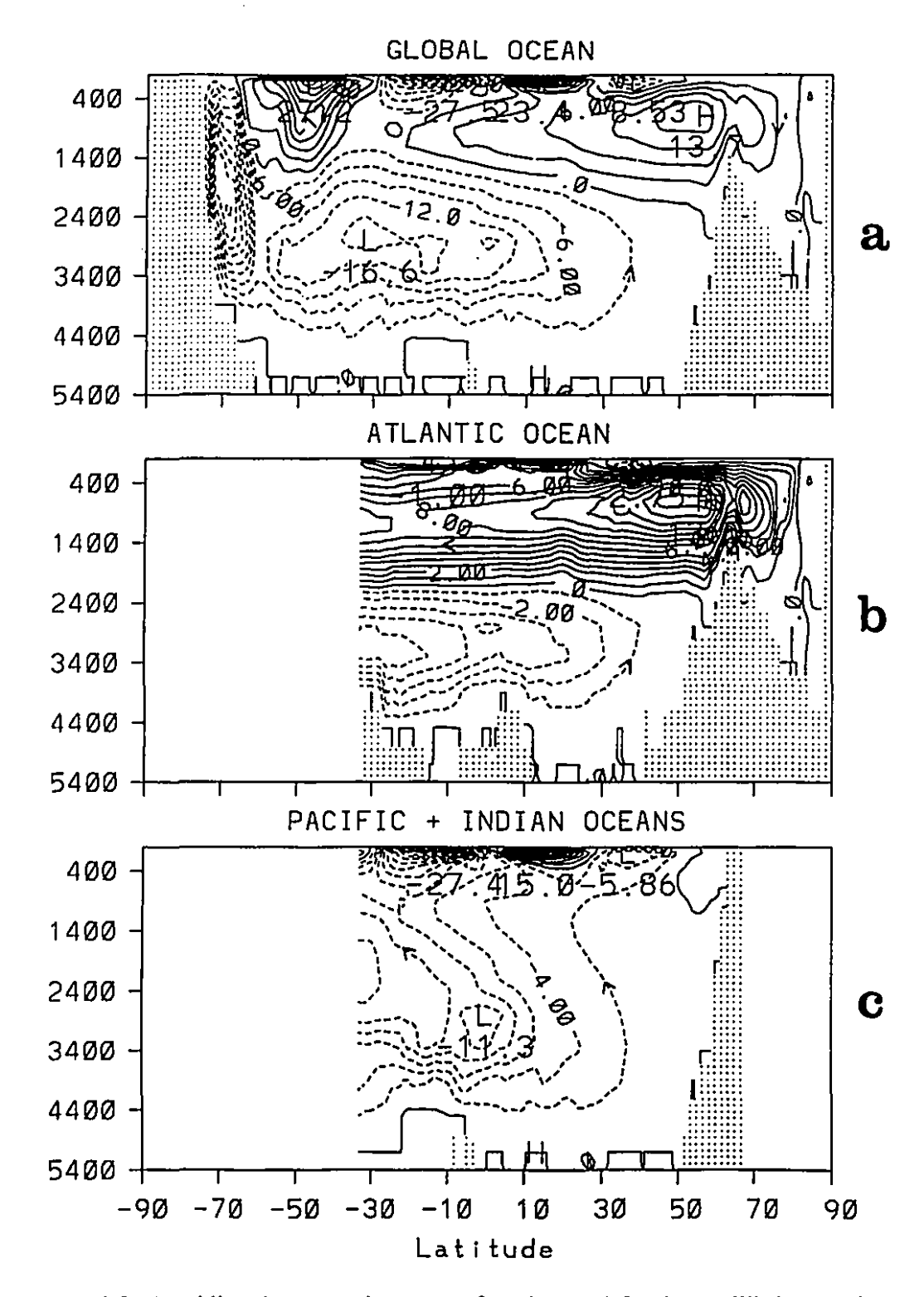


Figure 3.9: Meridional overturning streamfunction (Sv) for the equilibrium under diagnosed mixed boundary conditions a) global ocean b) Atlantic Ocean c) Pacific and Indian Oceans.

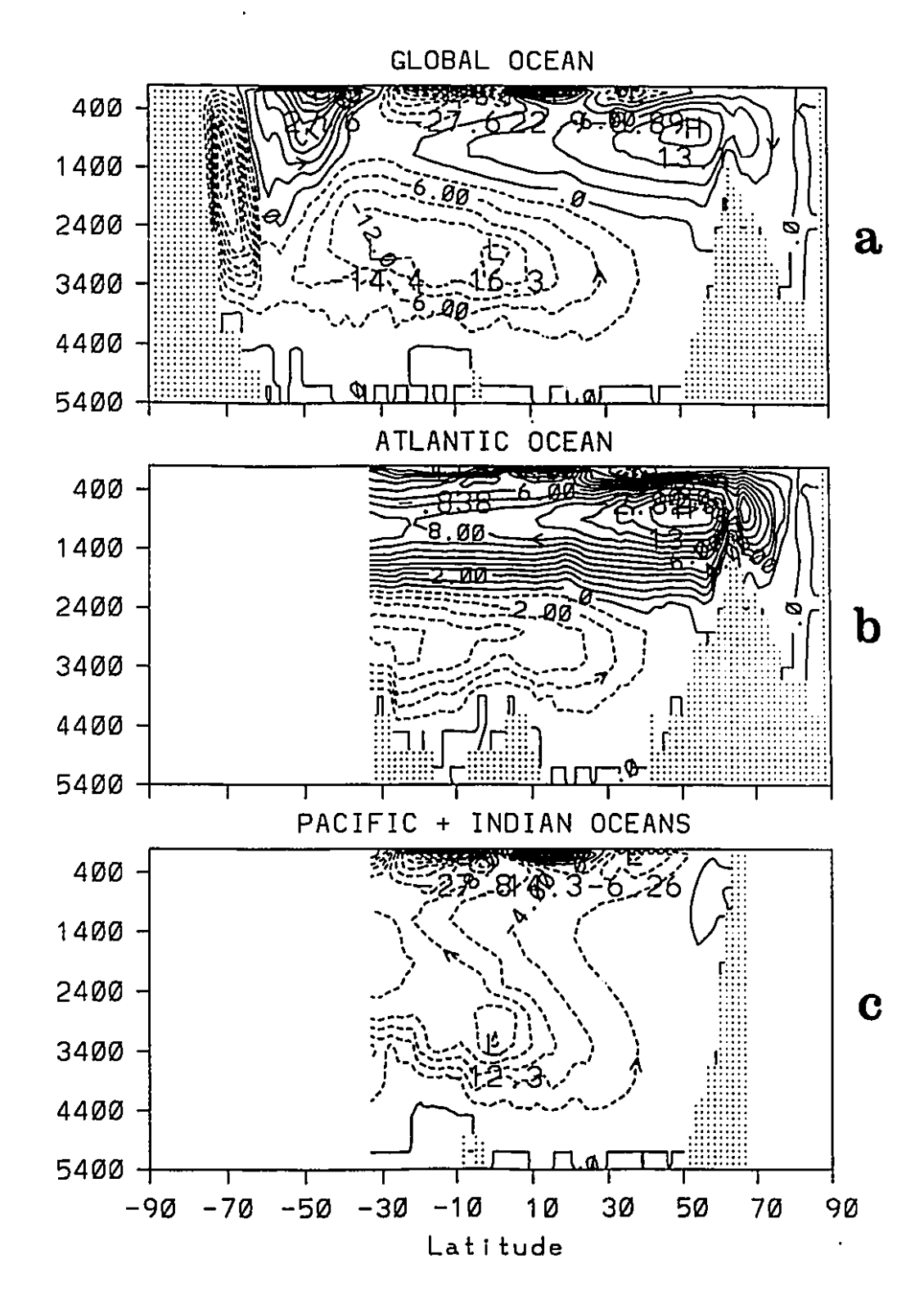
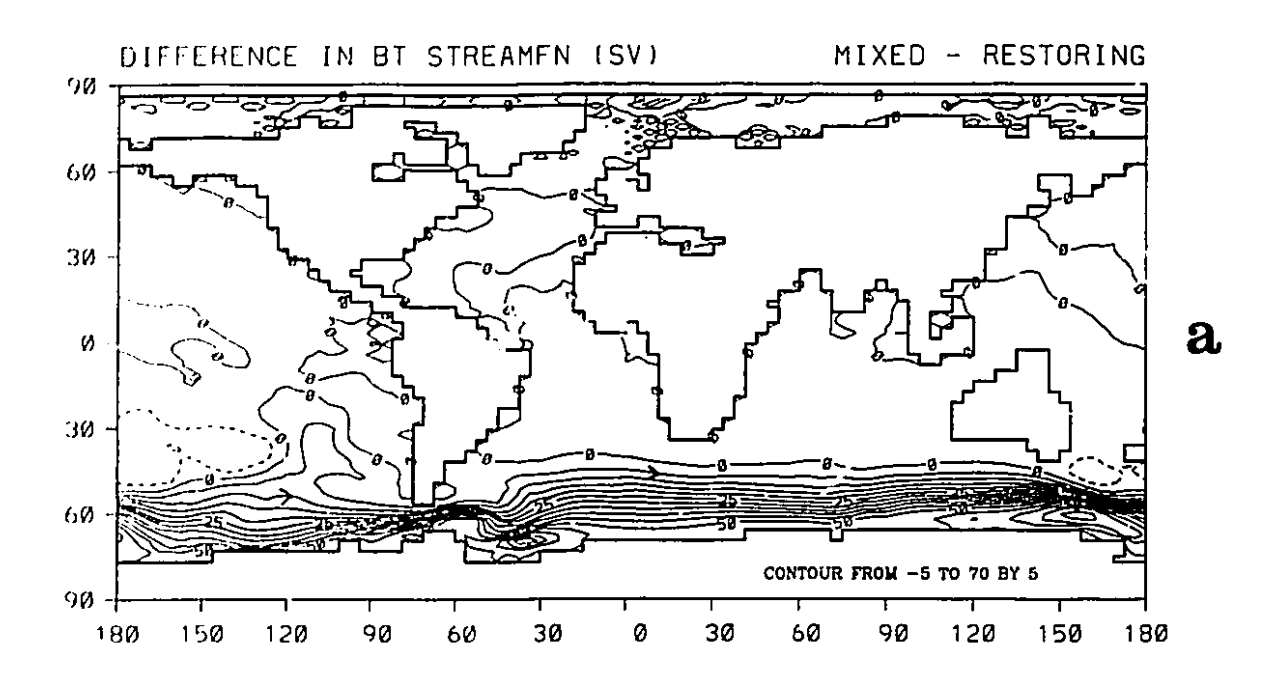


Figure 3.10: Meridional overturning streamfunction (Sv) for the equilibrium under diagnosed flux/flux boundary conditions a) global ocean b) Atlantic Ocean c) Pacific and Indian Oceans.



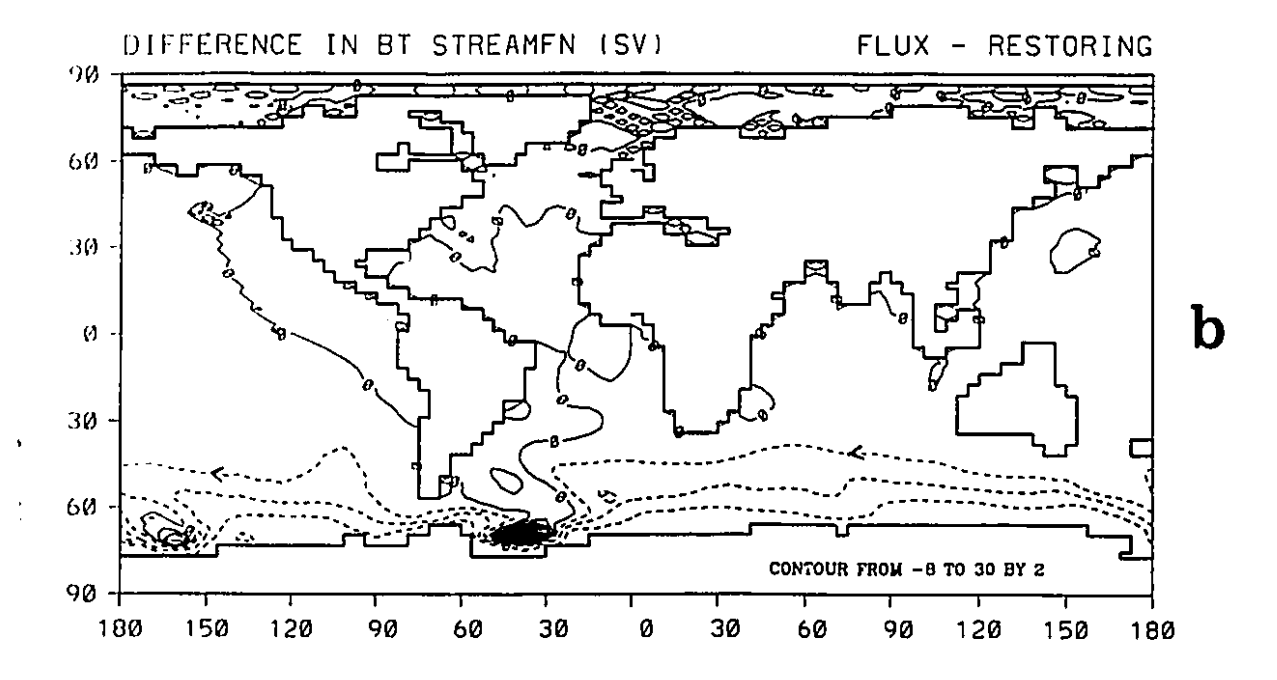


Figure 3.11: Difference in barotropic streamfunction (Sv) a) between the equilibrium under mixed boundary conditions and the spin-up under restoring boundary conditions b) between the equilibrium under flux/flux boundary conditions and the spin-up under restoring boundary conditions.

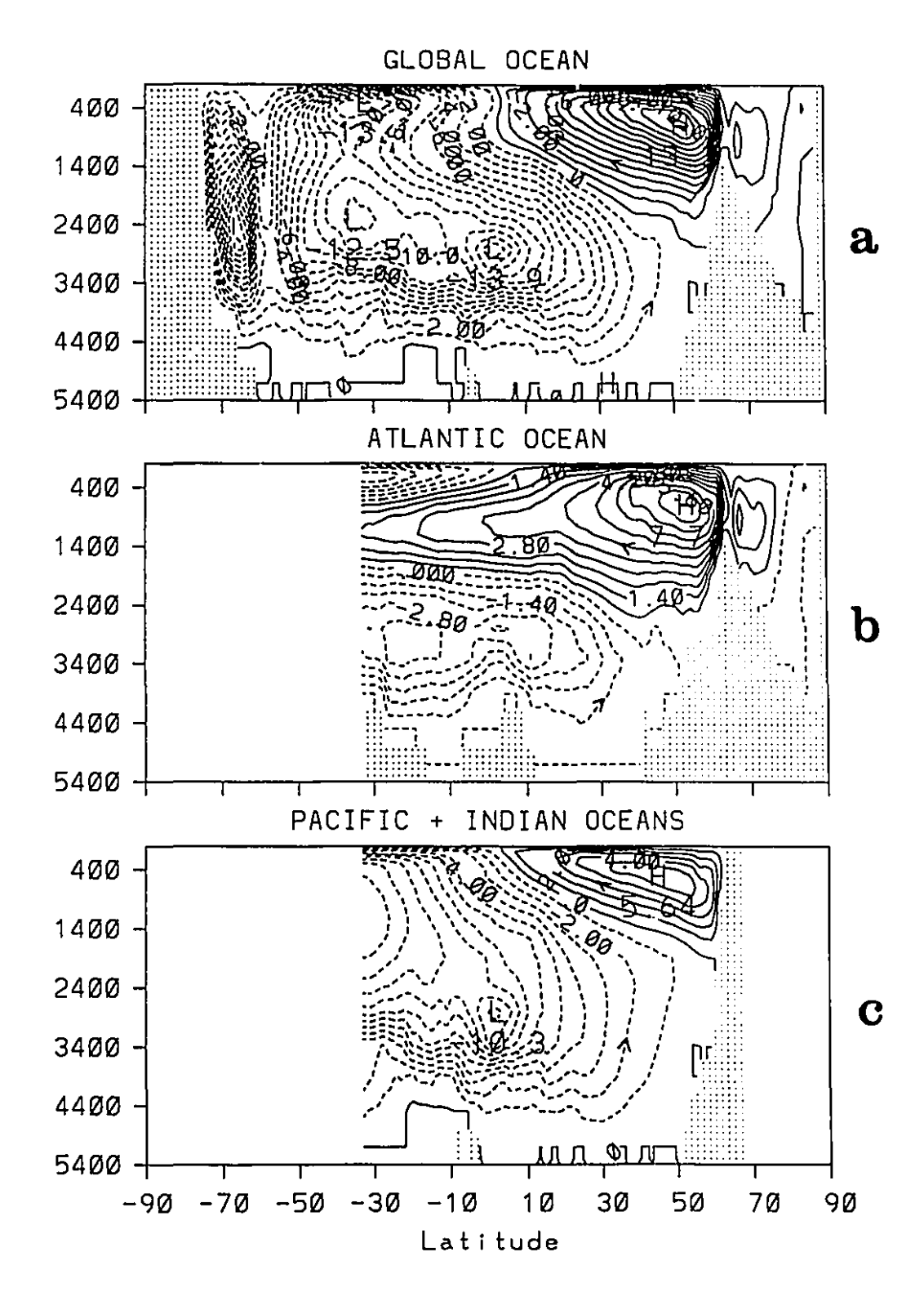


Figure 3.12: Meridional overturning streamfunction (Sv) for the spin-up under symmetric idealized restoring boundary conditions a) global ocean b) Atlantic Ocean c) Pacific and Indian Oceans.

Pacific counterpart despite the narrower basin width in the Atlantic, no doubt because of the Arctic connection and higher (cooler) latitude of sinking. The North Atlantic is also exporting water across 30°S at intermediate depths, whereas the North Pacific cell is confined to one hemisphere. Thus, even under such idealised and impartial boundary conditions, the global thermohaline circulation already starts to resemble the present-day situation.

The equilibrium surface heat flux diagnosed from this symmetric run (Fig.3.13) also demonstrates the persistence of the warm streak across the Indian Ocean sector of the ACC, here independent of any winds. Drake Passage too has a very distinctive pattern of heat fluxes associated with it, with heat loss west of the constriction but a very cool patch east of South America betraying the northward kink of the ACC: a similar feature can be picked out in the winddriven spin-up (Fig.3.8a) at the junction of the cold Malvinas and warm Brazil Currents. The larger heat gain in the equatorial Atlantic in Fig.3.13 compared to the other oceans is caused by the stronger upwelling in that ocean associated with the thermohaline circulation. Finally, the map of subsurface temperatures (230 m) in Fig.3.14 emphasizes further the importance of basin shape: the whole Atlantic is cool compared to the Pacific despite the identical restoring temperatures, due to the different areas of each ocean in the tropics which determine the basin mean temperature that is approached at equilibrium. This also applies to the two-basin model in the previous chapter, where the Pacific basin would have had a warmer basin-averaged restoring temperature than the Atlantic (as well as warmer temperatures at the northern boundary) even under the Symmetric Oceans boundary conditions.

In summary, the global model is clearly biased towards North Atlantic sinking; this is consistent with the study of Moore and Reason (1993), whose global model selected a *Conveyor* state with strong North Atlantic sinking (> 30 Sv) in all nine of their experiments under modified mixed boundary conditions (their Table 2). Iceland was missing in their model also: it is interesting to wonder whether the preference for *Conveyors* will be equally strong in models

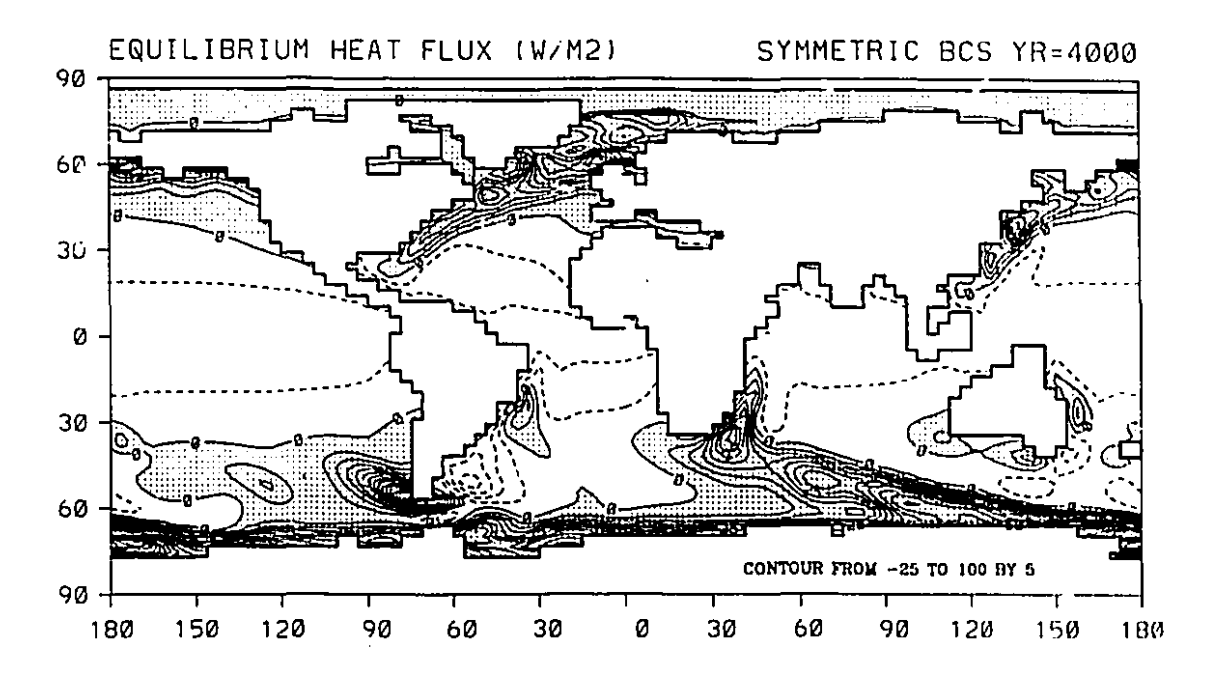


Figure 3.13: Diagnosed surface heat flux (W/m²) at equilibrium for the spin-up under symmetric idealized restoring boundary conditions. Positive values (heat flux out of the ocean) are shaded.

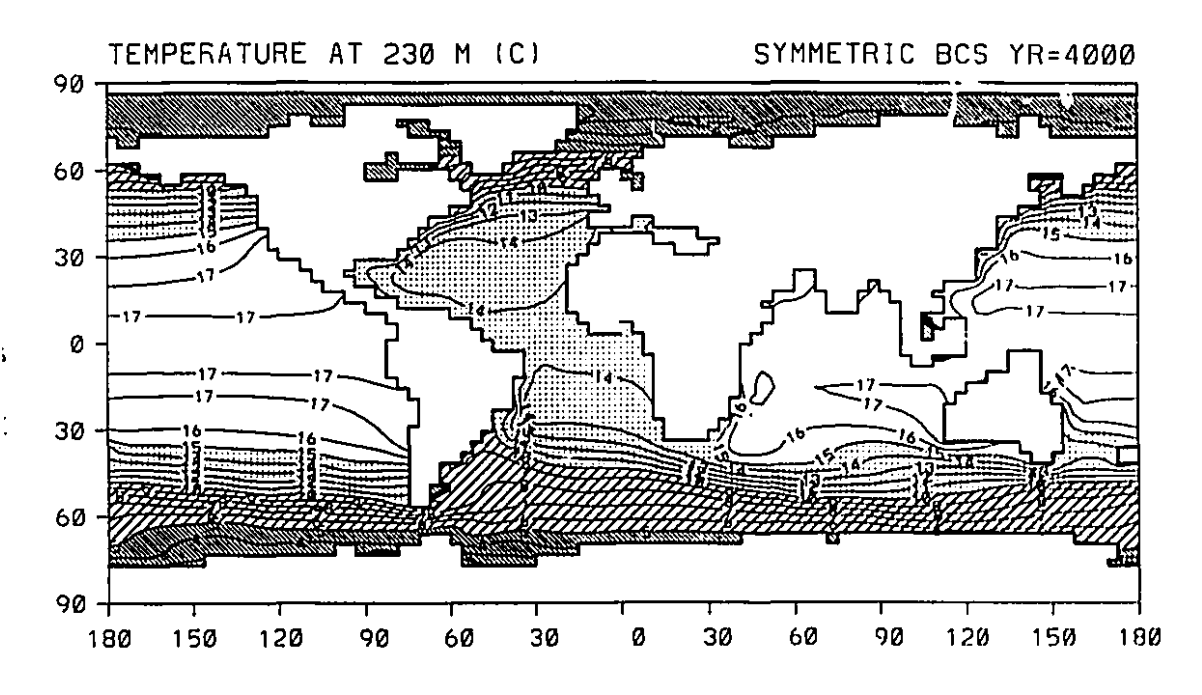


Figure 3.14: Temperature (°C) at 230 m for the spin-up under symmetric idealized restoring boundary conditions. Temperatures <15°C are dotted, < 10°C are striped, and < 5°C are closely striped.

3.3. Global Aspects of the Atlantic Thermohaline Circulation

Representing the compensation path for North Atlantic deep water formation remains one of the major hurdles for global climate models. The observational evidence reviewed in the Introduction seems to weigh in on the side of a purely cold water route through Drake Passage. However, both of the eddyresolving numerical models of the Southern Ocean published in recent years have evident warm water routes (FRAM Group, 1991, Semtner and Chervin, 1992) contributing to the return flow. The global simulations by Fujio et al. (1992), Hirst and Godfrey (1993) and Washington et al. (1994) all have barotropic leakage from the South Indian into the South Atlantic, although that of Moore and Reason (1993) does not. The present model also seems to unduly emphasize the warm water route, as shall be seen below. The purpose of this section will not however be to suggest remedies to this defect (if it is indeed a defect) but merely to explore in more detail global teleconnections of the Atlantic thermohaline circulation in the present model. The question asked is how does the global model differ from the idealised two-basin model in the previous chapter, or what are the roles of the Indian Ocean and Circumpolar Current in the more realistic geometry?

The communication between South Indian and South Atlantic waters at equilibrium may be seen in the barotropic streamfunction (Fig.3.3): a westward transport of approximately 8 Sv around the Cape of Good Hope is produced. The warm water route also dominates the time-dependent response to changes in the Atlantic thermohaline circulation. As an example, two experiments are carried out under mixed boundary conditions in which the hydrological cycle in the North Atlantic is perturbed by the addition of a small (0.2 m/y) positive or negative anomaly to the diagnosed salt flux field in the high latitude sinking region (the region shaded in Fig.3.15). Three hundred-year time series of the Atlantic



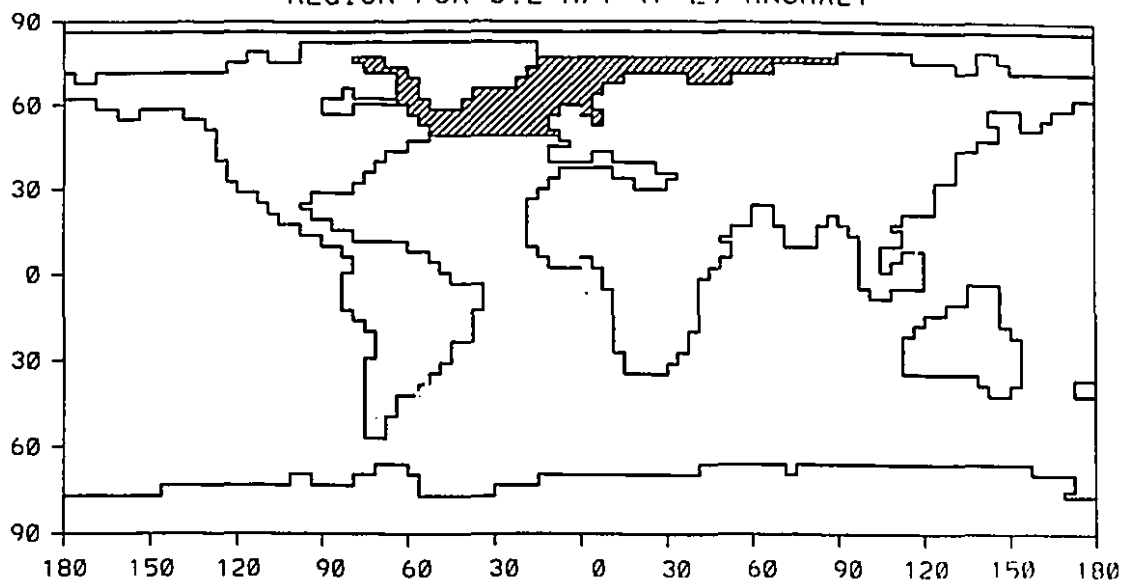


Figure 3.15: Region for positive or negative salt flux anomaly in perturbation experiment.

overturning and the barotropic transports through the Drake and Indonesian passages are plotted in Figs.3.16 and 3.17 for the added evaporation and precipitation experiments respectively. The maximum overturning decreases smoothly under the precipitation anomaly, while under the evaporation anomaly, it appears to reach a threshold after only about 100 years. In fact, although the maximum streamfunction stops increasing, the overturning cell continues to strengthen at midlatitudes and so does the outflow from the Atlantic. Thus, while there is an almost linear relationship between the maximum overturning and the outflow in the added precipitation experiment (Fig.3.18b) just as in the equilibrium experiments with the two-basin model, this does not hold for the added evaporation perturbation (Fig.3.18a). The Indonesian throughflow also increases systematically with the North Atlantic overturning while the Drake Passage transport decreases.

The global pattern is seen by plotting the horizontal map of the difference in barotropic streamfunction after, say 100 years (Fig.3.19a,b). A closed loop around Australia affects the entire Indian Ocean, unlike in Fig.3.14a,b where only

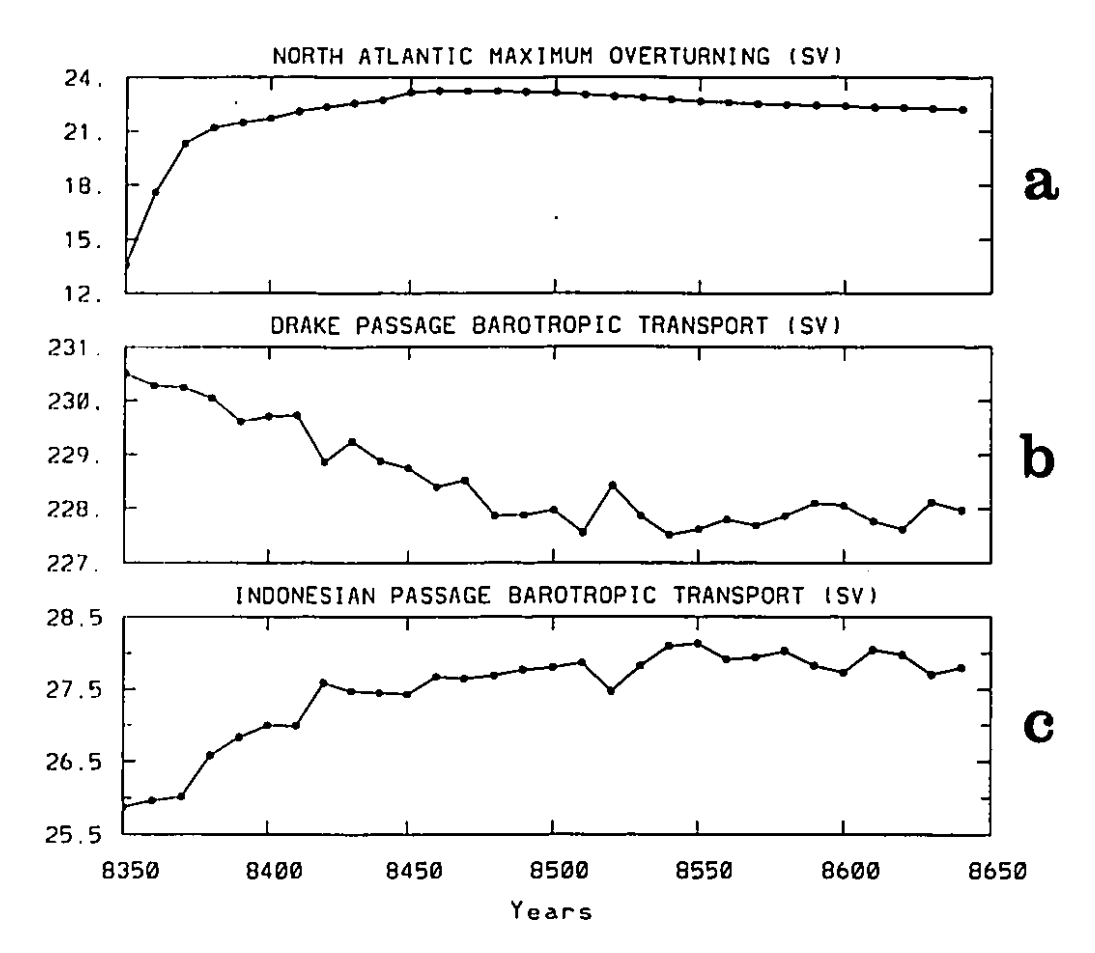


Figure 3.16: Time series of circulation changes in the added evaporation experiment a) maximum overturning (Sv) in the North Atlantic b) barotropic transport (Sv) through Drake Passage c) barotropic transport (Sv) through the Indonesian passage.

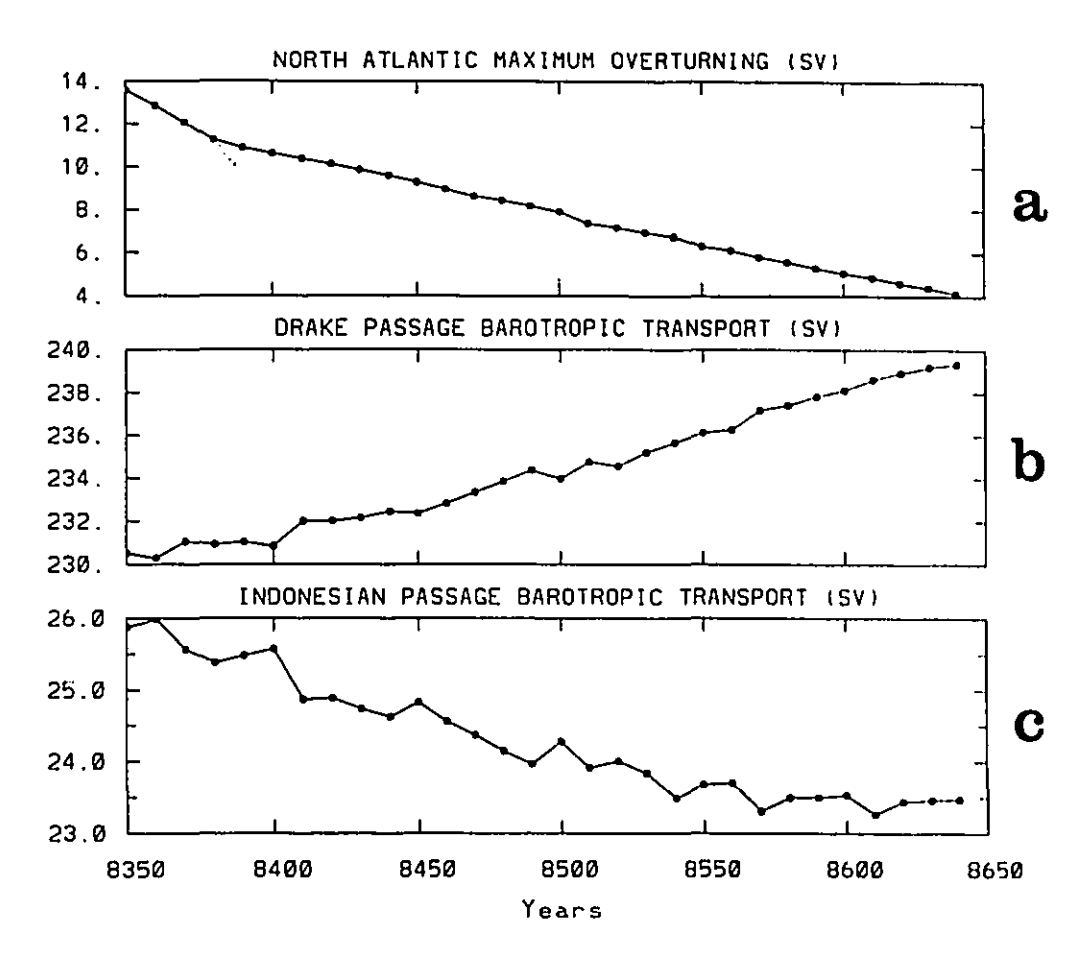


Figure 3.17: As in Fig.3.16, for the added precipitation experiment.

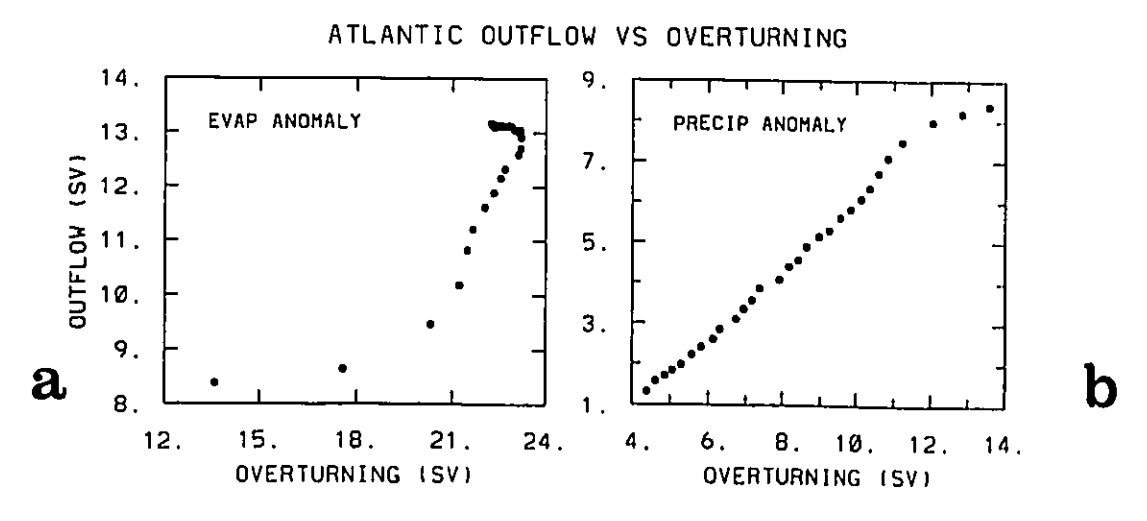
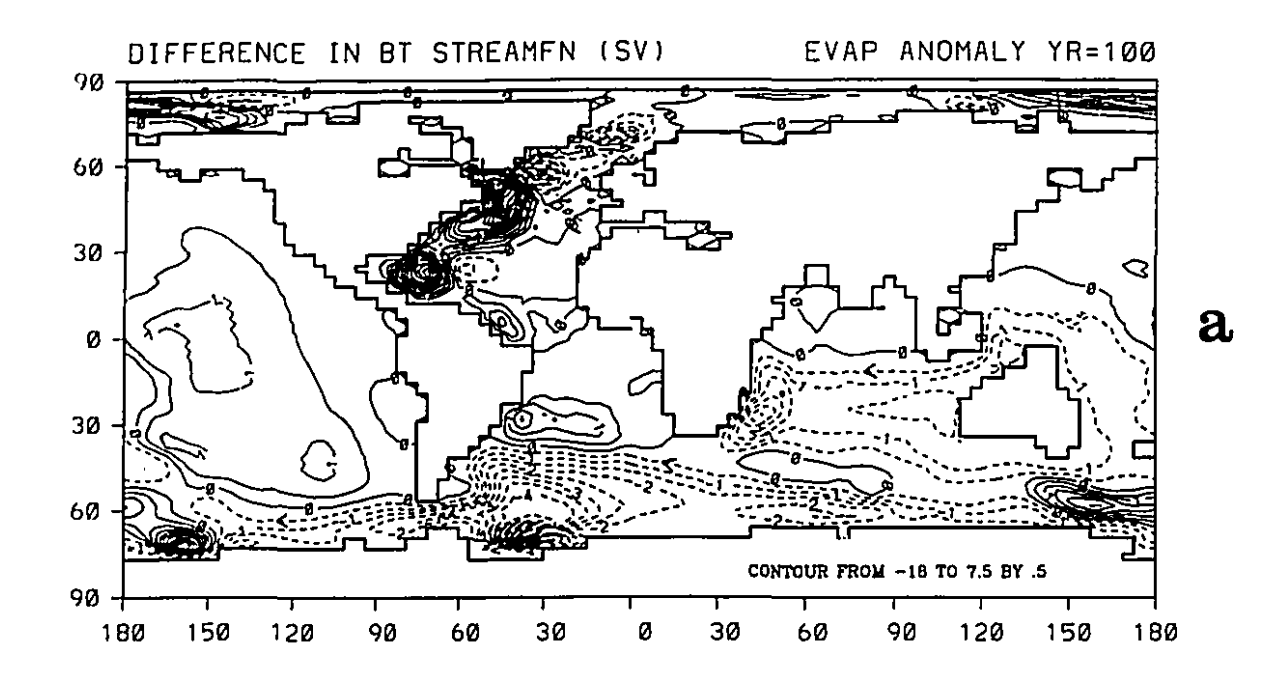


Figure 3.18: Atlantic outflow (Sv) versus maximum overturning (Sv) for a) the added evaporation experiment b) the added precipitation experiment.



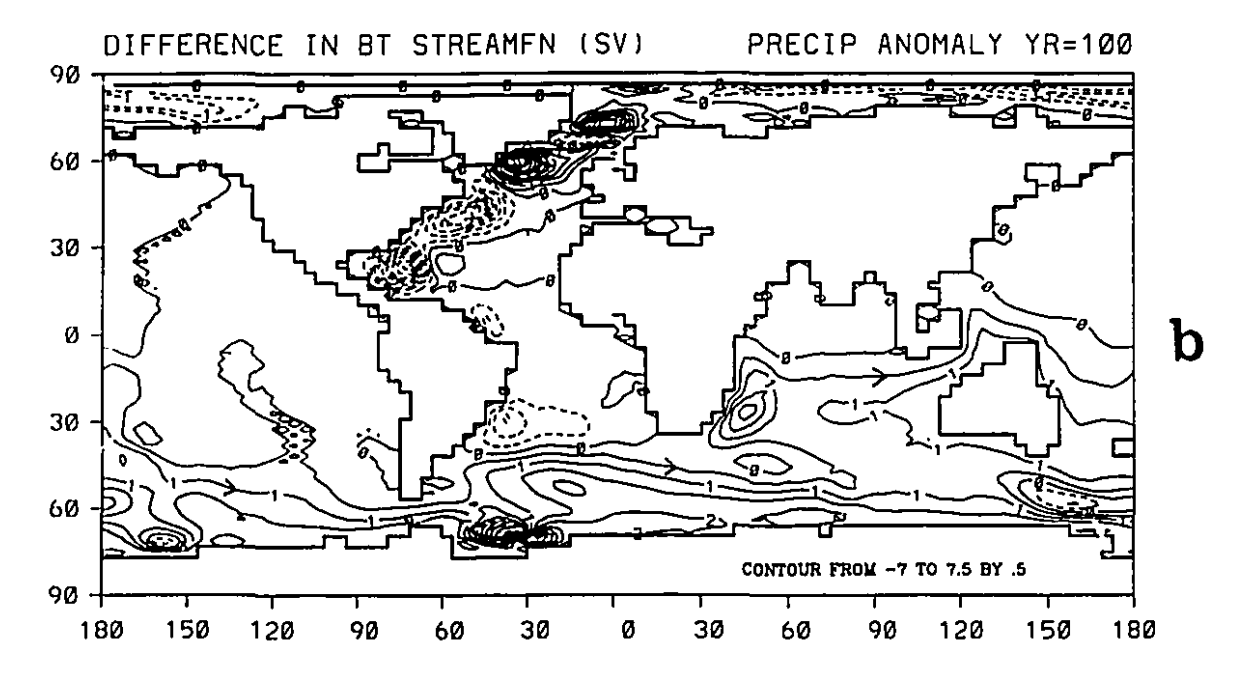
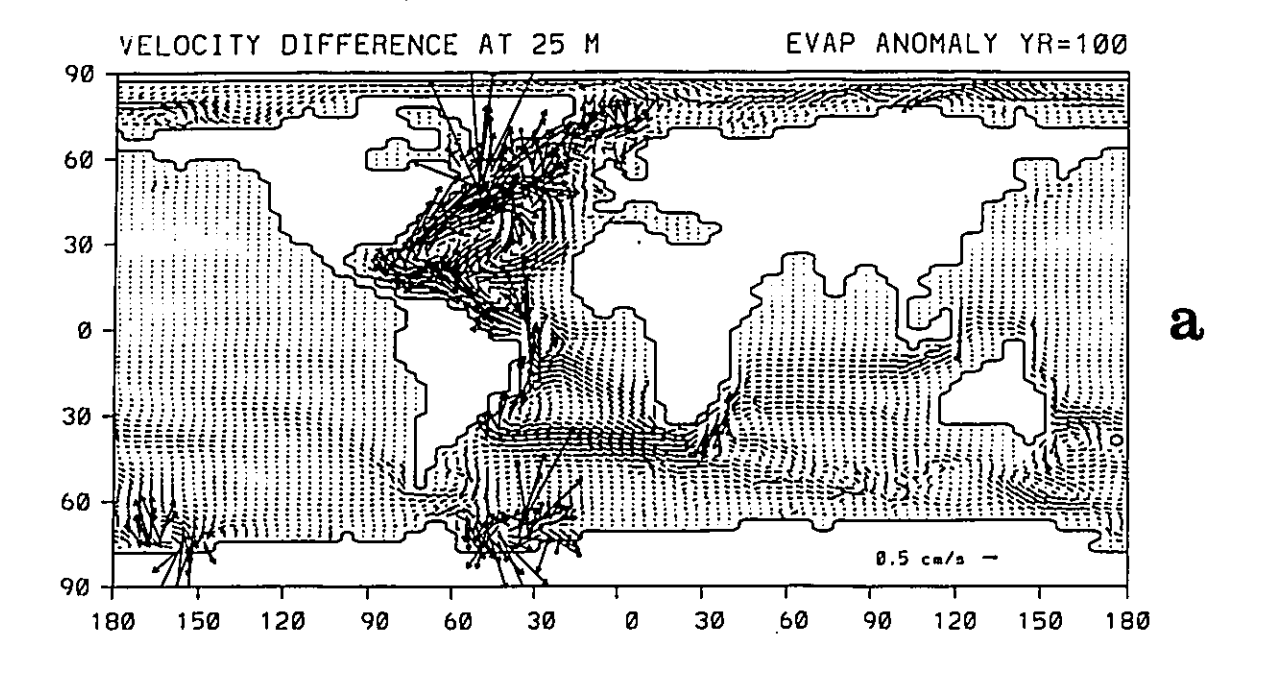


Figure 3.19: Difference in barotropic streamfunction (Sv) between a) the added evaporation b) the added precipitation experiment at 100 years, and the initial equilibrium under mixed boundary conditions.

the ACC was affected. The partly baroclinic warm water route is revealed more clearly in the velocity differences at individual depths (Figs.3.20, 3.21). The enhanced Atlantic overturning in the added evaporation experiment is supplied by an enhanced Indonesian throughflow which flows down the coast of Africa and enters the Atlantic either immediately or after a short detour to the southeast. In the South Atlantic, the anomalous circulation splits into two westward jets, one travelling straight across the ocean at 40°S and the other curving around the edge of the subtropical gyre. The change in Drake Passage transport is westward at both surface and deeper levels (Fig.3.20a,b), i.e. in the opposite direction to the cold water route. The added precipitation experiment is essentially a mirror image of the added evaporation experiment at 100 years (although a sum of the two difference plots in Fig.3.19a and b does reveal asymmetries in the Weddell Sea and the northern North Atlantic - this lack of symmetry in the Antarctic response is also seen in difference plots of the overturning streamfunction, Figs.3.22, 3.23).

The fast response of the Indian and Southern Oceans in these experiments is accomplished through wave propagation (e.g. Kawase, 1987). This is confirmed by a passive tracer experiment in which the dye is released at the surface in the North Atlantic convection region (the same region as in Fig.3.16): even by 100 years, anomalous heat or salt cannot have been advected as far as the Indonesian Passage (Fig.3.24). (The velocity field in this experiment is that of the equilibrium initial condition².) Bryan and Hsieh (1995) studied such a mechanism in the context of global sea level rise in a shallow-water model (1/3°x1/3°). A source in the North Atlantic initiated a coastal Kelvin wave which propagated southward along the east coast of North America to the equator where it was converted into an equatorial Kelvin wave. At the western boundary, the signal split again into coastally-trapped waves heading poleward in either hemisphere;

² More precisely, it is the velocity field from the mixed boundary conditions experiment at an earlier time (after 2000 years instead of 3950). All indications point to the southward spread of tracer being even slower at 3950 years, so Fig.3.24 overestimates rather than underestimates the distance travelled.



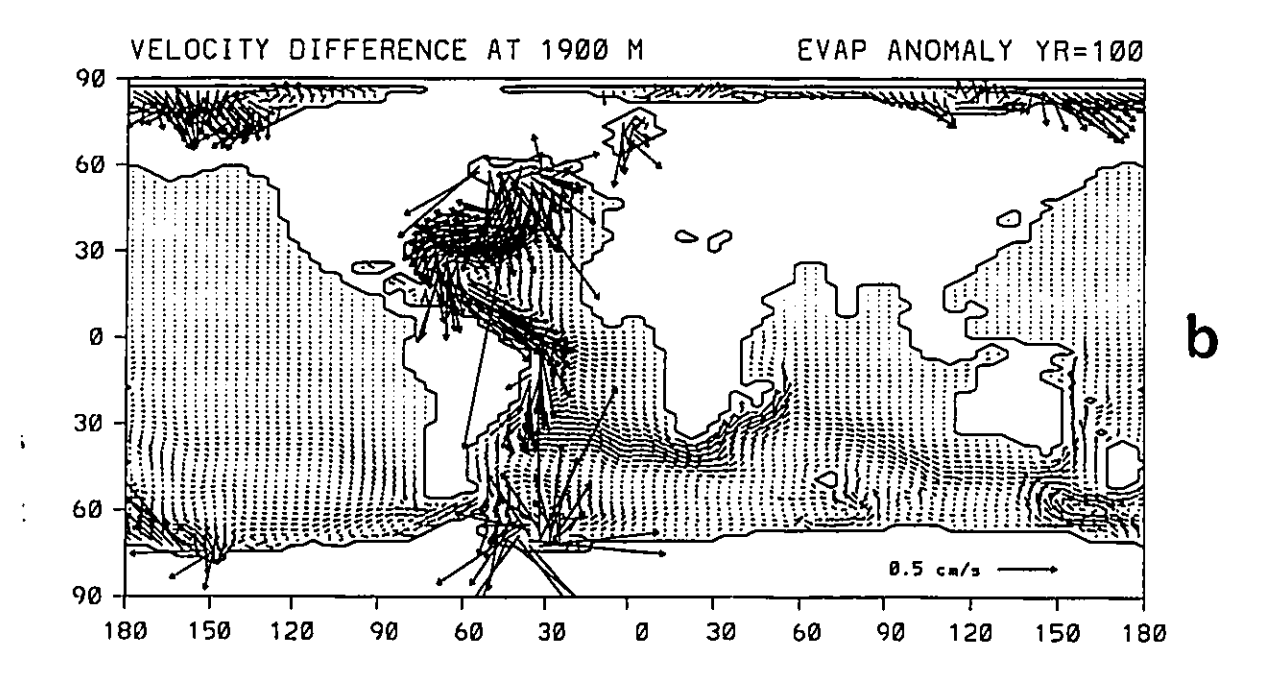
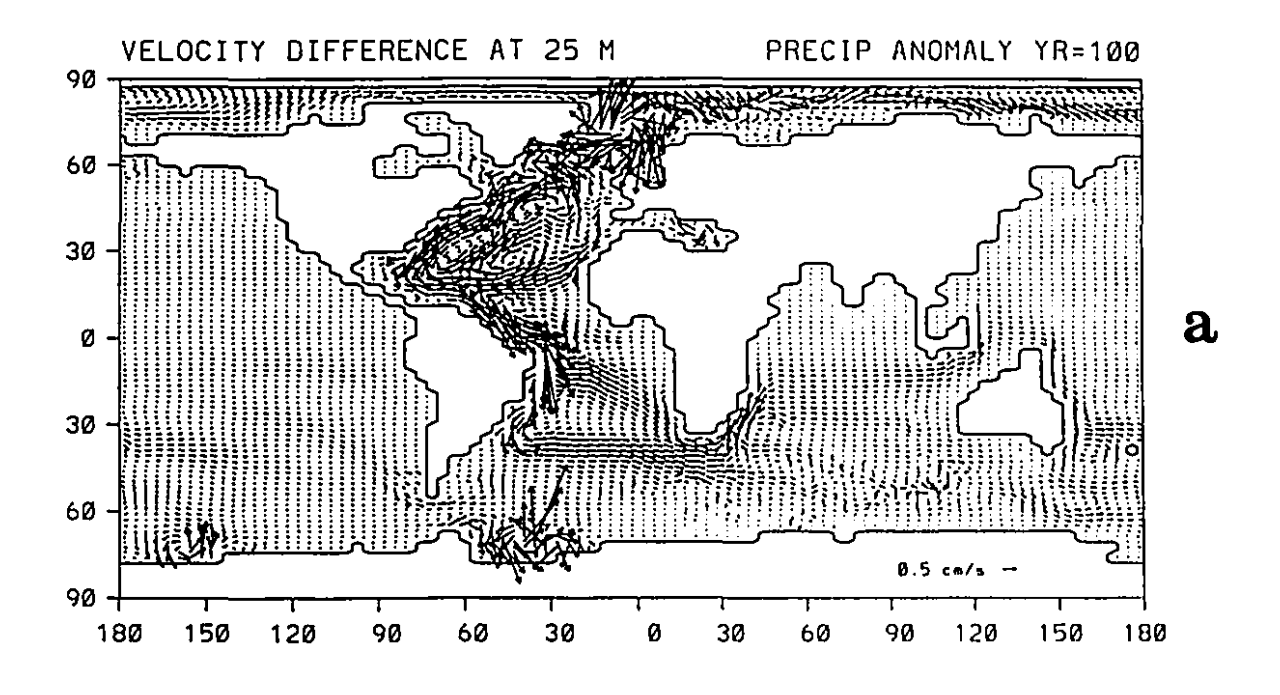


Figure 3.20: Difference in velocity at a) 25 m b) 1900 m between the added evaporation experiment at 100 years and the initial equilibrium under mixed boundary conditions.



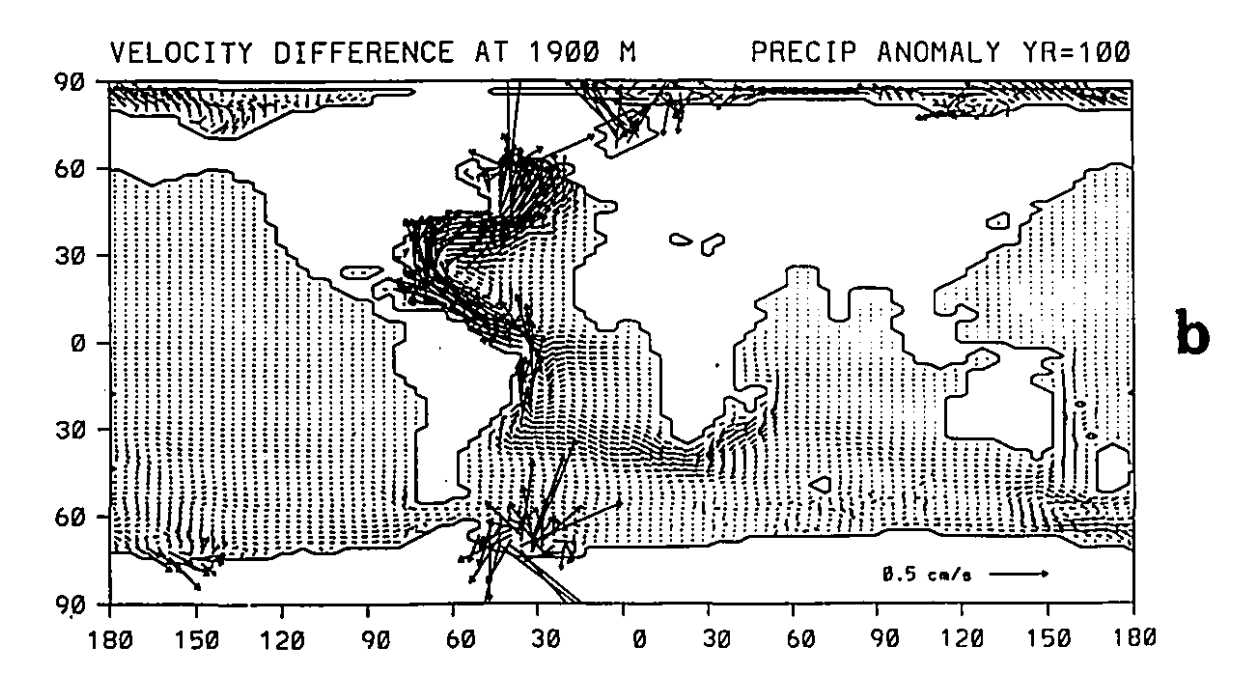


Figure 3.21: As in Fig.3.20, for the added precipitation experiment.

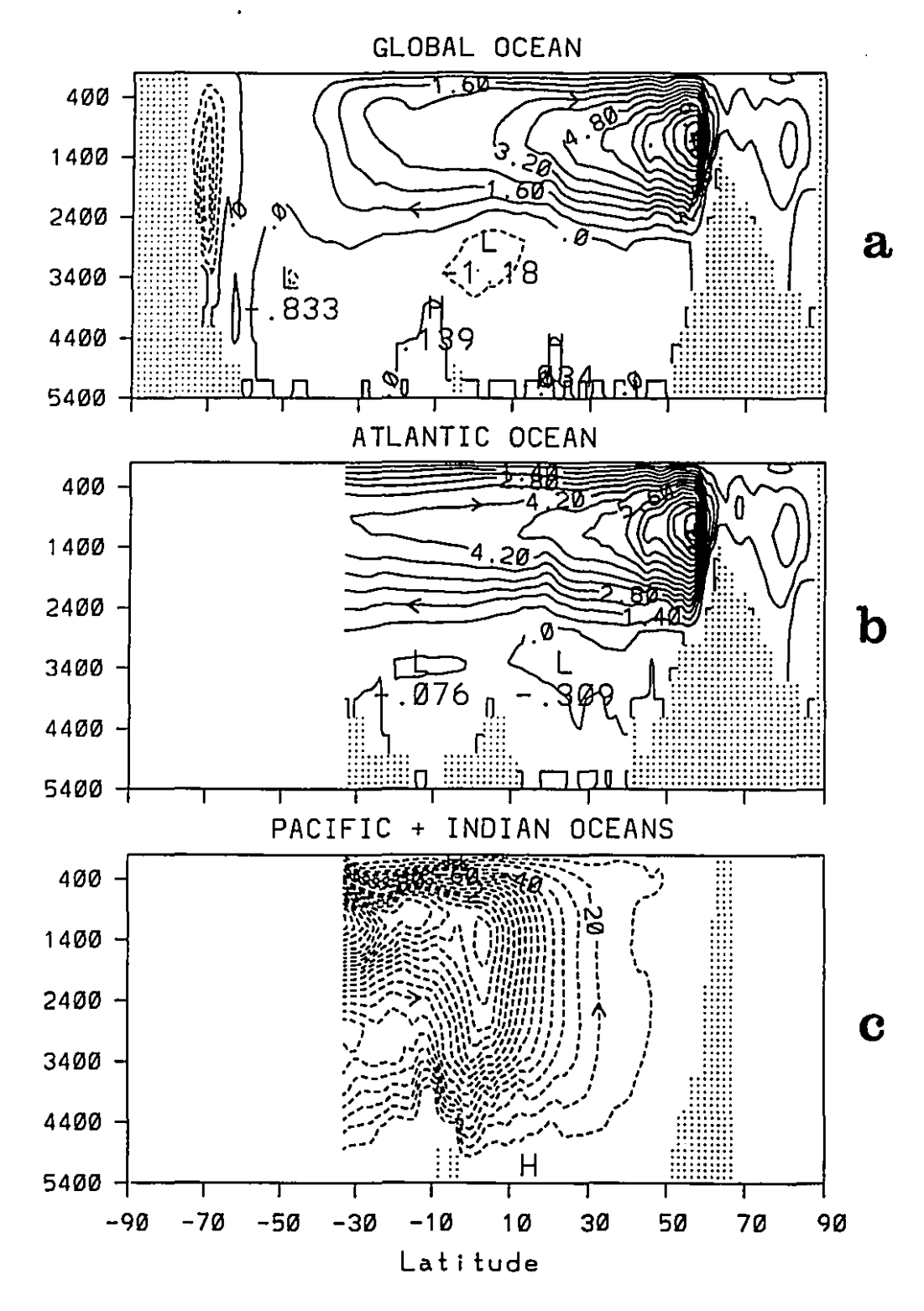


Figure 3.22: Difference in meridional overturning streamfunction (Sv) between the added evaporation experiment at 100 years and the initial equilibrium under mixed boundary conditions. a) global ocean b) Atlantic Ocean c) Pacific and Indian Oceans. Contour interval is 0.8 Sv in a), 0.7 Sv in b), and 0.1 Sv in c).

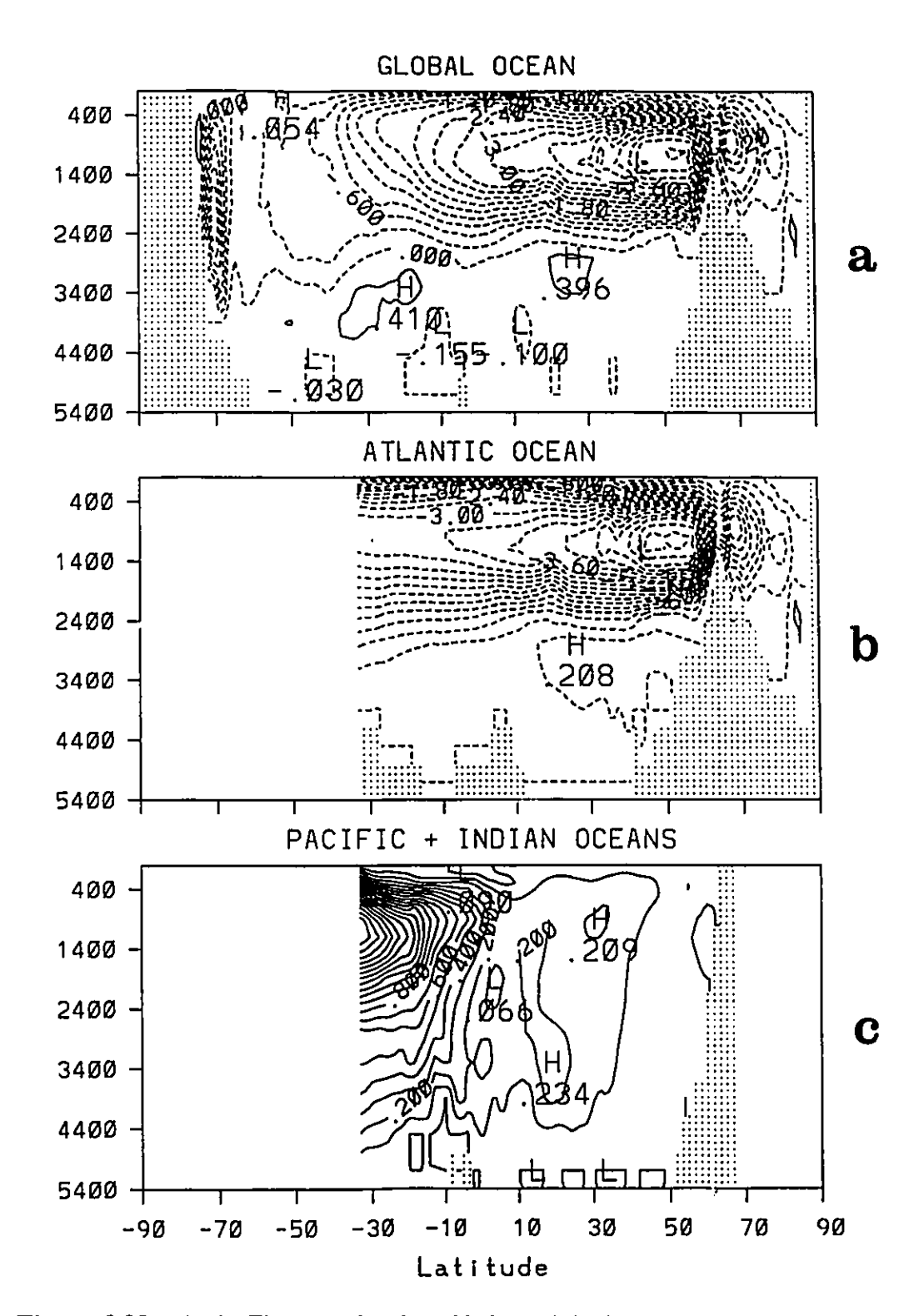
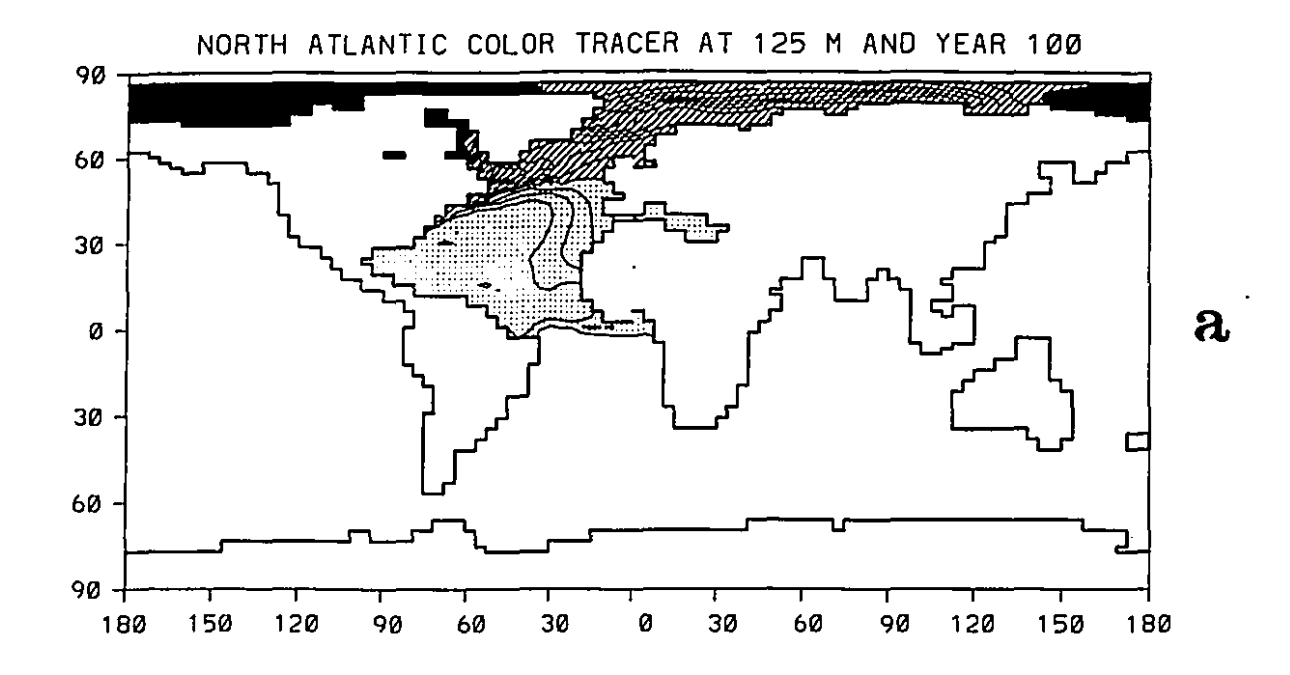


Figure 3.23: As in Fig.3.22, for the added precipitation experiment. Contour interval is 0.3 Sv in a), 0.3 Sv in b), and 0.1 Sv in c).



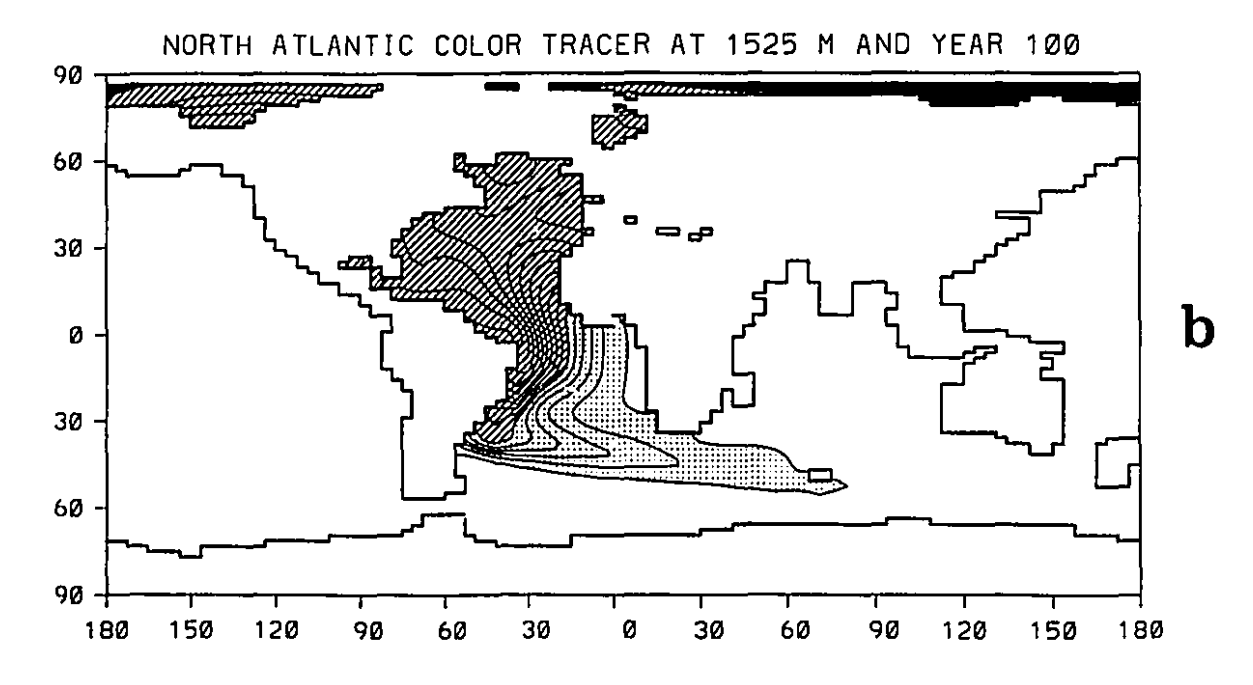


Figure 3.24: Passive tracer distribution at a) 125 m b) 1525 m one hundred years after the start of a continuous dye release uniformly over the same region as the evaporation or precipitation anomaly (Fig. 3.16). Units are arbitrary, but increasing concentrations are first dotted, dashed and then in solid black, and the same contours are used in both parts of the figure. The velocity field is that of the run under mixed boundary conditions, but after only 2000 years instead of 3950 years.

the southern wave followed the African continent around into the Indian Ocean where it travelled across to the Indonesian throughflow region within the equatorial waveguide. The total time to reach this point was approximately 1 year (with another year to reach Drake Passage in the eastern Pacific).

Kelvin and Rossby waves also exist in the present B-grid, but are significantly slowed and damped at this resolution. The continuous excitation by the imposed (P-E) anomaly also complicates the analysis of these experiments. However, the distinctive patterns of tracer change at 100 years (Figs. 3.25, 3.26, for the added evaporation experiment) can be understood by relating them to the anomalous circulation set up by the passage of the fronts. The accumulated temperature and salinity changes are small in the Pacific and Indian Oceans (not shown), but prominent in the South Atlantic, where they have the opposite sign to those in the North Atlantic. In the added evaporation experiment, for example, the largest warming is in the deep North Atlantic where a tongue of newly formed warm salty water extends out from the Icelandic rise. The extra salt in the northern North Atlantic is also being fairly efficiently exported to the Arctic. The South Atlantic, in contrast, both cools and freshens significantly over the top 1000 m. The subsurface cooling is large-scale (Fig. 3.26a), and is found to be well correlated with anomalous horizontal advection of the equilibrium tracer fields (while vertical advection appears to be involved in the warming of the Arctic).

In conclusion, the response to changes in the Atlantic Conveyor in the present model is global and involves both the ACC and the Indian Ocean, but the largest temperature and salinity changes are found in the South Atlantic, at least on these short (decadal to century) timescales. It is a delicate question also as to how relevant the global teleconnections are to the real ocean. The heat and salt budgets of the circumpolar region (Fig.3.27)³ immediately identify it as a problem

The non-zero global mean surface heat flux in Fig.3.27a, and the discrepancies between the oceanic transports of heat into enclosed regions like the Arctic and the region net surface exchanges, are probably associated with intermittent convection or transient waves in the deep ocean since the mismatches were often actually smaller at 3950 years than at 5600 years.

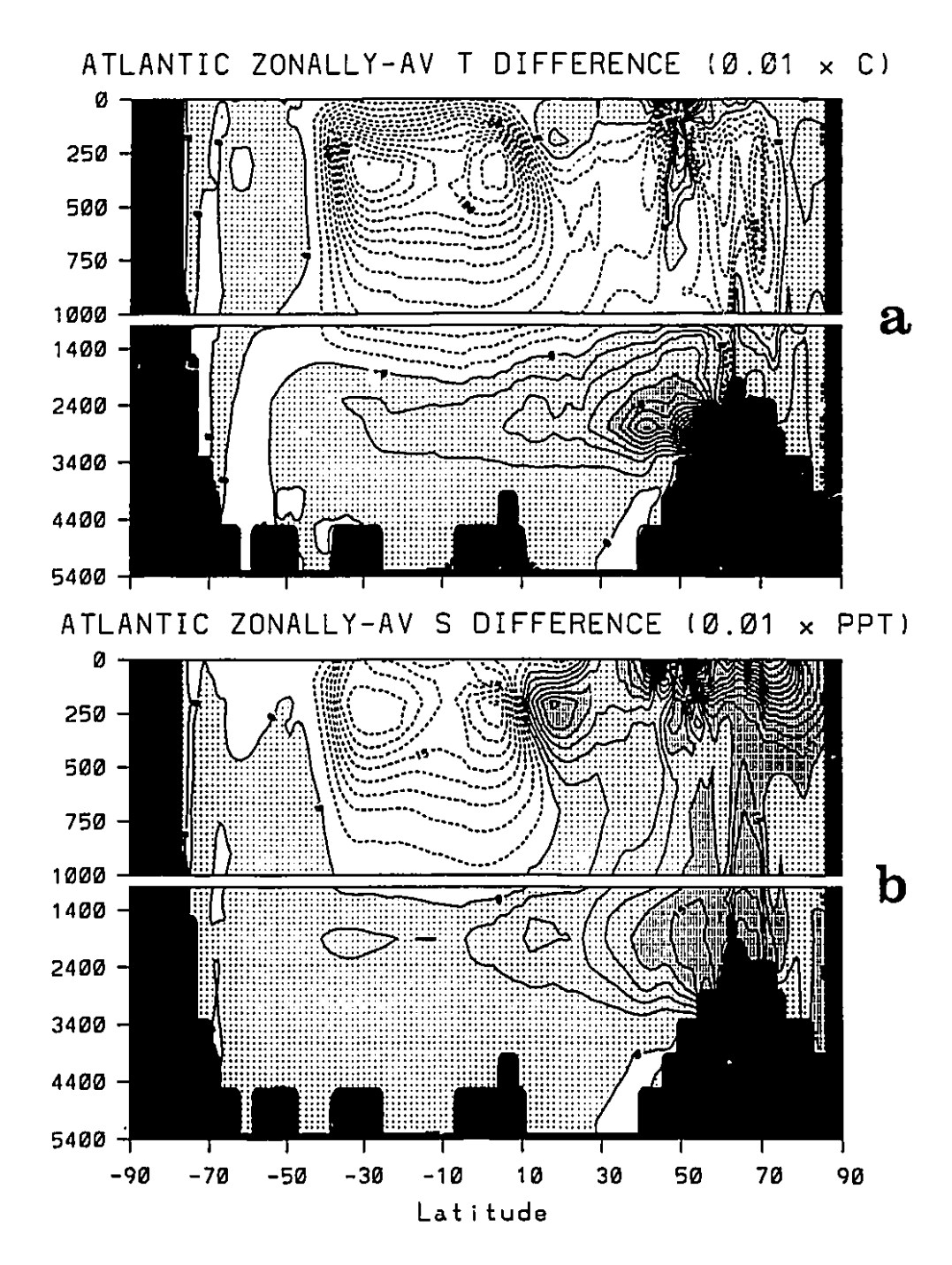
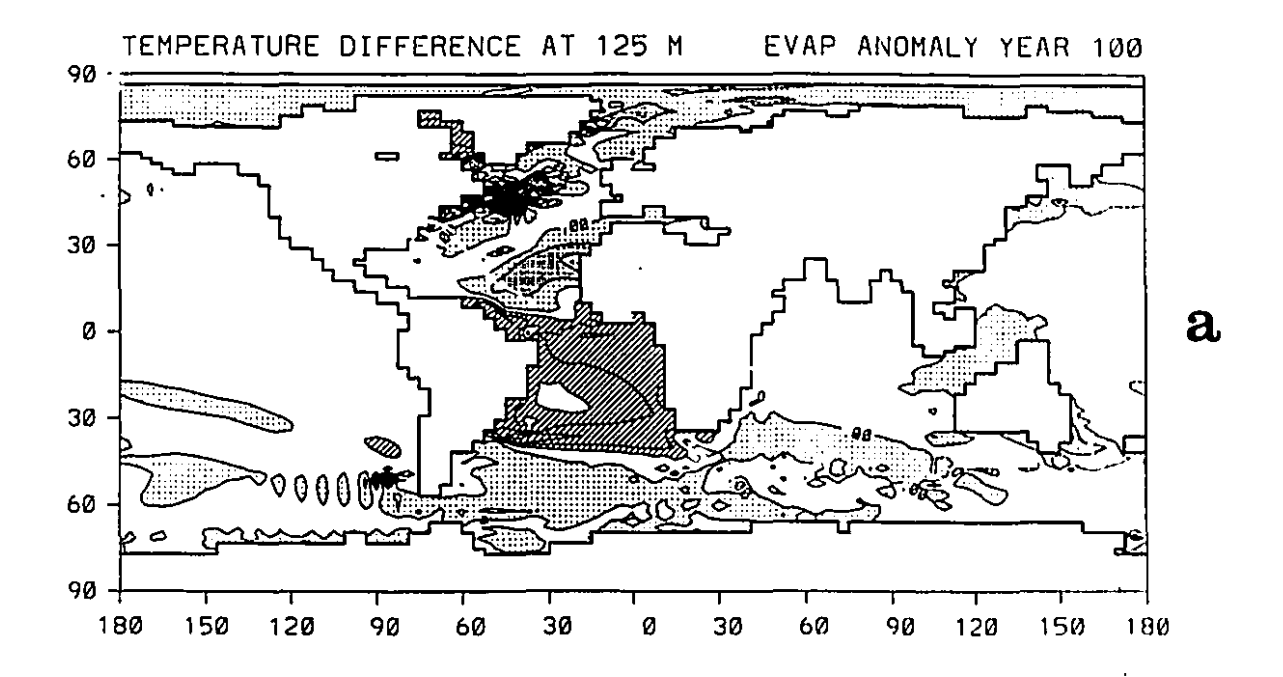


Figure 3.25: Difference in zonally-averaged a) temperature (°C) b) salinity (ppt) for the Atlantic basin of the added evaporation experiment after 100 years minus the equilibrium under mixed boundary conditions. Contour interval is 0.1°C in a), and 0.03 ppt in b); values > 0 are lightly shaded and values > 0.4°C and 0.12 ppt are heavily shaded.



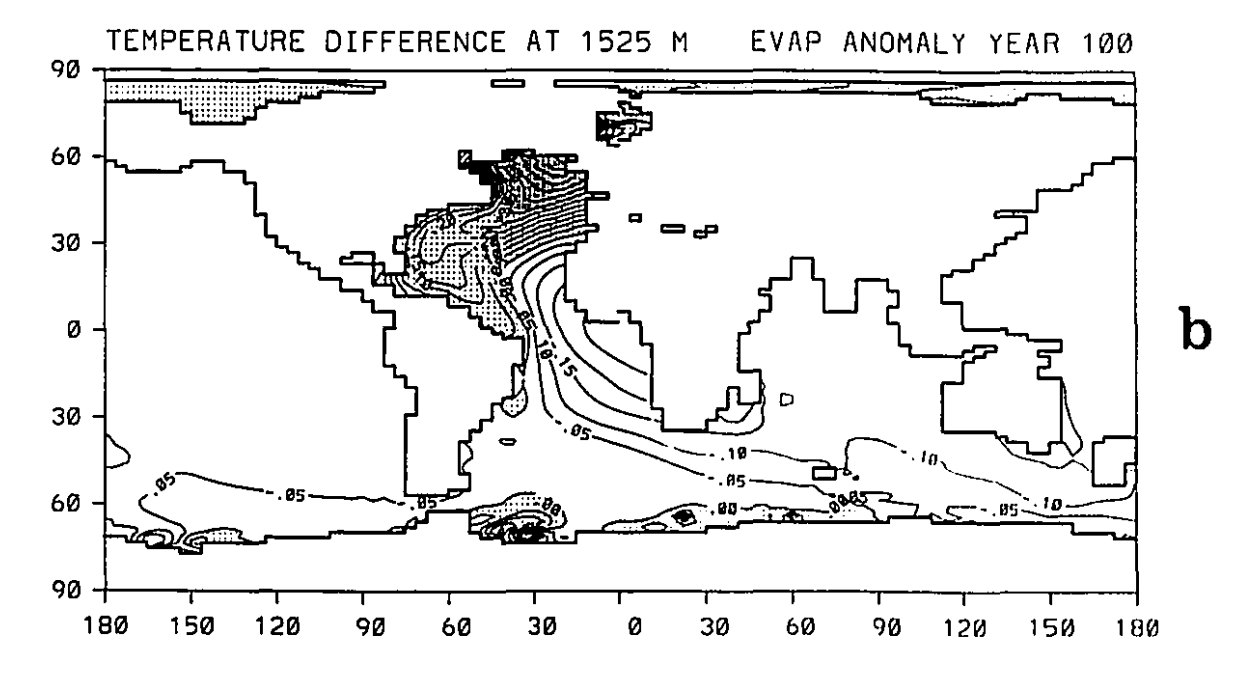
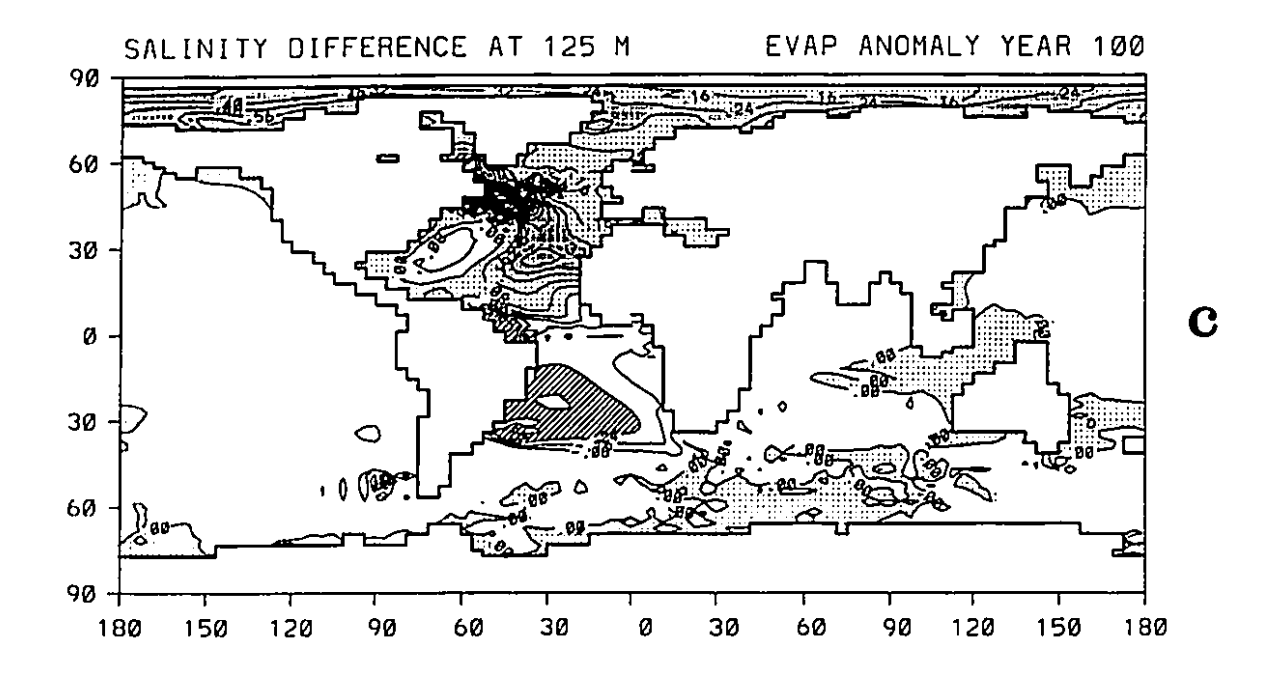


Figure 3.26: Difference in temperature (°C) at a) 125 m b) 1525 m and salinity (ppt) at c) 125 m d) 1525 m for the added evaporation experiment after 100 years minus the equilibrium under mixed boundary conditions. Contour interval is 0.3°C in a), 0.05°C in b), 0.08 ppt in c) and 0.03 ppt in d). Positive values are dotted, with closely-spaced dots indicating temperature increases > 0.3°C or salinity increases > 0.24 ppt, while stripes indicate temperature and salinity decreases of the same magnitude (< -0.3°C or < -0.24 ppt).



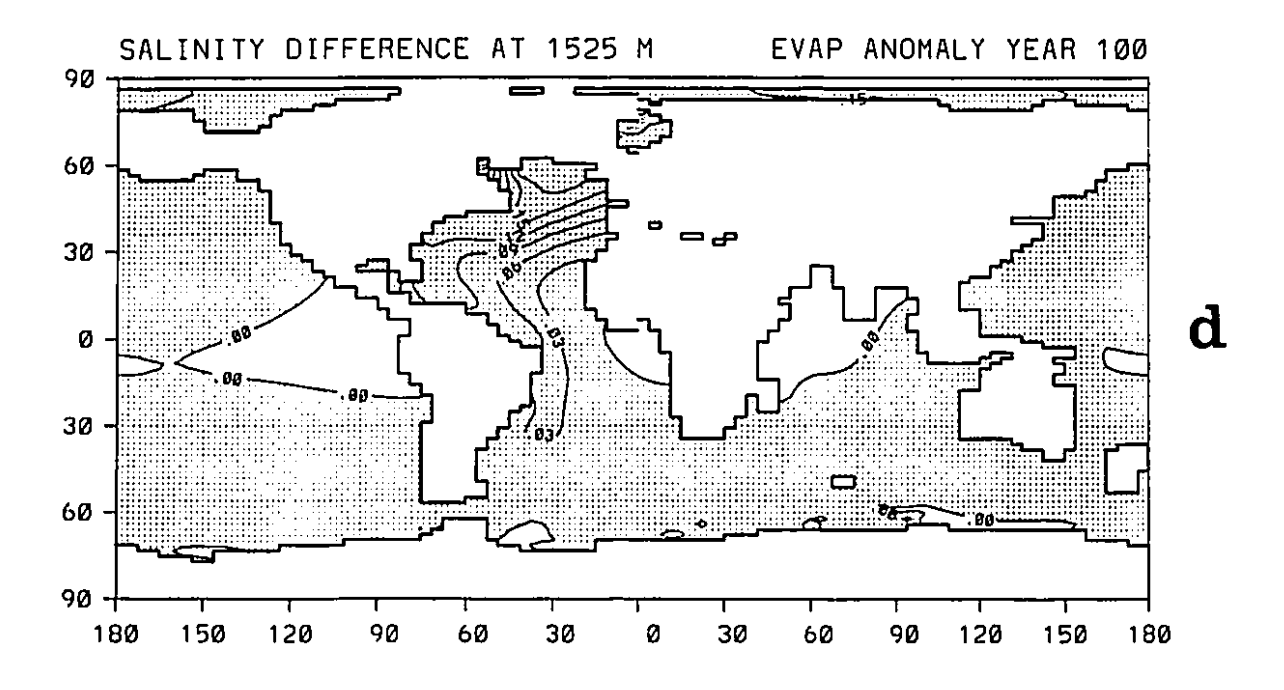


Figure 3.26. Suite.

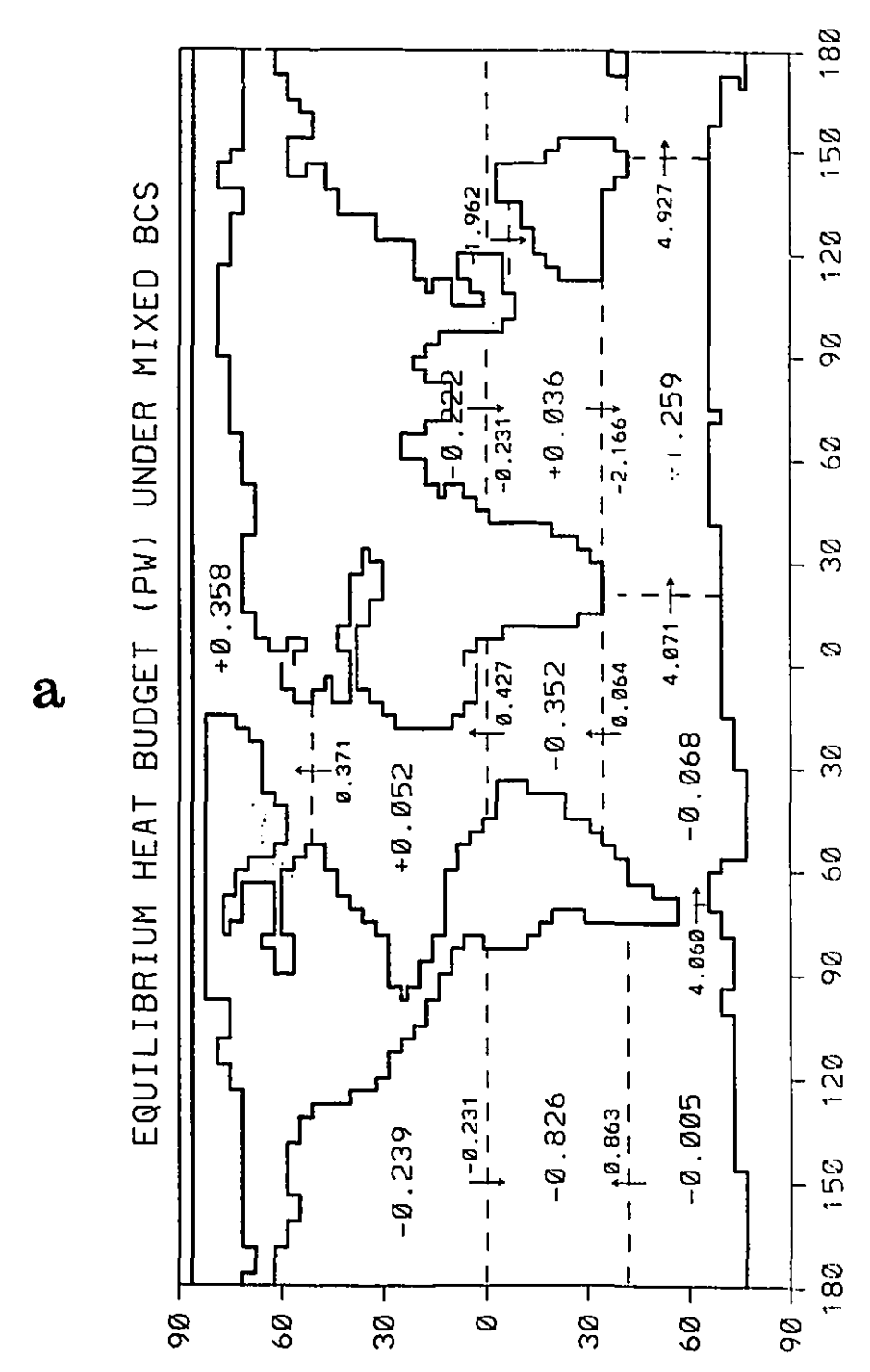
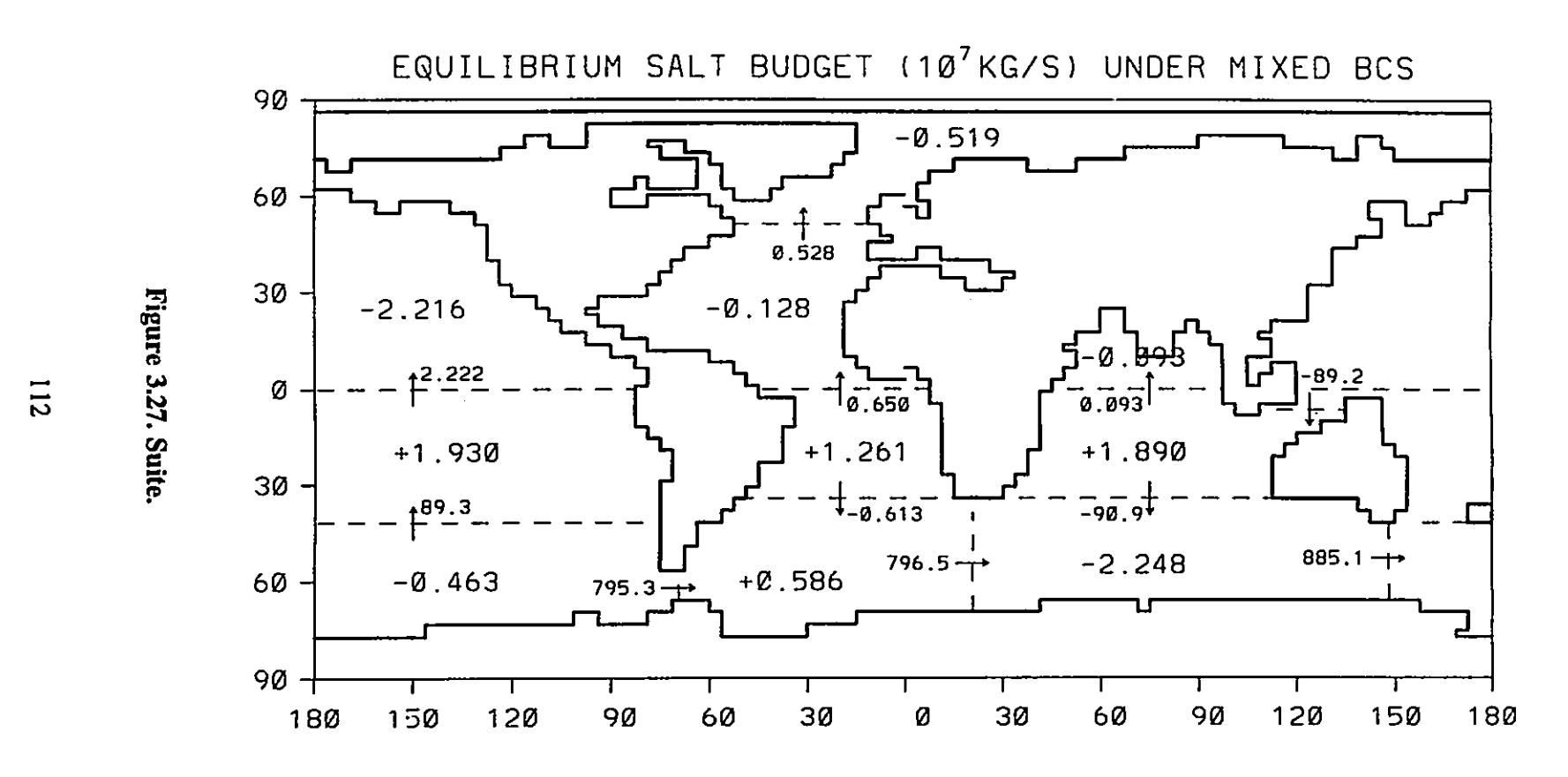


Figure 3.27: Circumpolar a) heat (1 PW=10¹⁵ W) and b) salt (10⁷ kg/s) budgets for the equilibrium under diagnosed mixed boundary conditions. The sign convention for the regional surface exchanges (in larger font) assumes heat fluxes positive out of the ocean and salt fluxes positive into the ocean. The Arctic is defined as north of 54.7°N while the boundaries between the South Atlantic or South Indian and the Southern Ocean or the South Pacific and the Southern Ocean are fixed at 33.4°S and 40.8°S respectively.

b



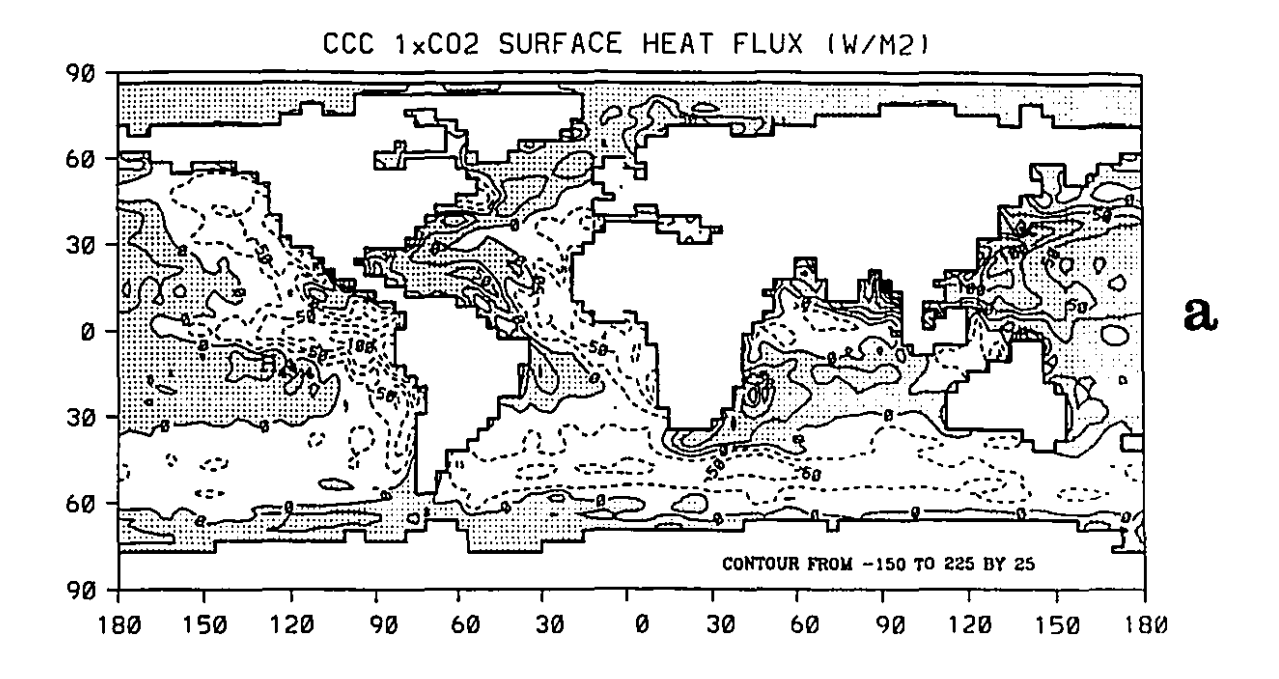
area in the model's climate. Reliable observations of the heat and salt transports and surface fluxes in the Southern Ocean are few and far between: nonetheless, obvious concerns do arise. Both the Atlantic and Pacific sectors of the circumpolar ocean are gaining heat from the atmosphere, and a meager 0.07 PW (1 PW=10¹⁵ W) of heat is crossing 34.3°S northward into the South Atlantic; in comparison, Rintoul (1991) suggests that the ACC loses 0.25 PW of heat in crossing the Atlantic and exports another 0.25 PW northward across 32°S. (The overall appearance of the meridional transports was already discussed in connection with the spin-up (Fig.3.8) where they were judged to be not unreasonable: they are very similar under mixed boundary conditions, and the global budgets are also qualitatively equivalent despite the differences in ACC transport.) The Atlantic is in fact almost isolated from the rest of the world oceans: the net transport of both heat and salt in the ACC barely changes as it passes through the Atlantic sector. In contrast, the Indian and Pacific basins are rather tightly coupled by a closed loop of large heat and salt transport around Australia associated with the strong Indonesian throughflow (25.9 Sv under mixed boundary conditions). Air-sea interaction is important in the circumpolar sector of the Indian Ocean where the convective streak identified earlier causes a net heat loss nearly as large as the gain due to the Indonesian throughflow. A final unrealistic feature is the net precipitation over the North Atlantic: this is insensitive to the choice of the boundary with the Arctic, and appears to be related to the anomalous precipitation over the Gulf Stream.

For this reason, it is not sensible to pursue a more in-depth analysis of the water masses involved in the warm and cold water routes in the model. Even in a better global model, the problem of the uncertainty of surface heat and freshwater fluxes in the Southern Ocean would remain. In the next section, a different approach is therefore attempted.

3.4. Incompatibility of AGCM Sea Surface Fluxes

In this final section, the equilibrium ocean circulation under the annual mean wind stresses and surface heat and freshwater fluxes from the Canadian Climate Centre second generation AGCM is evaluated. A short description of the atmospheric model is given in Appendix B: more details may be found in Boer et al. (1984a,b) and McFarlane et al. (1992). A satisfactory performance for the AGCM was determined on the basis of a comparison with the observed climate compiled from ten years of twice daily National Meteorological Centre (NMC) analyses. Differences between the screen temperatures over the oceans and the climatological values were in general < 5°C, except in certain high latitude locations in winter where the model field was too warm. Sea ice extents in the Arctic were comparable to those of Bourke and Garrett (1987), except for the great thicknesses produced by advection into the Canadian Archipelago and the coasts of Greenland, which were not simulated by the thermodynamic-only ice model. Sea ice extents in the Antarctic were also judged acceptable although observations with which to compare thicknesses were not available. The zonallyaveraged precipitation was in reasonable agreement with the climatology of Jaeger (1976), especially at low latitudes. Finally, an equilibrium simulation under doubled atmospheric CO₂, described in Boer et al. (1992), was broadly consistent with similar experiments by other groups, with a global mean warming of the surface air temperature of 3.5°C, an enhanced hydrological cycle (by about 4%) and sea ice retreat at both poles.

The atmospheric model's surface heat and freshwater fluxes are illustrated in Fig.3.28, for annual mean conditions averaged over the last ten years of an 18-year integration. The net surface heat flux is obtained as the sum of the radiative, sensible and latent heat contributions except under ice where the ice-ocean exchange is used, and a global net balance is ensured through a uniform correction of ~-0.64 W/m². The atmospheric variables unlike the oceanic variables are colocated, and on a coarser grid in the meridional direction than the ocean model, so a linear interpolation of both wind and buoyancy fluxes is carried out. Precipitation over land is provided for by partitioning the land area into 21



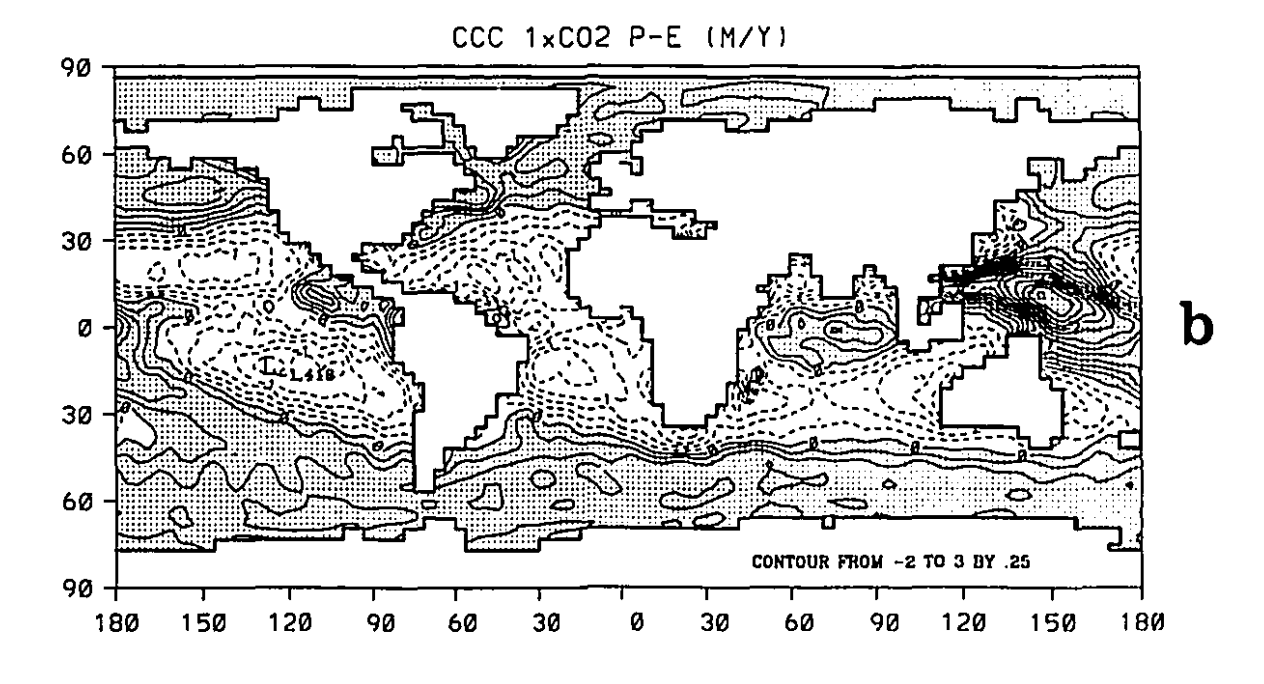


Figure 3.28: Surface a) heat (W/m²) and b) freshwater (m/y) fluxes from the Canadian Climate Centre atmospheric GCM. Positive values (heat out of the ocean, and (P-E)>0) are shaded.

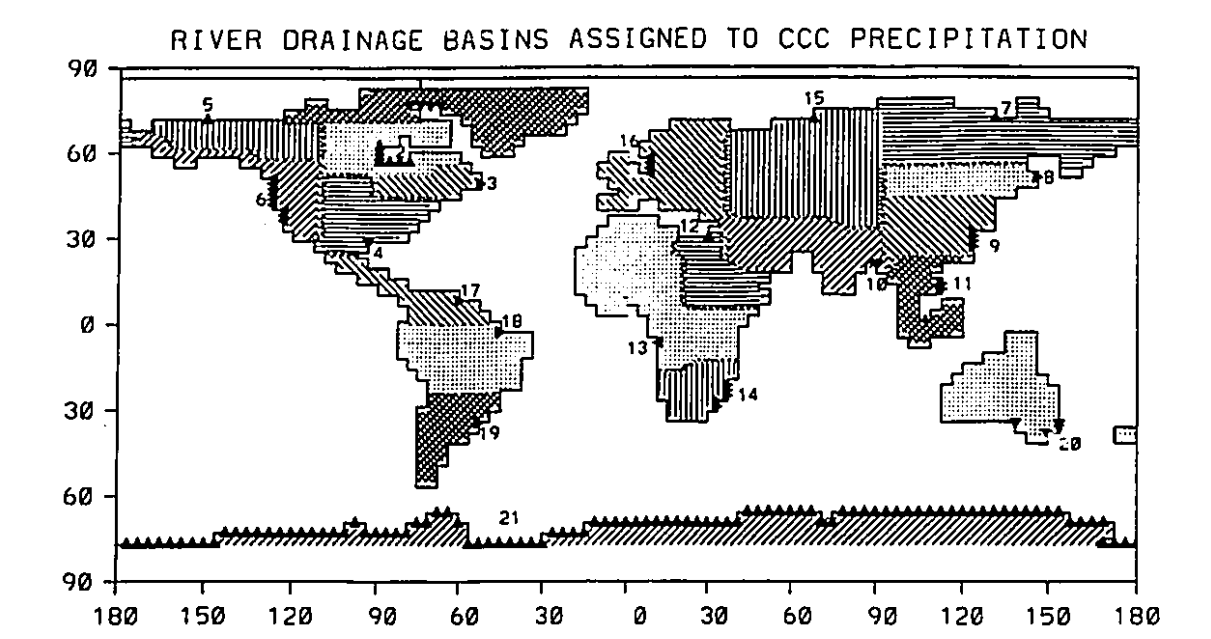


Figure 3.29: River drainage basins assigned to CCC precipitation over land.

				-
G	reenland=1	Lena=7	Congo=13	La Plata=19
Ηι	idson Bay=2	Amur=8	Limpopo=14	Миггау=20
St.	.Lawrence=3	Yangtze=9	Yenisei/Ob=15	Antarctica=21
M	lississippi=4	Ganges=10	Rhine=16	
M	lackenzie=5	Mekong=11	Orinoco=17	
	Columbia=6	Nile=12	Amazon=18	

approximate drainage basins (Fig.3.29) based on an atlas of world topography. (An additional constraint, which forces amalgamation of some drainage basins, is that there must be net precipitation in each region.) Runoff is channeled into the ocean through one or more gridpoints (indicated by triangles in Fig.3.29) located at major river mouths. The net precipitation over Antarctica is distributed semi-uniformly around the edges of the continent.

The CCC wind stresses have been compared to the Hellerman and Rosenstein (1983) climatology (used in Sections 3.1 to 3.3) by G. Flato (personal communication): the model overestimates magnitudes in the Southern Ocean by roughly 30% and underestimates the zonal wind stress in the tropics (most notably the Indian Ocean) by about the same amount. The AGCM also produces easterly flow along the coast of Antarctica which is absent from the observations. The

Canadian Climate Centre's fine resolution ocean model has been spun up under both these wind stress climatologies and restoring boundary conditions (to the modified Levitus fields described earlier): significant differences were found in the Indian Ocean region as anticipated, but very little change in the ACC due to compensation by JEBAR (W. Lee, personal communication). For the heat and freshwater fluxes, a simple test is to zonally and meridionally integrate them to obtain the implied ocean transports at equilibrium. These are illustrated in Fig.3.30: the global ocean heat transport is northward at almost all latitudes, while the Atlantic has southward transport south of about 10°S. The implied freshwater transports are equally difficult to reconcile with the present-day climatology approximated in Section 3.1. Clearly, the incongruities that necessitate massive flux corrections in other coupled climate models (e.g. Manabe et al., 1991) have not been resolved here.

Conclusive evidence, if needed, comes from a test in which the ocean model is spun up for 2000 years under the CCC stresses and buoyancy fluxes. starting from an initial condition which is a 400-year extension of the spin-up under restoring boundary conditions (Section 3.1) with the acceleration of the deep ocean switched off and the Hellerman and Rosenstein (1983) winds replaced by CCC winds. While 2000 years is not long enough to reach equilibrium, it is sufficient to confirm that the atmospheric forcing is incompatible with the ocean model's requirements. The barotropic and overturning streamfunctions are shown in Figs.3.31 and 3.32 (cf. the climatology in Figs.3.3 and 3.4). Deep sinking is occurring in the North Pacific (> 32 Sv) at mid-latitudes, and to lesser depths in the northern Indian Ocean, with upwelling in both the North Atlantic and Antarctic. The temperature and salinity fields are correspondingly poor, and are not shown. Repeating the run without river runoff (i.e. ignoring precipitation over land) to verify that the extemporary drainage basin distribution was not the source of the drift procured some small improvements in the Atlantic, but an overall climatology which was still unacceptable. As a curiosity, the flux corrections F₀, F_H diagnosed from a spin-up under both CCC fluxes and winds, and restoring

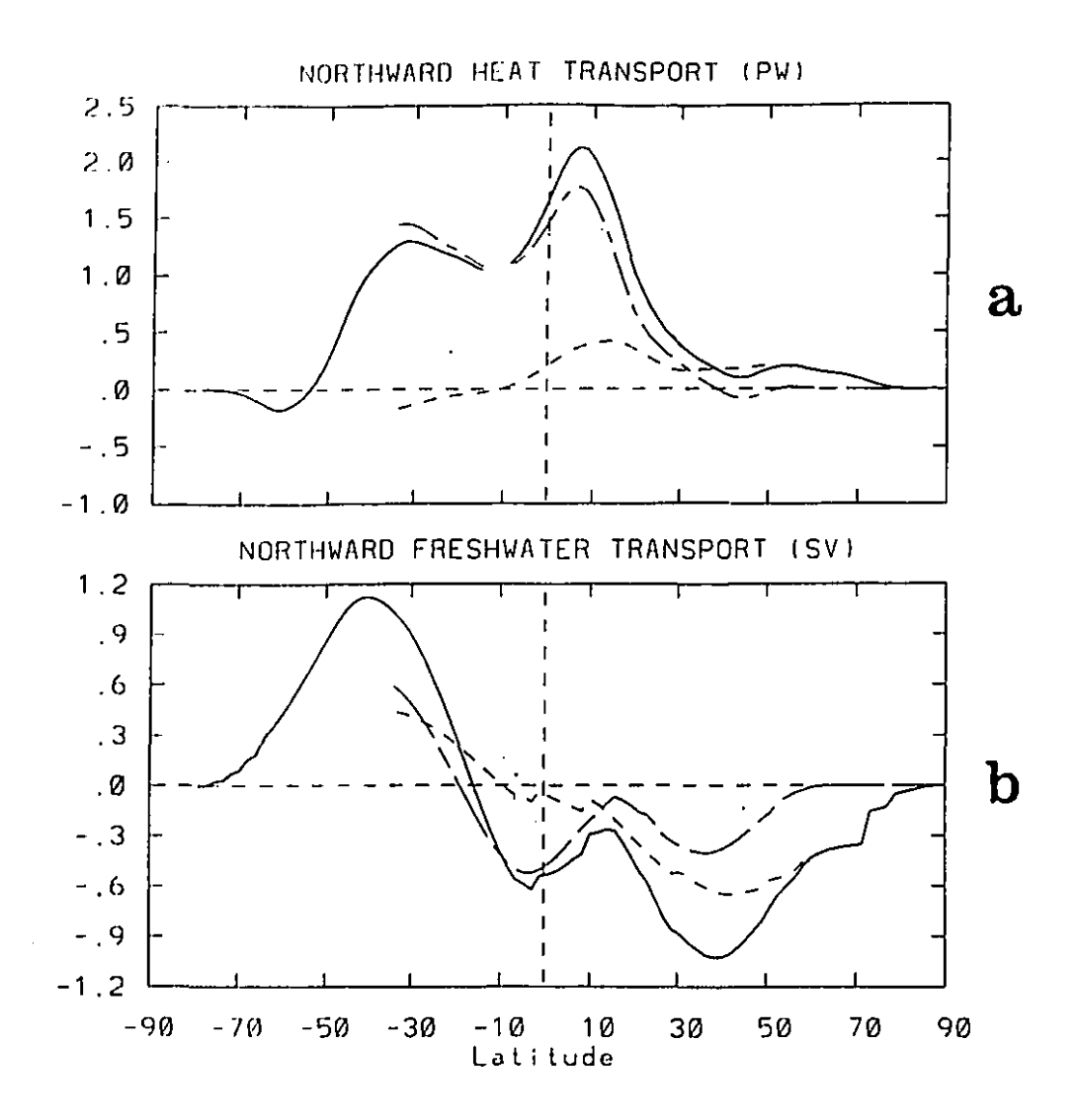


Figure 3.30: Implied meridional ocean transport at equilibrium from the CCC fluxes in Fig.3.28 a) heat (10¹⁵ W) and b) freshwater (Sv). Solid line: global ocean; dashed line: Atlantic; long dashes: Pacific + Indian.

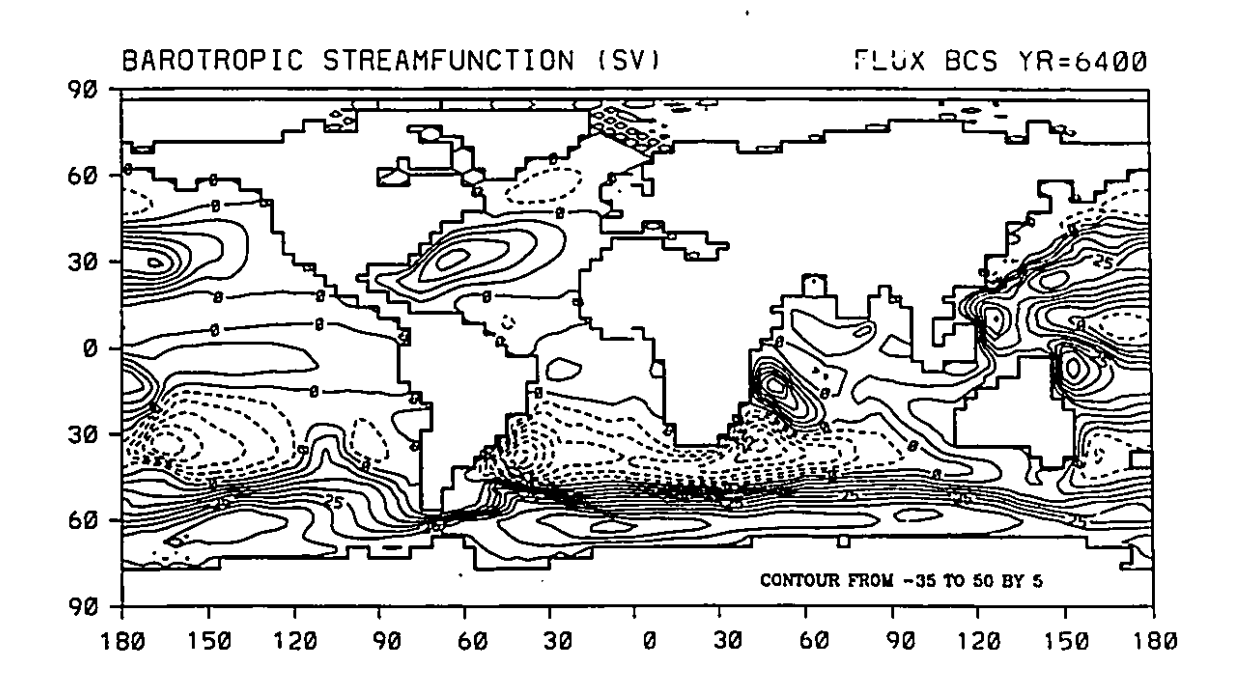


Figure 3.31: Barotropic streamfunction (Sv) at the end of 2000 years under CCC fluxes.

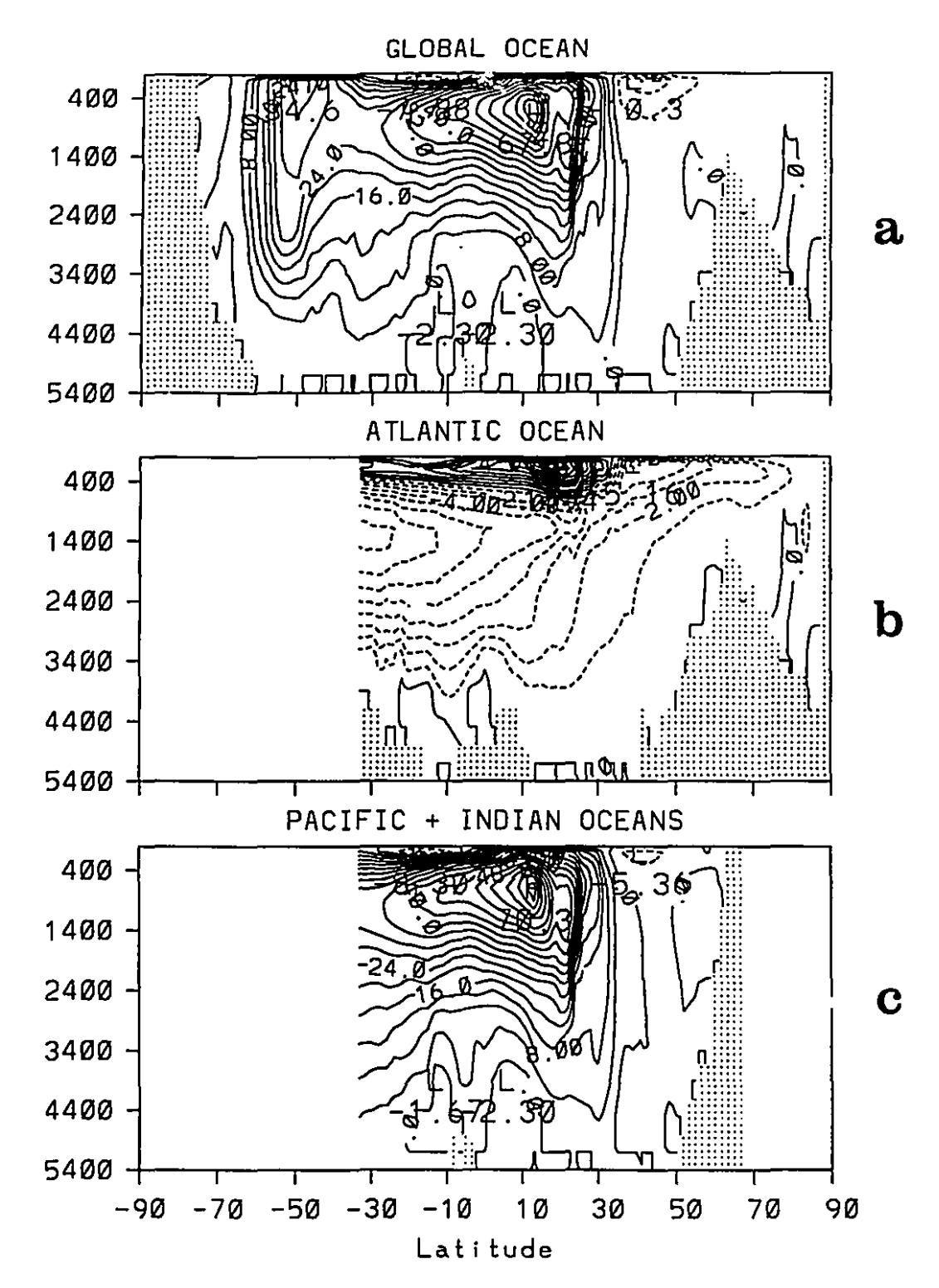


Figure 3.32: Meridional overturning streamfunction (Sv) at the end of 2000 years under CCC fluxes a) global ocean b) Atlantic Ocean c) Pacific and Indian Oceans.

boundary conditions (with λ the usual relaxation constant calculated from the 50-day restoring timescale):

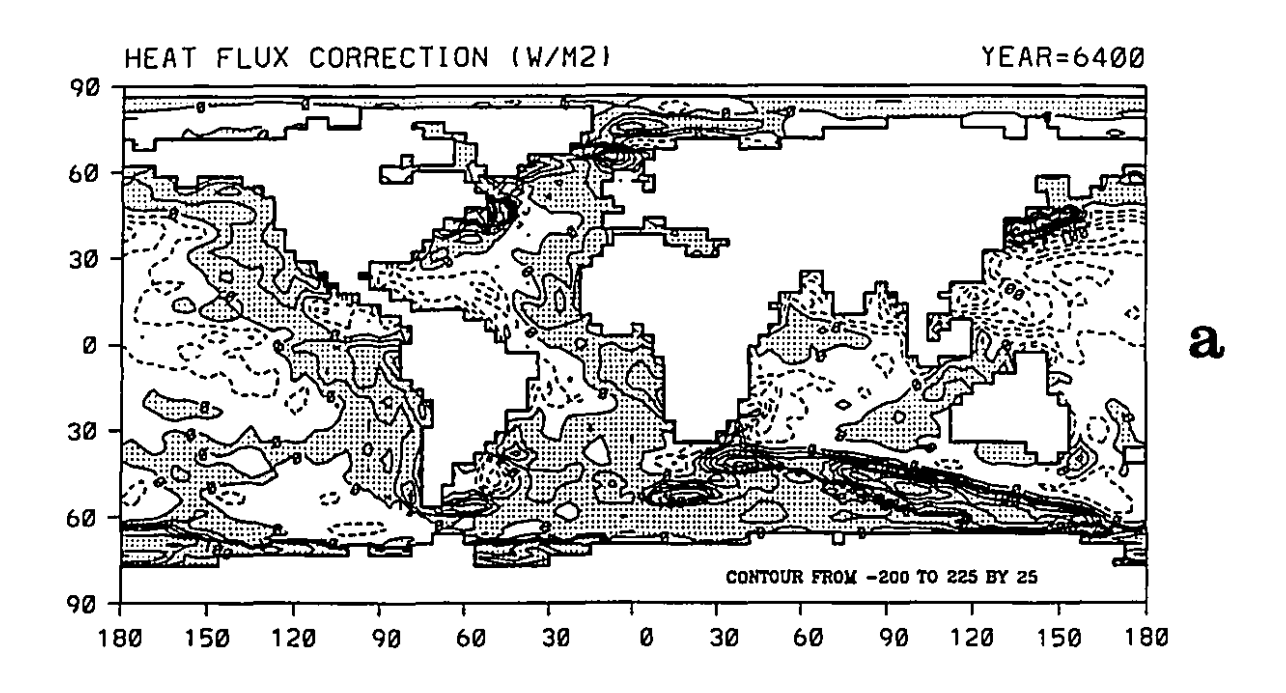
$$Q_{total} = Q_{AGCM} + F_{Q} \quad \text{where} \quad F_{Q} = \lambda (T - T^{*})$$

$$H_{total} = H_{AGCM} + F_{H} \quad \text{where} \quad F_{H} = \lambda (S - S^{*})$$
(3.1)

are shown in Fig.3.33: the magnitudes are comparable to or larger than the uncorrected fluxes in several locations.

Independent confirmation of the implied heat transports has recently been obtained from the AMIP (Atmospheric Model Intercomparison Project) which compared the equilibrium surface fluxes predicted by fifteen different climate AGCMs under identical boundary conditions consisting of observed SSTs and sea ice distributions for 1979-1988 (Gleckler et al., 1994). (The CCC implied heat transports were very similar to those in Fig.3.30 despite the slightly different prescribed surface climatology.) The AGCMs were found to differ not only between themselves, but also from the observations in fundamental ways (eight other models also reported equatorward transport in the southern hemisphere, for example). The large discrepancies between models were attributed to uncertainties in the cloud radiative forcing (Gleckler et al., 1994); in the CCC AGCM, another identified problem is moist convection in the Indonesian region (N. McFarlane, personal communication).

Certainly all the blame for the unconventional circulation in Fig.3.32 should not be placed on the atmospheric model: the ocean model has its own problems. A couple of other possibilities should also be considered: the first is that, as mentioned in Appendix B, the AGCM simulation uses an older SST dataset (Alexander and Mobley, 1976) in its slab ocean. In theory, this could account for some of the differences with the fluxes diagnosed from an ocean model spun up under modified Levitus SSTs. However, both the comparison of the zonally-averaged profiles in Fig.3.34, and the ressemblance between the implied ocean transports in the GCM II run and the AMIP run using different SST climatologies suggests that this is not likely to be a major issue. (It was not attempted to force the ocean model with the Alexander and Mobley (1976) SST



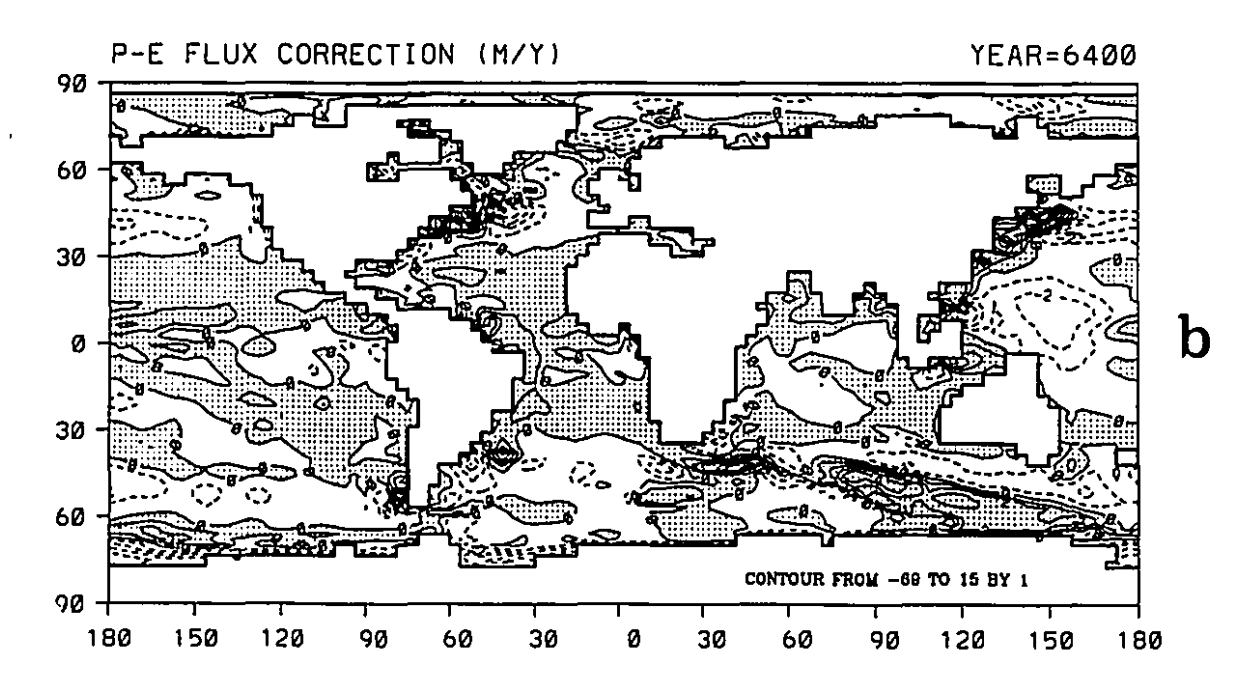


Figure 3.33: Flux corrections required for the CCC fields a) heat (W/m²) b) freshwater (m/y). Positive values are shaded.

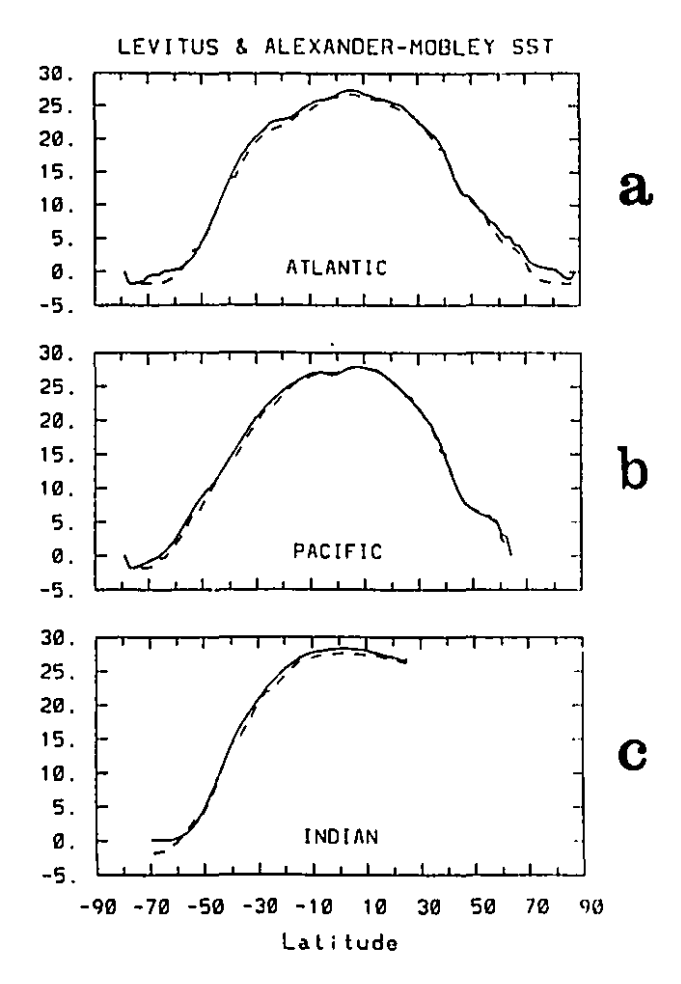


Figure 3.34: Zonally-averaged SST (°C) from the modified Levitus (solid line) and Alexander-Mobley (dashed line) climatologies a) Atlantic b) Pacific c) Indian Oceans.

field since there is no accompanying salinity data.) The second point is that only annual mean forcing has been attempted in this study. The experience of both Myers and Weaver (1992) and Hirst and Cai (1994) was that the inclusion of a seasonal cycle had minimal consequences for the annual mean overturning. Finally, the suggestion may be made that feedbacks in the coupled system will naturally correct the atmosphere-ocean exchange after coupling. While this is certainly an outcome to be hoped for, it seems quite improbable given the nonlinear feedbacks within the ocean's thermohaline circulation (e.g. Bryan, 1986). In conclusion, it would be very difficult to recommend coupling this version of the CCC AGCM to any ocean model without flux corrections.

Thus while mixed boundary conditions are a relatively unsophisticated

representation of the air-sea interaction, coupled atmosphere-ocean models are far from solving all of the problems. A middle way is to develop simpler stripped-down atmospheric models or to refine the simple mixed boundary conditions for climate studies: a small step in this direction will be ventured in the next chapter.

Chapter 4

Sea Surface Temperature - Evaporation Feedback

Mixed boundary conditions have been hallowed as the best first-order representation of the air-sea interaction in uncoupled ocean models, reproducing both the observed fast feedback for sea surface temperatures (SSTs) and the absence of feedback on the sea surface salinities (SSSs). In this chapter, a simple scheme for refining this boundary condition to include the SST-evaporation feedback is proposed. The importance of this feedback is suggested by the nearly linear relationship between observed SSTs and SSSs in the North Atlantic (Fig.4.1, from Duplessy et al., 1991b). Recent work by Zhang et al. (1993) and Rahmstorf and Willebrand (1995) has emphasized the role of another feedback: between SSTs and surface air temperatures. While this feedback is of great interest for climate, for this study the traditional restoring boundary condition on temperature will be accepted uncritically, allowing attention to be focused on the interaction between the ocean's thermohaline circulation and the hydrological cycle. The new parameterization is tested first in a couple of simple perturbation experiments in one-hemisphere box models, and then applied to three case studies taken from

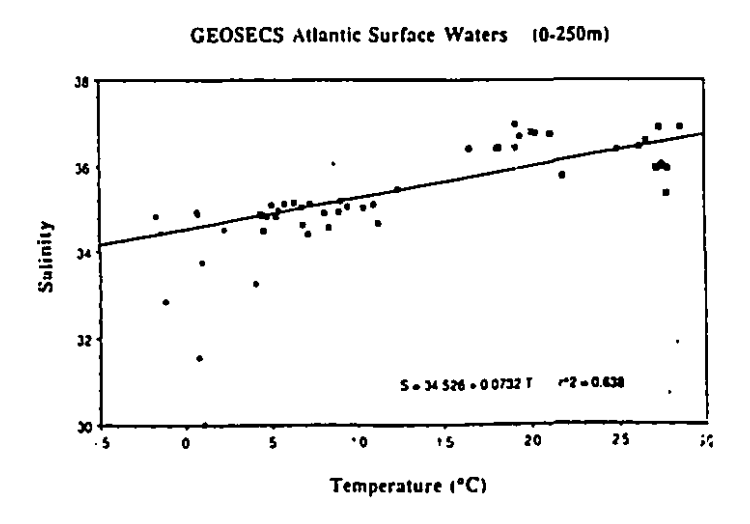


Figure 4.1: Observed sea surface salinity (psu) versus sea surface temperature (°C) in the North Atlantic (reproduced from Duplessy et al., 1991).

Weaver et al. (1993) and featuring internal variability of the thermohaline circulation on decadal, century and millennial timescales.

4.1. Diagnosing Evaporation from the Surface Heat Flux

The net heat flux at the ocean's surface is quite generally the sum of four components: the shortwave and longwave radiation (SW, LW) plus the latent and sensible heat losses (LH, SH).

$$Q = (SW + LW) + (LH + SH)$$
 (4.1)

In the present idealized study, the solar radiation SW will be taken as constant, neglecting clouds and seasonal forcing. The net longwave flux out of the ocean may be expanded in a Taylor series about the surface air temperature T_A , following Haney (1971):

$$LW = g(T_A)\sigma T_A^4 + 4g(T_A)\sigma T_A^3(T_O - T_A)$$
 (4.2)

where $g(T_A)$ is a function of T_A , and the second term, due to fluctuations in sea surface temperature T_O , is two orders of magnitude smaller than the first (Haney, 1971). The use of a fixed restoring temperature under mixed boundary conditions amounts to assuming a stationary atmosphere; it is consistent with this to therefore simply prescribe a fixed longwave contribution. The first two terms in the budget can then be collapsed into a single one, $R(\phi)$, the net radiation specified as a function of latitude. The remaining two terms can also be combined by means of the Bowen ratio B=SH/LH. Strictly speaking, the Bowen ratio should be a function of the saturation specific humidities at both T_O and T_A (or to be completely correct, the dew point temperature T_d), but at the present level of approximation, it is both sufficient and appropriate to merely take into account the colder and drier atmosphere at increasing latitudes. This property, together with the Clausius-Clapeyron relation, can be expressed through a fixed Bowen ratio increasing exponentially with latitude, causing latent heat fluxes to be strongly favoured over sensible at low latitudes, but less strongly at high latitudes.

As a consequence of these assumptions, it is now possible to diagnose the evaporation at each timestep from the net surface heat flux calculated from the restoring boundary condition, as follows:

$$E(\lambda, \phi) = \frac{1}{\rho_w L} \frac{(Q - R)}{(1 + B)}$$
(4.3)

where L is the latent heat of evaporation, ρ_w is the density of water, $R(\phi)$ and $B(\phi)$ are the latitude-dependent net radiation and Bowen ratio as described above, and $Q(\lambda,\phi)$ is the net upward surface heat flux = $\rho_w C_p \Delta z (T_O - T_A)/\tau$ (if C_p is heat capacity of water, Δz is upper-layer thickness and τ is the restoring timescale).

There remains the dilemma of how to predict precipitation without either a moisture transport equation or a cloud parameterization scheme (not to mention imaginary geography and flat orography in the box model geometries used below). The least complicated and therefore the most reasonable solution that could be found was to impose an extra constraint: that of satisfying the equilibrium (P-E) field from the spin-up under restoring boundary conditions. The equilibrium evaporation is known from equation (4.3), hence the equilibrium precipitation is simply the sum:

$$(P)_{eq} = (P-E)_{eq} + (E)_{eq}$$
 (4.4)

A second decision must however be made in anticipation of new precipitation created as the sea surface warms or cools. Again, there is no perfect way. A number of simple schemes are therefore implemented, and the results are compared to determine whether general conclusions can be drawn. Six such schemes characterized by varying degrees of complexity are described below. While none among them can pretend to be realistic, two properties help to distinguish some among them from complete ideality. The observed large-scale moisture transport in the atmosphere has well-defined latitudes of convergence and divergence near the equator and in the subtropics, respectively, and fluxes two or three times larger in the zonal than in the meridional direction (Peixoto and Oort, 1992). These two features have been incorporated into the majority of the six schemes. Briefly then, new precipitation is redistributed in one of the following

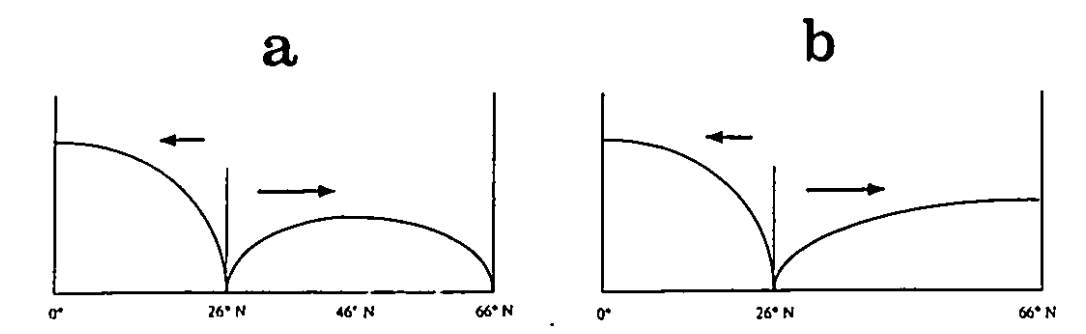


Figure 4.2: Redistribution schemes for new P a) scheme 3 b) scheme 4.

ways (a single hemisphere basin in the northern hemisphere is assumed throughout):

- I) uniformly over the basin;
- 2) uniformly around latitude circles;
- 3) dividing the basin into two regions, new evaporation is summed separately over the areas south and north of 26°N (the approximate latitude of the subtropical divergence). The new low latitude evaporation is returned to the ocean as new precipitation distributed uniformly (in m/y) over a cosine function between 0° and 26°N, while the high latitude evaporation is redistributed over a similar profile centered at 46°N (Fig.4.2a);
- 4) similar to (3), except that the high latitude precipitation is directed further poleward by centering the cosine function at the northern boundary of the basin (Fig.4.2b);
- 5) new evaporation is transported zonally in a direction and over a distance proportional to the eastward wind stress, and meridionally over a fixed distance in a direction either southward or northward depending on whether the original latitude is south or north of 26°N. Precipitation is distributed over a Gaussian function centered at the new latitude and longitude, or reflected back into the ocean domain if the predicted coordinates fall over land.
- 6) new precipitation is distributed non-uniformly over the whole basin, weighted according to the equilibrium precipitation field. As a function of time t:

$$P_{total}(x,y,t) = P_{eq}(x,y) + P_{new}(x,y,t) = C(t)P_{eq}(x,y)$$
 (4.5)

where the scalar C(t) is given by the sum over the basin of the total (new + equilibrium) evaporation divided by the sum of the equilibrium evaporation:

$$C(t) = \frac{\sum (E_{eq}(x,y) + E_{new}(x,y,t))}{\sum E_{eq}(x,y)}$$
(4.6)

The normalization of C(t) ensures conservation of water vapour by the anomalous evaporation and precipitation.

In summary, the six parameterizations do differ significantly so that a comparison between results obtained with them is a good test of the sensitivity to the choice in any particular experiment.

4.2. Role and Importance of the Evaporative Feedback

To establish confidence in the parameterization, an initial spin-up is carried out under mixed boundary conditions with a prescribed (P-E) profile adapted from observations. The annual mean zonally-averaged data of Baumgartner and Reichel (1975) is used to construct a zonally-uniform field with a realistic amplitude and meridional variation (Fig.4.3). The restoring temperatures are interpolated from

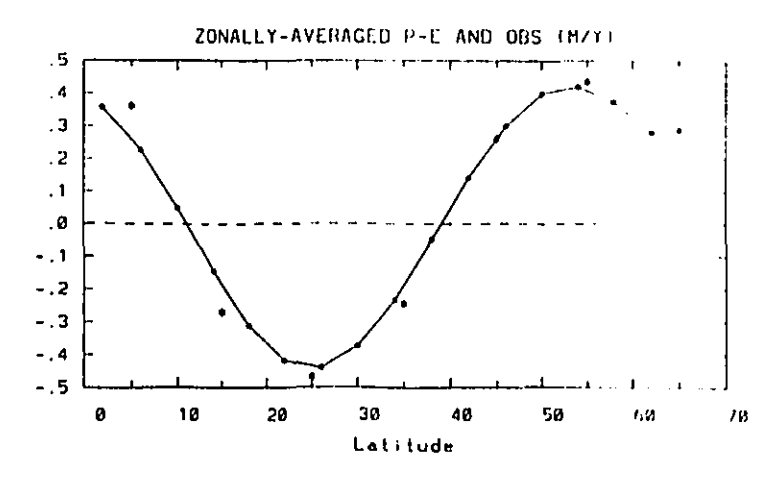


Figure 4.3: Zonally-averaged observed (P-E) (m/y) from Baumgartner and Reichel (Peixoto and Oort, 1992, p.171) and fitted curve. The data are averaged over both hemispheres and plotted as stars, while the nodes on the curve mark the latitudes of gridpoints.

zonally-averaged Levitus (1982) data for the surface ocean (Fig.4.4a), and an analytical formula from Marotzke (1990) is used for the meridional profile of zonal winds (Fig.4.5). Numerical parameters for the box ocean are given in Table 4.1.

The equilibrium overturning under these boundary conditions is a respectable 15.6 Sv; however the range of surface salinities obtained is too small (Fig.4.6). This is a common deficiency in spin-ups under prescribed climatological (P-E) profiles (e.g. Winton, 1993), due both to the zonal uniformity of the salt flux field and to the two reasons mentioned in the previous chapter: missing hydrological processes, and large horizontal diffusion in the ocean model. The zonally-averaged surface heat flux at equilibrium is shown in Fig.4.7: the magnitudes and equator-to-pole variation are again surprisingly reasonable (compared to Oberhuber (1988) for example) given that the restoring boundary condition was never formulated for such an intention.

The equilibrium evaporation is estimated using the radiation and Bowen ratio profiles illustrated in Fig.4.8a,b, which are cosine and exponential fits respectively to annual mean observations over the oceans in Budyko (1982, p.64). The zonally-averaged evaporation is depicted in Fig.4.9a, along with the observed values from Baumgartner and Reichel (1975): the magnitudes are a little large but in the right approximate range, and decrease poleward as desired. It would be tempting to attribute the discrepancy in magnitude to the ocean-only world in the model while the observed values are averaged over both land and ocean, but in fact the parameterization is not good enough to justify such faith. The equilibrium precipitation is shown in Fig.4.9b: the magnitudes and latitudinal dependence are again satisfactory (in particular, the subtropical desert between the equatorial and high latitude precipitation maxima stands out well). Although the bias in both P and E compared to Baumgartner and Reichel is systematic, it was preferred not to tune them by altering the radiation or Bowen ratio profiles since these were physically chosen and the error in observations of P or E over the ocean is so large (e.g. Blanc, 1985).

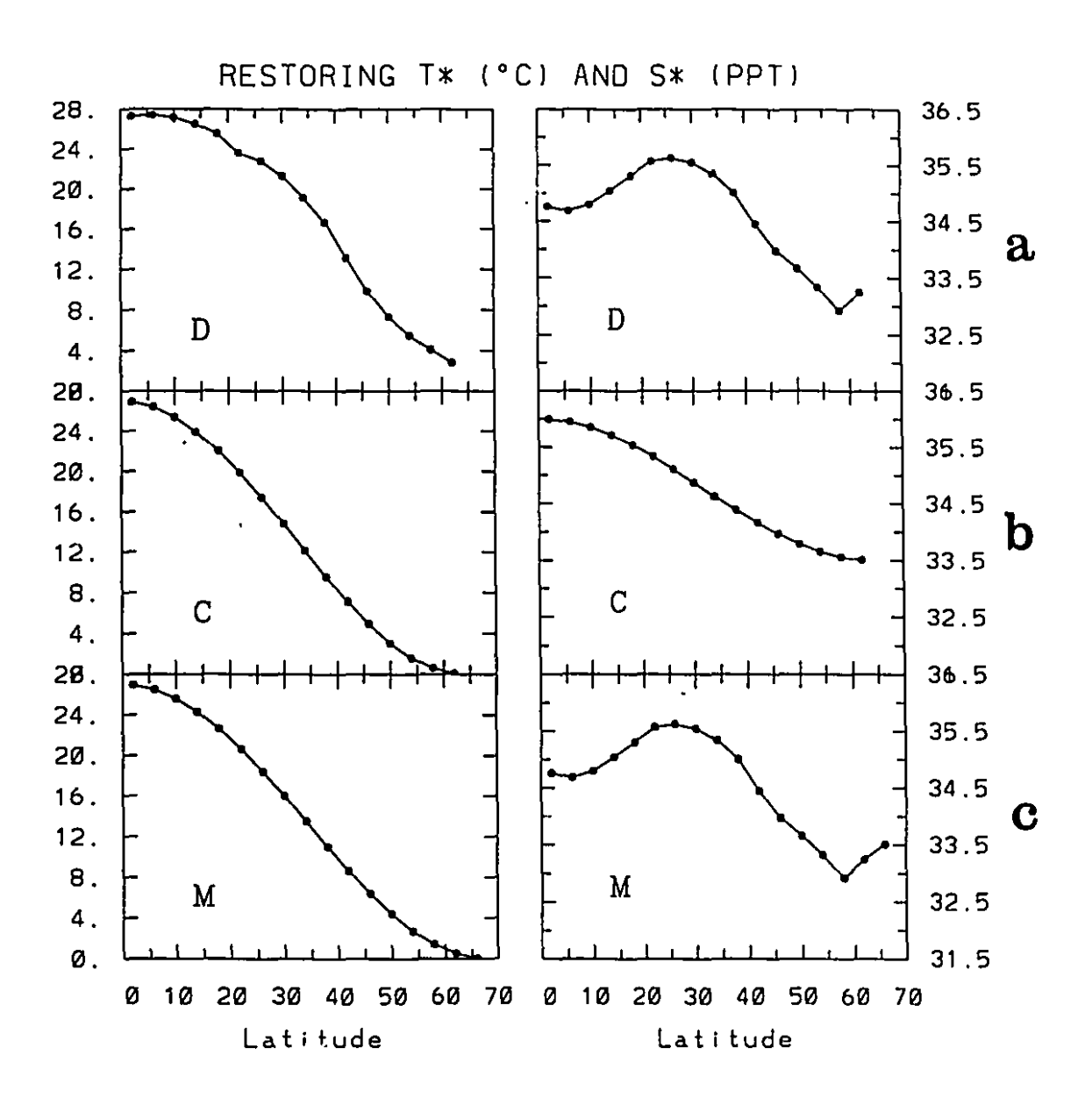


Figure 4.4: Restoring temperatures (°C) and salinities (ppt) for all experiments in this chapter. In the decadal variability spinup (D), zonally-averaged surface temperatures and salinities (both hemispheres combined) from Levitus (1982) are used. In the century timescale variability spinup (C), both temperature and salinity follow half-cosine curves decreasing from 27°C and 36 ppt at the equator to 0° and 33.5 ppt at the northern boundary. In the millenial variability spinup (M), a cosine curve is used for the temperature and Levitus zonally-averaged data for the salinity. The preliminary experiments in Section 4.2 use the same restoring temperatures as the decadal spinup.

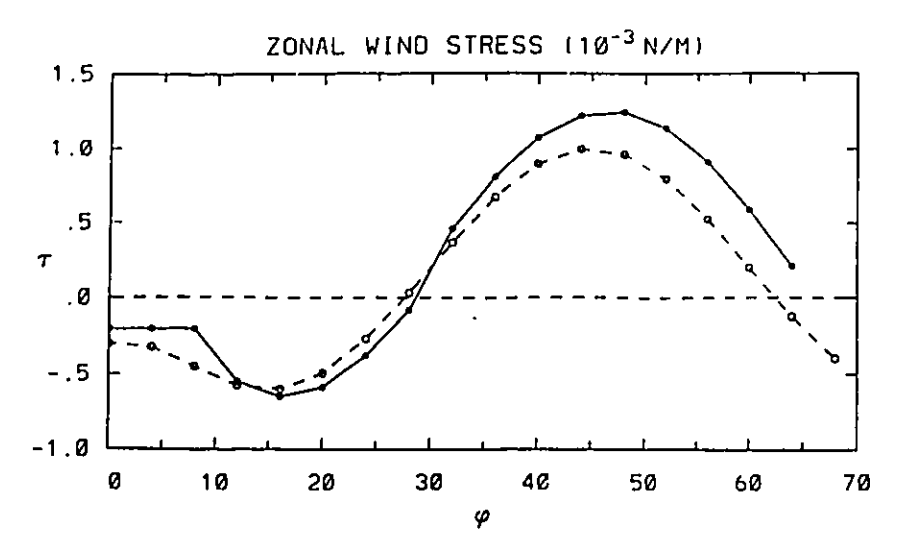


Figure 4.5: Meridional profiles of zonal wind stress (10⁻³ N/m) used in this chapter. The preliminary experiments, the decadal runs, and the century runs use the analytic profile of Marotzke and Willebrand (1991), in black circles, and the millennial runs use the analytic profile of Bryan (1986), in white circles.

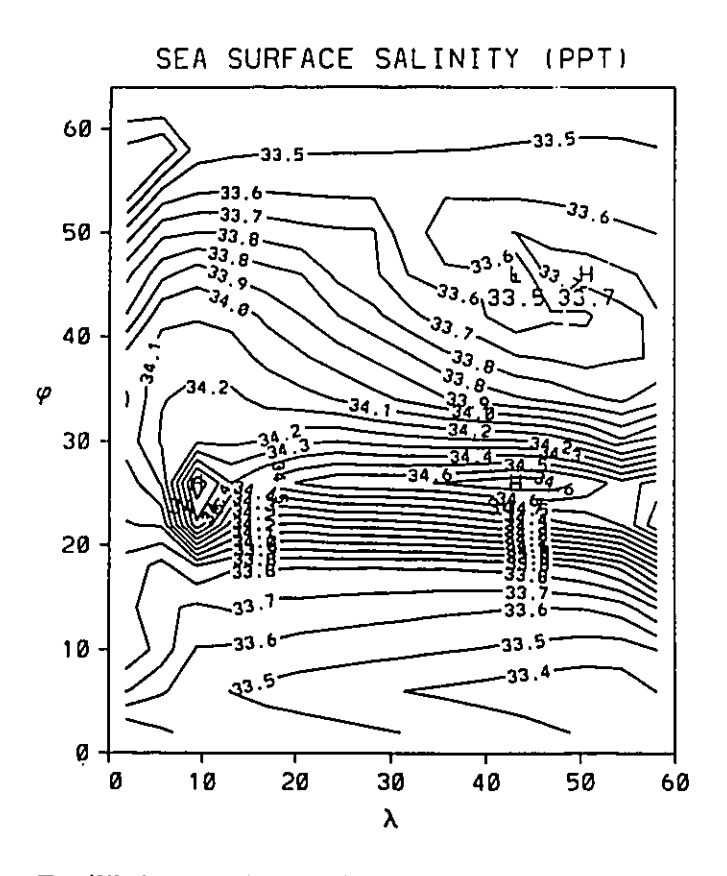


Figure 4.6: Equilibrium surface salinity (ppt) distribution in the spinup under fixed observed (P-E).

Table 4.1. Numerical Parameters for Spin-ups An Chapter 4

numerical model: Cox (1984)

Preliminary Spin-up under Fixed (P-E)

basin geometry: 60° wide, 0-64°N, flat bottom

resolution: zonal: 3.75°

meridional: 4°

vertical: 15 levels (depths in m: 50, 125, 225, 350, 500, 700, 959, 1250, 1650, 2100, 2550, 3000, 3500, 4000,

4500)

length of spin-up: 2998 years

timesteps: barotropic vorticity: 2 hours

tracer: 5 days

eddy mixing coefficients:

 $A_{MH}=2.5\times10^5 \text{ m}^2/\text{s}$

 $A_{MV}=1.x10^{-4} \text{ m}^2/\text{s}$

 $A_{TH}=1.x10^3 \text{ m}^2/\text{s}$

 $A_{TV}=5.x10^{-5} \text{ m}^2/\text{s}$

boundary conditions:

wind stresses: analytic profile of Marotzke and Willebrand (1991)

(see Fig.4.5)

restoring T*: zonally-averaged annual mean Levitus SST (averaged

over both hemispheres)

restoring timescale: 40 days

(P.E): meridional profile fitted to zonally-averaged-annual-mean

global (land + ocean, both hemispheres combined) data from

Baumgartner and Reichel (1975) (Peixoto and Oort, 1992,

p.171

Decadal Variability Spin-up

basin geometry: same as above resolution: same as above length of spin-up: 3997 years timesteps: same as above eddy mixing coefficients: same as above

boundary conditions for spin-up:

wind stresses: same as above restoring timescale: 25 days

restoring T* and S*: zonally-averaged annual mean Levitus SST

and SSS (averaged over both hemispheres)

method of diagnosing heat and salt fluxes at equilibrium: 20-

year average

initial condition for mixed boundary conditions experiment: resting, homogeneous ocean

Century Timescale Variability Spin-up

basin geometry: same as above resolution: same as above length of spin-up: 3997 years timesteps: same as above eddy mixing coefficients: same as above

boundary conditions for spin-up: wind stresses: same as above.

restoring timescale: 30 days

restoring T* and S*: half-cosine profiles from 0 to 27°C and

36.0 to 33:5 ppt

method of diagnosing heat and salt fluxes at equilibrium: 20-

year average

initial condition for mixed boundary conditions experiment; end of spin-up under restoring boundary conditions:

Millennial Variability Spin-up

basin geometry: 60° wide, 0-68°N, flat bottom, symmetry condition

at equator

resolution: zonal: 3.75°

meridional: 4°

vertical: 23 levels (depths in m: 50, 100, 150, 200, 250, 300, 350, 400, 475, 575, 700, 850, 1025, 1225, 1450, 1700, 2000, 2350, 2750, 3150, 3550, 4000, 4500)

length of spin-up: 1999 years

timesteps: barotropic vorticity: 2 hours

tracer: 2.5 days

eddy mixing coefficients:

 A_{MH} : 2.5x10⁵ m²/s

A_{MV}: 1.x10⁻³ m²/s A_{TH}: 2.x10³ m²/s

 A_{TV} (k_v): 1.x10⁻⁴ m²/s

boundary conditions:

wind stresses: analytic profile of Bryan (1986)

(see Fig.4.5)

restoring T*: half-cosine profile from 0 to 27°C

restoring S*: zonally-averaged annual mean Levitus SSS

(averaged over both hemispheres)

restoring timescale: 25 days

method of diagnosing heat and salt fluxes at equilibrium:

instantaneous

initial condition for mixed boundary conditions experiment: end of spin-up under restoring boundary conditions

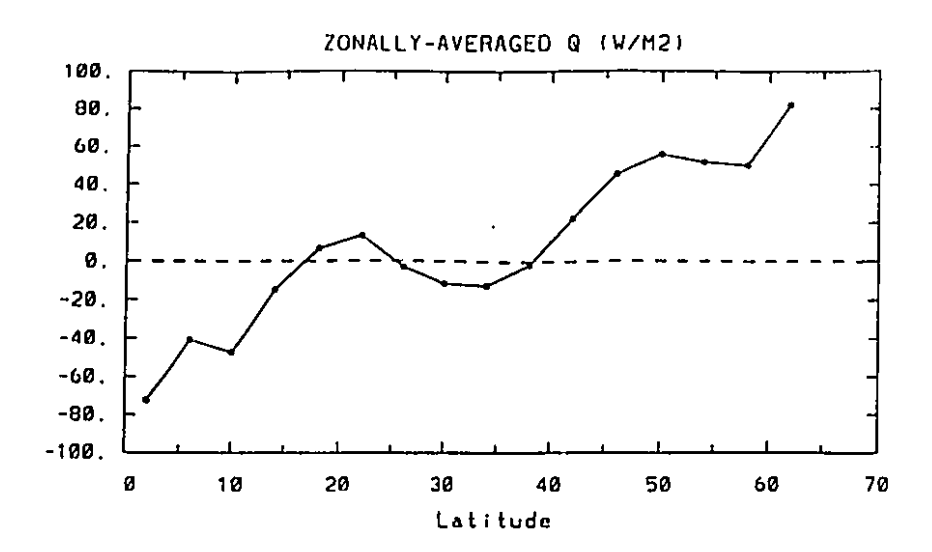


Figure 4.7: Zonally-averaged diagnosed surface heat flux (W/m²) for the spinup under fixed observed (P-E).

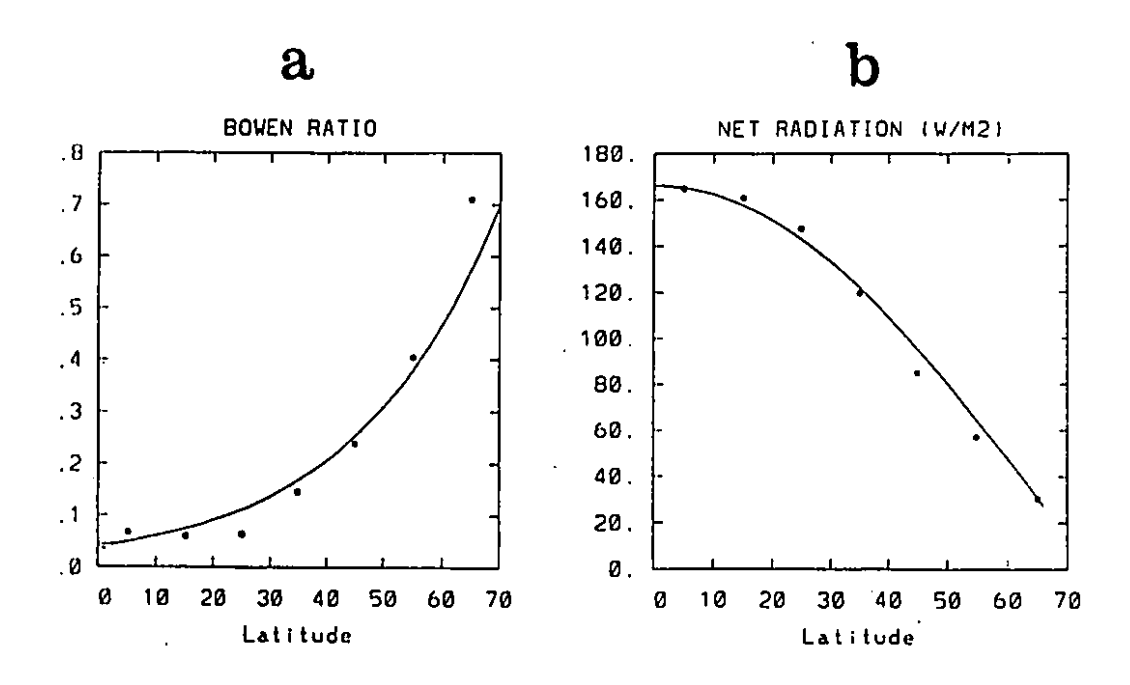
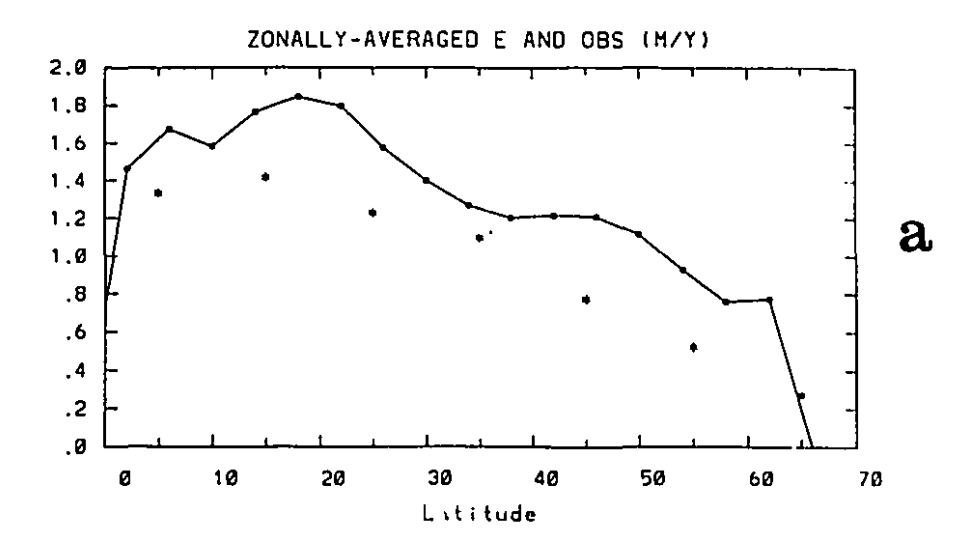


Figure 4.8: a) Bowen ratio over the ocean as a function of latitude: observed data (stars) from Budyko (1982, p.64, both hemispheres combined) and fitted profile (solid curve). b) similarly for the net radiation into the ocean's surface, $-R(\phi)$, as a function of latitude.



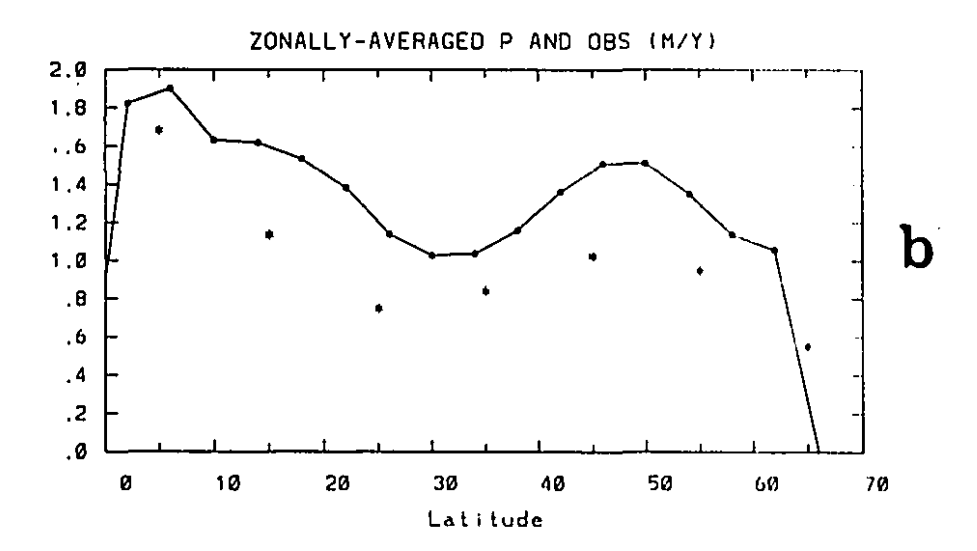


Figure 4.9: Zonally-averaged equilibrium evaporation and precipitation (m/y) estimates for the spinup under fixed observed (P-E), and observed values (stars) from Baumgartner and Reichel (Peixoto and Oort, 1992, p.171).

The horizontal distributions of P and E are shown in Fig.4.10, and may be compared with global maps of the observed fields reproduced in Fig.4.11 (from Peixoto and Oort, 1992). The evaporation distribution is not displeasing, with a maximum in the western boundary current and peak values near 2 m/y just north of the equator, although the midlatitude maximum is too strong. It must be recognized however that this is not entirely for the right physical reasons: the western boundary maximum in the model for example exists only because of poleward heat transport in the ocean while in the real world this would be a centre of high evaporation even in the absence of ocean currents due to the advection of cold dry continental air over the oceans. The precipitation map looks very like the evaporation: this is unfortunate, if unavoidable, as it reflects the fact that the (P-E) is a small quantity compared to either the P or E. Overall however, the inferred P and E fields are good enough to continue with the parameterization.

4.2.1. Preliminary Experiments

Two preliminary experiments are therefore performed to assess the role and magnitude of the evaporative feedback. A perturbation in the meridional overturning circulation is produced through a salt flux anomaly (0.01 Sv distributed uniformly across the northernmost row of grid boxes for twenty years) of either positive or negative sign, accelerating the overturning to nearly 21 Sv in the former case and decelerating it to about 11 Sv in the latter. The flux anomaly is then removed, and the response of the ocean as it adjusts back towards equilibrium is monitored.

In Fig.4.12, a time series of the maximum overturning in the basin is shown for two runs starting from the accelerated initial condition (after the positive salt flux anomaly): one under the standard mixed boundary conditions and the other with the new feedback. The precipitation redistribution scheme used is the first one - the other five possibilities are not illustrated as results are almost

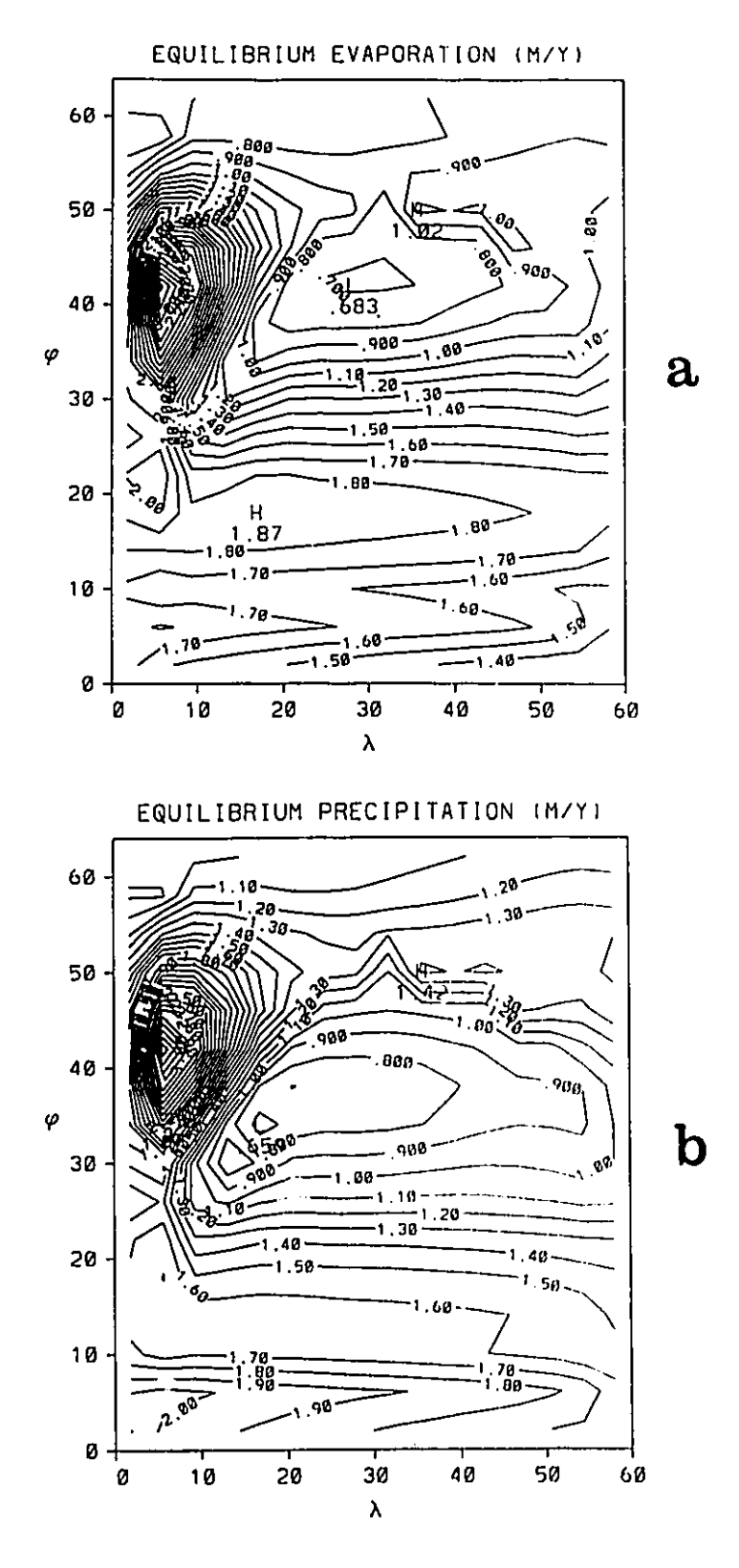
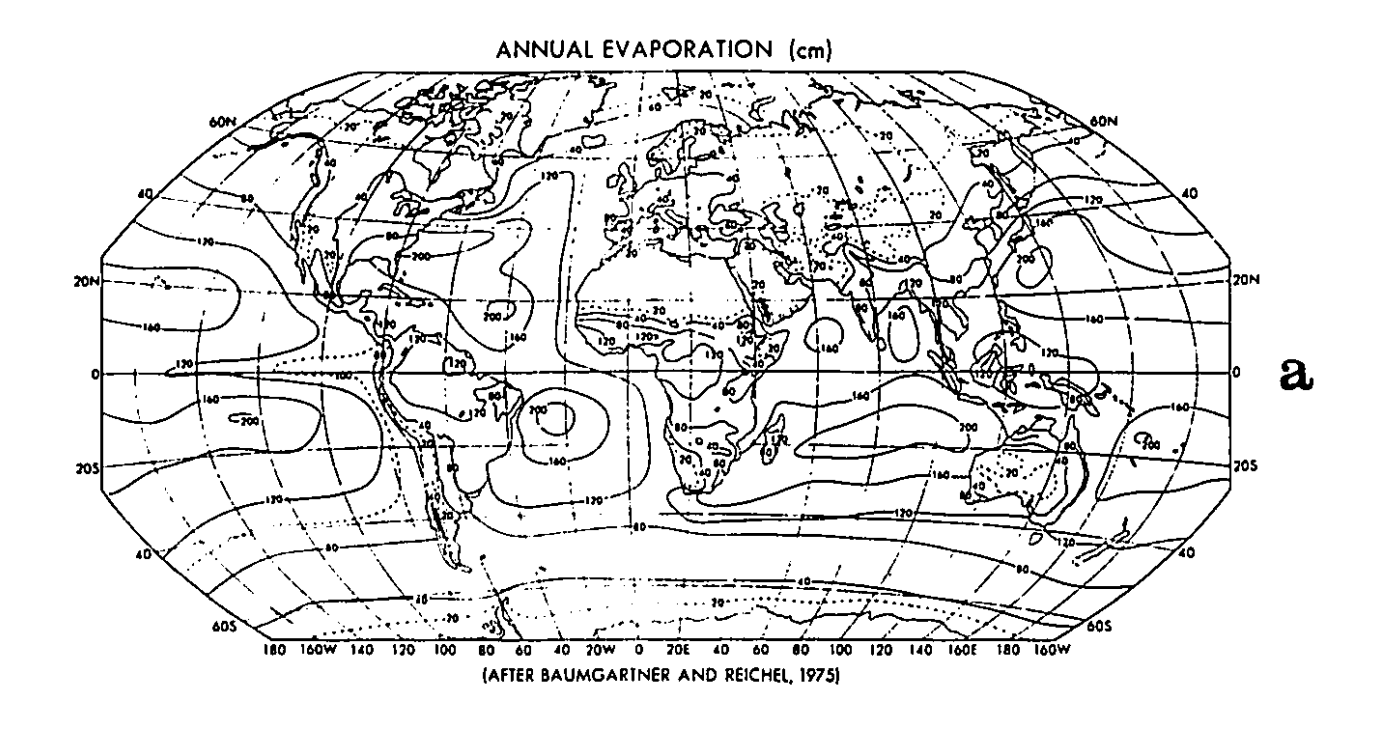


Figure 4.10: Equilibrium a) evaporation and b) precipitation (m/y) estimates for the spinup under fixed observed (P-E).



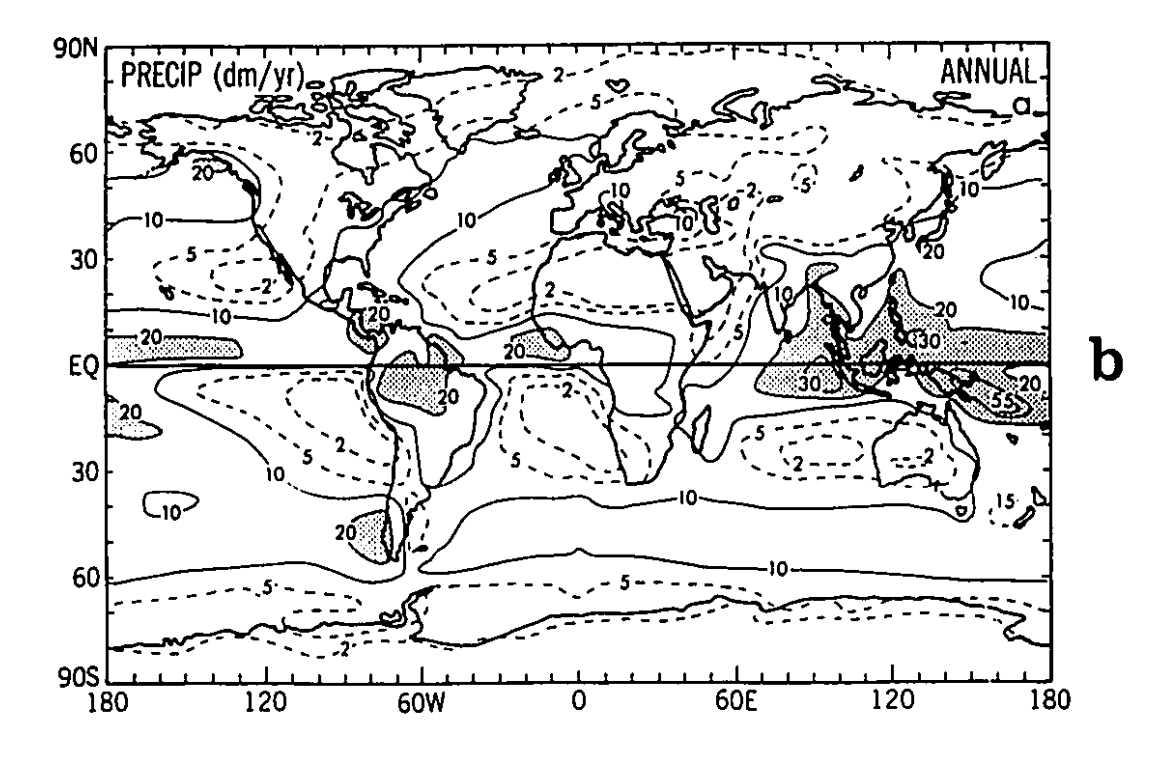


Figure 4.11: Observed global annual mean a) evaporation (cm/y) and b) precipitation (dm/y) distributions, reproduced from Peixoto and Oort (1992).

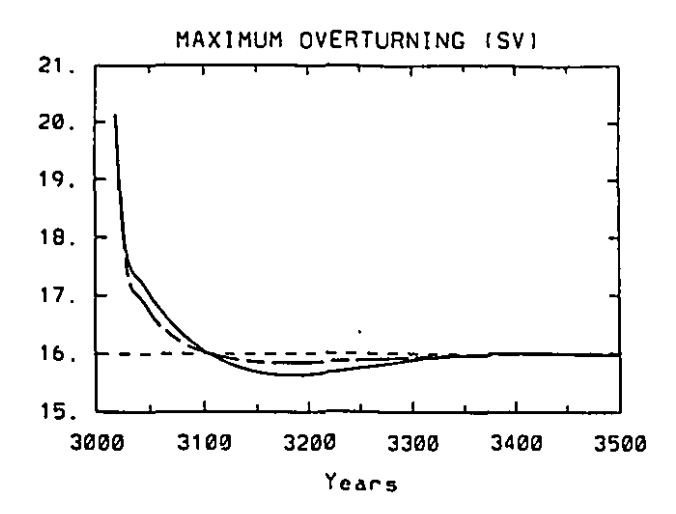


Figure 4.12: Maximum overturning (Sv) as a function of time in preliminary experiment with initially accelerated overturning (dashed line: under mixed boundary conditions; solid line: with SST-evaporation feedback and precipitation scheme 4).

identical. There is in fact very little difference even between the two runs in Fig.4.12, and by 500 years, both have returned to a state very similar to the spin-up equilibrium. A closer look reveals, however, an amplification of the response under SST-evaporation feedback. That is, the overturning is stronger/weaker in the run with evaporation than in the control run when the latter is accelerated/decelerated compared to equilibrium.

The positive sign of the feedback can be understood as follows: a positive perturbation to the thermohaline circulation warms the high latitudes through advection, increasing the surface heat flux out of the ocean and hence the evaporation. This raises the sea surface salinity which feeds back on to the enhanced overturning. The increased poleward heat transport does also cool the low latitudes but the largest changes in SST are almost always at high latitudes or along the western boundary, more specifically in convective areas. Negligible changes in the equatorial SSTs reflect the dominance of the wind-driven upwelling, which is essentially fixed through time. (One of the later experiments

¹ Multiple equilibria are however a possibility under the mixed boundary conditions, and the altered salt content due to the external perturbation is another factor that conceivably might cause the final equilibrium to differ from the steady state at the end of the spin-up.

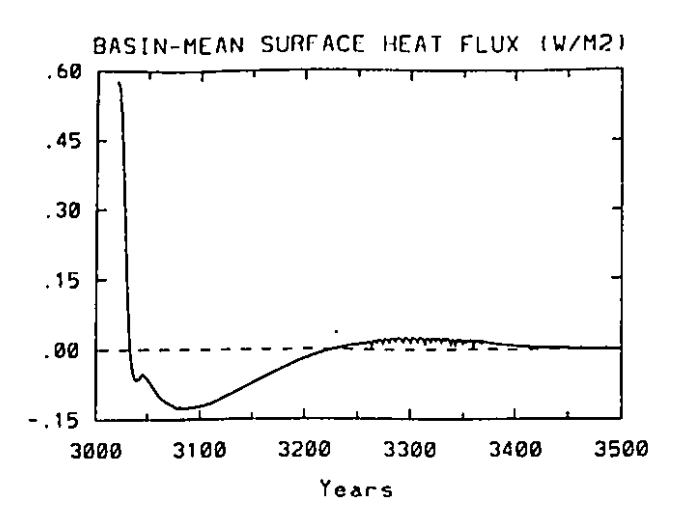


Figure 4.13: Basin mean surface heat flux (W/m²) as a function of time in preliminary experiment with initially accelerated overturning and SST-evaporation feedback with precipitation scheme 4.

starting from the initial condition with decelerated overturning, where the response is stronger, was in fact repeated setting all new evaporation south of 26°N to zero: the results were almost identical to the run with evaporation everywhere, from the time series of maximum overturning or basin-mean surface heat flux.)

The feedback is a little more complicated than this of course. equilibrium basin-mean surface heat flux is very close to zero so, from the comments above, the non-zero heat flux following the perturbation can be more or less identified with SST anomalies at high latitudes, with positive values indicating a warm anomaly and so on. The time series of basin-mean surface heat flux in Fig.4.13 changes sign before the streamfunction crosses below its asymptotic value, suggesting that the high latitude SSTs are not simply responding to advective changes in heat transport. (The sign of the mean heat flux is also a good indicator of the sign of new evaporation (increase or decrease with respect to E_{co}), although the latitude-dependent Bowen ratio prevents a linear proportionality between the two quantities.) A more ubiquitous complication is the new precipitation, which could invalidate the chain of reasoning from warm SSTs directly to enhanced SSSs. But because all of the precipitation schemes in Section 4.1 transport evaporated moisture away from its source and dilute it by spreading it over larger areas, the new (P-E) field tends to look very like the new E with only a small offset due to new P. In contrast, the new evaporation acts locally and in just those crucial areas where the circulation is changing.

The specific mechanism for the dispersal of the salty anomaly in the enhanced overturning experiments in Fig.4.12 is very much analogous to the beginning of a loop oscillation (Welander, 1986; Winton, 1993). The anomaly, initially in the surface ocean at high latitudes, shoots down the convective pipe to the deep ocean, where it is advected slowly around with the overturning circulation (Fig.4.14). While it is in the northern half of the basin, it speeds up the overturning (Fig.4.15a), but by the time it crosses into the southern half of the basin, only the low-latitude portion of the deep overturning is still being accelerated, and the high latitude circulation (where the peak value is located) is decelerated relative to equilibrium (4.15c). The anomaly does not penetrate up through the thermocline at the equator so the oscillation dies out after only half a cycle. (In contrast, persistent loop oscillations are apparently relatively easily excited in two-dimensional models, e.g. Winton, 1993, Mysak et al., 1993, L. Zhang, personal communication, but this may also reflect different (P-E) fields.)

The magnitude of the new evaporation is small in the runs with the accelerated overturning initial condition, with local maxima of less than 0.15 m/y even in the early years when the adjustment is the most vigorous. In the experiments starting from reduced overturning, the response is more dramatic. Two time series of maximum overturning are shown in Fig.4.16 for the control run under mixed boundary conditions and the evaporation feedback run using precipitation scheme 6 (the other five experiments are qualitatively similar). The recovery is slower after the fresh anomaly than after the salty anomaly (nearly one thousand years versus a few hundred years in Fig.4.12), and all of the runs with evaporative feedback permanently overshoot the original level of overturning. The slower timescale comes from the interruption of high-latitude convection: the fresh surface anomaly shuts down the fast pipe to the deep ocean. This is also the explanation for the larger response: the salty anomaly eliminates itself while the fresh anomaly lingers at the surface and continues to interact with the SST

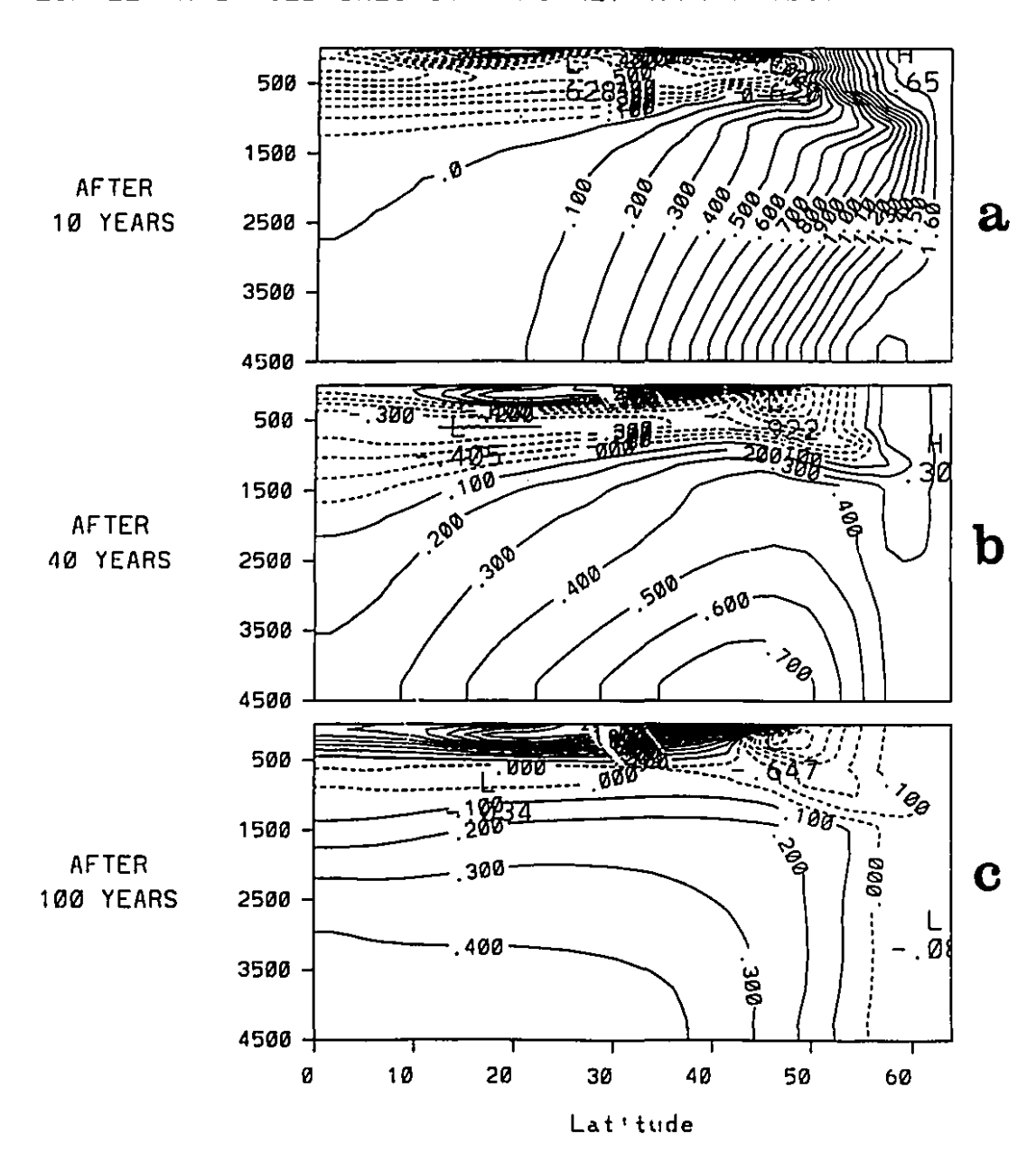


Figure 4.14: Propagation of zonally-averaged salinity (ppt x 100) anomaly (perturbation experiment minus spinup final equilibrium) in meridional plane in salty anomaly experiment with SST-evaporation feedback and precipitation scheme 4.

ZONALLY-AVERAGED STREAMFUNCTION ANOMALY (SV)

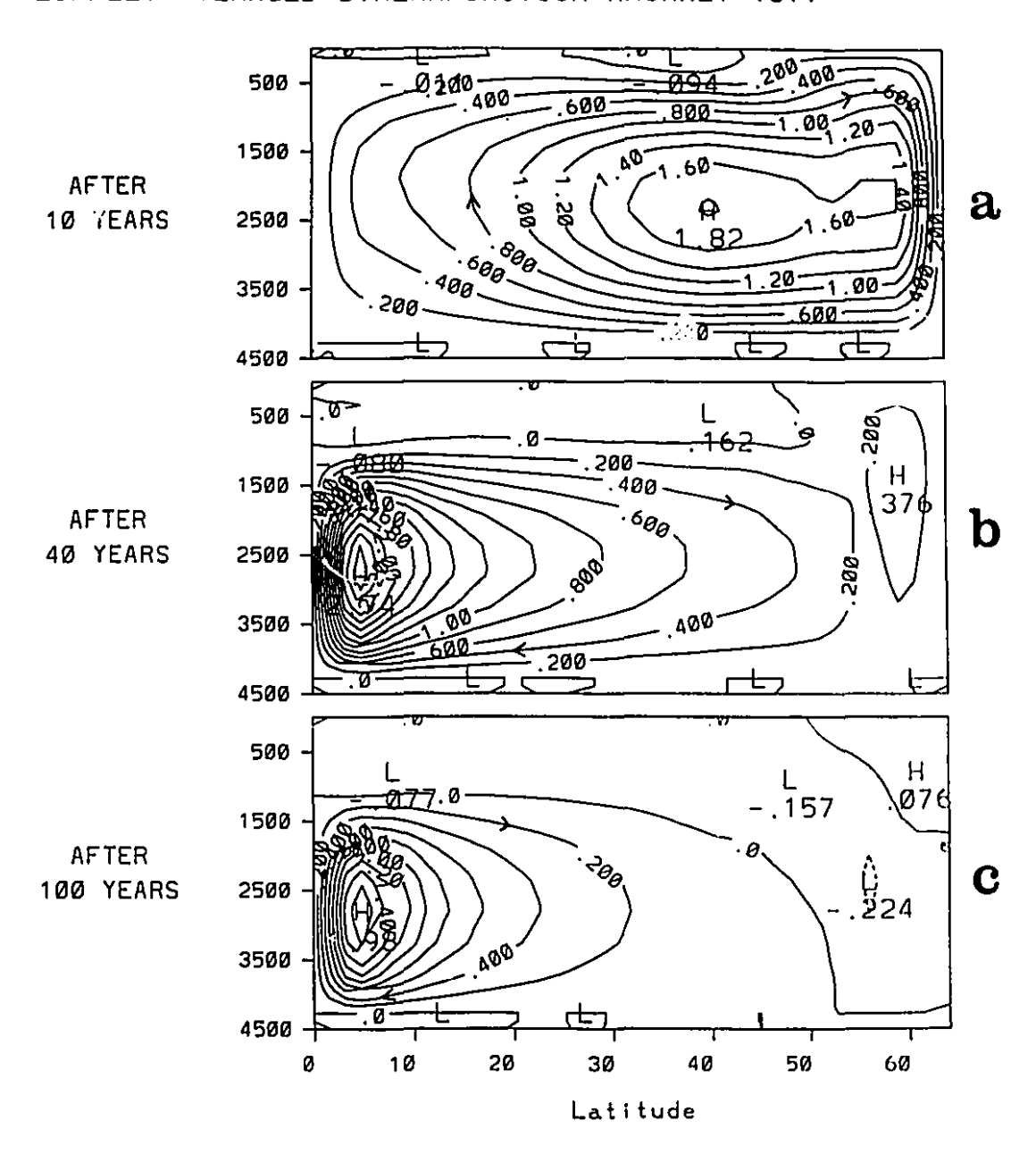


Figure 4.15: Streamfunction (Sv) anomaly (perturbation experiment minus spinup final equilibrium) at same times as in Fig.4.10.

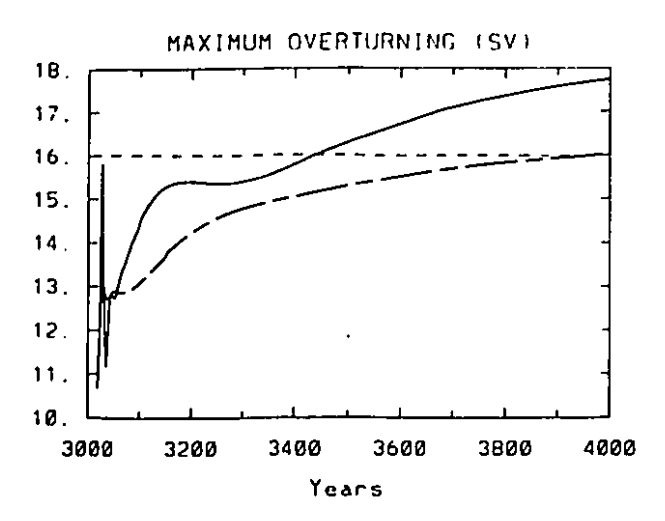


Figure 4.16: Maximum overturning (Sv) as a function of time in preliminary experiment with initially reduced overturning (dashed line: under mixed boundary conditions; solid line: with SST-evaporation feedback and precipitation scheme 6).

-evaporation feedback. The stabilization of the water column allows the SST to cool, reducing evaporation and freshening the surface still further. One thousand years later, the SSS anomaly at high latitudes has intensified rather than disappearing (Fig.4.17). The increased overturning is initially surprising in view of this, but turns out to be a regional effect. The geostrophic rim current around the fresh pool (Fig.4.18a) induces vertical velocities at the basin walls which appear in zonal average as a local intensification of the meridional overturning (Fig.4.18b). This enhanced overturning is stable for at least another thousand years, although the very long-term behaviour is unknown.

In summary, the SST-evaporation feedback <u>is</u> potentially important in time-dependent studies of the ocean's thermohaline circulation, at least as far as the present simple parameterization allows one to judge. It is effective primarily in convective regions, and especially if freshening can trigger nonlinear amplification, and constitutes a positive feedback for the thermohaline circulation. As hoped, the parameterization is not overly sensitive to the precipitation scheme; in fact, a separate series of experiments in which the flux anomaly was maintained throughout the run exhibited the strongest responses under different precipitation schemes from the experiments in this chapter, encouraging the belief that no

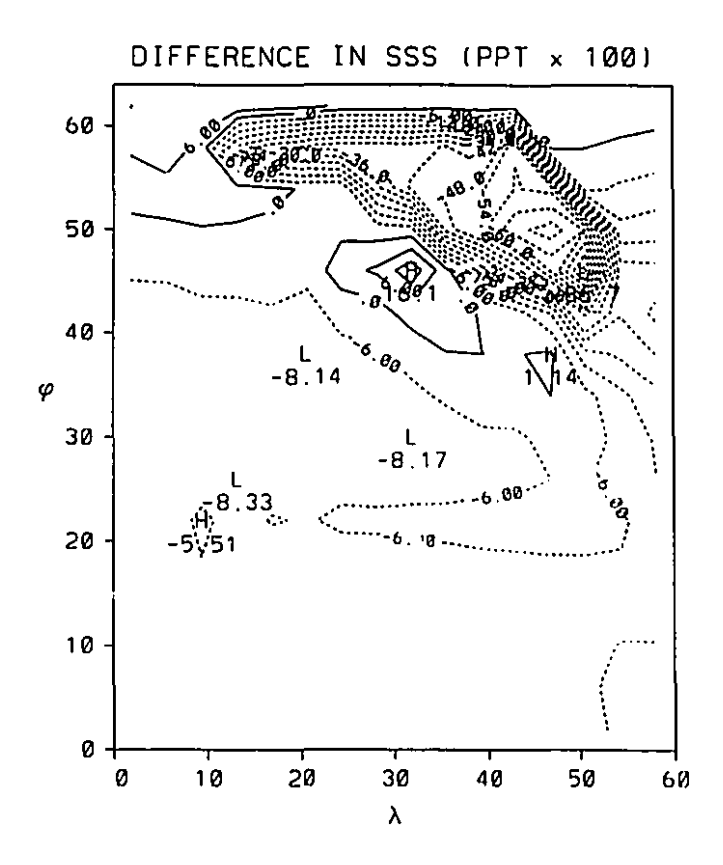
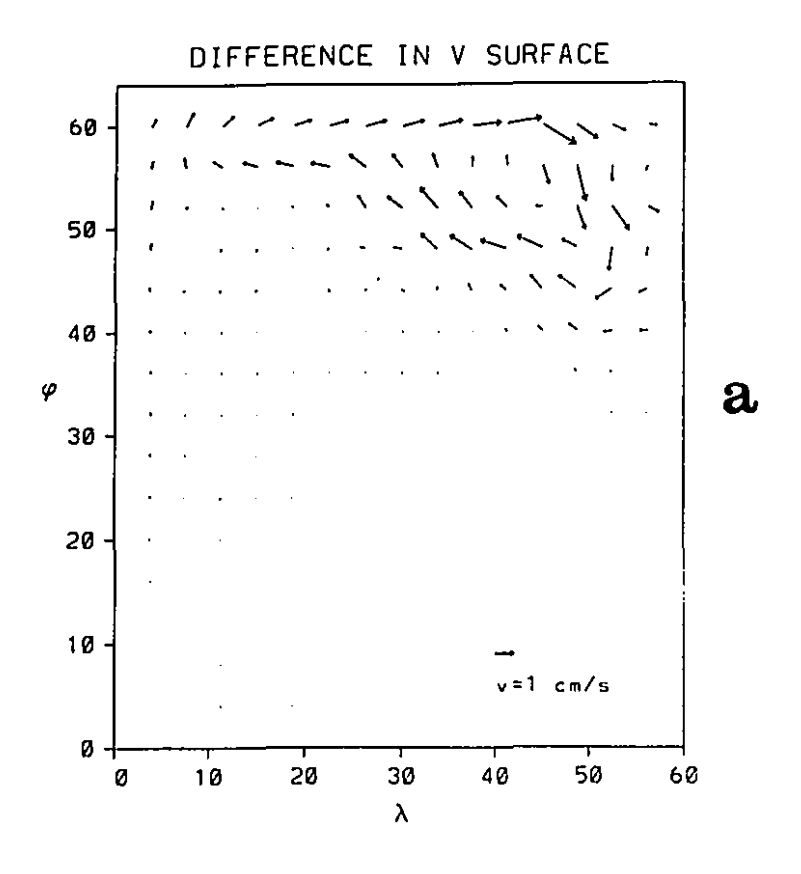


Figure 4.17: Surface salinity (ppt) anomaly (perturbation experiment minus initial condition with reduced overturning) after 1000 years with SST-evaporation feedback and precipitation scheme 6.



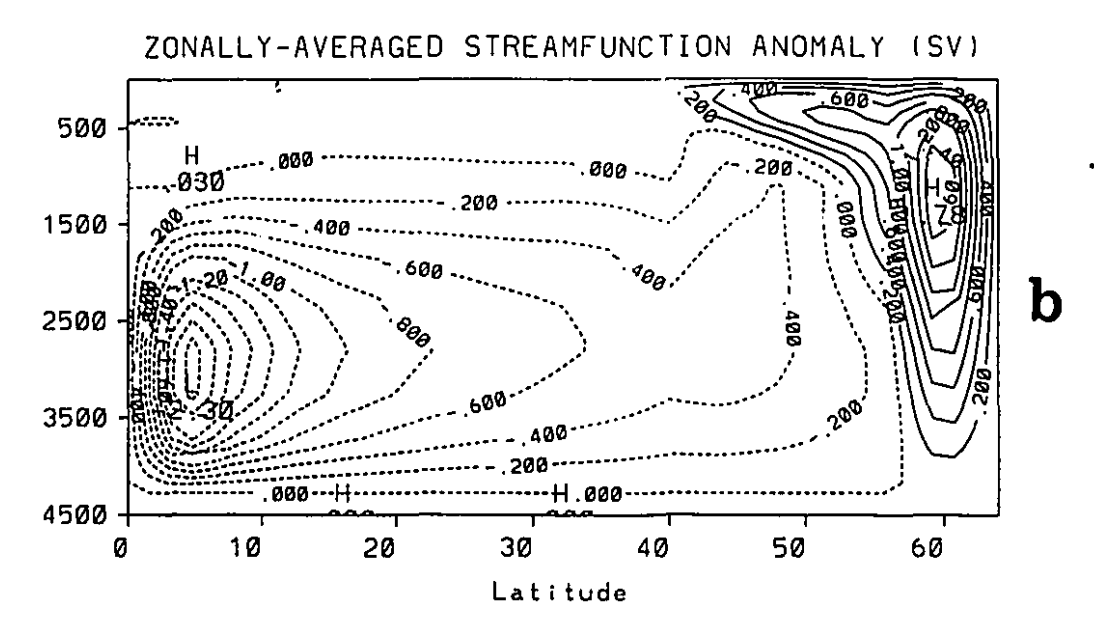


Figure 4.18: a) Difference in surface velocity (perturbation experiment minus initial condition with reduced overturning) after 1000 years with SST-evaporation feedback and precipitation scheme 6 b) difference in overturning streamfunction (Sv).

definite properties attached to any particular precipitation scheme are biasing the results.

4.3. Decadal Variability

As described in Chapter 1, spontaneous internal decadal variability of the ocean's thermohaline circulation was first found in an uncoupled ocean model by Weaver and Sarachik (1991a), and at least one long-lived salinity anomaly similar to the one travelling around the high latitude region in their model has been convincingly documented in the North Atlantic (the GSA). Decadal oscillations can be produced in a model very similar to the one in the preliminary experiments merely by switching to the (P-E) field diagnosed from a spin-up under a restoring profile of zonally-averaged Levitus SSS.

4.3.1. Under Mixed Boundary Conditions

The numerical parameters for the spin-up are given in Table 4.1, and the surface heat and freshwater fluxes diagnosed at the end of 4000 years are shown in Fig.4.19. When the ocean is spun up for a second time under mixed boundary conditions, a regular oscillation appears almost immediately in the basin-mean surface heat flux and persists for the 5000 years of the integration, with an average period of just over 9 years and an amplitude of 6-8 W/m² (Fig.4.20). Interestingly, the oscillation is not the same as in the very similar study by Weaver and Sarachik (1991a), because perhaps of the different basin length or the different winds or the coarser resolution, or a combination of such factors. This is immediately apparent from the three distinct peaks per period in the time series of basin-mean kinetic energy density (Fig.4.21b) compared with the simpler single frequency in their Fig.4. Since only a two-dimensional description of the oscillation was given in Weaver et al. (1993), more details are provided below.

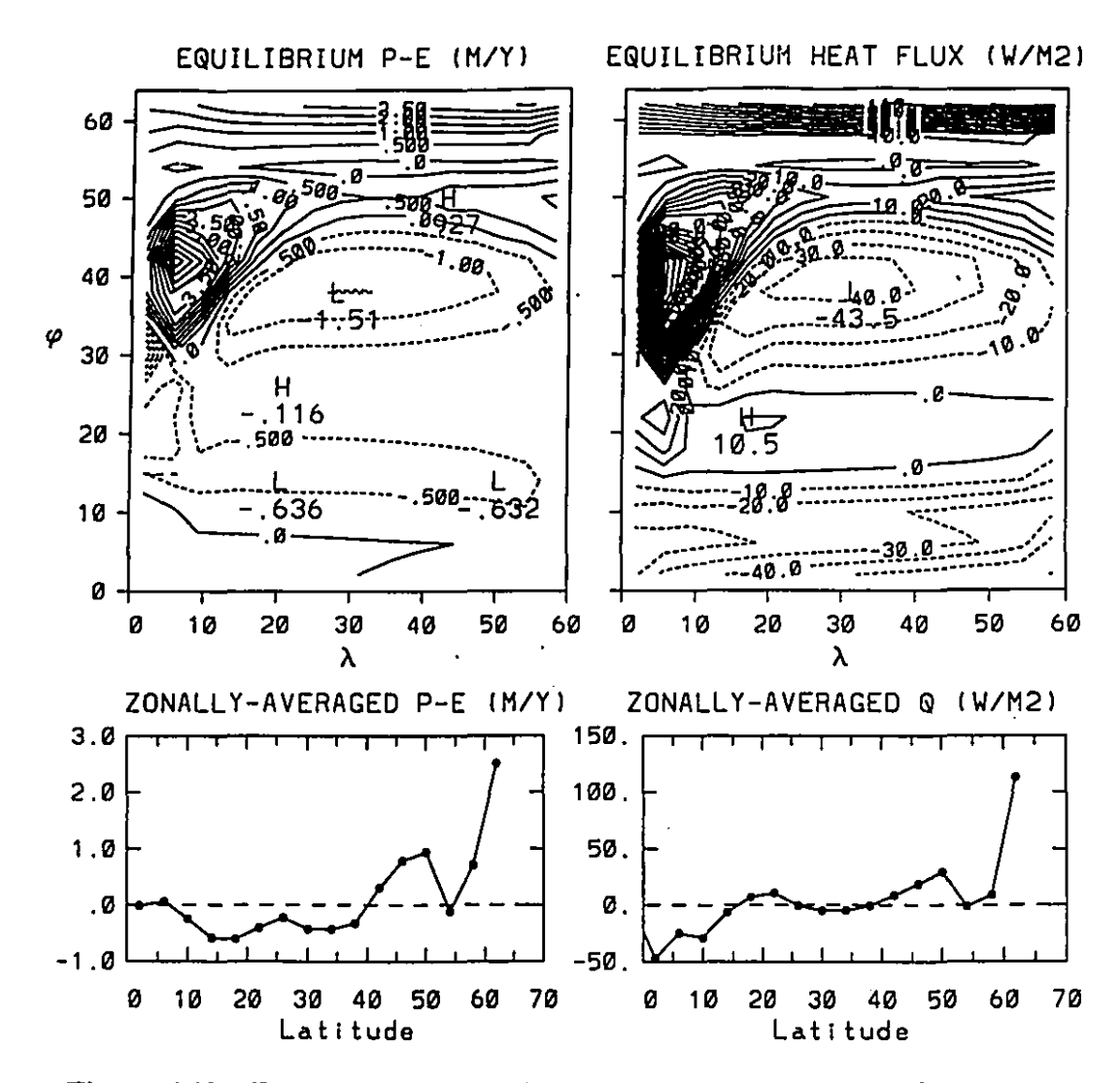


Figure 4.19: Equilibrium (P-E) (m/y) and surface heat flux (W/m²) diagnosed from the decadal spinup.

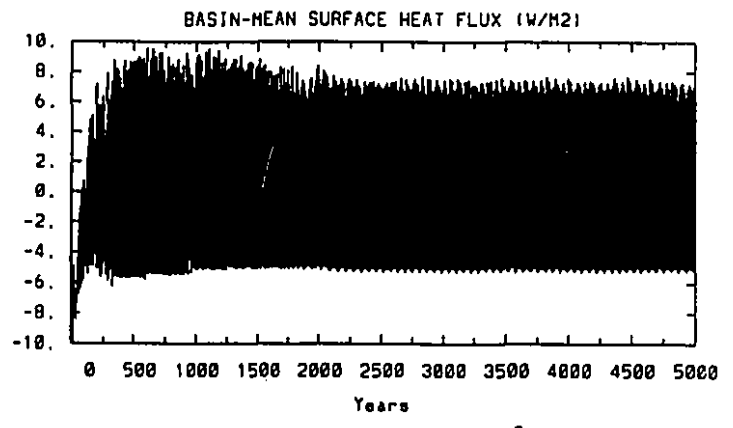


Figure 4.20: Basin mean surface heat flux (W/m²) as a function of time for decadal variability control run under mixed boundary conditions.

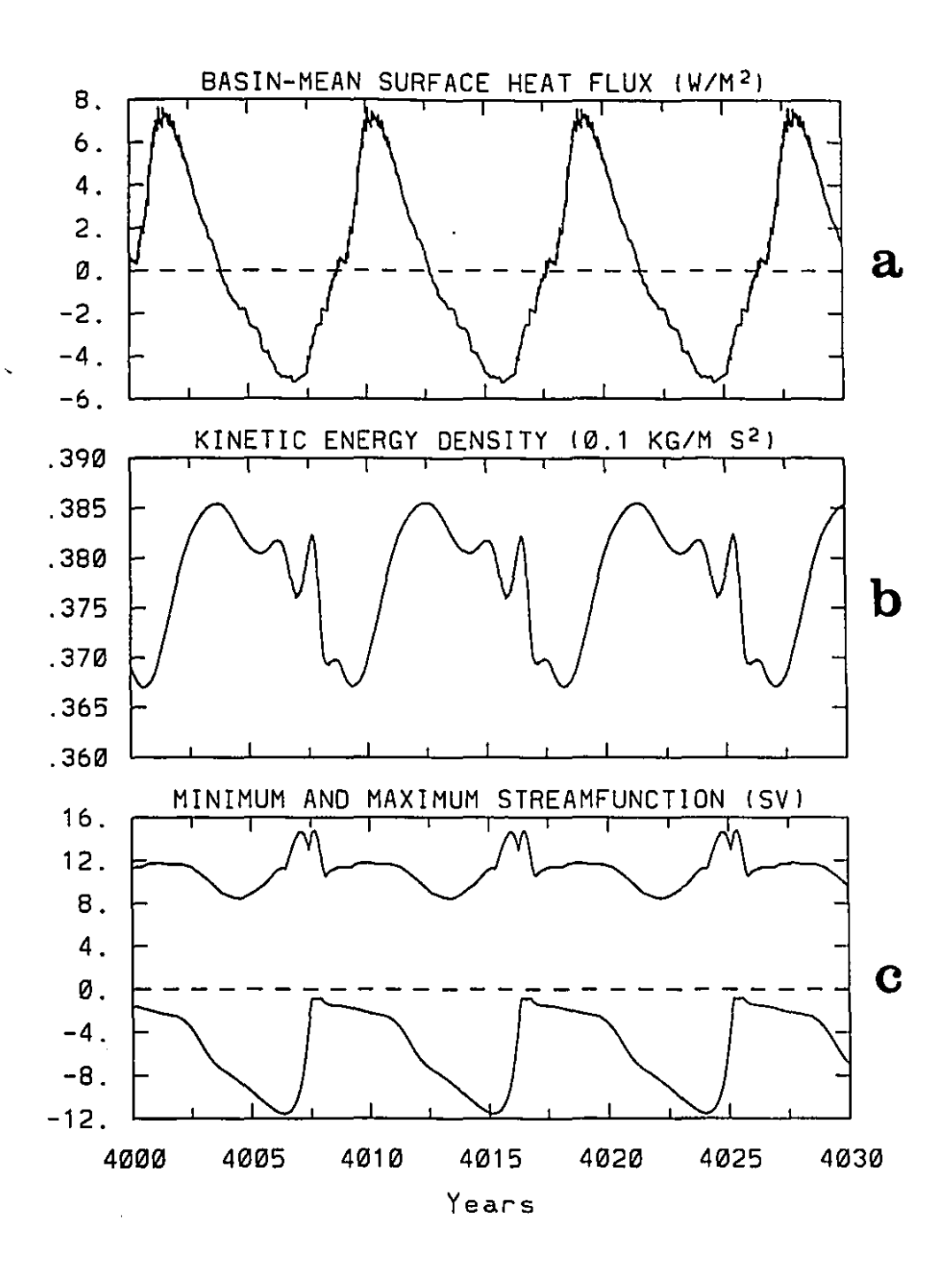


Figure 4.21: Expanded time series of a) basin mean surface heat flux (W/m²), b) basin mean kinetic energy density (0.1 kg m⁻¹ s⁻²), and c) maximum and minimum overturning (Sv) starting at year 4000 of decadal variability control run in Fig.4.20.

One way to visualize the oscillation is as a fluctuation in heat content. As starting point, the time of minimum basin-mean surface heat flux is chosen: the kinetic energy is then in between two peaks, while the basin-mean temperature lags the surface heat flux by a quarter cycle throughout the oscillation. The thermohaline circulation at this time consists of a strong forward cell, not much weaker than in the spin-up, but with sinking at about 54°N instead of at the northern boundary as was the case under restoring boundary conditions, and a narrow deep reverse cell of nearly equal strength wedged in between 54°N and the northern boundary. The surface has freshened considerably under mixed boundary conditions (Fig.4.22 shows the difference with the spin-up under restoring boundary conditions), and surface convection has been disabled everywhere except in the western boundary current (compare Figs. 4.23a and b), allowing the ocean surface to cool nearly to the atmospheric temperature in two zonal bands along 50° and 62°N (compare Figs.4.24a and b). The minimum cooling and freshening are aligned along 54°N, the transition latitude between the subtropical gyre and the northern boundary current, where both horizontal advection and convection were minimum under restoring boundary conditions. The consequence is a local minimum in the diagnosed (P-E) field (Fig.4.17), which maintains a saltier streak along 54°N, well within the polar halocline, under mixed boundary conditions. An anomalous counterclockwise horizontal circulation is set up at high latitudes (Fig.4.25a), driving a dipole of vertical velocities at the eastern boundary (Fig.4.25b) that manifests itself as a reverse cell in the zonally-averaged meridional overturning.

The fresh surface layer over the northern half of the basin stabilizes it to both the surface heat loss (now much reduced) and the subsurface warming by the northern limb of the subtropical gyre (now enhanced by the thermohaline circulation crossing eastward at 54°N instead of at the northern boundary). A pool of warm water accumulates below the halocline until instability becomes unavoidable. Convection breaks out first at the eastern boundary at ~54°N, and rapidly spreads westward and southward (Fig.4.26), causing the nearly linear rise

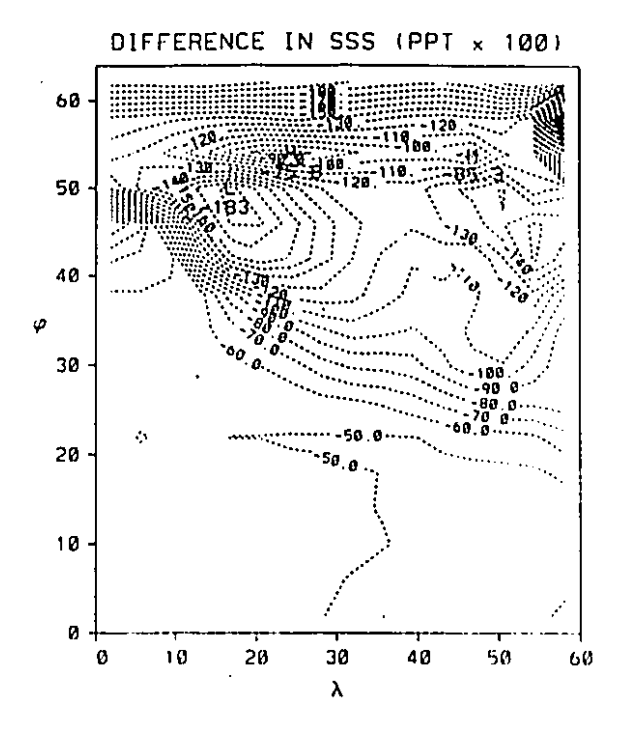


Figure 4.22: Difference in surface salinity (ppt x 100) for decadal control run at the time of minimum basin mean surface heat flux minus equilibrium under restoring boundary conditions.

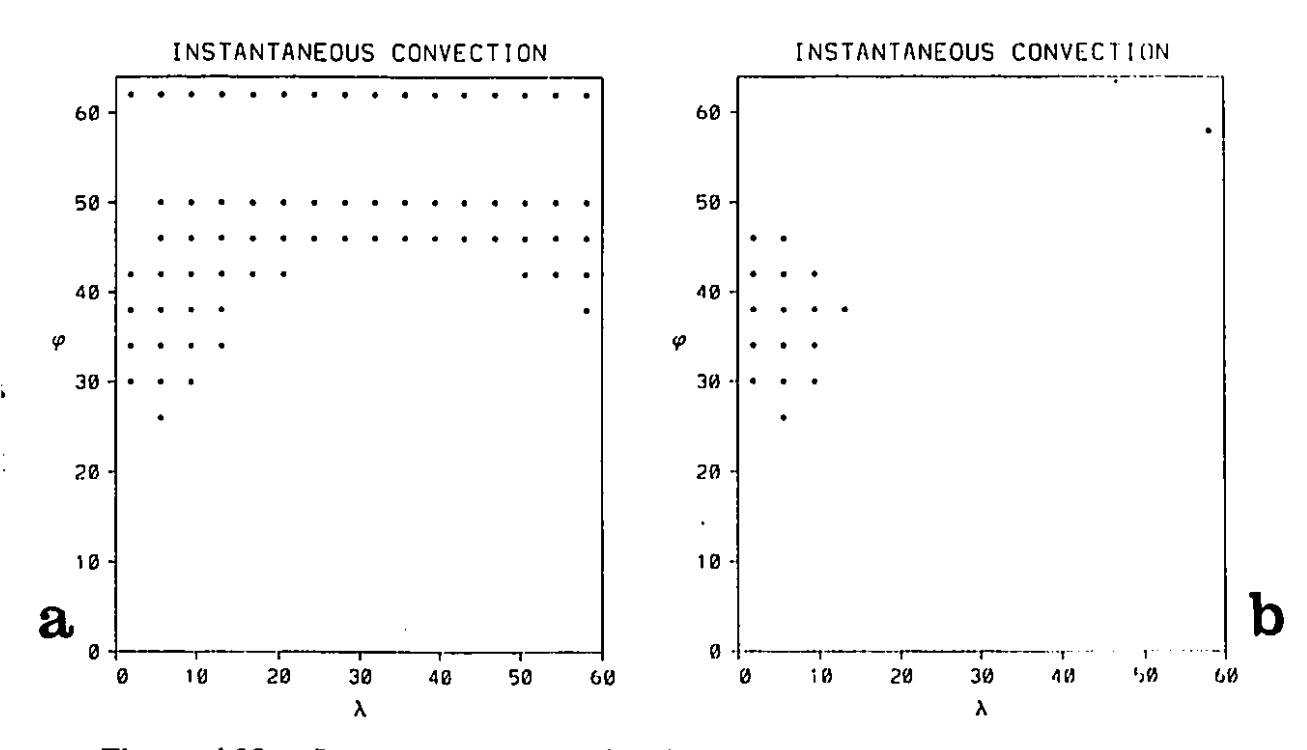


Figure 4.23: Instantaneous convection between top two levels in decadal experiment a) under restoring boundary conditions b) under mixed boundary conditions at time of minimum surface heat flux.

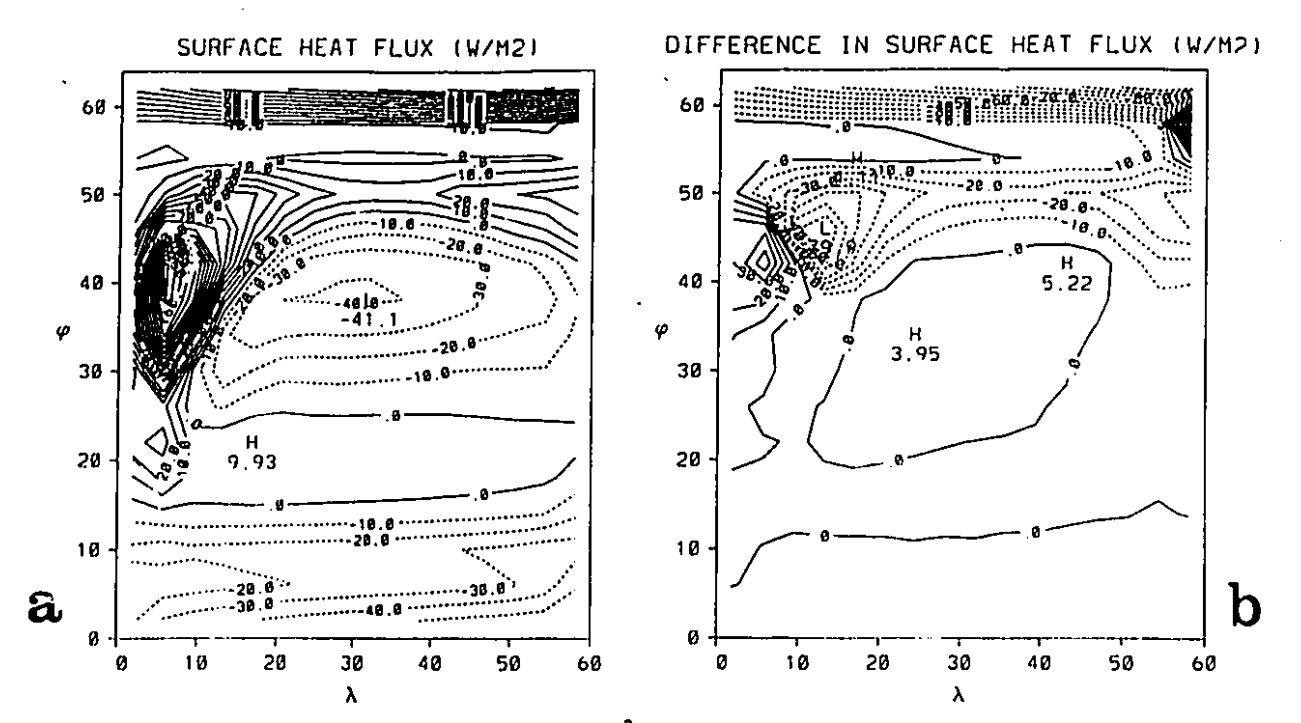


Figure 4.24: a) Surface heat flux (W/m²) under restoring boundary conditions in decadal run. b) difference in surface heat flux (W/m²) between mixed boundary conditions at time of minimum surface heat flux and equilibrium under restoring boundary conditions.

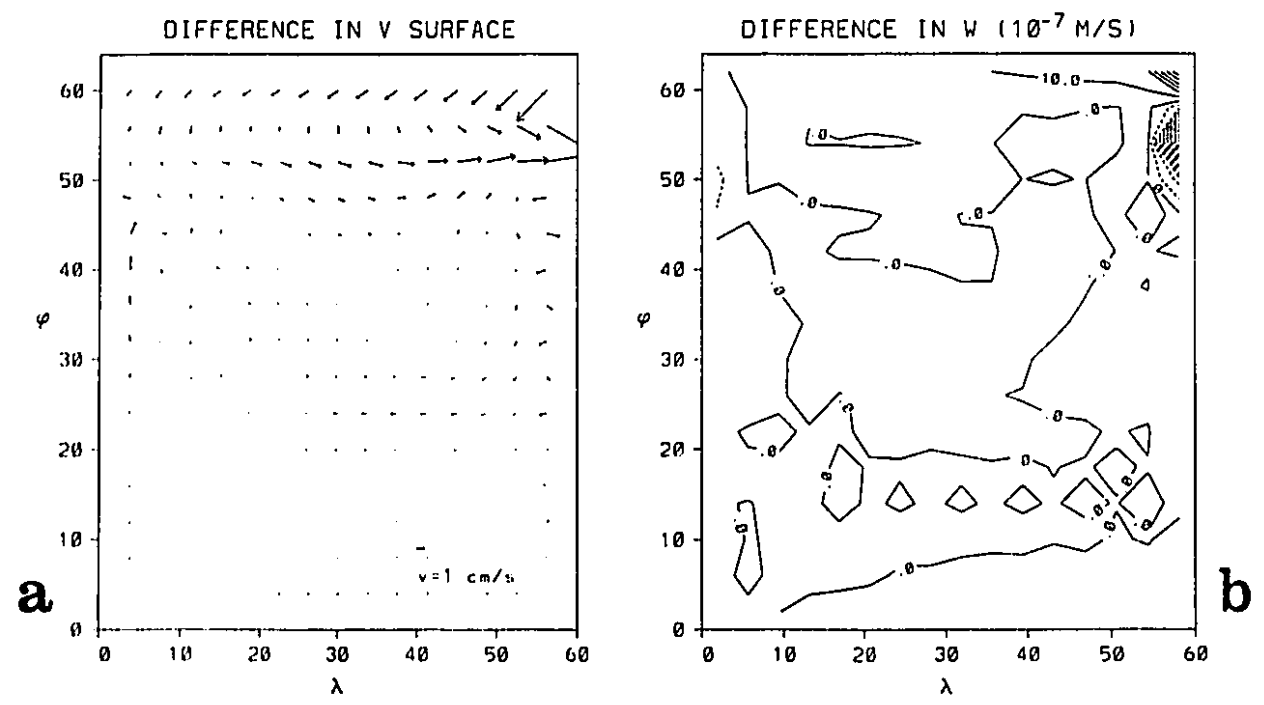


Figure 4.25: Velocity difference in decadal experiment between mixed boundary conditions at time of minimum surface heat flux and restoring boundary conditions a) horizontal velocity at 25 m b) vertical velocity (10⁻⁷ m/s).

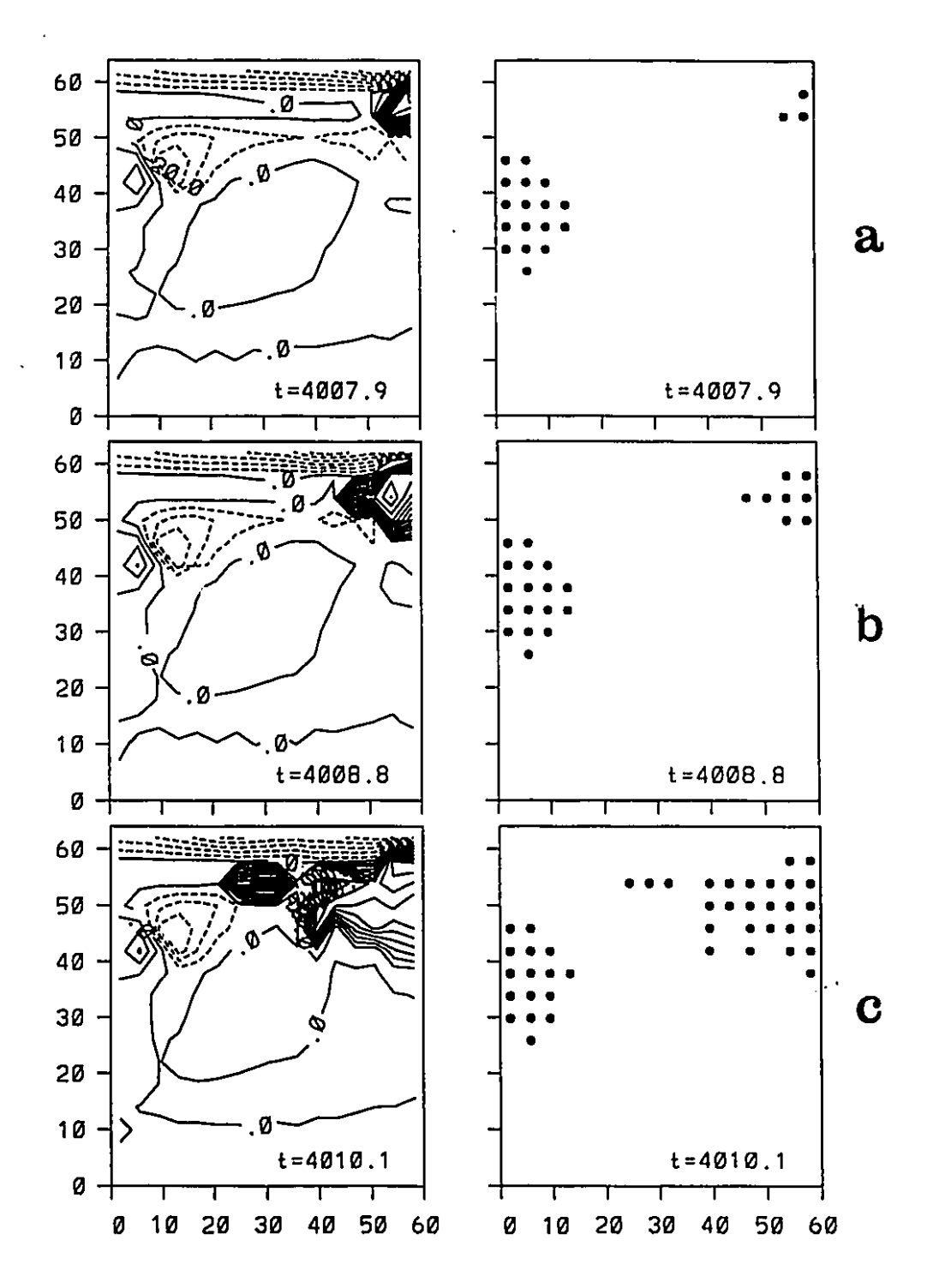


Figure 4.26: Surface heat flux (W/m²) anomaly (mixed boundary conditions minus equilibrium under restoring boundary conditions) and convection between top two levels at six successive times during decadal oscillation.

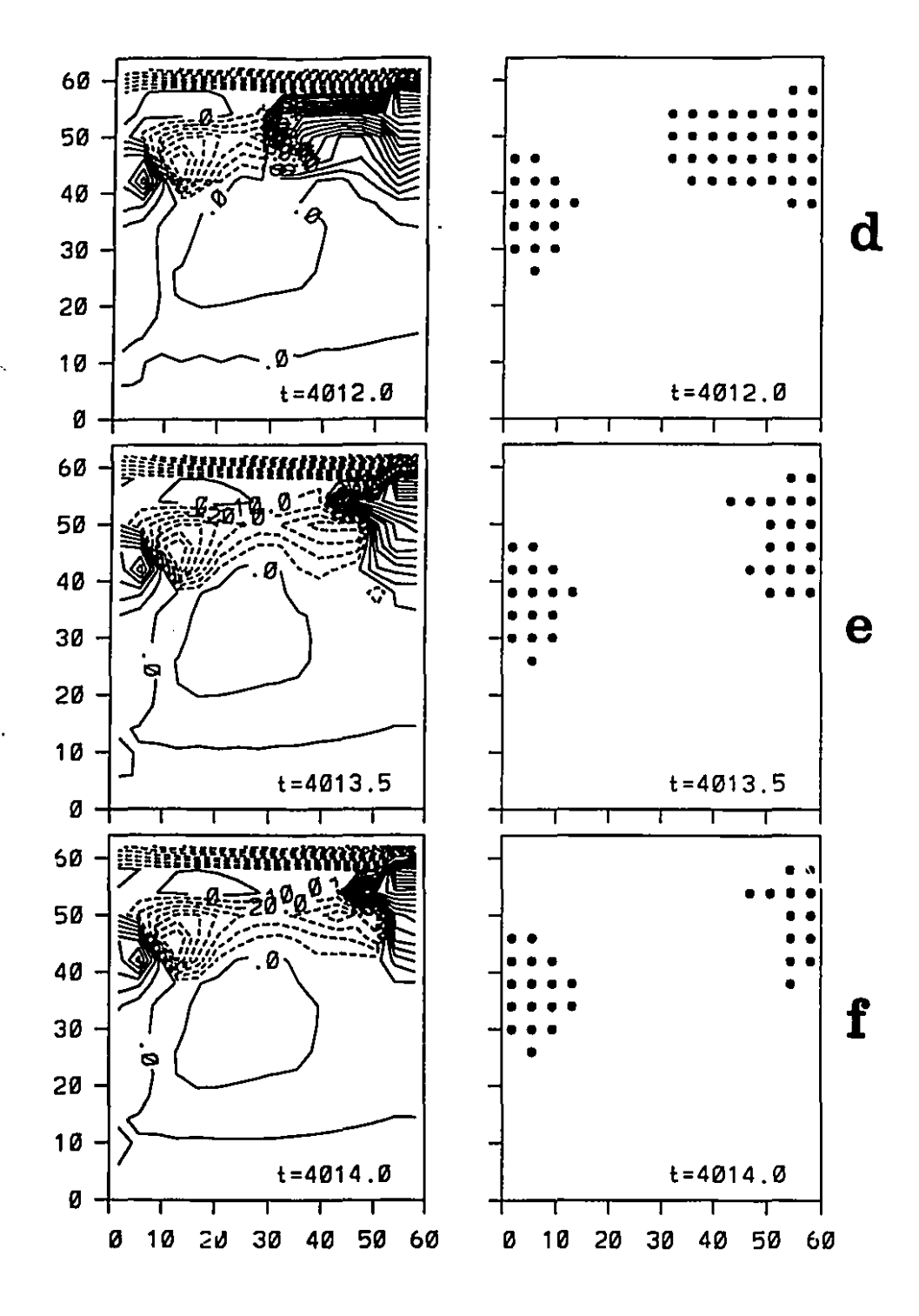


Figure 4.26. Suite.

in basin-mean surface heat flux during the first half of the oscillation cycle. Less than four years later, the water column has been homogenized to great depths along the eastern boundary (Fig.4.27). The ebb of the oscillation is related to convection exhausting itself in the central basin; the tongue of heat loss retreats eastward (Fig.4.26e,f), while the fresh halocline spreads back equatorward from the northern boundary (not shown).

It is difficult to determine what sets the period of the oscillation, but there are indications that it may still be an advective timescale as in Weaver and Sarachik (1991a), and not simply linked to the life cycle of the convective patch. At the time of minimum surface heat flux (4006.6 yrs), the forward cell is relatively strong (see the time series of maximum streamfunction in Fig.4.21), and the zonal circulation associated with it is downwelling fresh water at high latitudes along the eastern boundary (Fig.4.28a). When convection breaks out at 4007.6 years, a blob of fresh water is isolated in the northeast corner of the basin (Fig.4.28c). A zonal pressure gradient is created along the northern boundary, causing a westward acceleration in the frictional boundary layer. The fresh anomaly propagates westward (left panel of Fig.4.29a-e), aided by the convergence of zonal velocities immediately ahead of it (right panel of Fig.4.29a-e) which drive a local downwelling anomaly (not shown) that disrupts the normally tightly stratified halocline. The anomalous pulse of vertical velocity is also responsible for the sudden "disappearance" of the reverse cell at 4007.9 yrs, by cancelling out in zonal average the upwelling centre at the eastern boundary (see Fig.4.25b). Once the downwelling anomaly has reached the western boundary (at about 4011 years) and turned southward, the reverse cell starts to reappear in the meridional overturning streamfunction. By this time, the zonal velocities all along the northern boundary have reversed their direction, but the halocline is returning to its original position as the fresh surface layer starts to slump southward (Fig.4.29). Meanwhile, convection in the eastern and central basin is nearing its maximum extent, and the warm salty water churned up to the surface has produced a geostrophic circulation counterclockwise around it (Fig.4.30). The southward

ZONAL TEMPERATURE SECTIONS AT 54 N

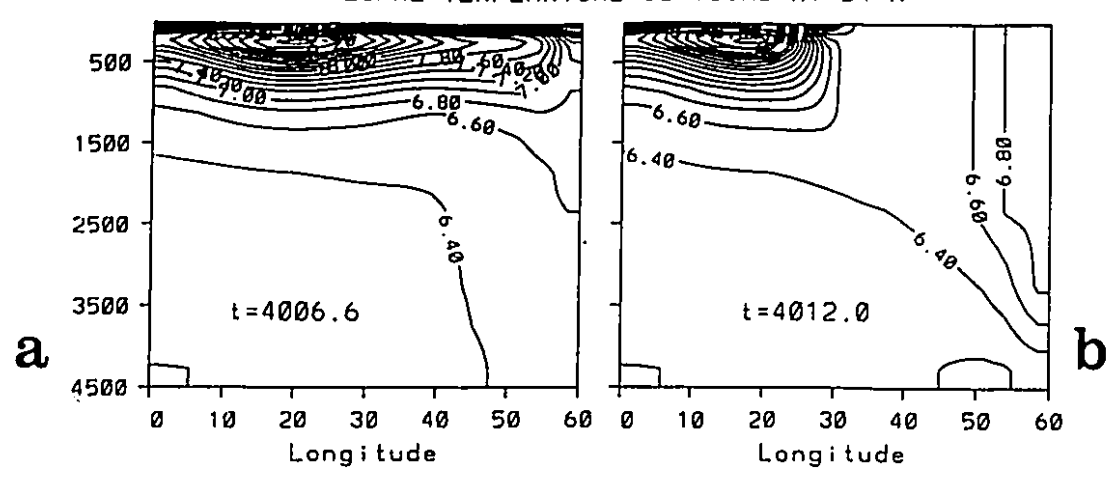


Figure 4.27: Zonal-vertical section of temperature (°C) at two times during the decadal oscillation under mixed boundary conditions a) time of minimum surface heat flux b) two years after the time of maximum surface heat flux.

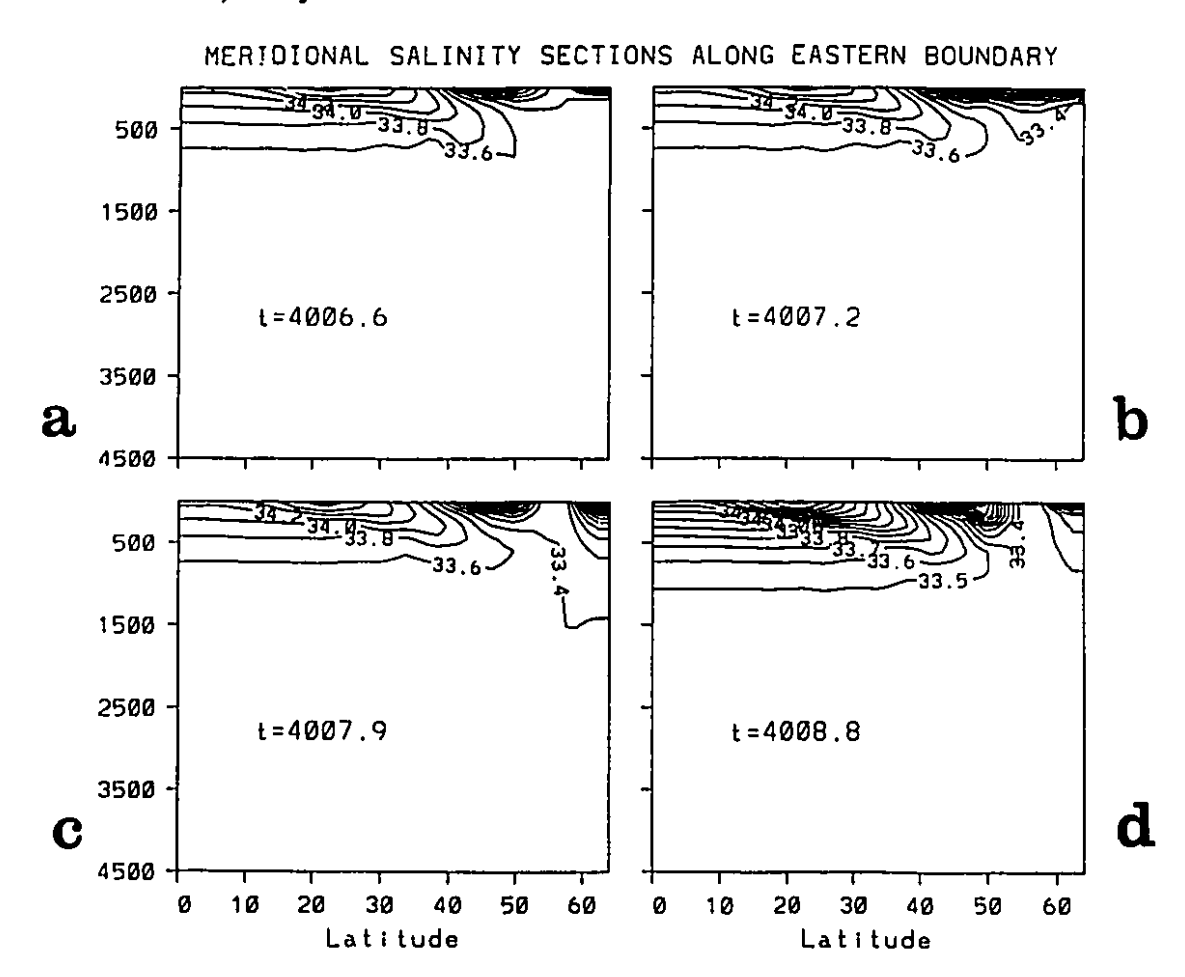


Figure 4.28: Meridional-vertical sections of salinity (ppt) along eastern boundary at four successive times in the decadal variability control run.

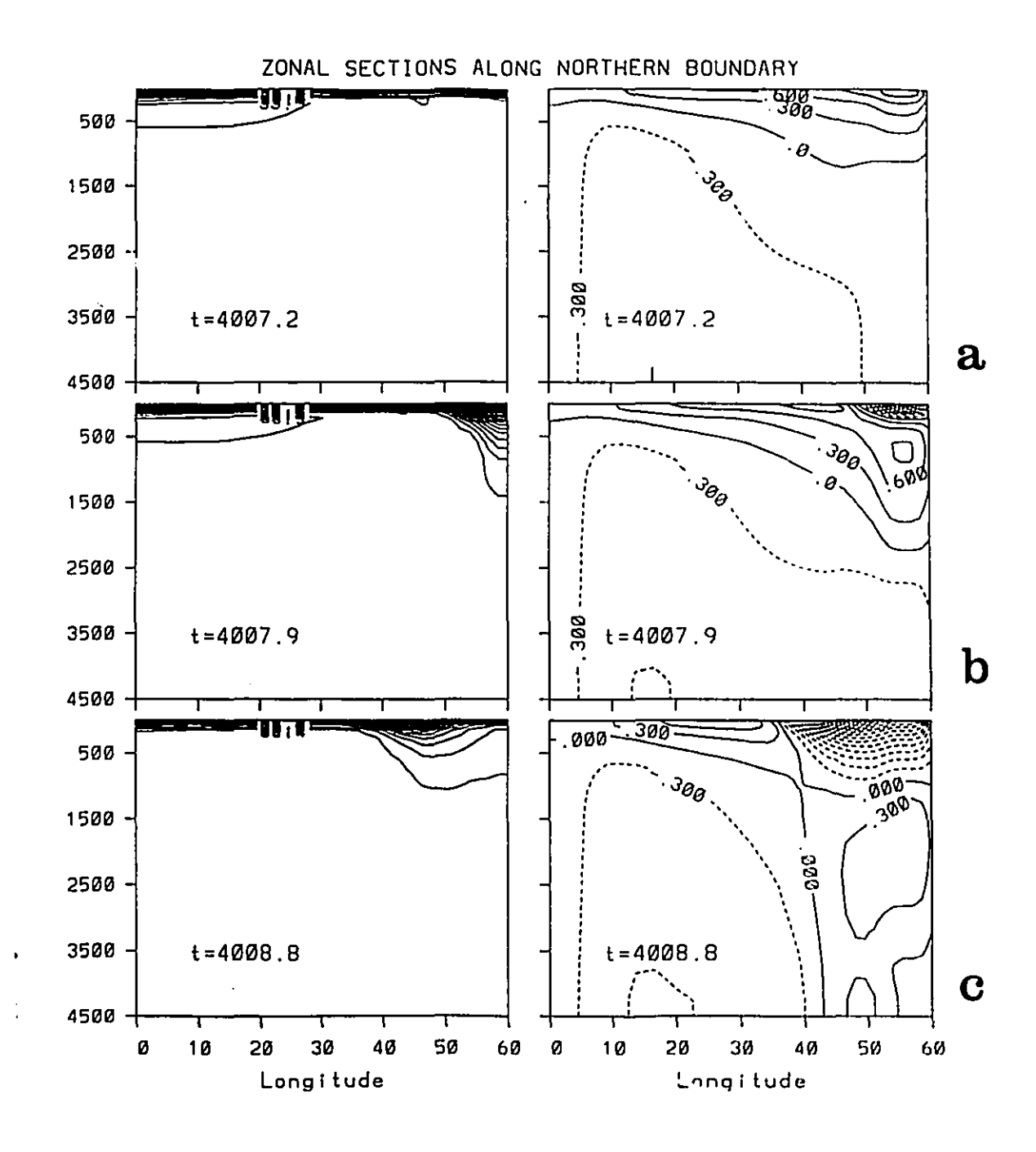


Figure 4.29: Zonal-vertical sections of salinity (ppt) and zonal velocity (m/s) along northern boundary at five successive times in the decadal variability control run. Negative velocities are contoured in dashed lines.

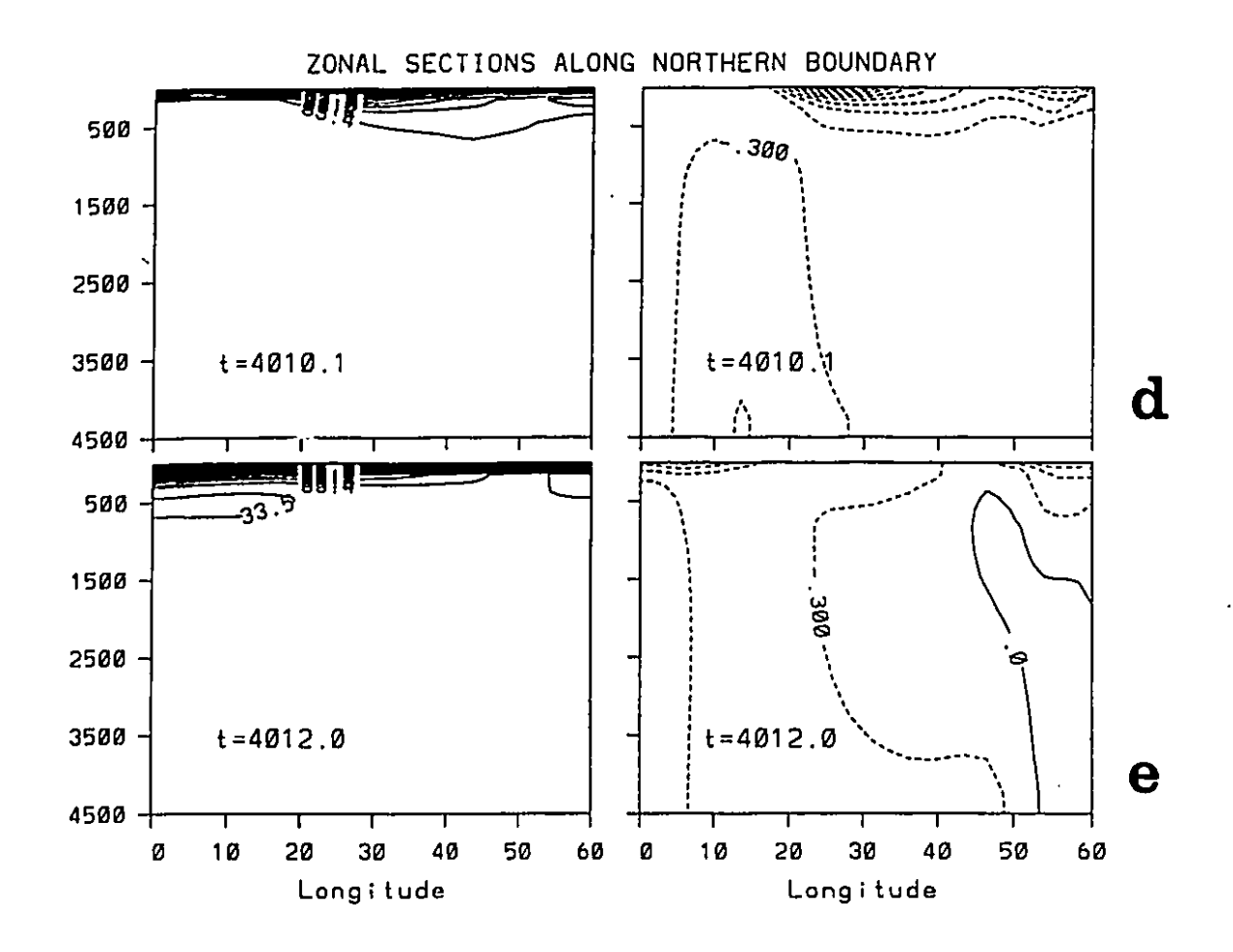


Figure 4.29. Suite.

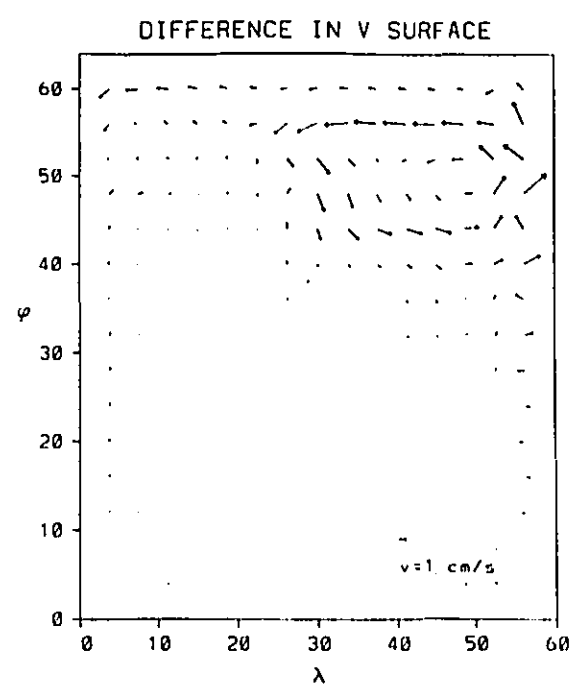


Figure 4.30: Difference in surface velocity between two times: t=4012.0 years (two years after the time of maximum surface heat flux) and t=4006.6 years (time of mininum surface heat flux) in the decadal variability control run.

velocities on the western side of the whirlpool, in combination with the southward Ekman drift, advect the freshening from the north back down across 54°N and on eastward through the shrinking convective patch. The reestablishment of the halocline allows the subsurface warming to penetrate back into the eastern half of the basin again, and the whole cycle of heat storage and release starts anew.

The difference between this oscillation and that of Weaver and Sarachik (1991a) is underscored by comparing the total buoyancy forcing shown in Myers and Weaver (1992) with that in the present model. The present model is haline dominated at high latitudes (Fig.4.31b) while theirs is thermally dominated (their Fig.9b), resulting in a net buoyancy gain here (Fig.4.31a) and a net loss in their case. That advective decadal variability can be supported under such different conditions reinforces the belief that this is a possible mechanism in the real world.

4.3.2. With Evaporative Feedback

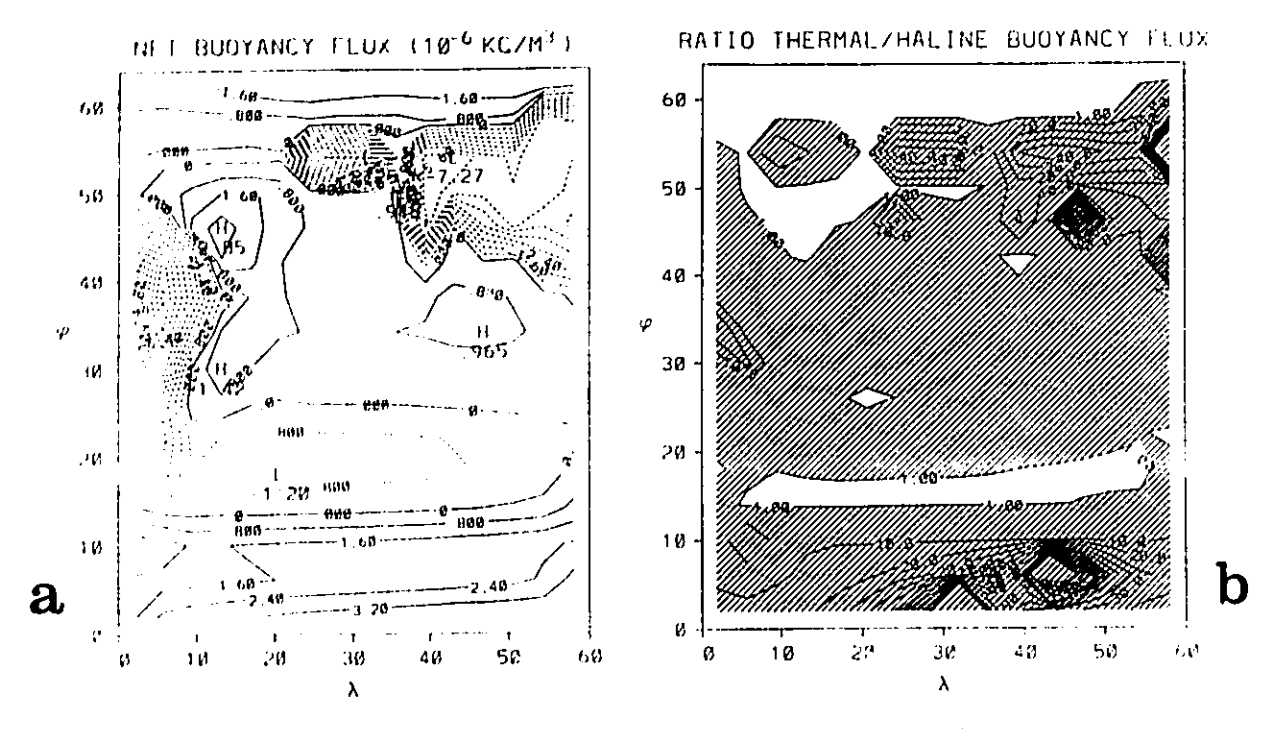


Figure 4.31: a) Net surface buoyancy (thermal + haline) flux (10⁻⁶ kg/m⁻¹) b) ratio of thermal/haline buoyancy fluxes, both at t=4010.1 years (the time of maximum surface heat flux) in the decadal variability control run.

The equilibrium evaporation and precipitation fields inferred from equations (4.3) and (4.4) for the decadal model are shown in Fig.4.32. A new complication has arisen: negative precipitation is predicted for the northern half of the subtropical gyre. This is a consequence of using the diagnosed (P-E) field to constrain the equilibrium precipitation (see Section 4.1): a greater salt flux is being imposed than can plausibly be provided by evaporation at that sea surface As mentioned earlier, under (P-E) profiles prescribed from temperature. observations, the range of sea surface salinity tends to be too small. The decadal model's diagnosed (P-E) achieves a better SSS distribution (Fig.4.33) by exaggerating the magnitude of the fluxes (contrast the peak values of > 6 m/y in Fig.4.32 to the maximum of < 2.5 m/y for the North Atlantic shown in Schmitt et al., 1989). The negative precipitation can therefore be viewed as a "salt flux correction" no different from those resorted to in fully coupled atmosphere-ocean models, and needed for the model to maintain the desired surface salinities despite the absence of runoff and sea ice and the presence of unrealistically high diffusion.

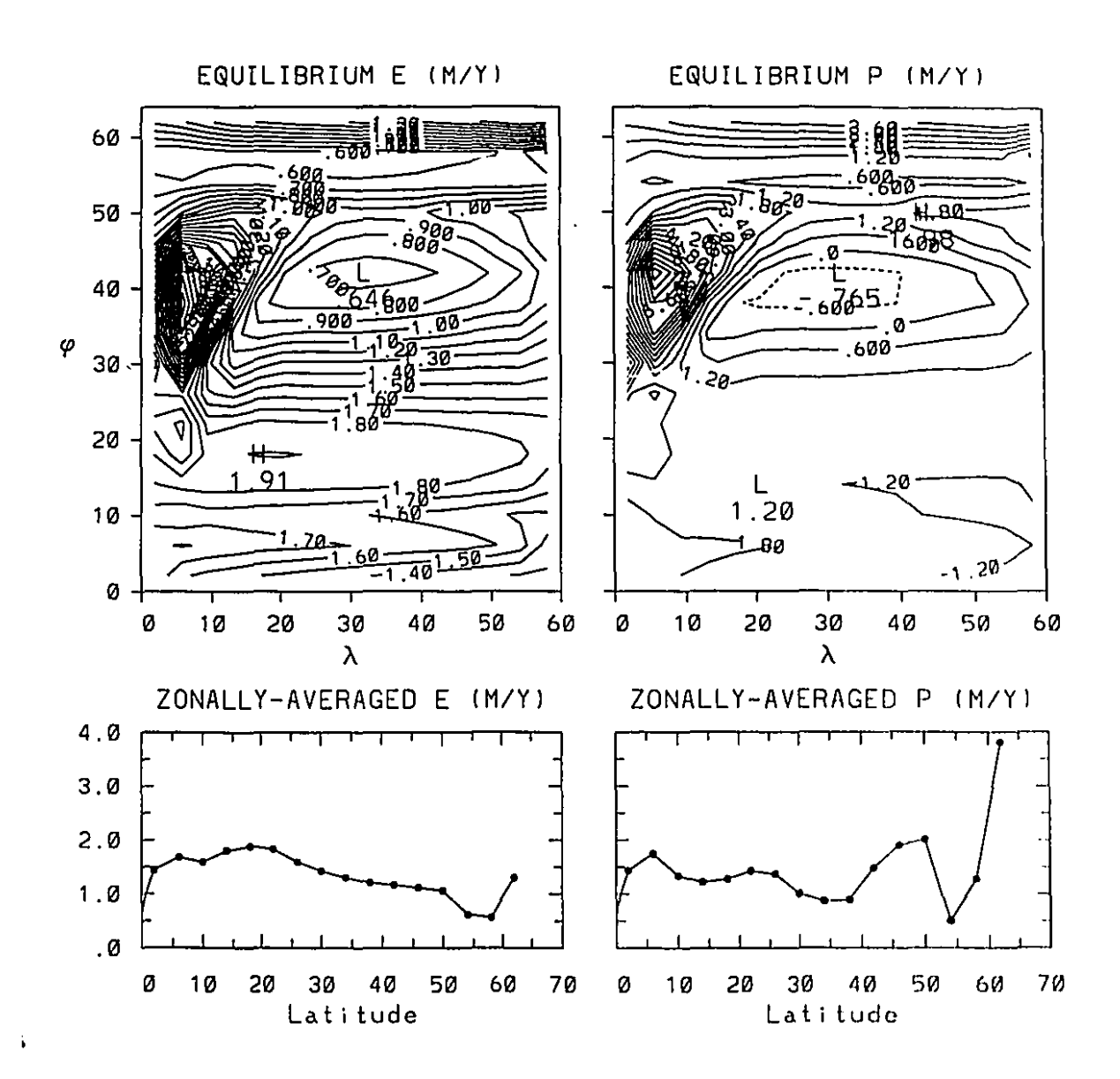


Figure 4.32: Equilibrium evaporation and precipitation (m/y) estimates for the decadal experiment.

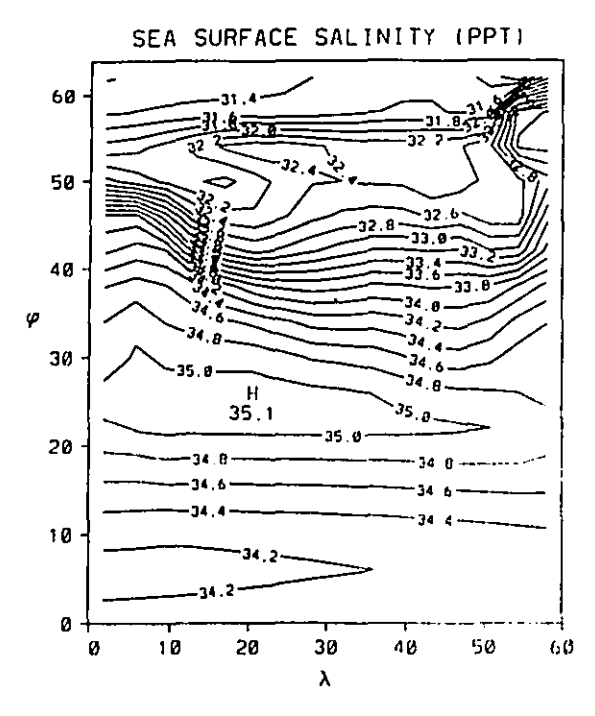


Figure 4.33: Equilibrium surface salinity (ppt) distribution in the decadal control run under mixed boundary conditions at t=3997.3 years (cf. Fig.4.6).

etc. The equilibrium precipitation in this region is simply set to zero, and the flux correction added on to the diagnosed evaporation at each timestep. One further stipulation was made: that the precipitation should not be allowed to decrease further in this region so negative tendencies at these gridpoints were instead spread evenly over the rest of the basin. Testing indicated that this could alter detailed aspects of the results but was unlikely to result in qualitative differences. The possibility of removing the negative precipitation by adjusting the radiation was also considered, but unjustifiably large corrections were found to be required despite the small magnitude of the total flux correction (only about 0.04 Sv integrated over the entire area). The present method was therefore preferred, and was applied also to the century and millennial timescale variability experiments in the next two sections, where the same circumstances were encountered.

The six different experiments under SST-evaporation feedback and different precipitation schemes, and the control run under mixed boundary conditions are compared in Fig.4.34 depicting thousand-year time series of the basin-mean

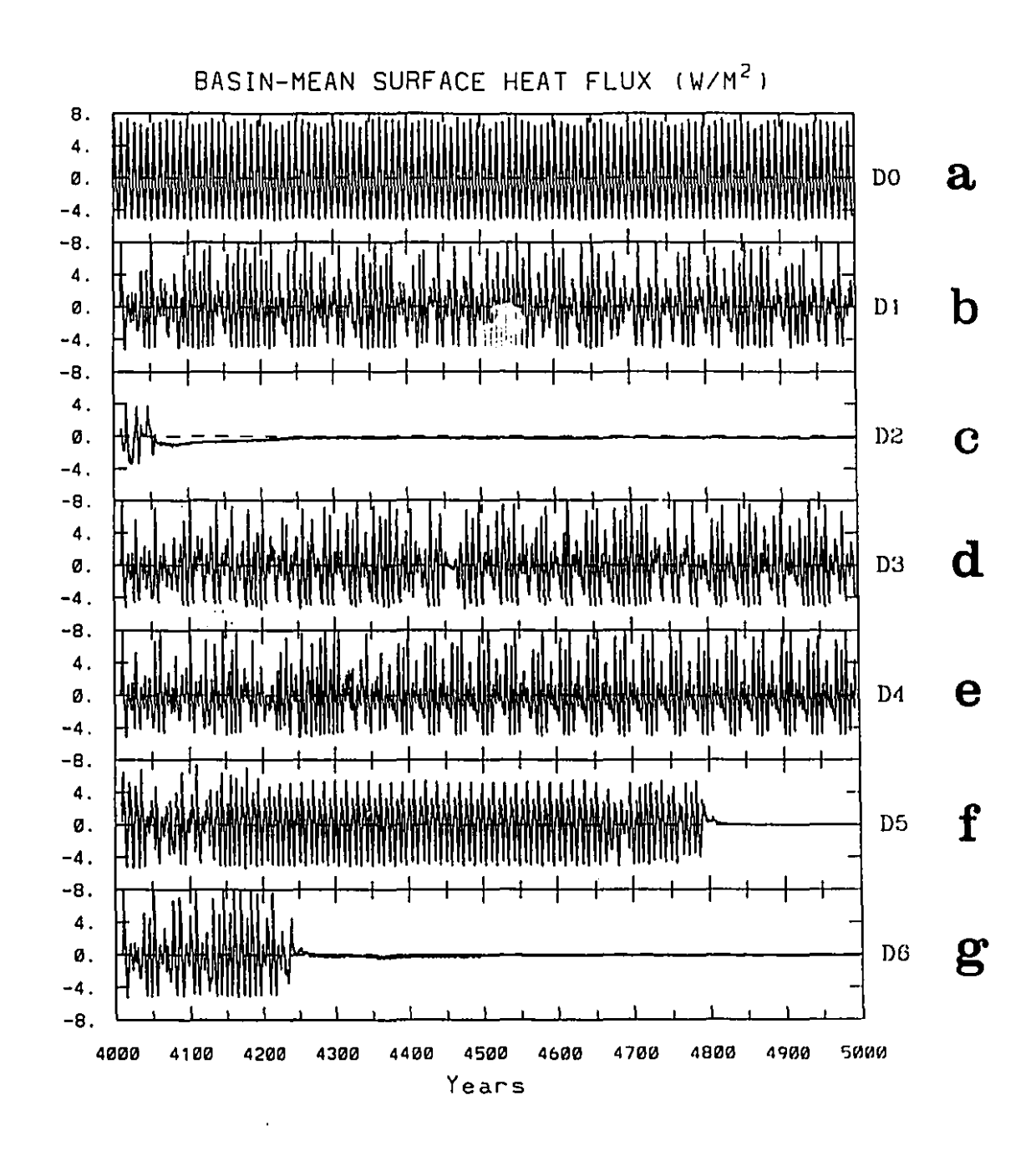


Figure 4.34: Basin mean surface heat flux (W/m^2) as a function of time for the decadal experiments with evaporative feedback. The initial condition for all runs is the spinup under mixed boundary conditions (D0) at year 4008.8, and runs (D1) through (D6) use the precipitation redistribution schemes 1 through 6.

surface heat flux. All runs start from the same initial condition: year 4008.8 of the spin-up under mixed boundary conditions. Decadal variability is exhibited by five out of the six experiments, failing only in run D2 (new precipitation redistributed uniformly around latitude circles), but the periods are generally shorter (< 8 years in all cases) and the appearance more irregular than under mixed boundary conditions. The oscillation also dies out in runs D5 and D6 after only a few hundred years: this was not the case starting from other initial conditions so is probably associated with the pseudo-stochastic appearance of the time-varying (P-E) field. In Weaver et al. (1993), for example, switching from double to single precision mathematics shortened the lifetime of a decadal oscillation by increasing the background noise due to round-off error. In contrast, the failure of the oscillation in D2 is more likely to be a property of the particular precipitation scheme since the behaviour re-occurred starting from other initial conditions. The steady state that replaced the limit cycle in these experiments wa generally one with a fairly strong (> 7 Sv) reverse cell at high latitudes.

The mechanism for the decadal variability appears largely unchanged under the evaporative feedback. However, two factors produce a tendency for reinforcement of the fresh halocline in the northern basin, which may account for the collapse of the oscillation in some runs. Fig.4.24 above showed the widespread cooling of the sea surface under mixed boundary conditions at the time of minimum surface heat flux (4006.6 yrs). Fig.4.26c demonstrates that even at the warmest point of the cycle (4010.1 yrs), the SST along the northern boundary is still cool compared to the steady state under restoring boundary conditions. Averaged over the whole basin, and over one oscillation cycle, the mean SST cannot be any different from under restoring boundary conditions (except during the initial disequilibrium period) because it is so tightly constrained by the Newtonian boundary condition. However, the spatial distribution can be different, and in this case the consistently cooler temperatures along the northern boundary throughout the oscillation lead to reduced evaporation and hence freshening at this latitude under the evaporative feedback. Fig.4.35 shows the basin-mean sea

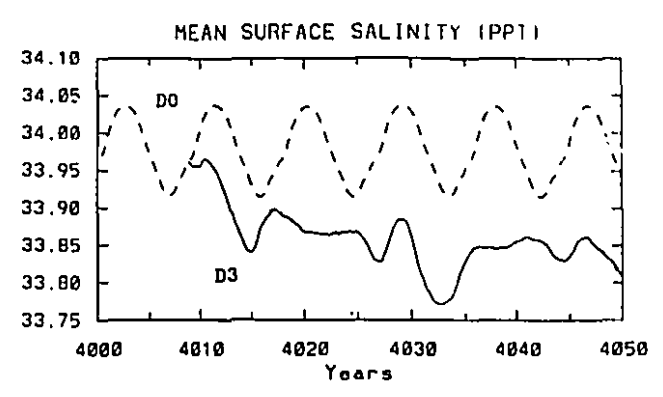


Figure 4.35: Basin mean surface salinity as a function of time, for D0 under mixed boundary conditions (dashed line) and D3 (solid line) with SST-evaporation feedback and precipitation scheme 3. The initial condition for D3 is the mixed boundary condition run at t=4008.8 when the basin mean surface heat flux changes sign from negative to positive.

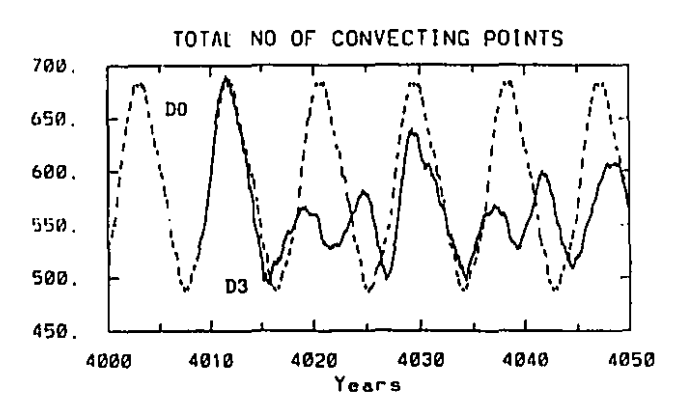


Figure 4.36: Total number of convective points as a function of time in D0 (dashed line) and D3 (solid line) as in Fig.4.31.

surface salinity dropping throughout the first 50 years of run D3 (after which it levels off).

The second factor is the nonlinearity demonstrated in Section 4.2.1. The SST-evaporation runs are deliberately started at the beginning of the warm half of the cycle as the surface heat flux switches from negative to positive. Initially the positive feedback between warm SSTs and enhanced SSSs is effective: the time series of total number of convective points in the basin (Fig.4.36) shows that the first peak is actually higher than under mixed boundary conditions. However, by the time the oscillation has been through a single cold phase, the convection never again recovers to the same level. Just as in the preliminary experiments,

fresh anomalies have a much more permanent effect than salty anomalies.

In summary, the SST-evaporation feedback does not appear to fundamentally alter either the mechanism or the timescale of the decadal variability, but both the stochastic effect and the net cooling at high latitudes under mixed boundary conditions may terminate the oscillation sooner.

4.4. Century Timescale Variability

As mentioned earlier, loop oscillations are a dominant source of variability in two-dimensional ocean mode's but appear rarer in three-dimensional OGCMs. The century timescale variability considered in the present chapter was obtained by Weaver et al. (1993) in both their "temperature-dominant" and "salinity-important" experiments under strong stochastic forcing in the (P-E) field. Unfortunately, the small amplitude of the variability and the large amplitude of the noise prevent any detailed analysis of the oscillation, unlike in studies such as Mikolajewicz and Maier-Reimer (1990), Mysak et al. (1993) and Winton (1993) where it was possible to trace the advection of salinity anomalies around the overturning loop. Attempts to intensify the variability in the present model by varying the magnitude of the stochastic forcing, by expanding the basin into two hemispheres or by exciting a resonant response to time-dependent forcing, as suggested by Winton (1993), met with little success. This section will show however the presence of century timescale variability under mixed boundary conditions and the potential influence of the SST-evaporation feedback.

The numerical model in this section is very similar to the one in the preceding section, and is described in Table 4.1. The restoring temperatures and salinities for the spin-up are smooth half-cosine functions rather than Levitus zonally-averaged data (Fig.4.4b) but the winds are unchanged (Fig.4.5). The diagnosed heat and freshwater fluxes resemble the decadal fields up to a point, but with much reduced freshening at the northern boundary and evaporation instead

of precipitation in the equatorial region (Fig.4.37). The control run under mixed boundary conditions consists of a 6000-year integration under the diagnosed (P-E) field plus a white noise component generated by the same subroutine as in Chapter 2 (Section 2.2), with a standard deviation of 0.48 m/y (~50% of the globally averaged annual mean precipitation), a fixed autocorrelation timescale of one month and an isotropic spectrum for wavenumbers 2 through 8 across a 60° wide basin (see Weaver et al. (1993) for more details). Physically, the white noise represents the effect of passing weather systems for example, which the ocean is expected to integrate into a red noise response (Hasselmann, 1976) irrespective of any deterministic long timescale variability.

The last 2000 years of the integration are retained for spectral analysis, during which the basin-mean surface heat flux, basin-mean kinetic energy density, maximum overturning streamfunction, and total number of convectively unstable points were all sampled at yearly intervals. Each time series is detrended (the remaining trends were very tiny) and the power spectral densities evaluated using MATLAB's intrinsic functions "spectrum" and "specplot", with a Hanning window and a 128-point FFT (fast Fourier transform). The power spectra are shown in Fig.4.38: both the heat flux and the kinetic energy time series have a clear amplification of the power at low frequencies superimposed upon a nearly-white background. Convection, which is sometimes used as a proxy for deep water formation (e.g. Mikolajewicz and Maier-Reimer, 1994, who presented time series of potential energy release through convection), has a similar peak at centennial timescales, but the response of the overturning streamfunction appears closer to pure red noise. These results are not easily interpreted, and further analysis (e.g. to formally differentiate the low-frequency peak from red noise) would require more sophisticated statistical techniques.

Fortunately, it is still possible to unambiguously demonstrate the influence of the SST-evaporation feedback. The results are shown in Fig.4.40 and Fig.4.41 for runs under two of the precipitation schemes described in Section 4.1 (the equilibrium P and E fields are pictured in Fig.4.39) and a similar time series of

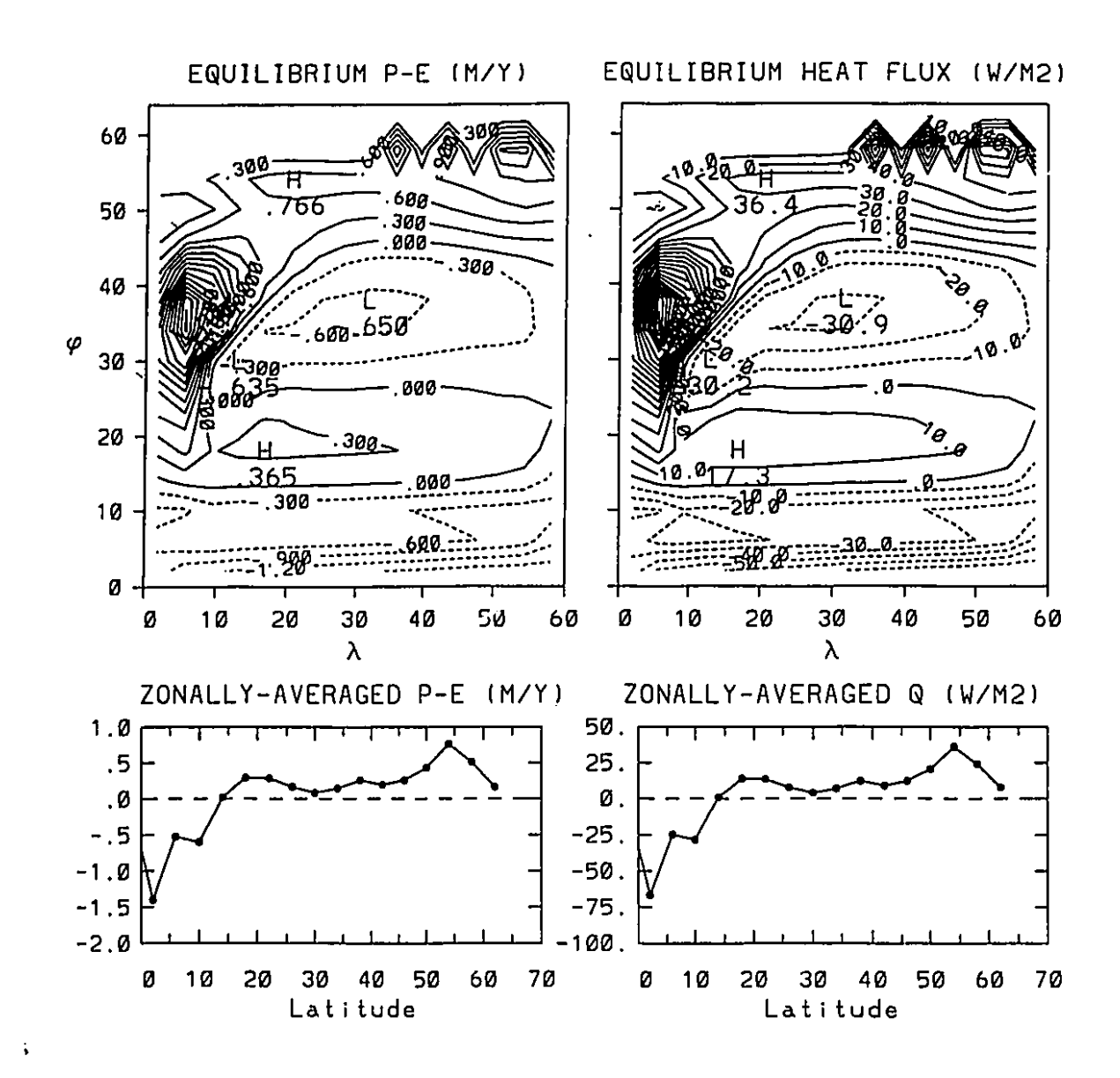


Figure 4.37: Equilibrium (P-E) (m/y) and surface heat flux (W/m²) diagnosed from the century spinup.

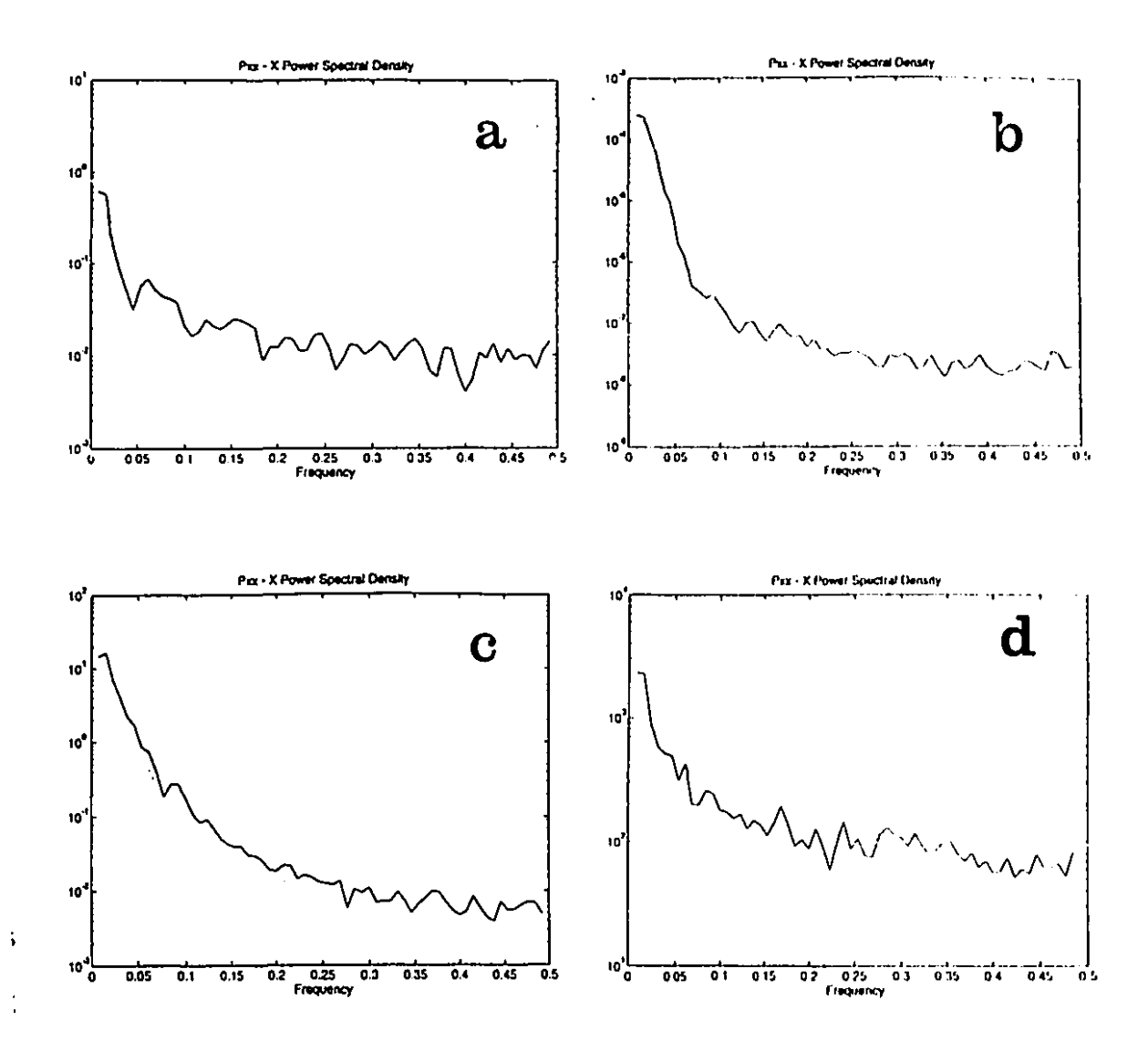


Figure 4.38: Power spectrum of time series of a) basin mean surface heat flux (W/m²), b) kinetic energy density (0.1 kg m⁻¹ s⁻²), c) maximum overturning (Sv), d) total number of convective points, in the control run under mixed boundary conditions. The units on the x-axis are cycles/year.

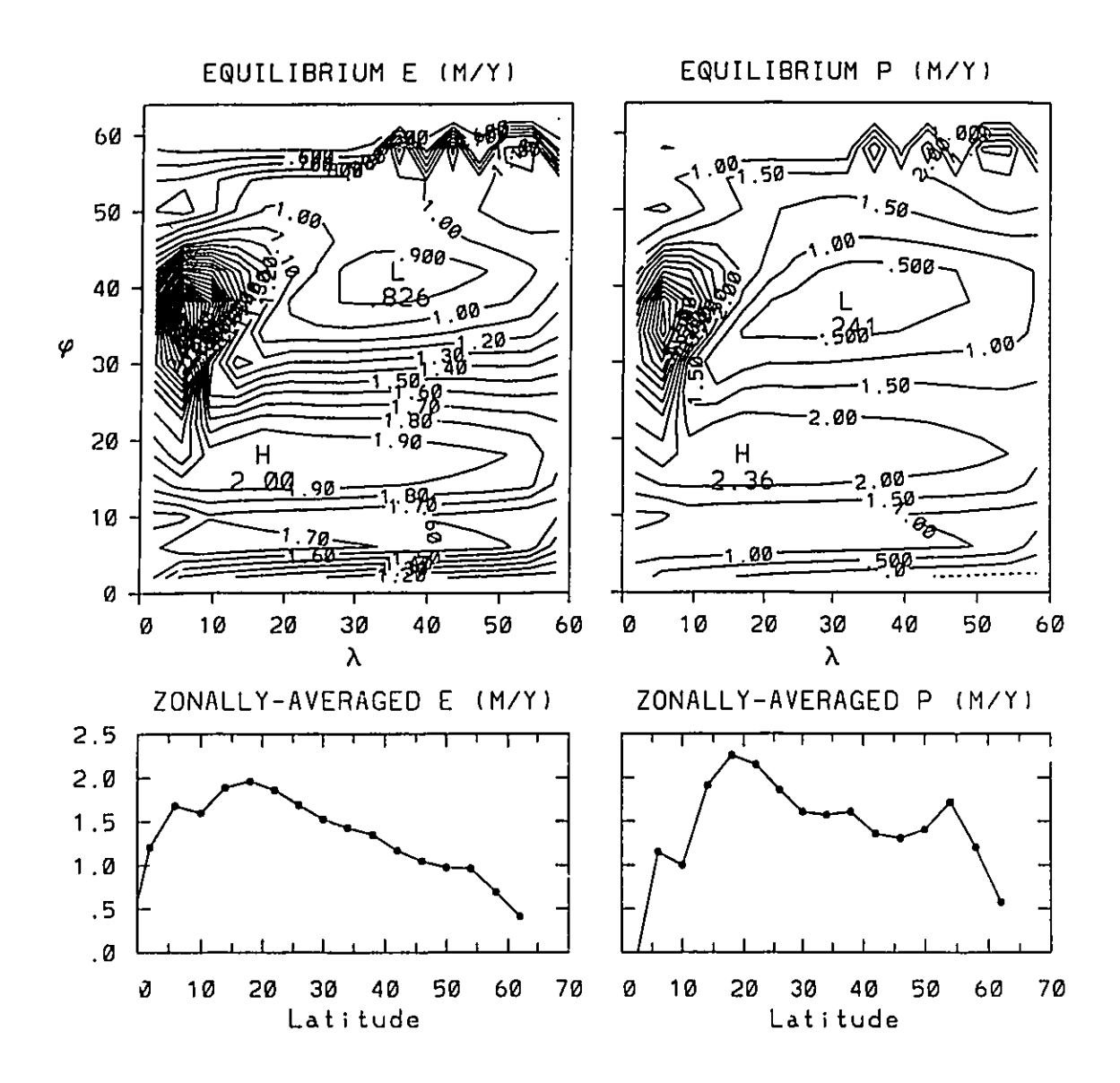


Figure 4.39: Equilibrium evaporation and precipitation (m/y) estimates for the century experiment.

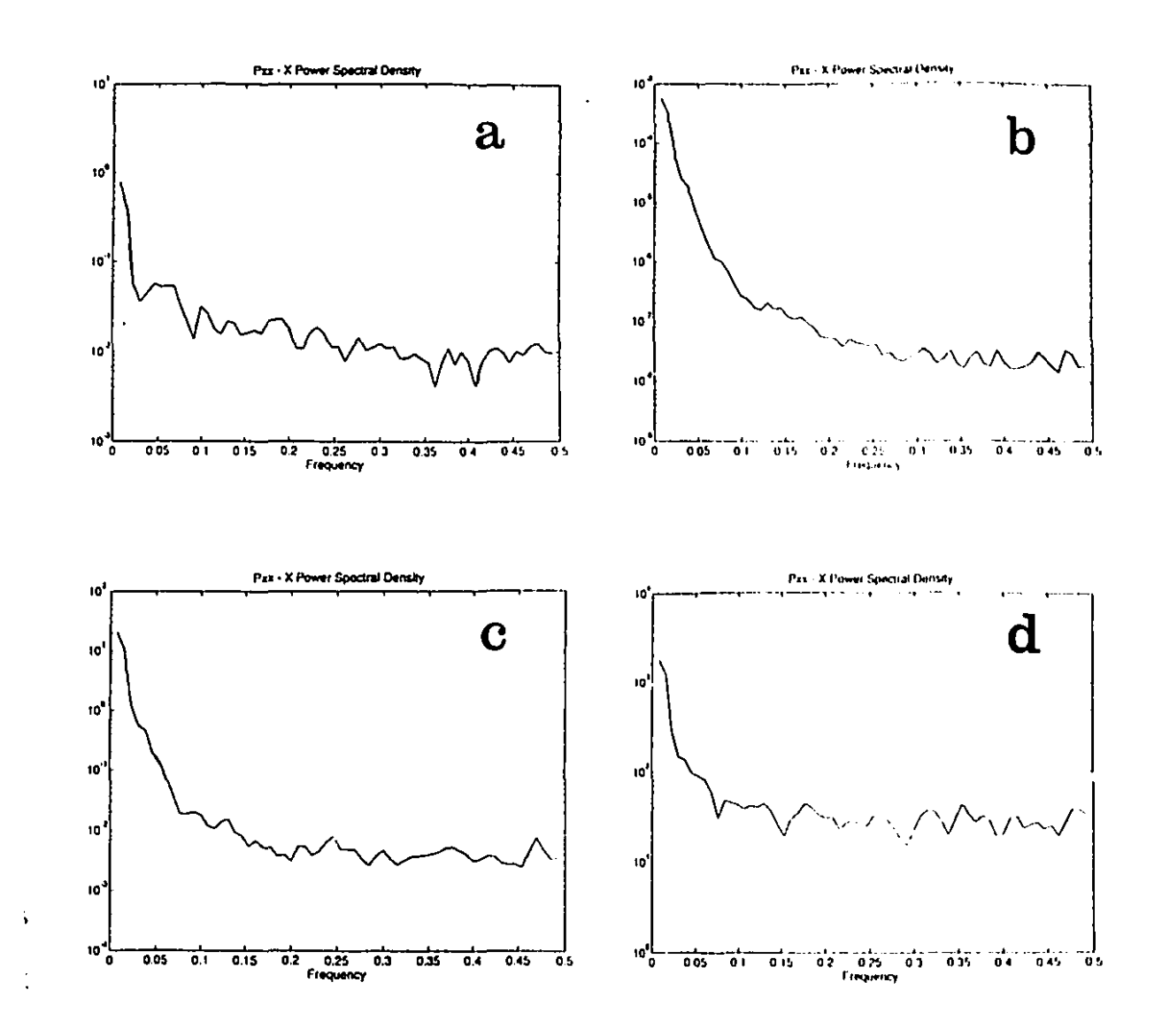


Figure 4.40: As in Fig.4.38, for the century experiment with evaporative feedback and precipitation redistribution scheme 2.

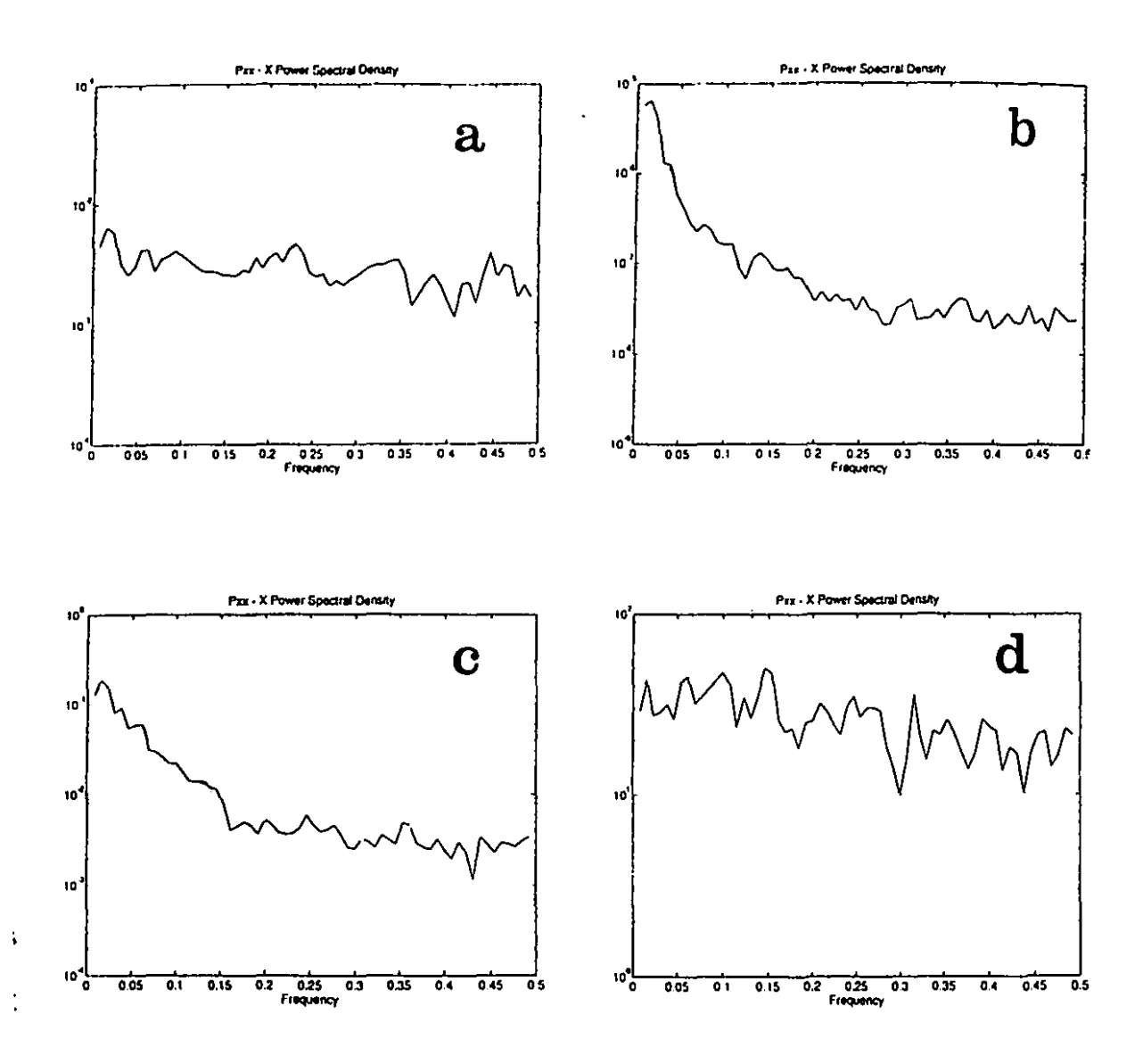


Figure 4.41: As in Fig.4.38, for the century experiment with evaporative feedback and precipitation redistribution scheme 1.

stochastic forcing. In run C2, with new precipitation distributed uniformly around latitude circles, spectra very similar to the control run were found (Fig.4.40). However, in run C1, with new precipitation spread uniformly over the basin, a nearly pure white noise spectrum was produced for the surface heat flux and convection, and visibly whitened spectra for the kinetic energy and meridional overturning (Fig.4.41). Clearly, the SST-evaporation feedback can be significant -however, scheme 1 is also the least realistic of all the precipitation schemes so this evidence for the sensitivity of century scale variability to (P-E) requires further testing.

4.5. Millennial Variability

Although millennial timescale variability is a well-known feature of the climate record (the Dansgaard-Oeschger oscillations), the extreme flush/collapse cycles on millennial timescales in the uncoupled ocean models of Weaver and Sarachik (1991b) and Weaver et al. (1993) may not appear completely realistic. However, Winton (1993) has confirmed that more reasonable amplitudes and a range of timescales may be produced under different salinity forcing shapes and diffusivities, and a number of other suggestions have been made for moderating flushes in OGCMs: the seasonal cycle (Myers and Weaver, 1992), stochastic freshwater forcing (Weaver et al., 1993), finite heat capacity of the atmosphere (Zhang et al., 1993), or multiple deep water formation locations (Winton, 1993). The SST-evaporation feedback is conceivably another factor that might alter the flush/collapse oscillations produced under mixed boundary conditions.²

² Other explanations for the Dansgaard-Oeschger oscillations involving other aspects of the hydrological cycle have also been suggested: e.g. interbasin water vapour transport, Broecker et al. (1990b) and nonlinear ice feedbacks, Birchfield et al. (1994), but only strictly internal ocean variability will be considered here.

4.5.1. Under Mixed Boundary Conditions

A number of details (winds, mixing coefficients, equatorial boundary conditions, etc.) differ between the model in this section and those in the previous sections, and are listed in Table 4.1. The number of levels was also increased from the 15 in Weaver et al. (1993) to 23 in this study because of numerical difficulties. The diagnosed (P-E) field is shown in Fig.4.42 and has the strongest high latitude freshening of any of the models in this chapter. The control run under mixed boundary conditions starts from the end of the spin-up under restoring boundary conditions: its evolution is shown in Fig.4.43. Flushes are identified by extreme peaks of surface heat loss > 110 W/m², spaced very regularly at intervals of just under 2000 years (save for the first which is delayed somewhat). In the real world, surface heat fluxes of several hundred W/m² do occur in the Gulf Stream region in January according to Esbensen and Kushnir (1981) - however the value reported here is a basin average and is associated with overturning streamfunction maxima of nearly 190 Sv. The nearly collapsed thermohaline circulation in between flushes is illustrated in Fig.4.44, and is familiar in appearance from studies of the polar halocline catastrophe phenomenon. The northern half of the basin is haline stratified (and unstably thermally stratified over at least the top 500 m) driving a reverse overturning cell, while the southern half is more conventionally thermally stratified with a positive overturning circulation. Sinking occurs to intermediate depths (1500 m) between the two cells, and the forward cell appears to penetrate a little way below the reverse cell. The deep ocean is very warm and horizontally quite homogeneous due to the absence of deep convection, and a surface heat uptake of a few W/m² in basin average is still occurring. The first flush occurs after ~4200 years: convection breaks out first at the eastern boundary and spreads counterclockwise around the northern and western margins until the whole northern half of the basin is affected. The fresh halocline then starts to reform in the northwest corner.

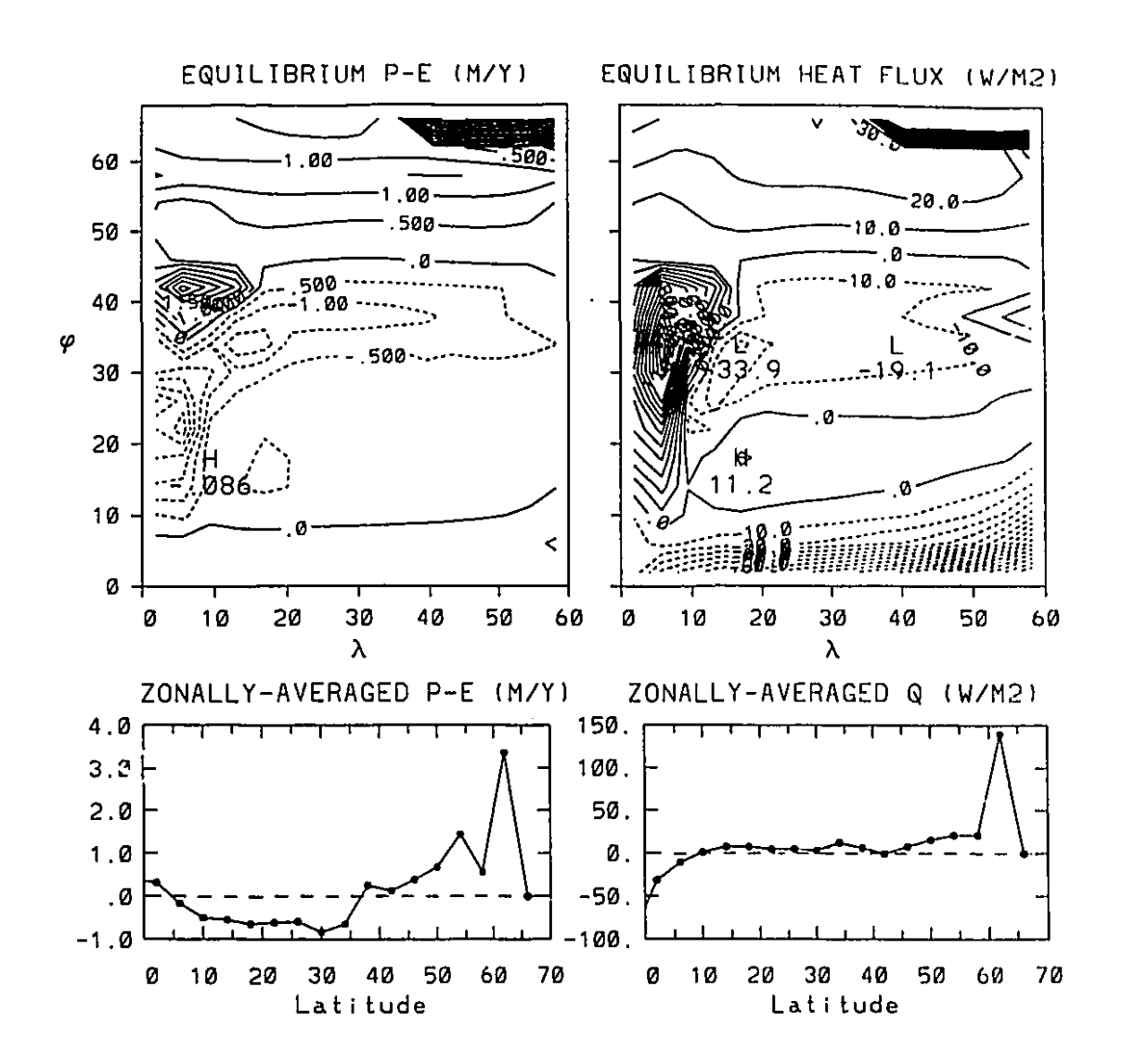


Figure 4.42: Equilibrium (P-E) (m/y) and surface heat flux (W/m²) diagnosed from the millennial spinup.

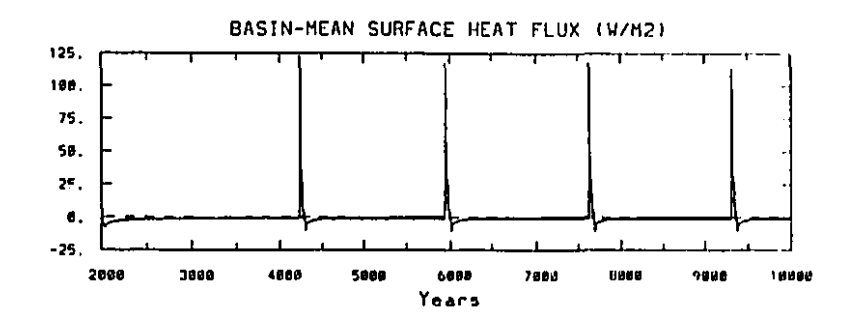


Figure 4.43: Basin mean surface heat flux (W/m²) as a function of time for the millennial variability run under mixed boundary conditions. The initial condition is the end of the spinup under restoring boundary conditions.

4

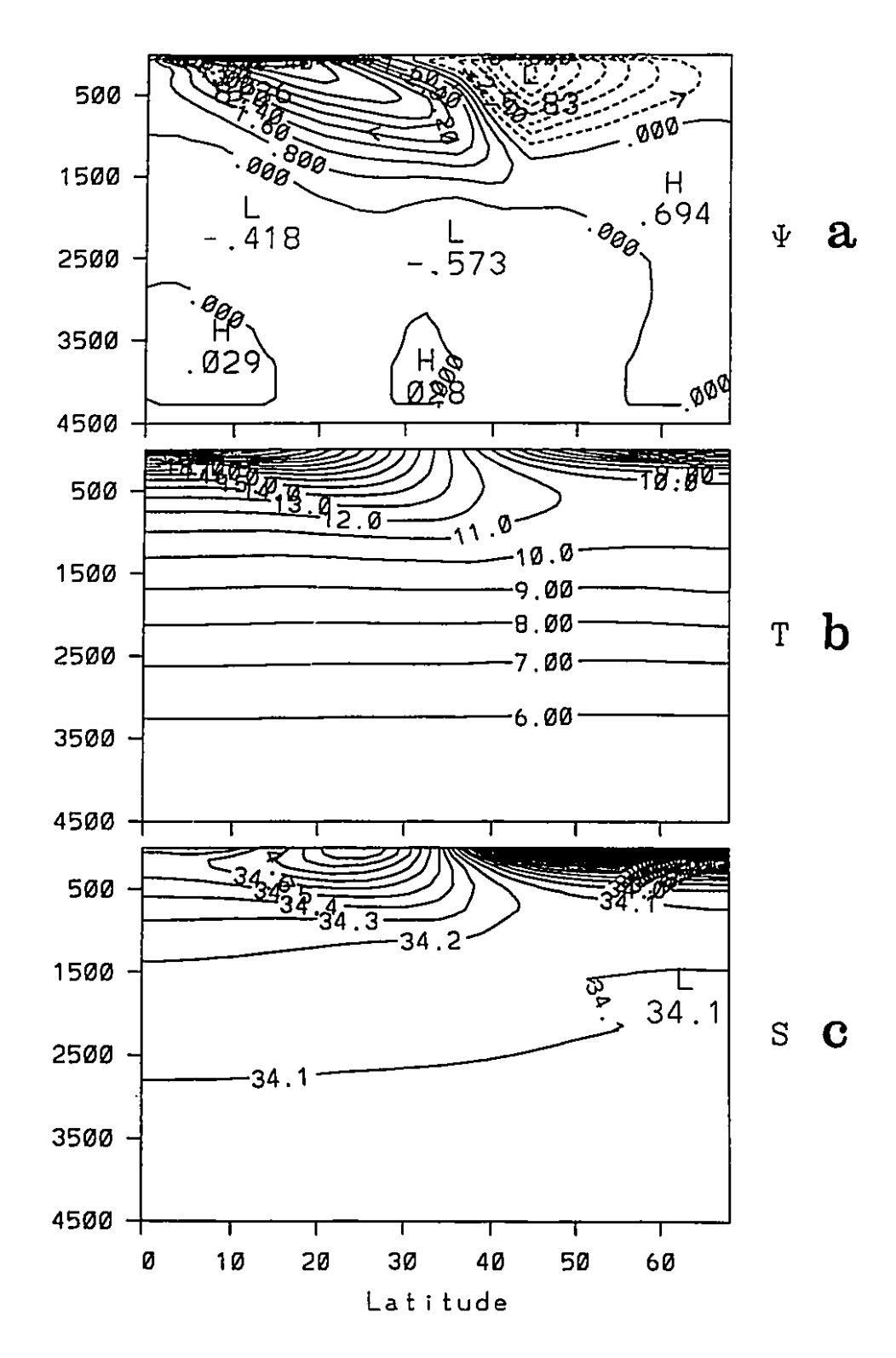


Figure 4.44: a) Meridional overturning at t=2698.2 years in the millennial run under mixed boundary conditions b) zonally-averaged temperature (°C) c) zonally-averaged salinity (ppt).

The equilibrium evaporation and precipitation in the millennial model are illustrated in Fig.4.45. As mentioned, the catastrophically large surface heat fluxes in Fig.4.43 are physically implausible; it is thus not necessarily alarming to find that the simple surface heat budget referenced to the present-day climate in Section 4.1 breaks down during these events. Negative evaporation is predicted at one gridpoint in the eastern equatorial region during flushes. This is associated with a SST which is so cold compared to the restoring temperature (perhaps due to upwelling associated with the impossibly strong overturning) that the heat flux into the ocean exceeds the prearranged radiative input. Although the negative latent heat flux required to make up the deficit is small, it proved to be difficult to eliminate the problem by manipulating the profile of prescribed net radiation, and the pragmatic approach of simply setting negative values to zero was therefore accepted with resignation. In the future, a better boundary condition on temperature may render this measure unnecessary.

4.5.2. With Evaporative Feedback

A variety of responses were triggered in this model under the various precipitation redistribution schemes. In M3 and M4, decadal variability was excited (Fig.4.46c,d) while in M6, the flush/collapse sequence was preserved but with a much shorter timescale of only about 400 years (Fig.4.46f), and the remaining three experiments exhibited a combination of these two behaviours (Fig.4.46a,b,e).

The last 500 years of the decadal oscillation in run M3 are illustrated in Fig.4.47a, along with an expanded view of the last 10 years (Fig.4.47b). The evolution of the maximum and minimum streamfunction over the period of the oscillation is very similar to the decadal variability in Section 4.3 (compare Figs.4.47c and 4.21c), as is the timing with respect to the peaks of surface heat flux. Intuitively, it seems plausible that the same mode of oscillation could be

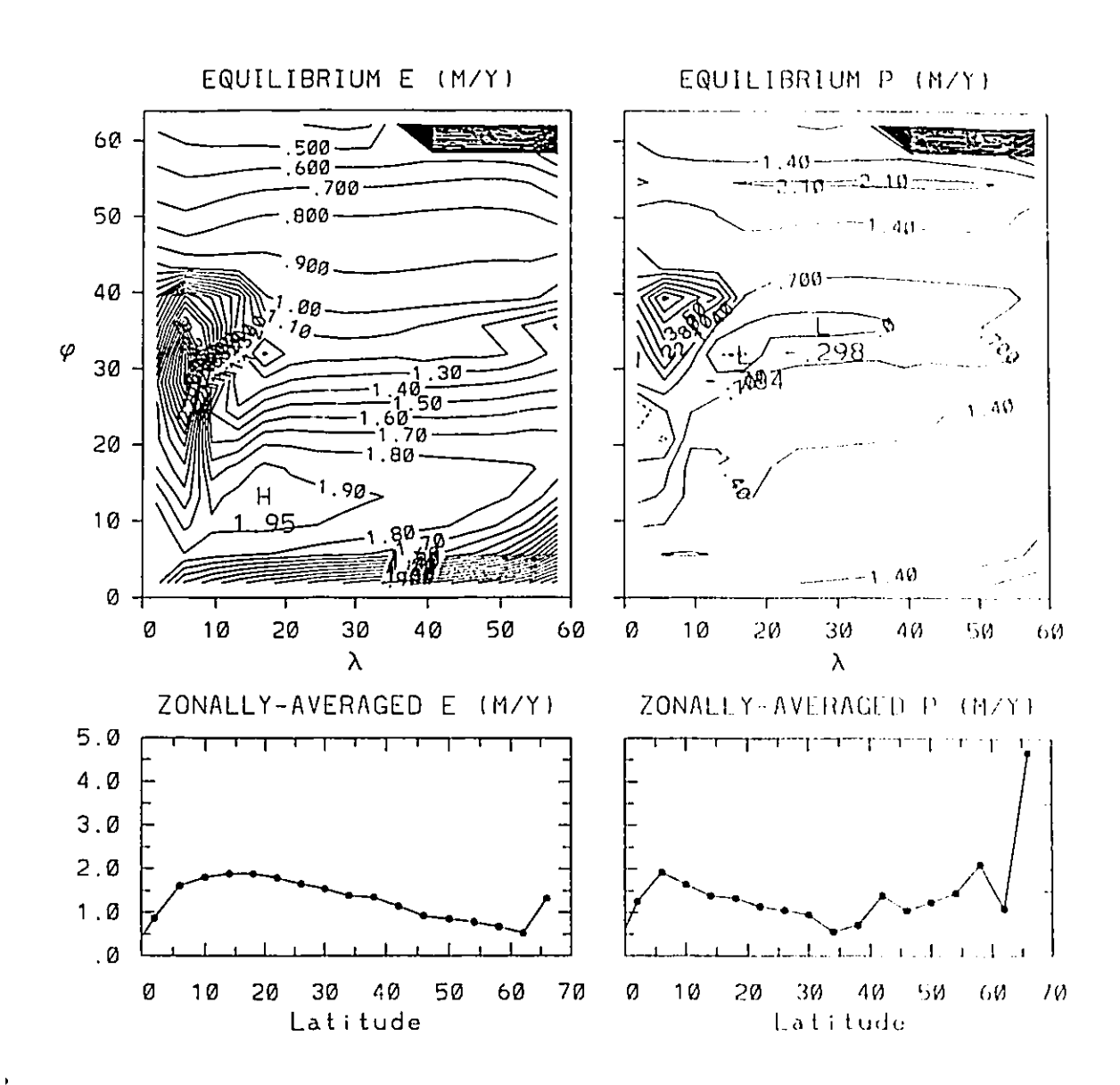


Figure 4.45: Equilibrium evaporation and precipitation (m/y) estimates for the millennial experiment.

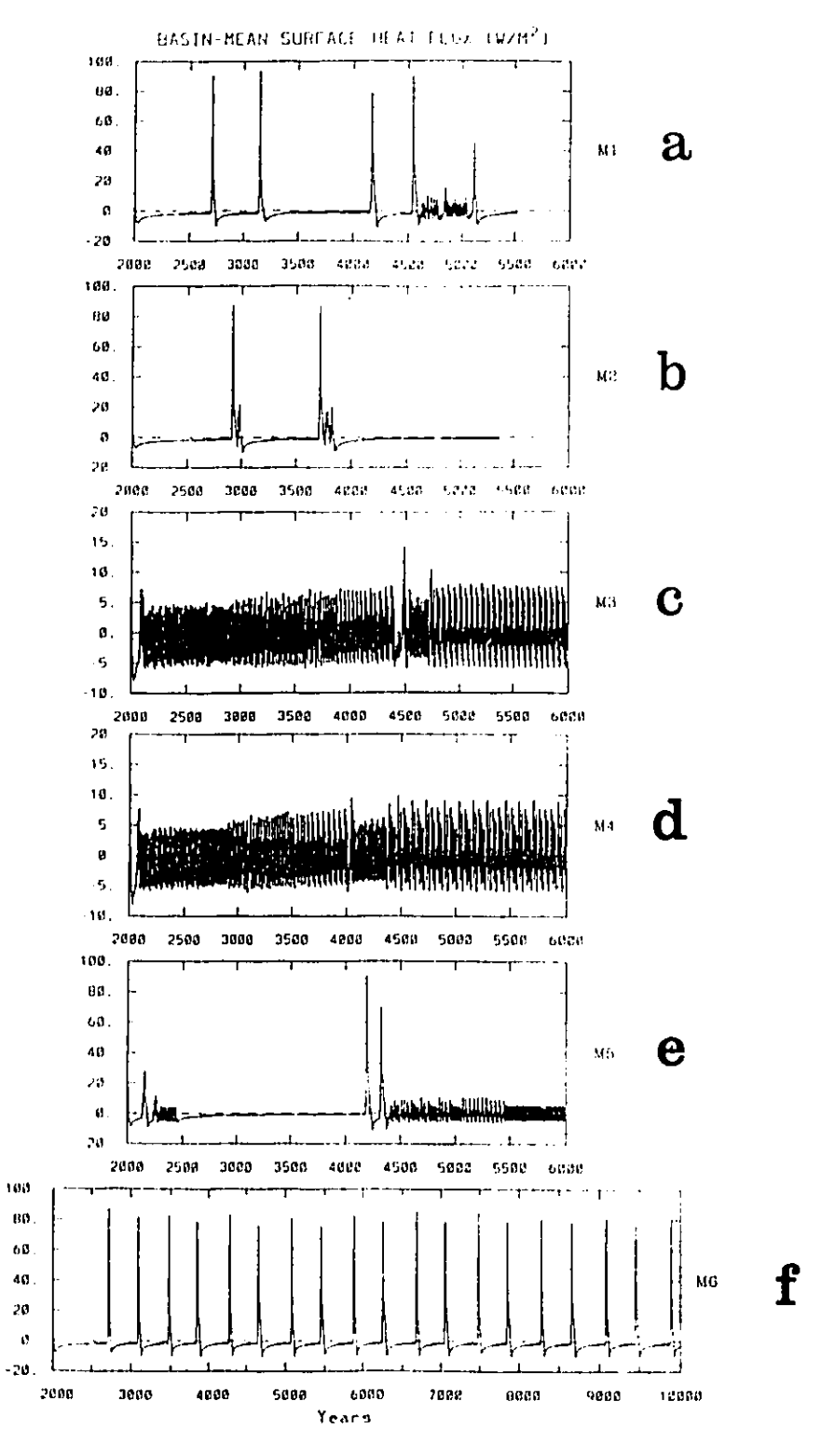


Figure 4.46: Basin mean surface heat flux (W/m^2) as a function of time for millennial experiments under the six different precipitation schemes (MI) to M6). The initial condition for all runs is the end of the spinup under restoring boundary conditions.

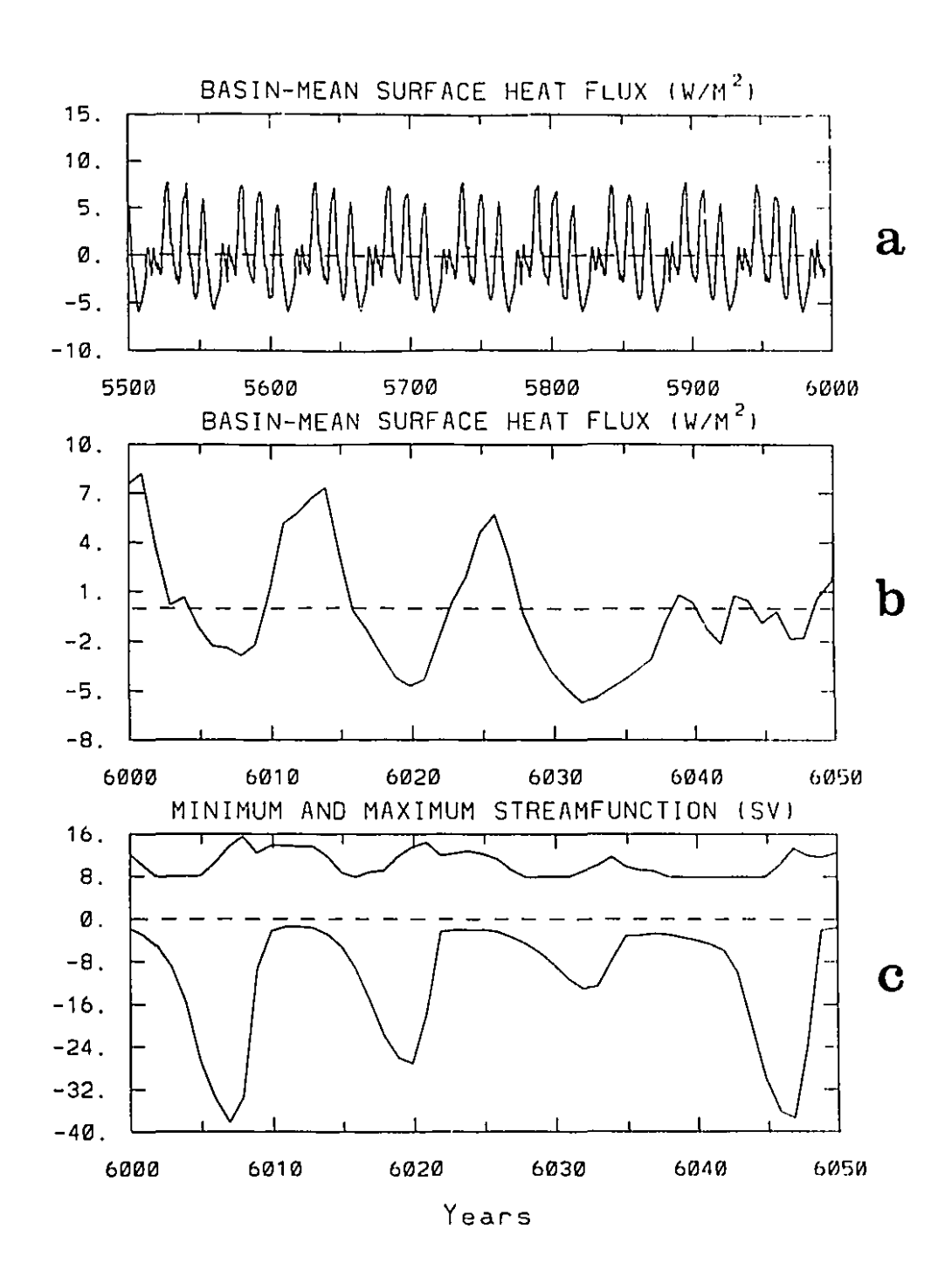


Figure 4.47: a) Last 500 years of surface heat flux (W/m^2) time series for experiment M3 under SST-evaporation feedback and precipitation scheme 3, b) last 50 years of the same time series, c) 50-year time series of minimum and maximum streamfunction (Sv).

excited under the millennial (P-E) field, given the overall resemblance of the boundary conditions. One difference however is that under the magnified northern freshening in the millennial case, the reverse cell grows to nearly 40 Sv during some cycles compared to only about 16 Sv in the decadal runs. It is not possible to establish conclusively why the decadal oscillation is triggered in experiment M3 while the thermohaline circulation stays collapsed in run M6, eventually leading to a flush, but one possible clue is that the anomalous (P-E) calculated just before the onset of the decadal variability in run M3 has net evaporation over most northern latitudes in M3 where M6 has precipitation.

The more startling result is the short timescale of the flushes in M6. Under the evaporative feedback, flushes are occurring five times more often, but releasing nearly as much heat in each event as in the control run. Over the course of the eight thousand year integration, a total of 1.60×10^{23} J of heat is expelled in M6 compared to 0.55×10^{23} J or only one third as much in the control run. In the stochastically forced runs of Weaver et al. (1993) in contrast, the magnitude of flushes decreased as their frequency increased.

The level-mean vertical temperature profiles at 2698 years (just before the first flush in M6) do not show the run with evaporative feedback storing appreciably more heat during the collapsed stage than the control run - compare the solid curve and the open circles in Fig.4.48b. Instead, M6 appears to be more efficient at evacuating the stored-up heat during the flush. The efficiency is low in both runs: as seen by the dashed lines in Figs.4.48b and c, the deep ocean is still much warmer even right after a flush than it ever was under restoring boundary conditions. (The warmer ocean before the first flush in the control run compared to M6 - solid lines in Figs.4.48b and c - is simply because of the longer delay before flushing.) The control run cools right down to the ocean floor during its first flush, while only the top 3500 m are affected in M6. In terms of basin mean temperature however, both lose approximately half of the increase since the switch from restoring boundary conditions, which is $1/2 \times 3^{\circ}C = 1.5^{\circ}C$ for M6 and $1/2 \times 5^{\circ}C = 2.5^{\circ}C$ for the control run. Since M6 flushes five times more often

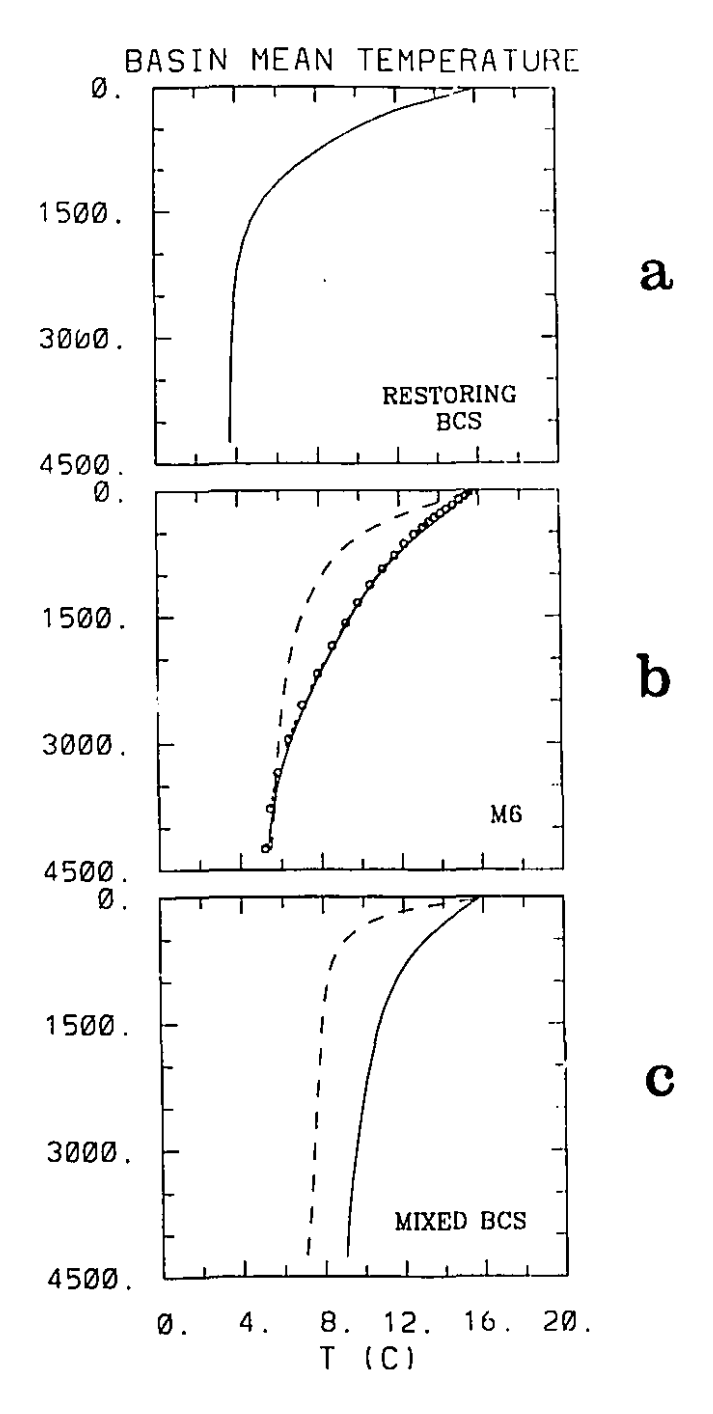


Figure 4.48: Basin mean vertical temperature (°C) profile in the runs a) under restoring boundary conditions b) M6 under SST-evaporation feedback c) control run under mixed boundary conditions. In b) and c), the solid line is immediately before the first flush in each experiment (at t=2698.2 years in b and t=4217.1 years in c) and the dashed line is immediately after the flush (t=2758.1 years and t=4277.1 years). The open circles in b) are the vertical temperature profile of the control run at the earlier time (t=2698.2 years).

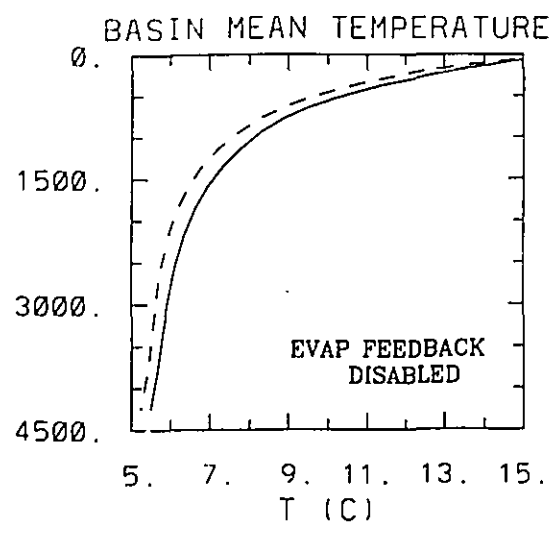


Figure 4.49: Basin mean vertical temperature (°C) profile immediately after the first flush (t=2758.1 years) for experiment M6 (solid line) and for a test run in which the evaporative feedback is disabled just before the flush starts (dashed line).

than the control run thereafter, a threefold increase in efficiency is again estimated. The key is simply that the rate of warming slows after the first few hundred years, as the heat has to penetrate to deeper and deeper levels through diffusion, so it is more efficient (in the sense of releasing more heat to the atmosphere) to go through the early stages of the collapsed phase more often. The stochastically-forced runs of Weaver et al. (1993) therefore probably also have increased "efficiency" (in the sense of releasing more heat over a fixed period of time) since many smaller fluctuations are interspersed between the diminished flushes.

Surprisingly, the role of the SST-evaporation feedback during a flush appears to be to hinder it rather than to help it, at least under this precipitation parameterization. In Fig.4.49, two vertical temperature profiles are compared right after the first flush in run M6 and in an additional experiment in which the evaporative feedback was switched off immediately upon initiation of the flush. The basin cools right down to the ocean floor in the latter experiment, and the total surface heat loss is increased by about 20%. (The second flush is also delayed for > 1000 years if the evaporation is not switched back on after the first flush.) The reason is shown in Fig.4.50: during the collapsed stage, both the

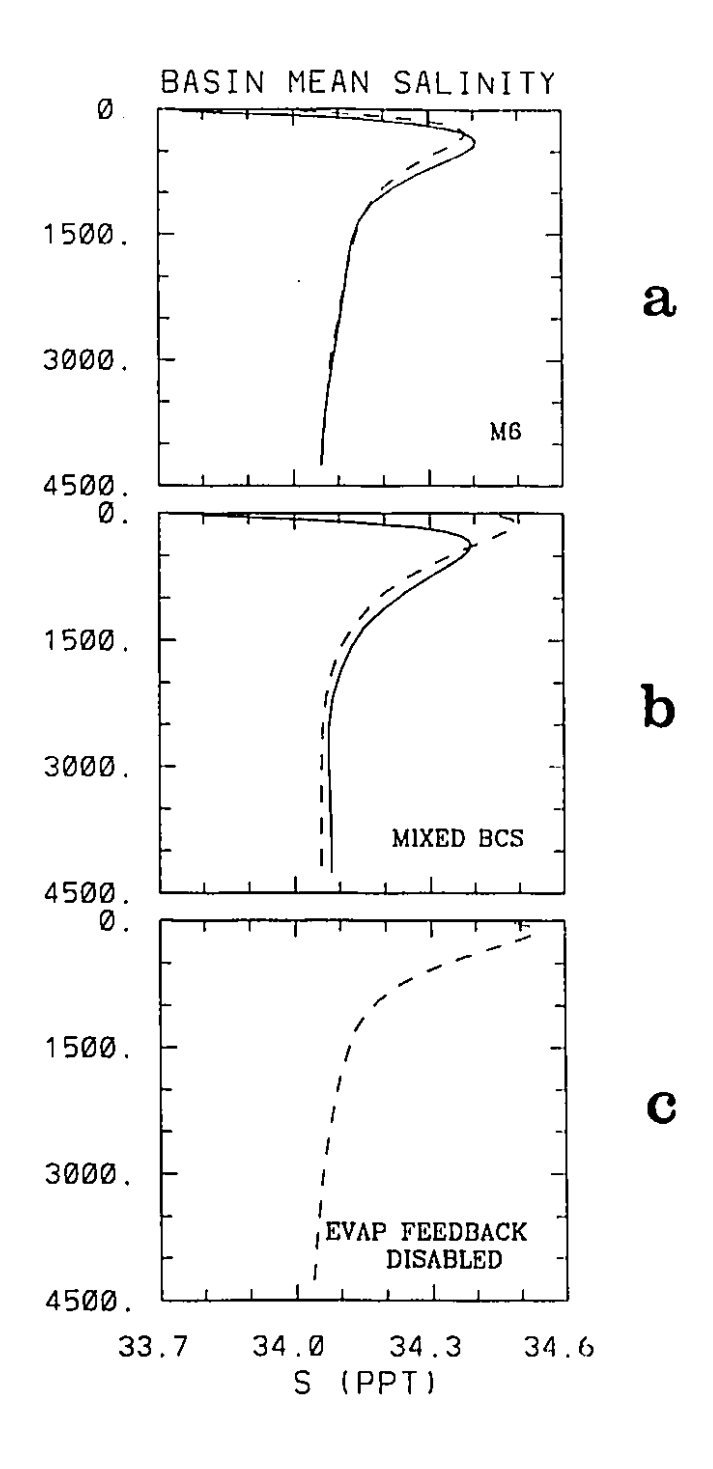


Figure 4.50: Basin mean vertical salinity (ppt) profile in a) M6 b) under mixed boundary conditions c) the test run where the evaporative feedback is disabled just before the flush starts. In a) and b), the solid line is before the beginning of the flush and the dashed line is 20 years into the flush. Only the dashed line is drawn in c) since the initial condition is the same as in M6.

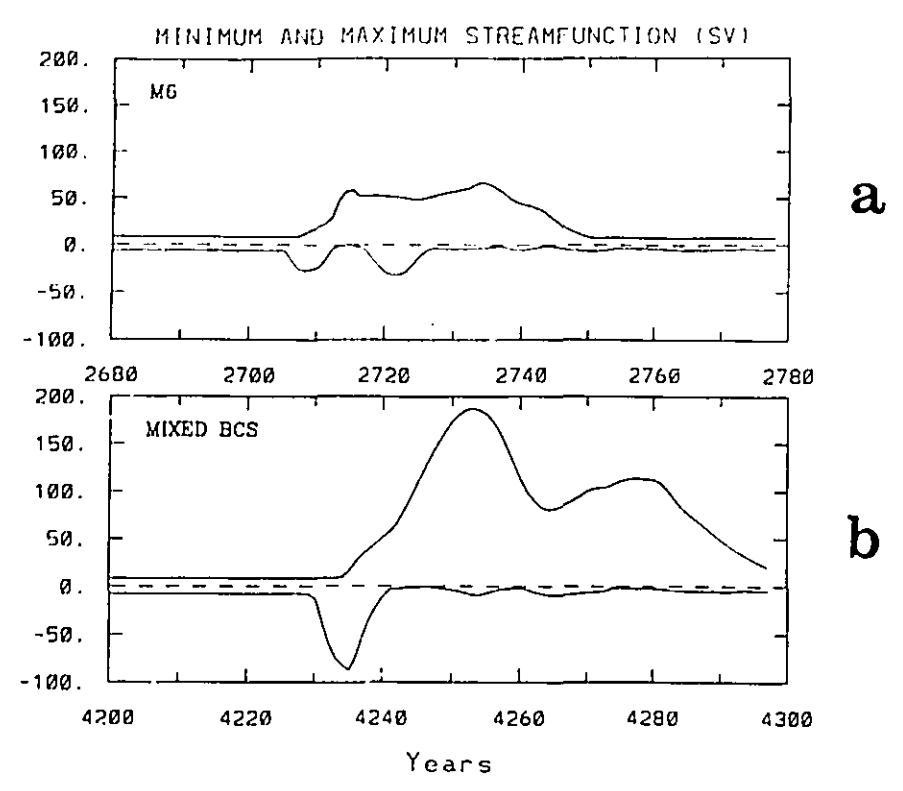


Figure 4.51: Maximum and minimum overturning (Sv) as a function of time during the first flush in a) M6 b) under mixed boundary conditions.

control run and M6 are stabilized by a fresh surface layer in basin average (Figs.4.50a and b, solid lines). The halocline is almost completely destroyed during the flush in the control run (Fig.4.50b, dashed line) and also in the additional experiment where the evaporative feedback is disabled (Fig.4.50c, dashed line) but persists throughout the flush in M6 (Fig.4.50a, dashed line). The precipitation scheme in M6 distributes new precipitation over the equilibrium P field, as described in Section 4.1. Two strong maxima of freshening are found adjacent to the northern boundary of the basin in this field (Fig.4.45); this is the origin of the halocline which reappears at the termination of the flush. The large anomalous evaporation due to surface heat loss during the flush is thus transported to high latitudes and helps to limit the magnitude of the flush under this precipitation scheme. This is seen also in the evolution of the maximum streamfunction during the first flush, which peaks at less than 70 Sv in M6 while the control run continues to climb to nearly 200 Sv (Fig.4.51). In more general

situations however, one might expect the anomalous evaporation to enhance convection during the flush - this may occur even in the present run, where it could be contributing to the enhanced efficiency.

The role of the evaporation feedback between flushes is more interesting. The difference in meridional overturning between M6 and the control run at 2698 years (just before the first flush in M6) is shown in Fig.4.52a: the reverse cell at high latitudes is stronger by nearly 1 Sv while the forward cell is slightly weaker. This is associated with an intensification of the meridional surface salinity gradient, due to anomalous freshening in the northern two thirds of the basin and an opposite tendency at low latitudes (Fig.4.52c). The cause is the cooling/warming of the surface at high/low latitudes compared to the spin-up under restoring boundary conditions with its one basin-wide overturning cell.

The difference in zonally-averaged temperature between M6 and the control run at this time (Fig.4.52b) is small (< 1°C everywhere) as already mentioned, but its distribution is significant. The largest warming occurs near the centre of the basin, immediately below the fresh halocline. In a two-dimensional sense, this may be understood as an anomalous advection by the intensified reverse cell (Fig.4.52a) of the mean temperature stratification (Fig.4.44b). Warm water is subducted at midlatitudes between the reverse and forward cells, and upwelled through the thermocline at high latitudes, producing the two maxima in temperature difference seen in Fig.4.52b. For the salt transport, the Ekman component is relatively more important: this agrees with Marotkze (1990) who found that the wind-driven salt transport became important following the development of a polar halocline at previously unstratified polar latitudes. The extra warming in the subsurface layer destabilizes it with respect to the surface, while the extra salt destabilizes it with respect to the deep ocean. It has not been attempted to quantify which of the heat and salt transports is the most important in triggering the early onset of the flush in M6; the point made is merely that it is the fast upper-ocean advective timescale of these processes that allows the usual long (millennial) diffusive timescale to be bypassed in M6.

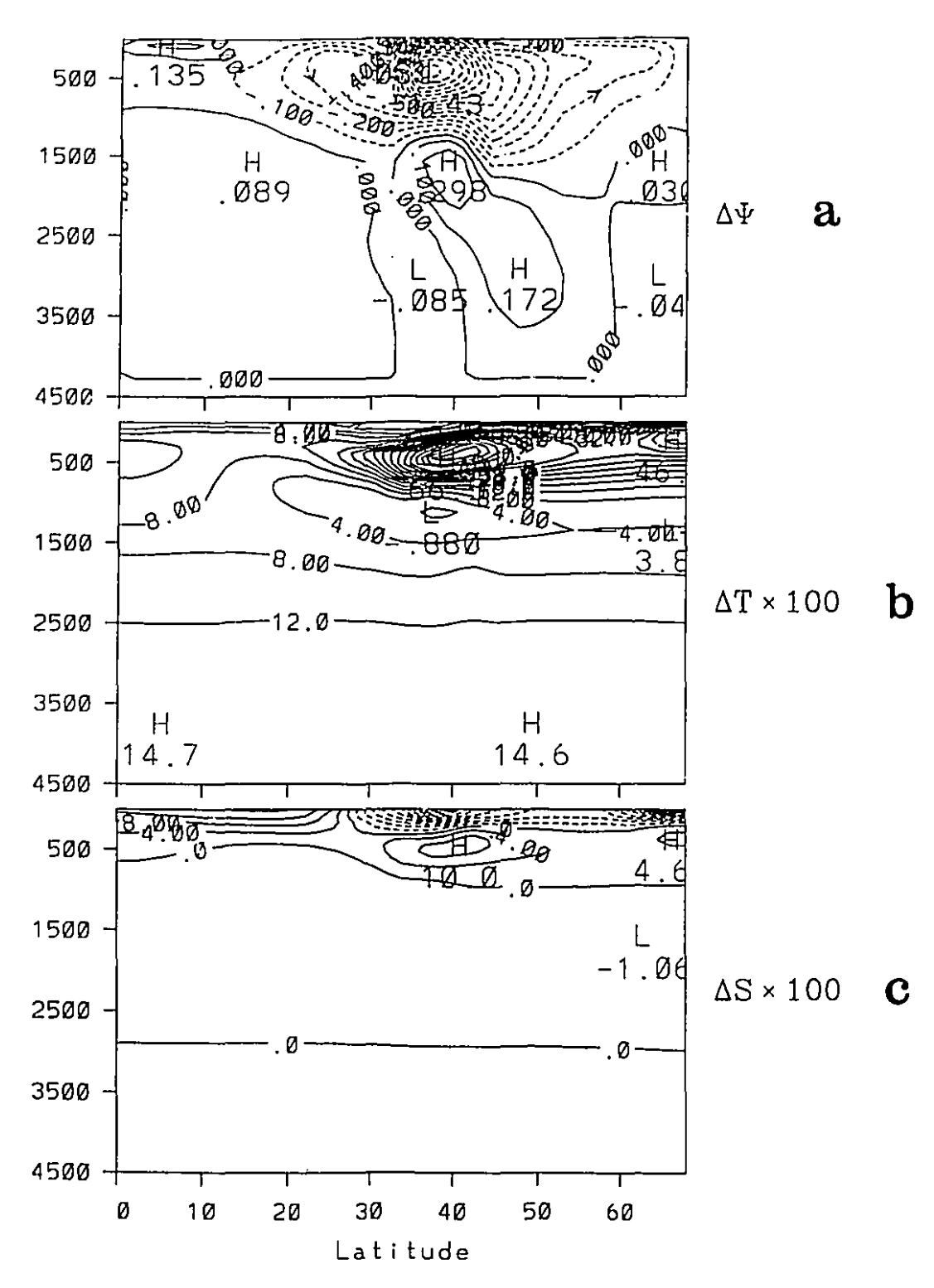


Figure 4.52: Difference in a) meridional overturning streamfunction (Sv) b) zonally-averaged temperature (100 x $^{\circ}$ C) c) zonally-averaged salinity (100 x ppt) at t=2698.2 years in M6 minus the control run under mixed boundary conditions.

The fast timescale is actually latent even in the control run under mixed boundary conditions. This is seen by decomposing the high latitude ocean (north of 38°N) into three layers: the top 100 m (the polar halocline layer), an intermediate layer about 1000 m thick containing the thermohaline overturning cell, and the deep ocean below this. The mean temperature and salinity in each layer is plotted as a function of time in Figs.4.53 and 4.54 for experiment M6 and the control run. In both runs, only the deep layer warms on the diffusive timescale, while the intermediate layer warms rapidly within the first century or so. Thus even a semi-collapsed overturning circulation may play a role in hastening the onset of a flush, and preventing the extreme warming of the deep ocean. (Surprisingly, the deep ocean also freshens very slightly between flushes, unlike in Weaver and Sarachik (1991b), where horizontal and vertical diffusion spread salt out from the equatorial surface ocean. The reason is unknown, but may reflect some detail like the relative strengths of the forward and reverse cells in the semi-collapsed state.)

In conclusion, the flush/collapse oscillations are relatively sensitive to the SST-evaporation feedback, providing yet another reason to suspect that such variability found in idealized uncoupled ocean models may be considerably modified in the real world. Different types of variability were produced under the different precipitation parameterizations; however, the intensification of the polar halocline between flushes under SST-evaporation feedback is expected be a general property.

In evaluating the parameterization developed in Section 4.1 for climate studies, a weak point remains the uncertainty associated with atmospheric water vapour transport, and ultimately of course a dynamic atmospheric model will be needed to most accurately forecast the location of precipitation. An easier task for future studies will probably be to take into account the atmospheric warming associated with latent heat release upon condensation. However, the simple parameterization suggested in this chapter has served its purpose well, in demonstrating the feedback between the thermohaline circulation and the

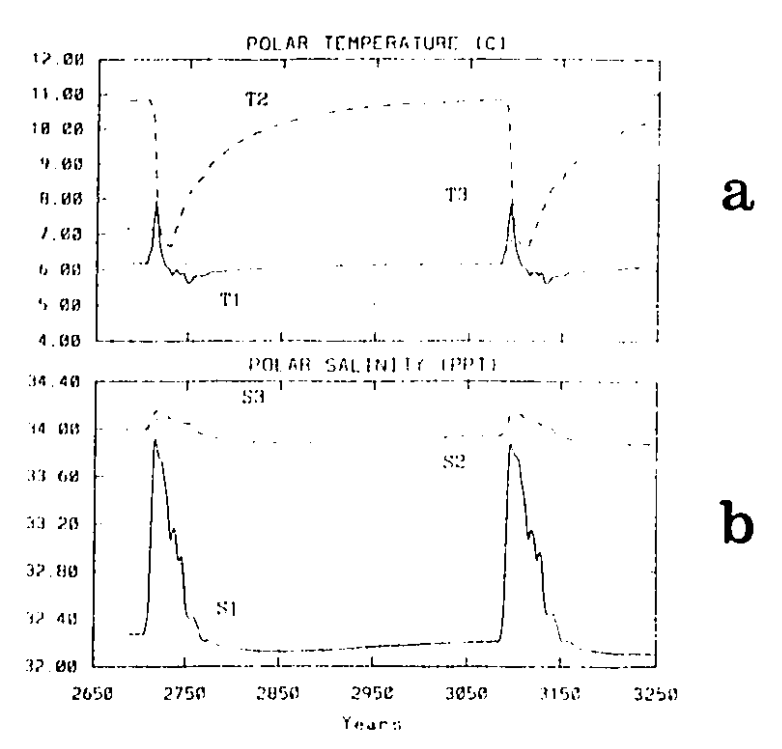


Figure 4.53: a) Time series of the average temperature (°C) north of 36°N in: TI, the upper ocean above 100 m, T2 the intermediate layers between 100 and 1025 m, T3 the deep ocean below 1025 m, for the first two flushes in experiment M6. b) Similar time series for salinity.

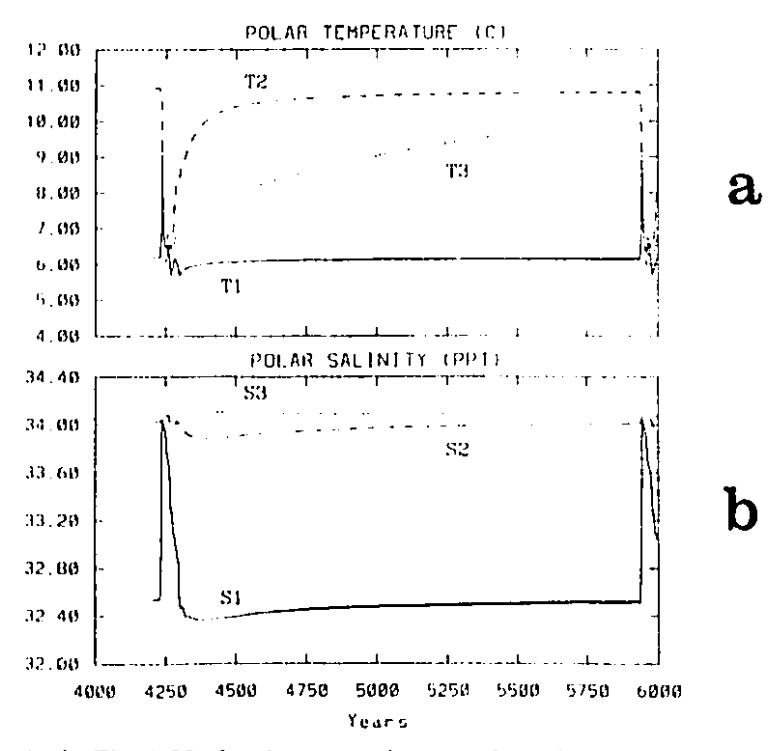


Figure 4.54: As in Fig.4.53, for the control run under mixed boundary conditions.

hydrological cycle, and in providing a first estimate of its magnitude.

Chapter 5

Conclusions

A first theme of this thesis has been the role of basin geometry in determining the uniqueness of the present-day thermohaline circulation. In Chapter 2, the asymmetric geometry of the idealized two-basin model was found to strongly favour equilibria with sinking in the Southern Ocean only or also in the North Atlantic. Under restoring boundary conditions, the location of deep water formation could be predicted from the maximum in surface restoring density. North Atlantic sinking was favoured over North Pacific because of the northern extension of the basin, while the influence of southern sinking was weakened by the Antarctic Circumpolar Current isolating the high southern latitudes. Under mixed boundary conditions, *Conveyors* and *Southern Sinking* equilibria were preferred over *Inverse Conveyor* or *Northern Sinking* states even under a (P-E) field with more precipitation over the North Atlantic than over the North Pacific. This conflicts with the suggestion by Broecker et al. (1990a) that the modern thermohaline circulation is driven by the atmospheric freshwater export from the Atlantic.

Another new result was the range of *Conveyor* equilibria under mixed boundary conditions. The hypothesis by Toggweiler and Samuels (1993a, 1995) that the Southern Ocean winds govern the outflow of North Atlantic Deep Water was found to be inconsistent with the results from the two-basin model, where the Atlantic outflow was instead almost linearly proportional to the maximum overturning. A potential role for the southern hemisphere winds as one factor changing the large-scale pressure gradients that drive the meridional overturning was nonetheless acknowledged. The exceptional feature in rare cases with North Pacific sinking was a very strong halocline in the Southern Ocean, where it caused the sign of the pole-to-pole surface density contrast to be reversed. The importance of the Southern Ocean to the global thermohaline circulation was

further emphasized by the approximately linear relationship between the Atlantic overturning and the meridional gradient of zonally-averaged depth-integrated steric height from the northern boundary of the ocean to the southern tip of Africa. Physically, this may reflect frictional control of the western-intensified thermohaline circulation, providing partial justification for the use of simple frictional flow laws in box models of the thermohaline circulation. On the other hand, the linear relationships between meridional velocity and local meridional density gradient that are postulated in most two-dimensional plane models of the overturning circulation could not be validated, emphasizing the need for improved dynamics in this case.

The climatology of the global model in Chapter 3 was also strongly influenced by the basin geometry. A *Conveyor* circulation was a robust characteristic of the model under restoring, mixed and (diagnosed) flux boundary conditions, and appeared in vestigial form even under artificial symmetric restoring boundary conditions (and no winds). Under mixed boundary conditions, the response to perturbations of the Alantic thermohaline circulation was characterized by prominent temperature and salinity changes in the South Atlantic, associated with anomalous horizontal advection set up after the passage of propagating waves. Global teleconnections involved a warm water route through the Indian Ocean, while observations suggest instead the predominance of the cold water route through Drake Passage, implying that even models (like this one) tuned to reproduce the right global tracer distributions and overturning circulation may still be unreliable for climate prediction studies.

A more detailed investigation of the water masses in the Southern Ocean region of the global model was thwarted by the absence of faith in the heat and freshwater fluxes diagnosed from a restoring boundary condition. The surface fluxes from the Canadian Climate Centre second generation atmospheric general circulation model also had to be discarded, on the basis of the implied ocean heat and salt transports which were incompatible with the present-day thermohaline circulation. It would therefore be difficult to recommend coupling this version of

the CCC atmospheric model to an ocean model without flux corrections.

A fresh approach was taken in Chapter 4 where a new extension of the traditional mixed boundary conditions was developed to include the previously neglected sea surface temperature-evaporation feedback in time-dependent studies of the ocean's thermohaline circulation. Climatological profiles of the latitude-dependent Bowen ratio and net radiation over the ocean were combined with the net surface heat flux to estimate the total evaporation. The equilibrium precipitation distribution was then inferred as a remainder from the prescribed (P-E) field, while new precipitation due to time-varying evaporation was distributed according to one of several simple schemes. The positive sign of the feedback for the thermohaline circulation was demonstrated in two preliminary experiments with initially perturbed overturning, and the larger response in the case of initially reduced overturning and high latitude freshening was explained by the nonlinear interaction with convection.

The final theme of this thesis was the effect of the SST-evaporation feedback upon internal variability of the ocean's thermohaline circulation. Three case studies in simple hemispheric box models were discussed. A decadal oscillation under mixed boundary conditions was described as a convective instability due to subsurface warming below the polar halocline, with a possibly advective timescale associated with cyclonic propagation of a fresh anomaly around the poleward perimeter of the basin. The mechanism and timescale of the oscillation were substantially unchanged under the SST-evaporation feedback, although the stochastic effect associated with the time-varying (P-E) field plus net freshening at high latitudes related to the cooling of the sea surface under mixed boundary conditions could shorten the lifetime of the oscillation. In the second example, with a different (P-E) field, weak century timescale variability was excited by the superposition of a white noise component upon the freshwater forcing, but was also demonstrated to be potentially vulnerable to the SSTevaporation feedback. Finally, millennial flush/collapse oscillations of the thermohaline circulation were produced under a (P-E) field with strong polar freshening. Under SST-evaporation feedback, this was replaced with either irregular decadal variability or periodic "flushes" on a short (centuries) timescale. The rapid timescale was discovered to be latent in thermohaline circulations that do not completely collapse during the decoupled phase, with advective subsurface warming by the shallow overturning circulation and probably wind-driven salt transport potentially hastening the onset of the flush.

In conclusion, no fundamental alterations of these three mechanisms for internal variability of the thermohaline circulation were found under the present simple parameterization of the SST-evaporation feedback, which would tend to support the accepted use of fixed (P-E) fields as a first-order approximation to airsea interaction in uncoupled ocean models. In the future however, it may be interesting to consider other aspects of the hydrological cycle in the North Atlantic such as sea ice and Arctic freshwater export, and their roles in low frequency variability of the thermohaline circulation.

Appendix A - The Bryan-Cox OGCM

The Bryan-Cox ocean general circulation model (Cox, 1984) is a primitive equation model formulated in spherical coordinates. The Boussinesq, hydrostatic and rigid lid assumptions are made, and sub-grid scale mixing of momentum and tracers is parameterized by Laplacian horizontal and vertical viscosities (A_{MH}, A_{MV}) and diffusivities (A_{TH}, A_{TV}) . The model equations are solved using centred time (leapfrog) differencing for the advective terms (with forward Euler timesteps at regular intervals to prevent the solution splitting) and forward differencing for the diffusive terms. The Coriolis term is handled semi-implicitly so as to allow a timestep longer than the inertial period, and so is the hydrostatic component of pressure. The rectangular grid structure follows an Arakawa B-scheme with horizontal velocities and tracers carried on separate meshed lattices, while vertical velocity is calculated at levels intermediate between the main grids. The finite differencing scheme conserves energy, apart from dissipative effects, in the sense that exchanges between the kinetic and potential energy pools are accomplished without leakage (Semtner, 1986). Heat and salt are conserved separately, and density is calculated using a third-order polynomial approximation at each depth to the Knudsen pressure-dependent equation of state (Fofonoff, 1962). Surface wind stresses and buoyancy fluxes are prescribed as body forces over the depth of the top layer.

The newer MOM (Modular Ocean Model) version of the code (Pacanowski et al., 1991) is intended as a more user-friendly and more flexible version of the same model, with a number of new options. For consistency, only those options to make it as similar as possible to the old Cox (1984) model were used in this thesis (for example, the metric terms were neglected in the momentum equations). Two remaining differences were the substitution of the UNESCO (1981) equation of state for the older Knudsen version, and the replacement of the successive-overrelaxation Poisson solver for the barotropic streamfunction by a conjugate

gradient method.

Appendix B - The Canadian Climate Centre AGCM

The original version (GCM I) of the CCC AGCM and its equilibrium climate were described in Boer et al. (1984a,b): seven variables (vorticity, divergence, geopotential, temperature, dew-point depression, vertical velocity and surface pressure) are solved for using seven equations (vorticity and divergence of horizontal wind, thermodynamic and moisture equations, surface pressure, continuity and the hydrostatic assumption). Horizontal and vertical eddy fluxes are parameterized, and vertically propagating gravity waves are included separately. The second generation version (GCM II) features in addition a slab ocean, thermodynamic sea ice, an interactive cloud scheme and a single layer soil model with fairly sophisticated treatment of land surface processes. The resolution is described as T32/L10, signifying triangular spectral truncation at 32 longitudinal waves, and ten vertical levels.

The slab ocean in GCM II consists of a homogeneous layer 50 m deep with interactive exchange of heat with the atmosphere through both turbulent and radiative processes, plus prescribed internal heat fluxes parameterizing horizontal heat transport and exchange of heat with the deep ocean. The heat budget for the ocean layer is written as:

$$\rho_{w}C_{w}H\frac{\partial T_{w}}{\partial t} = F_{a} - R \tag{A.1}$$

where ρ_w and C_w are the density and heat capacity of water, H is the depth of the layer, F_a is the exchange of heat with the atmosphere and R is the residual term representing internal heat fluxes. F_a is calculated as the sum of solar and terrestrial radiation plus latent and sensible heat exchange. R is calculated for each month of the year as the difference between the monthly mean net surface heat flux F_a from a simulation with prescribed climatological SSTs (Alexander and Mobley, 1976) and the net surface heat flux deduced from the change in local heat storage of the slab implied by the SST climatology:

$$R = (\overline{F}_{a}) - \rho_{w}C_{w}H\frac{\partial \overline{T}_{w}}{\partial t}$$
(A.2)

where the overbar signifies a monthly mean. This strategy is intended to ensure a distribution of SSTs close to climatology while avoiding explicitly modelling advective and deep ocean exchanges. A similar (but more complicated) residual is calculated in ice-covered areas.

The sea ice model is a simple snow-ice model of the type proposed by Semtner (1976). Ice begins to form when the temperature of the ocean mixed layer decreases below 271 K, but the surface is not considered ice-covered until a minimum mass is exceeded. The mixed layer temperature is maintained at freezing point from then on, but the surface temperature (T_s) is free to evolve in response to the net heat fluxes from the atmosphere and through the ice, and satisfies an energy balance equation:

$$C_{s} \frac{\partial T_{s}}{\partial t} = F_{a} - F_{i} + L_{f} \left(\frac{\partial M_{s}}{\partial t} + \frac{\partial M_{i}}{\partial t} \right)$$
(A.3)

where L_f is the latent heat of fusion, C_s is an effective heat capacity (a mass-weighted mean of the snow and ice heat capacities), F_a is the diurnally-varying surface heat flux and F_i is the internal heat flux due to heat conduction through the snow and ice layers, assumed constant with depth, and calculated as:

$$F_{i} = \frac{T_{s} - T_{b}}{[(M_{i}/\rho_{i}k_{i}) + (M_{s}/\rho_{s}k_{s})]}$$
(A.4)

where T_b is the temperature at the base of the ice (271 K), T_s is the moving diurnal mean of the surface temperature, M_i and M_s are ice and snow masses (per unit area) with corresponding densities ρ_i and ρ_s and heat conductivities k_i and k_s . Melting may occur at both the air-ice and sea-ice interfaces, and snow whose density exceeds that of the underlying ice is converted to ice. The area covered by leads (or thin ice) is estimated from a simple empirical function of the sea ice mass, and is retained for use in the calculation of albedo. An ice-ocean flux F_o must be specified at the bottom of the ice layer, as mentioned above, and is adjusted during the spinup to produce the correct ice area and mass according to

climatology. Only a few annual cycles are needed for the values of $F_{\rm o}$ to converge.

References

- Alexander, R. C. and R. L. Mobley, 1976: Monthly average sea surface temperatures and ice pack limits on a 1° global grid. Mon. Wea. Rev., 104, 143-148.
- Anderson, D. L. T. and J. Willebrand, 1992: Recent advances in modelling the ocean circulation and its effects on climate. Rep. Prog. Phys., 55, 1-37.
- Baumgartner, A. and E. Reichel, 1975: The World Water Balance, Elsevier, Amsterdam, 179 pp.
- Berger, W. H., 1987: Ocean ventilation during the last 12,000 years: Hypothesis of counterpoint deep water production. Marine Geol., 78, 1-10.
- Birchfield, E. G., H. Wang and J. R. Rich, 1994: Century/millennium internal climate oscillations in an ocean-atmosphere-continental ice sheet model. J. Geophys. Res., 99, 12459-12470.
- Blanc, T. V., 1985: Variation of bulk-derived surface flux, stability and roughness results due to the use of different transfer coefficient schemes. J. Phys. Oceanogr., 15, 650-659.
- Boer, G. J., N. A. McFarlane and R. Laprise, 1984a: The climatology of the Canadian Climate Centre general circulation model as obtained from a fiveyear simulation. Atmos.-Ocean, 22, 430-473.
- Boer, G. J., N. A. McFarlane and M. Lazare, 1992: Greenhouse gas-induced climate change simulated with the CCC second generation general circulation model. J. Climate, 5, 1045-1077.
- Boer, G. J., N. A. McFarlane, R. Laprise, J. D. Henderson and J.-P. Blanchet, 1984b: The Canadian Climate Centre spectral atmospheric general circulation model. Atmos.-Ocean, 22, 397-429.
- Bond, G., W. Broecker, S. Johnsen, J. McManus, L. Labeyrie, J. Jouzel and G. Bonani, 1993: Correlations between climate records from North Atlantic sediments and Greenland ice. Nature, 365, 143-147.
- Bourke, R. H. and R. P. Garrett, 1987: Sea ice thickness distribution in the Arctic Ocean. Cold Reg. Sci. Technol., 13, 259-280.
- Boyle, E. A., 1990: Quaternary deepwater paleoceanography. Science, 249, 863-

- Boyle, E. A. and L. D. Keigwin, 1985: Comparison of Atlantic and Pacific paleochemical records for the last 215,000 years: changes in deep ocean circulation and chemical inventories. Earth Planet Sci. Lett., 76, 135-150.
- Broecker, W. S., 1989: The salinity contrast between the Atlantic and Pacific Oceans during glacial time. Paleoceanogr., 4, 207-212.
- Broecker, W. S., 1991: The great global conveyor. Oceanography, 4, 79-89.
- Broecker, W. S. and G. H. Denton, 1990: What drives glacial cycles? Sci. Am., 262-1, 49-56.
- Broecker, W. S., D. M. Peteet and D. Rind, 19°5: Does the ocean-atmosphere system have more than one stable mode of operation? Nature, 315, 21-26.
- Broecker, W. S., T. H. Peng, J. Jouzel and G. Russell, 1990a: The magnitude of global fresh-water transports of importance to ocean circulation. Climate Dyn., 4, 73-79.
- Broccker, W. S., G. Bond, M. Klas, G. Bonani and W. Wolfli, 1990b: A salt oscillator in the glacial Atlantic? 1. The concept. Paleoceanogr., 5, 469-477.
- Bryan, F. O., 1986: Maintenance and variability of the thermohaline circulation. Ph.D. thesis, Princeton University, 254 pp.
- Bryan, F. O., 1987: Parameter sensitivity of primitive equation ocean general circulation models. J. Phys. Oceanogr., 17, 970-985.
- Bryan, K., 1984: Accelerating the convergence to equilibrium of ocean-climate models. J. Phys. Oceanogr., 14, 666-673.
- Bryan, K. and W. W. Hsieh, 1995: The steric component of sea level rise associated with enhanced greenhouse warming; a model study. Submitted to J. Phys. Oceanogr.
- Bryan, K. and L. J. Lewis, 1979: A water mass model of the world ocean. J. Geophys. Res., 84, 2503-2517.
- Bryan, K., S. Manabe and R. C. Pacanowski, 1975: A global ocean-atmosphere climate model. Part II. The ocean circulation. J. Phys. Oceanogr., 5, 30-46.

- Budyko, M. I.. 1982: *The Earth's Climate: Past and Future*. Academic Press, London, 307 pp.
- Colin de Verdière, A., 1988: Buoyancy driven planetary flows. J. Mar. Res., 46, 215-265.
- Cox, M. D., 1984: A primitive equation, three-dimensional model of the ocean. GFDL Ocean Group Tech. Rept. No 1.
- Cummins, P. F., 1991: The deep water stratification of ocean general circulation models. Atmosphere-Ocean, 29, 563-575.
- Dansgaard, W. S. J. Johnsen, H. B. Clausen, D. Dahl-Jensen, N. S. Gundestrup,
 C. U. Hammer, C. S. Hvidberg, J. P. Steffensen, A. E. Sveinbjörnsdottir,
 J. Jouzel and G. Bond, 1993: Evidence for general instability of past climate from a 250-kyr ice-core record. Nature, 364, 218-220.
- Dean, W. E., J. V. Gardner and E. Hemphill-Haley, 1989: Changes in redox conditions in deep-sea sediments of the subarctic North Pacific Ocean: Possible evidence for the presence of North Pacific deep water. Paleoceanogr., 4, 639-653.
- Delworth, T., S. Manabe and R. J. Stouffer, 1993: Interdecadal variations of the thermohaline circulation in a coupled ocean-atmosphere model. J. of Climate, 6, 1993-2011.
- Dickson, R. R. and J. Brown, 1994: The production of North Atlantic Deep Water: Sources, rates and pathways. J. Geophys. Res., 99, 12319-12341.
- Dickson, R. R., J. Meincke, S.-A. Malmberg and A. J. Lee, 1988: The "Great Salinity Anomaly" in the northern North Atlantic 1968-1982. Prog. Oceanogr., 20, 103-151.
- Döscher, R., C. W. Böning and P. Herrmann, 1994: Response of circulation and heat transport in the North Atlantic to changes in thermohaline forcing in northern latitudes: a model study. J. Phys. Oceanogr., 24, 2306-2320.
- Duplessy, J.-C. and N. J. Shackleton, 1985: Response of global deep-water circulation to Earth's climatic change 135,000-107,000 years ago. Nature, 316, 500-507.
- Duplessy, J. C., Shackleton, N. J., R. G. Fairbanks, L. Labeyrie, D. Oppo and N. Kallel, 1988: Deepwater source variations during the last climatic cycle and their impact on the global deepwater circulation. Paleoceanogr., 3,

- Duplessy, J. C., E. Bard, M. Arnold, N. J. Shackleton, J. Duprat and L. Labeyrie, 1991a: How fast did the ocean-atmosphere system run during the last glaciation? Earth and Planetary Science Lett., 103, 27-40.
- Duplessy, J.-C., L. Labeyrie, A. Juillet-Leclerc, F. Maitre, J. Duprat and M. Sarnthein, 1991b: Surface salinity reconstruction of the North Atlantic Ocean during the last glacial maximum. Oceanological Acta, 14, 311-324.
- England, M. H., 1993: On the formation of the global-scale water masses in ocean general circulation models. J. Phys. Oceanogr., 23, 1523-1552.
- Esbensen, S. K. and Y. Kushnir, 1981: The heat budget of the global ocean: An atlas based on estimates from surface marine observations. Oregon State Univ. Clim. Res. Inst. Rept. 29, 27 pp.
- Fairbanks, R. G., 1989: A 17,000-year glacio-eustatic sea level record: Influence of glacial melting rates on the Younger Dryas event and deep-ocean circulation. Nature, 342, 637-642.
- Field, M. H., B. Huntley and H. Miller, 1994: Eemian climate fluctuations observed in a European pollen record. Nature, 371, 779-783.
- Fieux, M., C. Andrié, P. Delecluse, A. G. Ilahude, A. Kartavtseff, F. Mantisi, R. Molcard and J. C. Swallow, 1994: Measurements within the Pacific-Indian oceans throughflow region. Deep-Sea Res., 41, 1091-1130.
- Fofonoff, N., 1962: The Sea: Vol. 1 (ed. M. Hill). Interscience, New York, pp.3-30.
- FRAM Group, 1991: An eddy-resolving model of the southern ocean. EOS Trans. AGU, 72, 169, 174-175.
- Fujio, S., T. Kadowaki and N. Imasato, 1992: World ocean circulation diagnostically derived from hydrographic and wind stress fields. 2. The water movement. J. Geophys. Res., 97, 14,439-14,452.
- Gates, W. L. and A. B. Nelson, 1975: A new (revised) tabulation of the Scripps topography on a 1° global grid. Part II: Ocean depths. R-1227-1-ARPA, The Rand Corporation, Santa Monica, CA, 132 pp.
- Gill, A. E. and K. Bryan, 1971: Effects of geometry on the circulation of a threedimensional southern-hemisphere ocean model. Deep-Sea Res., 18, 685-

- Gleckler, P. J., D. A. Randall, G. Boer, R. Colman, M. Dix, V. Galin, M. Helfand, J. Kiehl, A. Kitoh, W. Lau, X.-Z. Liang, V. Lykossov, B. McAvaney, K. Miyakoda, S. Planton, 1994: Cloud-radiative effects on implied oceanic energy transports as simulated by atmospheric general circulation models. PCMDI Rept. No. 15, Lawrence Livermore National Laboratory, 13 pp.
- Godfrey, J. S., 1989: A Sverdrup model of the depth-integrated flow for the world ocean allowing for island circulations. Geophys. Astrophys. Fluid Dynamics, 45, 89-112.
- Gordon, A. L., 1986: Interocean exchange of thermocline water. J. Geophys. Res., 91, 5037-5046.
- Gordon, A. L., R. F. Weiss, W. M. Smethie and M. J. Warner, 1992: Thermocline and intermediate water communication between the South Atlantic and Indian Oceans. J. Geophys. Res., 97, 7223-7240.
- Greatbatch, R. J. and S. Zhang, 1995: An interdecadal oscillation in an idealized ocean basin forced by constant heat flux. Submitted to J. of Climate.
- Greatbatch, R. J., A. F. Fanning, A. D. Goulding and S. Levitus, 1991: A diagnosis of interpentadal circulation changes in the North Atlantic. J. Geophys. Res., 96, 22009-22023.
- GRIP (Greenland Ice-Core Project) members, 1993: Climate instability during the last interglacial period recorded in the GRIP ice core. Nature, 364, 203-207.
- Haney, R. L., 1971: Surface thermal boundary condition for ocean circulation models. J. Phys. Oceanogr., 1, 241-248.
- Hasselmann, K., 1976: Stochastic climate models. Tellus, 28, 473-484.
- Hastenrath, S., 1982: On meridional heat transports in the world ocean. J. Phys. Oceanogr., 12, 922-927.
- Hautala, S. L. and S. C. Riser, 1989: A simple model of abyssal circulation, including effects of wind, buoyancy and topography. J. Phys. Oceanogr., 19, 596-611.
- Hautala, S. L., D. H. Roemmich and W. J. Schmitz, 1994: Is the North Pacific

- in Sverdrup balance along 24°N? J. Geophys. Res., 99, 16041-16052.
- Hellerman, S. and M. Rosenstein, 1983: Normal monthly wind stress over the world ocean with error estimates. J. Phys. Oceanogr., 13, 1093-1104.
- Hirst, A. C. and W. Cai, 1994: Sensitivity of a world ocean GCM to changes in subsurface mixing parameterization. J. Phys. Oceanogr., 24, 1256-1279.
- Hirst, A. C. and J. S. Godfrey, 1993: The role of Indonesian throughflow in a global ocean GCM. J. Phys. Oceanogr., 1057-1086.
- Holland, W. R., 1973: Baroclinic and topographic influences on the transport in western boundary currents. Geophys. Fluid Dynamics, 4, 187-210.
- Hsiung, J., 1985: Estimates of global oceanic meridional heat transport. J. Phys. Oceanogr., 15, 1405-1413.
- Huang, R. X., 1993: Real fresh water flux as the upper boundary condition for the salinity balance and thermohaline circulation forced by evaporation and precipitation. J. Phys. Oceanogr., 23, 2428-2446.
- Huang, R. X, 1994: Thermohaline circulation; Energetics and variability in a single-hemisphere basin model. J. Geophys. Res., 99, 12471-12485.
- Hughes, T. M. C. and Weaver, A. J., 1994: Multiple equilibria of an asymmetric two-basin ocean model. J. Phys. Oceanogr., 24, 619-637.
- Imbrie, J., E. A. Boyle, S. C. Clemens, A. Duffy, W. R. Howard, G. Kukla, J. Kutzbach, D. G. Martinson, A. McIntyre, A. C. Mix, B. Molfino, J. J. Morley, L. C. Peterson, N. G. Pisias, W. L. Prell, M. E. Raymo, N. J. Shackleton and J. R. Toggweiler, 1993: On the structure and origin of major glaciation cycles. 1. Linear response to Milankovitch forcing. Paleoceanogr., 7, 701-738.
- Jaeger, L. 1976: Monatskarten des Niederschlags für die ganz Erde. Ber. Dtsch. Wetterdienstes, 18, 38 pp.
- Johnsen, S. J., H. B. Clausen, W. Dansgaard, K. Fuhrer, N. Gundestrup, C. U. Hammer, P. Iversen, J. Jouzel, B. Stauffer and J. P. Steffensen, 1992: Irregular glacial interstadials recorded in a new Greenland ice core. Nature, 359, 311-313.
- Kallel, N., L. D. Labeyrie, A. Juillet-Leclerc and J.-C. Duplessy, 1988: A deep hydrological front between intermediate and deep-water masses in the

- glacial Indian Ocean. Nature, 333, 651-655.
- Kawase, M., 1987: Establishment of deep ocean circulation driven by deep-water production. J. Phys. Oceanogr., 17, 2294-2317.
- Kawase, M., 1993: Effects of a concave bottom geometry on the upwelling-driven circulation in an abyssal ocean basin. J. Phys. Oceanogr., 23, 400-405.
- Kawase, M. and D. Straub, 1991: Spinup of source-driven circulation in an abyssal basin in the presence of bottom topography. J. Phys. Oceanogr., 21, 1501-1514.
- Keigwin, L. D., 1987: North Pacific deep water formation during the latest glaciation. Nature, 330, 362-364.
- Keigwin, L. D. and G. A. Jones, 1994: Western North Atlantic evidence for millennial-scale changes in ocean circulation and climate. J. Geophys. Res., 99, 12397-12410.
- Keigwin, L. D., G. A. Jones, S. J. Lehman and E. A. Boyle, 1991: Deglacial meltwater discharge, North Atlantic deep circulation and abrupt climate change. J. Geophys. Res., 96, 16,811-16,826.
- Labeyrie, L. D., J. C. Duplessy and P. L. Blanc, 1987: Variations in mode of formation and temperature of oceanic deep waters over the past 125,000 years. Nature, 327, 477-482.
- Lehman, S. J. and L. D. Keigwin, 1992: Sudden changes in North Atlantic circulation during the last deglaciation. Nature, 356, 757-762.
- Levitus, S. 1982: Climatological Atlas of the World Ocean. NOAA Prof. Paper No. 13, U.S. Department of Commerce, NOAA, Washington, D.C.
- Levitus, S. 1989: Interpentadal variability of temperature and salinity at intermediate depths of the North Atlantic Ocean, 1970-1974 versus 1955-1959. J. Geophys. Res., 5, 6091-6132.
- Lynch-Steiglitz, J. and R. G. Fairbanks, 1994: A conservative tracer for glacial ocean circulation from carbon isotope and palaeo-nutrient measurements in benthic foraminefera. Nature, 369, 308-310.
- Lynch-Stieglitz, J., R. G. Fairbanks and C. D. Charles, 1994: Glacial-interglacial history of Antarctic Intermediate Water: Relative strengths of Antarctic versus Indian Ocean sources. Paleoceanogr., 9, 7-29.

- Maas, L. R. M., 1995: A simple model for the three-dimensional, thermally and wind-driven ocean circulation. Submitted to Tellus.
- Macdonald, A., 1993: Property fluxes at 30°S and their implications for the Pacific-Indian throughflow and the global heat budget. J. Geophys. Res., 98, 6851-6868.
- Manabe, S. and R. J. Stouffer, 1988: Two stable equilibria of a coupled oceanatmosphere model. J. Climate, 1, 841-866.
- Manabe, S., R. J. Stouffer, M. J. Spelman and K. Bryan, 1991: Transient responses of a coupled ocean-atmosphere model to gradual changes of atmospheric CO₂. Part I: Annual mean response. J. Climate, 4, 785-818.
- Marotzke, J., 1990: Instabilities and multiple equilibria of the thermohaline circulation. Ph.D. thesis, Institut for Meereskunde, Christian-Albrechts-Universität, Kiel, 126 pp.
- Marotzke, J., 1994: Ocean models in climate problems. In *Ocean Processes in Climate Dynamics: Global and Mediterranean Examples*. Kluwer Academic Publishers, The Netherlands, pp. 79-109.
- Marotzke, J. and J. Willebrand, 1991: Multiple equilibria of the global thermohaline circulation. J. Phys. Oceanogr., 21, 1372-1385.
- Marotzke, J. P. Welander and J. Willebrand, 1988: Instability and multiple steady states in a meridional-plane model of the thermohaline circulation. Tellus, 40A, 162-172.
- Matano, R. P. and S. G. H. Philander, 1993: Heat and mass balances of the South Atlantic Ocean calculated from a numerical model. J. Geophys. Res., 98, 977-984.
- McCartney, M.S., 1993: Crossing of the equator by the deep western boundary current in the western Atlantic Ocean. J. Phys. Oceanogr., 23, 1953-1974.
- McFarlane, N. A., G. J. Boer, J.-P. Blanchet and M. Lazare, 1992: The Canadian Climate Centre second generation general circulation model and its equilibrium climate. J. Climate, 5, 1013-1044.
- Mikolajewicz, U. and E. Maier-Reimer, 1990: Internal secular variability in an ocean general circulation model. Climate Dyn., 4, 145-156.
- Mikolajewicz, U. and E. Maier-Reimer, 1994: Mixed boundary conditions in

- ocean general circulation models and their influence on the stability of the model's conveyor belt. J. Phys. Oceanogr., 99, 22633-22644.
- Moore, A. M. and C. J. C. Reason, 1993: The response of a global ocean general circulation model to climatological surface boundary conditions for temperature and salinity. J. Phys. Oceanogr., 23, 300-328.
- Munk, W. H., 1966: Abyssal recipes. Deep-Sea Res., 13, 707-730.
- Myers, P. G. and A. J. Weaver, 1992: Low-frequency internal oceanic variability under seasonal forcing. J. Geophys. Res., 97, 12707-12730.
- Mysak, L. A., T. F. Stocker and F. Huang, 1993: Century-scale variability in a randomly forced, two dimensional thermohaline ocean circulation model. Climate Dyn., 8, 103-116.
- Oberhuber, J. M., 1988: An atlas based on the "COADS" data set: The budgets of heat, buoyancy and turbulent kinetic energy at the surface of the global ocean. Max Planck Institut für Meteorologie, Rept. No. 15.
- Oppo, D. W. and R. G. Fairbanks, 1987: Variability in the deep and intermediate water circulation of the Atlantic Ocean during the past 25,000 years: Northern Hemisphere modulation of the Southern Ocean. Earth and Plan. Sci. Letters, 86, 1-15.
- Oppo, D. W. and R. G. Fairbanks, 1990: Atlantic Ocean thermohaline circulation of the last 150,000 years: Relationship to climate and atmospheric CO₂. Paleoceanogr., 5, 277-288.
- Oppo, D. W. and S. J. Lehman, 1993: Mid-depth circulation of the subpolar North Atlantic during the last glacial maximum. Science, 259, 1148-1152.
- Pacanowski, R. C., K. W. Dixon and A. Rosati, 1991: The GFDL Modular Ocean Model Users Guide version 1.0. GFDL Ocean Group Tech. Rept. No. 2, 46 pp.
- Pedlosky, J., 1992: The baroclinic structure of the abyssal circulation. J. Phys. Oceanogr., 22, 652-659.
- Pedlosky, J. and D. C. Chapman, 1993: Baroclinic structure of the abyssal circulation and the role of meridional topography. J. Phys. Oceanogr., 23, 979-991.
- Peixoto, J. P. and A. H. Oort, 1992: Physics of Climate. American Institute of

- Physics, New York, 520 pp.
- Peterson, R. G., 1988: On the transport of the Antarctic Circumpolar Current through Drake Passage and its relation to wind. J. Geophys. Res., 93, 13993-14004.
- Rahmstorf, S. and J. Willebrand, 1995: The role of temperature feedback in stabilising the thermohaline circulation. Submitted to J. Phys. Oceanogr.
- Read, J. F. and R. T. Pollard, 1993: Structure and transport of the Antarctic Circumpolar Current and Agulhas Return Current at 40°E. J. Geophys. Res., 98, 12,281-12,296.
- Reid, J. L., 1961: On the temperature, salinity and density differences between the Atlantic and Pacific oceans in the upper kilometre. Deep-Sea Res., 7, 265-275.
- Reid, J. L. and R. J. Lynn, 1971: On the influence of the Norwegian-Greenland and Weddell seas upon the bottom waters of the Indian and Pacific oceans. Deep-Sea Res., 18, 1063-1088.
- Rhines, P. B, 1993: Oceanic general circulation: Wave and advection dynamics. In *Modelling Oceanic Climate Interactions*, eds J. Willebrand and D. L. T. Anderson. NATO ASI Series, Springer-Verlag.
- Rintoul, S. R., 1991: South Atlantic interbasin exchange. J. Geophys. Res., 96, 2675-2692.
- Rooth, C., 1982: Hydrology and ocean circulation. Prog. Oceanogr., 11, 131-149.
- Sarnthein, M., K. Winn, S. J. A. Jung, J.-C. Duplessy, L. Labeyrie, H. Erlenkauser and G. Ganssen, 1994: Changes in east Atlantic deepwater circulation over the last 30,000 years: Eight time slice reconstructions. Paleoceanogr., 9, 209-267.
- Schmitt, R. W., P. S. Bogden and C. E. Dorman, 1989: Evaporation minus precipitation and density fluxes for the North Atlantic. J. Phys. Oceanogr., 19, 1208-1221.
- Schmitz, W. J. and M. S. McCartney, 1993: On the North Atlantic circulation. Rev. Geophys., 31, 29-49.
- Schulman, E. E., 1975: A study of topographic effects. In *Numerical Models of Ocean Circulation Proceedings*. Ocean Affairs Board, Natl. Acad. of Sci.,

- pp.147-167.
- Semtner, A. J., 1976: A model for the thermodynamic growth of sea ice in numerical investigations of climate. J. Phys. Oceanogr., 6, 379-389.
- Semtner, A. J., 1986: Finite-difference formulation of a world ocean model. In *Advanced Physical Oceanographic Numerical Modelling*, ed. J. J. O'Brien. D. Reidel Publishing Company, pp.187-202.
- Semtner, A. J. and R. M. Chervin, 1992: Ocean general circulation from a global eddy-resolving model. J. Geophys. Res., 97, 5493-5550.
- Shackleton, N. J., J.-C. Duplessy, M. Arnold, P. Maurice, M. A. Hall and J. Cartlidge, 1988: Radiocarbon age of last glacial Pacific deep water. Nature, 335, 708-711.
- Sikes, E. L., L. D. Keigwin and W. B. Curry, 1991: Pliocene paleoceanography: Circulation and oceanographic changes associated with the 2.4 Ma glacial event. Paleoceanogr., 6, 245-257.
- Slowey, N. C. and W. B. Curry, 1992: Enhanced ventilation of the North Atlantic subtropical gyre thermocline during the last glaciation. Nature, 358, 665-668.
- Southon, J. R., D. E. Nelson and J. S. Vogel, 1990: A record of past oceanatmosphere radiocarbon differences from the Northeast Pacific. Paleoceanogr., 5, 197-206.
- Speer, K. G. and M. S. McCartney, 1992: Bottom water circulation in the western North Atlantic. J. Phys. Oceanogr., 22, 83-92.
- Stocker, T. F. and L. M. Mysak, 1992: Climatic fluctuations on the century timescale: A review of high-resolution proxy data and possible mechanisms. Climatic Change, 20, 227-250.
- Stocker, T. F. and D. G. Wright, 1991a: A zonally averaged ocean model for the thermohaline circulation. Part II. Interocean circulation in the Pacific-Atlantic basin system. J. Phys. Oceanogr., 21, 1725-1739.
- Stocker, T. F. and D. G. Wright, 1991b: Rapid transitions of the ocean's deep circulation induced by changes in surface water fluxes. Nature, 351, 729-732.
- Stocker, T. F., D. G. Wright and L. A. Mysak, 1992: A zonally-averaged, coupled

- ocean-atmosphere model for paleoclimate studies. J. Climate, 5, 773-797.
- Stommel, H., 1961: Thermohaline convection with two stable regimes of flow. Tellus, 13, 224-230.
- Stommel, H. and A. B. Arons, 1960: On the abyssal circulation of the world ocean II. An idealized model of the circulation pattern and amplitude in oceanic basins. Deep-Sea Res., 6, 217-233.
- Straub, D. N. and P. B. Rhines, 1990: Effects of large-scale topography on abyssal circulation. J. Mar. Res., 48, 223-253.
- Thouveny, N., J.-L. de Beaulieu, E. Bonifay, K. M. Creer, J. Guiot, M. Icole, S. Johnsen, J. Jouzel, M. Reille, T. Williams and D. Williamson, 1994: Climate variations in Europe over the past 140 kyr deduced from rock magnetism. Nature, 371, 503-506.
- Toggweiler, J. R. and B. Samuels, 1993a: Is the magnitude of the deep outflow from the Atlantic Ocean actually governed by southern hemisphere winds? In *The Global Carbon Cycle*, ed. M. Heimann. NATO ASI Series, Springer-Verlag, Berlin.
- Toggweiler, J. R. and B. Samuels, 1993b: New radiocarbon estimates on the upwelling of abyssal water to the ocean's surface. In *The Global Carbon Cycle*, ed. M. Heimann. NATO ASI Series, Springer-Verlag, Berlin.
- Toggweiler, J. R. and B. Samuels, 1995: Effect of Drake Passage on the global thermohaline circulation. Deep-Sea Res., accepted.
- Toggweiler, J. R., K. Dixon and K. Bryan, 1989: Simulations of radiocarbon in a coarse-resolution world ocean model. 1. Steady state prebomb distributions. J. Geophys. Res., 94, 8217-8242.
- Tomczak, M. and J. S. Godfrey, 1994: Regional Oceanography: An Introduction. Pergamon Press, U.K., 422 pp.
- Trenberth, K.E., 1994: Decadal variability and climate change in large-scale interaction between the atmosphere and the ocean. Contribution to IPCC 1995 assessment, Chapter 7.
- Tziperman, E., 1986: On the role of interior mixing and air-sea fluxes in determining the stratification and circulation of the oceans. J. Phys. Oceanogr., 16, 680-693.

- Tzedakis, P. C., K. D. Bennett and D. Magri, 1994: Climate and the pollen record. Nature, 370, 513.
- UNESCO, 1981: 10th report of the joint panel on oceanographic tables and standards. UNESCO Tech. Papers in Marine Sci. No. 36, Paris.
- Veum, T., E. Jansen, M. Arnold, I. Beyer and J.-C. Duplessy, 1992: Water mass exchange between the North Atlantic and the Norwegian Sea during the past 28,000 years. Nature, 356, 783-785.
- Vreugdenhil, C. B. and D. G. Wright, 1993: A zonally-averaged model for ocean circulation. Unpublished manuscript.
- Warren, B. A., 1983: Why is no deep water formed in the North Pacific? J. Marine Res., 41, 327-347.
- Washington, W. M., G. A. Meehl, L. Verplank and T. W. Bettge, 1994: A world ocean model for greenhouse sensitivity studies: resolution intercomparison and the role of diagnostic forcing. Climate Dyn., 9, 321-344.
- Weaver, A. J., 1994: Decadal-millennial internal oceanic variability in coarse resolution OGCMs. In *The Natural Variability of the Climate System on the 10-100 Year Timescales*. National Acad. Press, U.S.A.
- Weaver, A. J. and C. J. R. Garrett, 1993. On the sensitivity of the thermohaline circulation in ocean general circulation models to the vertical eddy diffusivity. Unpublished manuscript.
- Weaver, A. J. and T. M. C. Hughes, 1992: Stability and variability of the thermohaline circulation and its link to climate. In *Trends in Physical Oceanography*, Research Trends Series, vol. 1, pp. 15-70. Council of Scientific Research Integration, Trivandrum, India.
- Weaver, A. J. and T. M. C. Hughes, 1994: Rapid interglacial climate fluctuations driven by North Atlantic ocean circulation. Nature, 367, 447-450.
- Weaver, A. J. and W. G. Lee, 1995: A global OGCM for coupling to the Canadian Climate Centre AGCM: Climatology and Sensitivity Analysis. In preparation.
- Weaver, A. J. and E. S. Sarachik, 1990: On the importance of vertical resolution in certain ocean circulation models. J. Phys. Oceanogr., 20, 600-609.
- Weaver, A. J. and E. S. Sarachik, 1991a: Evidence for decadal variability in an

- ocean general circulation model: An advective mechanism. Atmosphere-Ocean, 29, 197-231.
- Weaver, A. J. and E. S. Sarachik, 1991b: The role of mixed boundary conditions in numerical models of the ocean's climate. J. Phys. Oceanogr., 21, 1470-1493.
- Weaver, A. J., S. M. Aura and P. G. Myers, 1994: Interdecadal variability in an idealized model of the North Atlantic. J. Geophys. Res., 99, 12,423-12,442.
- Weaver, A. J., J. Marotzke, P. F. Cummins and E. S. Sarachik, 1993: Stability and variability of the thermohaline circulation. J. Phys. Oceanogr., 23, 39-60.
- Welander, P., 1969: Effects of planetary topography on the deep-sea circulation. Deep-Sea Research, 16 (Suppl.), 369-391.
- Welander, P., 1982: A simple heat-salt oscillator. Dyn. Atmos. Oceans, 6, 233-242.
- Welander, P., 1986: Thermohaline effects in the ocean circulation and related simple models. In Large-Scale Transport Processes in Oceans and Atmospheres, eds. J. Willebrand and D. L. T. Anderson. D. Reidel Publishing, pp.163-200.
- Weisse, R., U. Mikolajewicz and E. Maier-Reimer, 1994: Decadal variability of the North Atlantic in an ocean general circulation model. J. Geophys. Res., 99, 12,411-12,422.
- Weyl, P. K., 1968: The role of the oceans in climate change: A theory of the Ice Ages. Meteor. Monogr., 8, 30.
- White, J. W. C., 1993: Don't touch that dial. Nature, 364, 186.
- Wijffels, S. E., R. W. Schmitt, H. L. Bryden and A. Stigebrandt, 1992: On the transport of freshwater by the oceans. J. Phys. Oceanogr., 22, 155-162.
- Winton, M., 1993: Numerical investigations of steady and oscillating thermohaline circulations. Ph.D. thesis, Univ. of Washington, 155 pp.
- Winton, M. and E. S. Sarachik, 1993: Thermohaline oscillations induced by strong steady salinity forcing of an ocean general circulation model. J. Phys. Oceanogr., 23, 1389-1410.

- Wright, D. G. and T. F. Stocker, 1991: A zonally averaged ocean model for the thermohaline circulation. Part I. Model development and flow dynamics. J. Phys. Oceanogr., 21, 1713-1724.
- Wright, D. G. and T. F. Stocker, 1992: Sensitivities of a zonally averaged global ocean circulation model. J. Geophys. Res., 97, 12,707-12,730.
- Wright, D. G., C. B. Vreugdenhil and T. M. C. Hughes, 1995: Vorticity dynamics and zonally-averaged ocean circulation models. Submitted to J. Phys. Oceanogr.
- Yin, F. L., I. Y. Fung and C. K. Chu, 1992: Equilibrium response of ocean deepwater circulation to variations in Ekman pumping and deep-water sources. J. Phys. Oceanogr., 22, 1129-1157.
- Zahn, R. and A. C. Mix, 1991: Benthic foraminefera δ¹³C in the ocean's temperature-salinity-density field: Constraints on ice age thermohaline circulation. Paleoceanogr., 6, 1-20.
- Zahn, R., T. F. Pedersen, B. D. Bornhold and A. C. Mix, 1991: Water mass conversion in the glacial subarctic Pacific (54-N, 148-W): Physical constraints and the benthic planktonic stable isotope record. Paleoceanogr., 6, 543-560.
- Zaucker, F., 1992: Observed versus modelled freshwater fluxes and their impact on the global thermohaline circulation. Ph.D. dissertation, Ruprecht-Karls-Univ., Heidelberg, Germany, 90 pp.
- Zaucker, F., T. F. Stocker and W. S. Broecker, 1993: Atmospheric freshwater fluxes and their effect on the global thermohaline circulation. J. Geophys. Res., 99, 12,443-12,458.
- Zhang, L., 1991: Simple models of thermohaline processes in the ocean. M.Sc. thesis, Dalhousie University, 68 pp.
- Zhang, S., R. J. Greatbatch and C. A. Lin, 1993: A re-examination of the polar halocline catastrophe and implications for coupled ocean-atmosphere modelling. J. Phys. Oceanogr., 23, 287-299.